Polarization Switching in Valence Tautomeric Complexes with Enantiopure Ligands

鄭, 文偉

A Dissertation Submitted to Kyushu University for the Doctorate Degree of Science

Polarization Switching in Valence Tautomeric Complexes with Enantiopure Ligands

Wenwei Zheng

Supervised by Professor Osamu Sato

Department of Chemistry, Graduate School of Science, Kyushu University

2025

Abstract

Dynamic polar materials, capable of switching between different polarization states in response to external stimuli, are attracting significant attention due to their potential applications in molecular sensors, memory devices, and energy harvesting systems. Non-ferroelectric materials with versatile electron dynamics, such as spin crossover, valence tautomerism, and double exchange, have emerged as promising candidates for achieving polarization switching. By rational molecular design and crystal engineering, several complexes exhibiting polarization switching by spin crossover and valence tautomerism have been developed in our laboratory. Among them, the light-induce polarization switching phenomenon holds the potential in the next-generation optoelectronic memory devices. However, the magnitude of light-induced polarization change remains limited with a record of *ca*. 0.3 μC cm^{-2}, which is far from the practical threshold (1 μC cm^{-2}) for capacitive memory. Addressing this limitation by discovering new non-ferroelectric materials capable of achieving significant light-induced polarization changes represents a critical challenge for future research.

In this thesis, we aim to enhance the efficiency of light-induced polarization change by rational molecular design. By density functional theory (DFT) screening based on a previously reported polarization switching material, $[Cr(RR\text{-cth})(\mu\text{-dhbq})Co(SS\text{-cth})_3](PF_6)_3$ (cth = 5,5,7,12,12,14-hexamethyl-1,4,8,11-tetraazacyclotetradecane, dhbq = 3,5-dihydroxy-1,4-benzoquinone), we noticed that the modification by introduction of the enantiopure cth ligand induces distortion in the molecular structure, leading to the significant stabilization of the metastable $[Co_{HS}^{2+}\text{-}dhbq^{2-}\text{-}Cr^{3+}]$ state. This feature could potentially enhance the lifetime of such a metastable state, thereby improving the photoconversion ratio and the induced polarization change. Moreover, as the introduction of chirality interrupts the crystallographic symmetry, the possibility of the molecules being packed in a polar space group would be largely increased even for the homometallic systems.

Following this approach, several polar crystals, including [Cr(SS-cth)(μ-dhbq)Co(SS-cth)$_3$]$(PF_6)_3$·2.5H_2O·0.5MeOH (**2-1**), [Cr(SS-cth)(μ-dhbq)Co(SS-cth)$_3$]$(AsF_6)_3$ (**3-1**), and two dinuclear Fe complexes (**4-1** and **4-2**), were synthesized and thoroughly characterized.

In **Chapter 2**, we investigated the synthesis of physical properties of complex **3-1**. The key challenge in obtaining the pure dinuclear [CoCr] complex with enantiopure ligand lies in the lack of chiral recognition, resulting in contamination of homometallic species. To address this issue, we propose a stepwise synthetic strategy by firstly binding the bridging dhbq ligand with the kinetically inert Cr^{3+} site. In this way, we successfully obtained the desired pure heterometallic species, as confirmed through mass spectrometry. Interestingly, the complex exhibits solvent-dependent valence tautomerism (VT). Magnetization measurements, UV-Vis spectroscopy, and IR spectroscopy in the pristine form revealed partial valence tautomerism with a transition temperature of approximately 170 K. Upon solvent removal, the electron transfer process became nearly complete, and the process was reversible upon reabsorption of the corresponding solvents. X-ray single-crystal structural analyses demonstrated that both forms, before and after the removal of crystalline solvents, are packed in the polar $P2_1$ space group, plausible for polarization switching behavior. Pyroelectric measurements revealed a thermally induced polarization change of approximately 0.27 μC cm^{-2} in the pristine form, while a shift in the transition temperature upon solvent removal could also be detected. These results clearly indicates the capability of this stepwise synthetic methodology in obtaining the dinuclear complexes with an enantiopure ligand and the solvent-dependent polarization switching behavior in such a system.

In **Chapter 3**, we investigated a photoinduced polarization switching behavior in **3-1**. Based on the results in Chapter 2, we proposed enhancing the efficiency of light-induced valence tautomerism (LIVT) by replacing the counterion with a larger anion, AsF_6^-, to further stabilize the [Co_{HS}^{2+}-$dhbq^{2-}$-Cr^{3+}] configuration. Additionally, by recrystallization the product in ethanol, we obtained an optimized molecular orientation in the new crystalline phase. Magnetization analysis confirmed valence tautomerism with a reduced transition temperature of 123 K. Notably, this

compound exhibits wavelength-dependent photomagnetization conversion. Remarkably, the efficiency of LIVT under 1340 nm reached virtually complete. This represents the first reported near-infrared light-excited valence tautomeric transition from [$Co_{LS}^{3+}Cr^{3+}$] to [$Co_{HS}^{2+}Cr^{3+}$] with full photoconversion. This feature might be related to the presence of a broad ligand-to-metal charge transfer (LMCT) band centered at 1400 nm of [Co_{LS}^{3+}-$dhsq^{3-}$-Cr^{3+}] configuration. Pyroelectric measurements after light irradiation revealed an exceptional light-induced polarization change of 2.25 μC cm^{-2}, a value significantly higher than that induced thermally. To clarify the potential differences between light- and thermally-induced states, low-temperature single-crystal structural analyses were conducted before and after 1340 nm irradiation. The post-irradiation results revealed a hidden phase characterized by breaking of translational symmetry, reorientation of host molecules, and directional ion displacement. This phenomenon underpins the larger light-induced polarization change and highlights a novel mechanism for near-infrared light-induced polarization changes via the hidden phase.

In **Chapter 4**, we extend our synthetic strategy to homometallic [Fe_2] complexes and discuss the potential photoinduced inversion of molecular dipole moments in such a system. Preliminary spectroscopic studies suggest the presence of a spin-delocalized ground state in this family of compounds. However, the introduction of enantiopure ligands leads to crystallization in the polar $P2_1$ space group with a slightly asymmetric chemical environments of the two Fe centers. DFT calculations revealed that opposite change in the electron densities on the two Fe sites would occur under irradiation with different wavelengths of light. This intriguing behavior suggests the potential for achieving the unprecedented light-induced polarization inversion using lasers of varying wavelengths.

The objective of this thesis is to design and develop versatile polar crystals exhibiting valence tautomerism through rational molecular design, innovative synthetic strategies, and crystal engineering. These efforts focus on achieving significant macroscopic polarization under controllable conditions. The introduction of the enantiopure cth ligand has been pivotal in breaking

molecular symmetry and obtaining polar crystals. The purification of [CrCo]$(PF_6)_3$ demonstrates the effectiveness of a stepwise synthetic approach in minimizing contamination, which could be extended to other systems with achiral ligands, enriching non-ferroelectric systems and enabling macroscopic polarization changes. Additionally, the synthesis of [CrCo]$(AsF_6)_3$ exemplifies how molecular design and advanced crystal growth techniques can enhance light-induced polarization changes. The polar homometallic $[Fe_2]$ introduces a novel pathway for polarization inversion by controlling directional electron redistribution between two Fe centers in electron-delocalized complexes. These findings open new avenues for exploring polar crystals with macroscopic polarization-switching capabilities, emphasizing the diversity and modifiability of non-ferroelectric crystals.

Contents

Chapter 1. Introduction

1.1 Basics of Molecular Magnetism & Electronically Liable Materials

The initial encounter with magnetic material dates back to approximately 600 B.C. with the discovery of lodestone (Fe_3O_4).[1, 2] This material played a paramount role in human development through the invention of the magnetic compass.[3, 4] However, the systematic investigation of magnetism remained dormant until the 1600s when William Gilbert made significant contributions to the field.[5, 6] Gilbert's experiments confirmed Earth's magnetism by observing the behavior of a versorium near a terrella-like compass needle.[7] Moreover, he was the first to demonstrate that magnetic iron loses its magnetism when heated to red heat, revealing the concept of a critical temperature at which magnetism disappears. This marked the beginning of humanity's fundamental understanding of magnetism. Subsequently, plenty of traditional magnets, including ferromagnetic or ferrimagnetic metal alloys, were discovered and utilized in essential applications such as magnetic storage, hard drives, and electromagnets. The exploration of molecular magnetism trace its origins back to the late 1960s when chemists began investigating the possibility of obtaining organic ferromagnets.[8] This pursuit was inspired by the discovery of certain organic substances exhibiting metal-like conductivity. Simultaneously, theories regarding ferromagnetic coupling were proposed, notably by Harden H. McConnel.[9] In 1967, a significant milestone occurred at *Bell* Laboratories where H. Hollis Wickman *et al*. reported the discovery of a ferromagnetic compound, chlorobis(diethyldithiocarbamate) Fe(III), with S = 3/2 and a critical temperature (T_c) at 2.46 K.[10] Subsequently, the field witnessed an influx of research on magnetic molecular materials, especially in the breakthrough discovery of the single molecular magnet Mn12 complex in 1993, which garnered widespread attention.[11] In contrast to conventional magnetic materials, which are typically characterized by their mechanical brittleness, lack of transparency, heaviness, and reliance on high-temperature processing, molecular magnetic materials offer a distinct advantage. These materials are constructed from discrete molecular

building blocks under moderate conditions. Through the principles of crystal engineering, chemists wield significant control over the connectivity, architectural design, and resultant magnetic properties of molecule-based magnets. This control is achieved by selecting and arranging appropriate building blocks with favorable geometries into arrays of varying dimensions, such as zero-dimensional (0-D), one-dimensional (1-D), two-dimensional (2-D), or three-dimensional (3-D) configurations.[12-14] Importantly, given the rapid pace of technological advancement, there is a growing demand for high-density and miniaturized devices to enhance processing speeds. Molecular-based magnetic materials inherently possess these qualities, making them highly desirable for such applications. Additionally, owing to their unique quantum-size effect, molecular magnets have the potential to exhibit spintronics or serve as qubits for quantum computing, capabilities not readily achievable with conventional magnets. Currently, the area of molecular magnetism represents a sophisticated and continually evolving interdisciplinary domain. Based on the foundational principles of coordination chemistry, it ingeniously integrates the investigation of novel physical properties, molecular design and synthesis of chemistry, and material science. This convergence has promoted molecular magnetism to the frontier of contemporary research, particularly concerning molecular materials that demonstrate multifunctionality.

Different types of magnetization manifest in molecular magnetism due to variations in magnetic coupling among spins under application of magnetic field (Figure 1.1). The saturation magnetization (Ms), which denotes magnetization under a strong applied magnetic field., is contingent on the quantity of spins present in each repeat unit and the characteristics of the interactions among these spins, whether ferromagnetic or antiferromagnetic. Similarly, the intensity of spontaneous magnetization, observed in the absence of applied fields, is influenced by the quantity of spins per repeat unit and their interactions with one another, along with the sample's history. The intensity of the external magnetic field needed to reach saturation varies depending

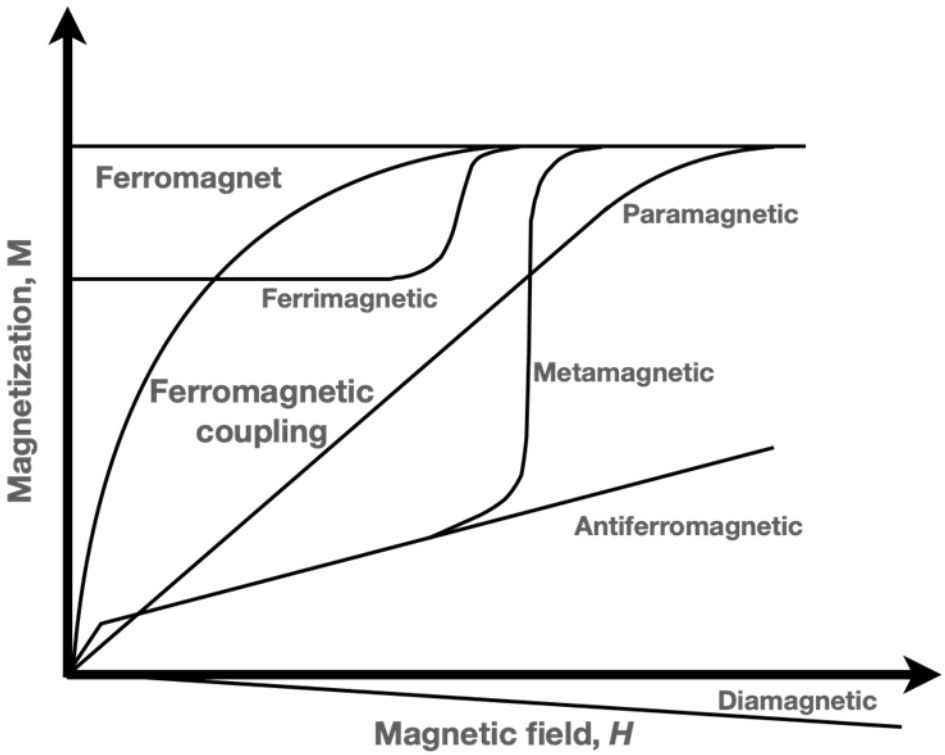

Figure 1.1 Schematic illustration of the fluctuation of magnetization (M) in response to the applied magnetic field (*H*).

on the interactions between ferromagnetic and antiferromagnetic couplings in the materials, along with the experimental temperature. Furthermore, molecular magnetic materials have unveiled plenty of novel and complicated magnetic phenomena, including single-molecule magnets, single-chain magnets, spin-crossover, valence tautomerism, and other magnetic bistable molecules, as well as mixed-valence complexes (MV), spin-flop transitions, and weak ferromagnetism.[15-20] Among them, spin-crossover (SCO), valence tautomerism (VT), and Robin-day MV have garnered significant attention due to their dynamic electronic configuration, which can be modulated by external factors such as temperature, light, and magnetic fields, *etc*.

Spin crossover complexes exhibit two distinct spin states, exemplify as ^{1}A and ^{5}T, which possess similar enthalpies but differing entropies.[21-23] This leads to a change in ΔG^{0} within a specific

temperature range. This temperature-dependent spin state equilibrium, where either the high-spin (*hs*) or low-spin (*ls*) form predominates, is referred to as entropy-driven equilibrium. At high temperatures, the *hs*-Fe^{II} form tends to be favored, while the *ls*-Fe^{II} form is favored at lower temperatures (Figure 1.2). The entropic driving force behind this phenomenon originates from vibrational effects: in the *hs*-Fe^{II} form, antibonding σ orbitals are occupied, leading to elongated Fe-L bond lengths and consequently an increased density of vibrational states.. Additionally, the stretching frequencies of *hs* and *ls* forms in Fe^{II} complexes exhibit significant differences, indicating a large ΔS^0, as supported by temperature-dependent heat capacity measurements.

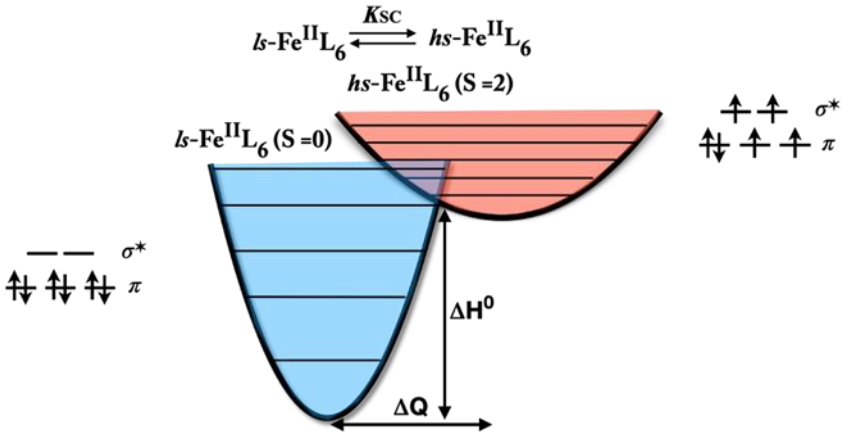

Figure 1.2 Schematic illustration of entropy-driven equilibrium in Fe^{II} SCO complexes.

Valence tautomerism refers to the reversible transfer of electrons between metal ions and their coordinating ligands, which is contingent upon temperature variations.[24, 25] This requires that the bridging ligands possess redox activity similar to that of the metal centers. Among the most commonly employed ligands in cobalt valence tautomerism systems are quinone-type ligands, which exist in both dianionic form (Catecholate, Cat) and radical form (semiquinone, SQ). The occurrence of valence tautomerism is on the energy of the quinone ligand orbitals overlapping with those of the metal, induced by thermal effects. Analogous to spin-crossover (SCO) complexes, the transition from *ls*- Co^{III} (featuring an electronic structure of $(\pi)^6(\sigma^*)^0$) to *hs*- Co^{II} (with an electronic structure of $(\pi)^5(\sigma^*)^2$) is characterized by longer Co-ligand bond lengths, which are

induced by a higher density of vibrational levels in the *hs*- Co^{II} form (Figure 1.3).

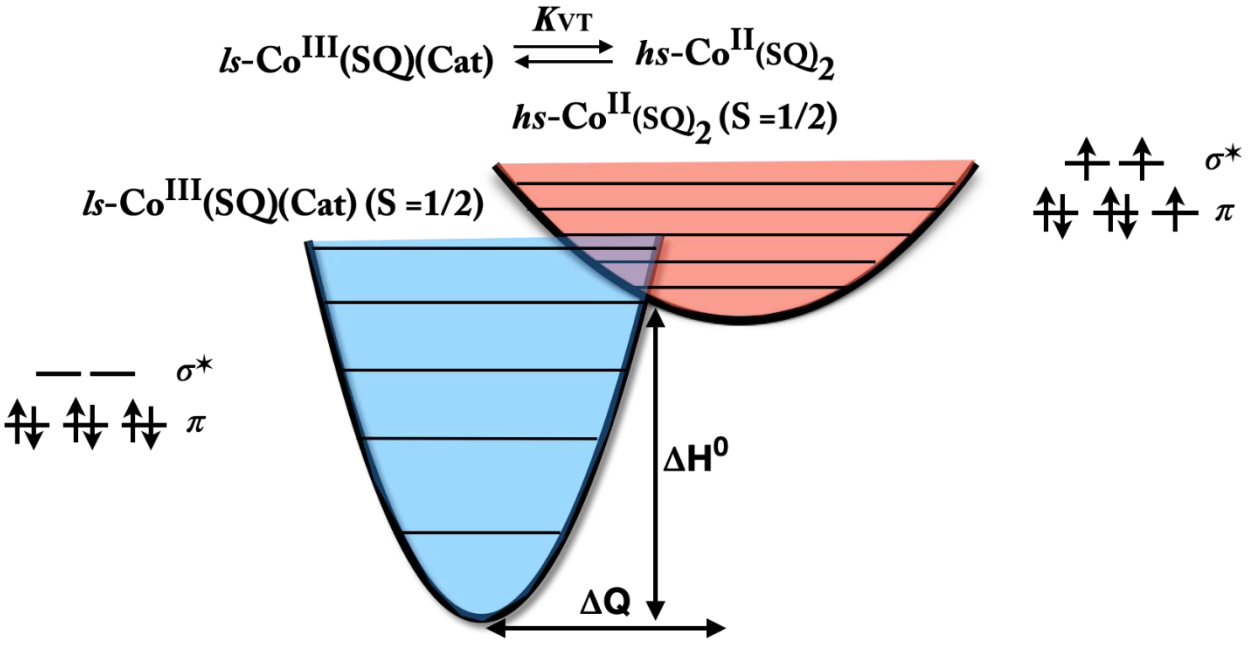

Figure 1.3 Schematic illustration of entropy-driven equilibrium in Co^{II} VT complexes.

Mixed-valence complexes have been a subject of investigation for more than five decades.[26, 27] Especially, in mixed-valence dinuclear complexes, two metal centers (A and B) with different oxidation states are present, allowing for the possibility of electron transfer (noted as •) between the two sites ($A^{\bullet}$--B←→ A--$B^{\bullet}$). When the electron resides on A, it occupies an antibonding orbital centered around A, causing the coordination sphere of A to expand compared to that of B. Conversely, when the electron is located on B, the coordination sphere of B undergoes expansion. Additionally, the metal-ligand bond length changed with the electron transfer between the two states, generally becoming longer in the M^{n+} state compared to the M^{n+1} oxidation state. To describe this antisymmetric breathing behavior of the coordination spheres, a vibrational coordinate Q is introduced, representing the corresponding nuclear relaxation effect (Figure 1.4). There are three possible scenarios: $Q < 0$ (where the bond length of the metal-ligand centered on site A is

expanded), Q = 0 (where the coordination spheres of both sites are identical), and Q > 0 (where the bond length is contracted, opposite to the case of Q < 0).

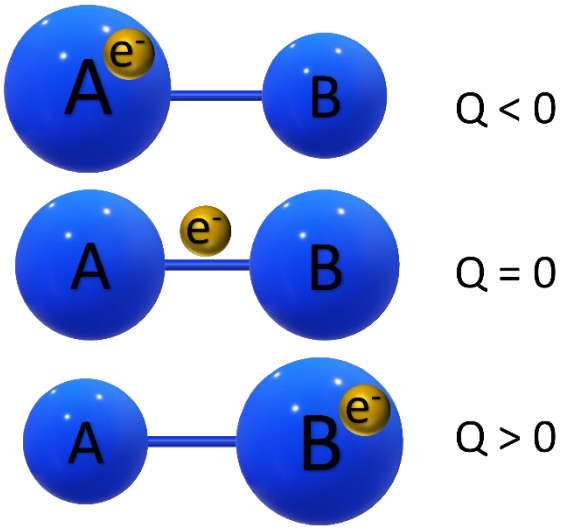

Figure 1.4 Three situations of asymmetric breathing vibration coordinate Q in a mixed-valence dinuclear compound.

Even if so, accelerating the deployment of multi-response molecules requires a crucial step: visualizing the microscopic changes in electronic configuration at a macroscopic level with an electric signal. Thus, it becomes imperative to appropriately design the electronic characteristics, incorporating elements such as ligand field and redox potential, along with optimizing the molecular arrangement within crystals. This strategic approach is indispensable for achieving practical applications. Currently, numerous dynamic crystals have been identified, operating on the principle of switching between different electronic states triggered by light, magnetic fields, and temperature fluctuations (Figure 1.5). Particularly, due to their polar packing mode, changes in electronic configuration can be discerned through pyroelectric currents. However, significant challenges remain in improving performance, refining manipulation methods, and transitioning toward device integration.

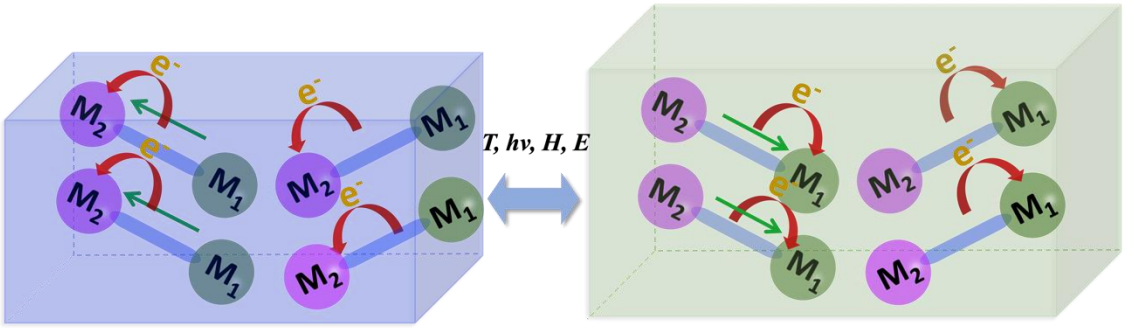

Figure 1.5 Schematic illustration of dynamic crystal whose distinct electronic configuration is switched by external stimuli.

1.1.1 Valence Tautomerism

The first case of valence tautomerism was reported by *et al* in 1980. [28] The Co^{II} was coordinated with a semiquinone, a catecholate, and bipyridine to form 4O/2N configuration where the reverse intramolecular electron transfer occurs between Co and semiquinone induced by temperature. Since then, numerous VT complexes with different metal centers (e.g. Mn, Fe, Ni, Cu, Rh, Ir even recently reported lanthanide) and different states (solid/solution) under various stimulation were successively reported.[29-33]

Contrary to the prevalent investigation of thermal-induced VT, the impact of pressure has been less explored due to practical challenges in experimental characterization. A previous study investigated the pressure effect on [Co(phen)(3,5-dbdiox)$_2$] (phen = 9,10-phenanthroline), wherein the electronic configuration of the cobalt center was measured using K-edge EXAFS and XANES at room temperature.[34] Under increasing pressure to 2.5 GPa, the complex underwent a pressure-induced VT transition from *hs*-Co^{II} to *ls*-Co^{III}. Furthermore, temperature-dependent magnetization studies of [Co(cth)(phendiox)]PF_6 · H_2O (cth = 5,5,7,12,12,14-hexamethyl-1,4,8,11-tetraazacyclotetradecane) were conducted under pressure, revealing that the transition temperature

rises with increasing pressure and exhibits a more gradual shift.[35] Both findings suggest that under high pressure, Co VT complexes stabilize at *ls*-Co^{III} with a smaller molecular volume, resembling the characteristic pressure-induced spin crossover phenomenon.

In 2008, Sato *et al*. reported a notable observation regarding the pressure-induced effects on VT transitions in two dinuclear Co complexes.[36] These complexes share similar molecular structures and bridging ligands, with complex 1 utilizing tpa (tris(2-pyridylmethyl)amine) and complex 2 employing dpqa (di(2-pyridylmethyl)-N-(quinoline-2-ylmethyl)). Under normal pressure of 1 kbar, both complexes exhibited VT transitions with different transition behavior observed via magnetization. Intriguingly, when a minimal pressure of approximately 1.3 kbar was applied to both complexes, the $\chi_m T$ value increased, and the transition temperature shifted to a lower range, suggesting stabilization of *hs*-Co^{II} and/or *ls*-Co^{II} under external pressure (Figure 1.6a). This behavior contrasts with previous cases where applying pressure favored the smaller volume *ls*-Co^{III} state. However, as pressure increased further to around 5 kbar, the transition temperature shifted towards higher temperature ranges, as commonly observed in mononuclear Co VT complexes, yet transitions below 100 K were scarcely influenced (Figure 1.6b-c). The authors attribute this phenomenon to pressure-induced enlargement of the energy difference in enthalpy between valence tautomeric isomers, favoring the stabilization of the *ls*-Co^{II} form over *ls*-Co^{III}, while also affecting ligand-field strength and intermolecular interactions. Consequently, under pressure, charge transfer between *ls*-Co^{III}-$dhbq^{2-}$—*ls*- Co^{II} and *ls*-Co^{III}-$dhsq^{3-}$-*ls*-Co^{III} in the two dinuclear Co VT complexes was hindered, with only spin crossover on the Co center occurring. Thus, the magnetization at low temperatures is attributed to *ls*-Co^{II} rather than the radical of $dhsq^{3-}$.

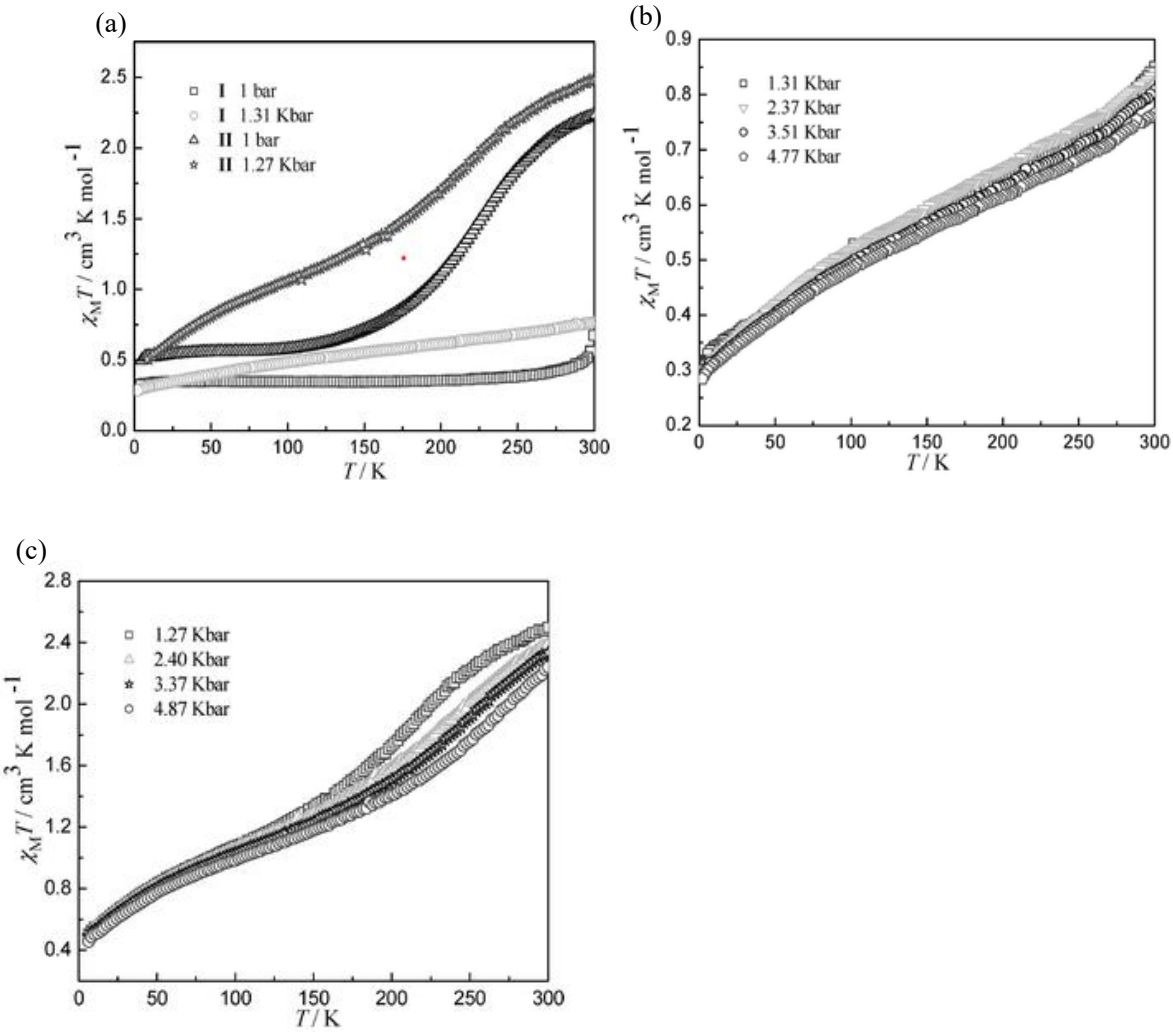

Figure 1.6 (a) Magnetization of complexes 1 and 2 under a normal and minimal pressure. (b) Magnetization of complex 1 under pressure upon to 5 kbar. (c) Magnetization of complex 2 under pressure upon to 5 kbar. [Adapted from Ref. 36]

Following the initial discovery of magnetic field-induced iron (II) spin crossover, it was predicted that valence tautomerism could similarly be induced by magnetic fields, particularly within the critical range of 140 to 220 T in typical Cobalt complexes.[37] This prediction was based on estimating the energy difference between the two spin states at varying temperatures. Subsequently, Mischenko and colleagues experimentally confirmed the magnetic-field-induced VT transition.

They achieved this by subjecting [Co(bpy)(3,5-dbdiox)$_2$] to varying magnetic fields at a temperature of 4.2 K. Following the meticulous elimination of potential interference from paramagnetism under high magnetic fields, the magnetization behavior of the cobalt complex revealed a distinct and seamless transition from *ls*-Co^{III} to *hs*-Co^{II} at approximately 100 T (Figure 1.7). The entropy variation correlated with this transition and the energy difference between the

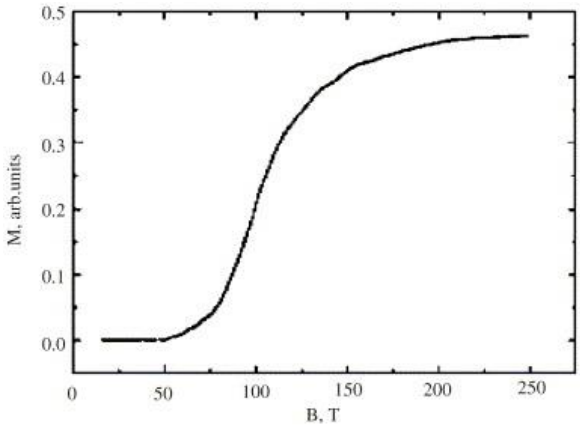

Figure 1.7 The variation of magnetization on [Co(bpy)(3,5-dbdiox)$_2$] under varying magnetic field. [Adapted from Ref. 37]

two tautomers, as derived from the measured critical field, were found to be consistent with those obtained from thermally induced VT transitions. Beyond the influence of external perturbations on valence tautomerism, the intrinsic components of the molecule, such as ancillary ligands, counter ions, and solvents, also exert a significant impact on the modulation of VT transitions.

Valence tautomerism manifests under two essential conditions: firstly, there must be a low degree of covalency in the interaction between the metal ion and the electroactive ligand; secondly, the energy levels of their frontier orbitals should closely align. Importantly, these complexes should display localized electronic structures, minimal orbital mixing, and a narrow energy gap between their electronic tautomers. Introducing redox-active ligands not only facilitates valence tautomerism but also extends the scope to additional switching capabilities via electrochemical

processes. This approach has demonstrated significant efficacy in fine-tuning the critical temperature (T_c) where both tautomers coexist in equal proportions. Moreover, it allows precise manipulation of the net magnetic moments and optical properties of the tautomeric isomers. While historically, valence tautomeric complexes have predominantly relied on quinone or quinone-type ligands paired with various transition metal ions, recent advancements have broadened the repertoire of electroactive ligands.[28, 38-46] This expansion comprises diverse compounds such as Schiff-base, phenoxyl, tetraphenylporphyrin, and polychlorotriphenylmethyl radicals.[44, 47-56] Sato *et al*. reported a new dinuclear cobalt complex with a qpda ligand (dpqa = di(2-pyridyl-methyl-N-(quinoline-2-ylmethyl)amine) that demonstrated a 25% increase in photo-induced valence tautomerism compared to a tpa-type dinuclear cobalt complex (tpa = tris(2-pyridylmethyl)amine).[57] This enhancement was explained by examining the temperature-dependent *hs* to *ls* relaxation of the converted high-spin fraction after irradiation, measured from 10 to 70 K (Figure 1.8).

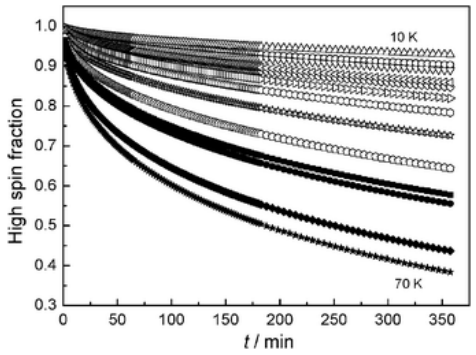

Figure 1.8 Temperature-dependent VT relaxation of photo-induced metastable, measured at 5 K intervals ranging from 10 to 70 K. [Adapted from Ref. 57]

The complex exhibited a smaller thermal activation factor and activation energy, suggesting that at low temperatures, phonon lattice vibration modes influence the relaxation mechanism referring the ground state vibration mode, affecting the tunneling process. Consequently, the relaxation time of the photo-induced metastable state could be extended by increasing intermolecular interactions.

Therefore, the qpda complex, with its greater π-π and C-H···π interactions, affected the relaxation process of the metastable state, resulting in a longer relaxation time compared to the tpa-type complex.

As the second coordination sphere, the influence of counterions on valence tautomerism (VT) is attributed to changes in internal molecular chemical pressure and crystal packing, resulting in varying transition temperatures and the generation of VT. Early investigations into the effect of isolated counterions were challenging due to the presence of solvents in most molecules. However, Dei's group provided an opportunity to explore the effect of different counter anions on [Co(cth)(phendiox)]Y (Y = PF^{6-}, I^{-}, and BPh^{4-}).[35] They found that as the volume of the anions increased, the transition temperature of the Co complexes also increased. Larger anions enhance molecular steric hindrance, preventing the expansion of the crystal lattice during the VT transition. This phenomenon, described as "chemical environmental pressure," is analogous to how physical pressure controls the transition temperature by modifying crystal volume. Interestingly, an opposite trend in VT transition was observed with the complex containing BPh^{4-}. This is attributed to the relatively delocalized electrons in BPh^{4-}, which alter intermolecular coulombic interactions, stabilizing the *ls*-Co^{III} state.

An alternative approach to influencing VT properties is through solvation. Similar to the mechanism by which counter ions affect VT transitions, the size and nature of solvent molecules can alter molecular arrangement and structure. Notably, solvents can readily form hydrogen bonds with the main molecular framework, significantly impacting the electronic configuration. Furthermore, solvents can be relatively easily removed and reabsorbed within the crystal lattice, enabling reversible control of the VT transition by simply adding or removing the solvent. The Dei group investigated the solvation effect on [Co(Me_2tpa)(DBCat)](PF_6).[58] The mononuclear cobalt complex was crystallized separately using ethanol and toluene. Despite both complexes sharing

the same crystal structure and a similar packing pattern, their VT transition properties exhibited significant differences. The magnetization of [Co(Me_2tpa)(DBCat)](PF_6)·toluene displayed a two-step complete valence tautomerism with a much lower transition temperature and better photoinduced VT efficiency compared to the ethanol counterpart (Figure 1.9). This improved

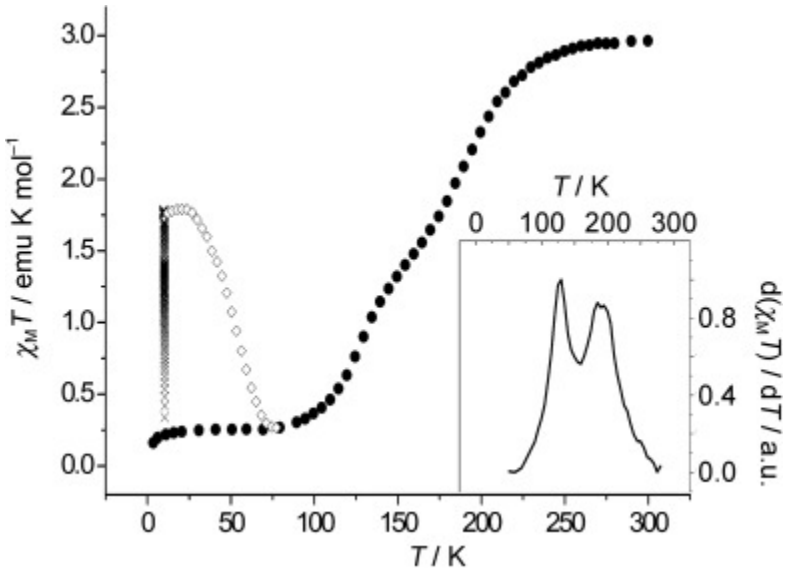

Figure 1.9 Thermal and light-induced valence tautomerism of [Co(Me_2tpa)(DBCat)](PF_6)·toluene. [Adapted from Ref. 58]

photomagnetic conversion efficiency may be attributed to the larger crystal unit volume when toluene is used, which reduces chemical pressure. Although a detailed explanation was not provided, this study confirms that toluene plays a major role in altering intermolecular interactions. Certainly, as the number of valence tautomerism complexes has grown, our understanding of the origins and mechanisms of VT has deepened. Various factors, including the metal center, ligands, counter ions, solvents, and packing modes, have been identified as influential in altering VT transitions. These factors do not only act in isolation; but also, their cooperative interactions contribute to the diverse and complex properties of VT complexes.

Despite this progress, chemists still face challenges in establishing a definitive set of guidelines

for designing and synthesizing functional VT molecules. The intricate nature of molecular interactions and the interplay of various factors make it difficult to predict and control VT behavior reliably. Therefore, further investigation and the accumulation of more data on VT complexes and effectors are essential to advancing our ability to design desired functional molecules.

1.1.2 Light Induced Excited Spin State Trapping (LIESST)

Light, as a non-contact and effective stimulus, has significant advantages in controlling molecular metastable systems via ultra-fast response. One of the most common phenomena, aside from thermally induced spin state transitions, is the Light-Induced Excited Spin State Trapping (LIESST) effect. The first case of LIESST was reported by McGarvey et al., where a spin-crossover iron (II) complex could be excited from a low spin state to a high spin state using green light irradiation below 50 K.[59] This phenomenon, where the excited spin state can be steadily trapped under light irradiation, is known as LIESST. Hauser later expanded this behavior by demonstrating that the excited spin state could be switched back to the low spin state using alternate light (red light), a process known as reverse-LIESST.[60]

The process of Light-Induced Excited Spin State Trapping (LIESST) can be illustrated as shown in Figure 1.10.[61] At low temperatures, irradiation of the low spin (LS) state with a 514.5 nm laser

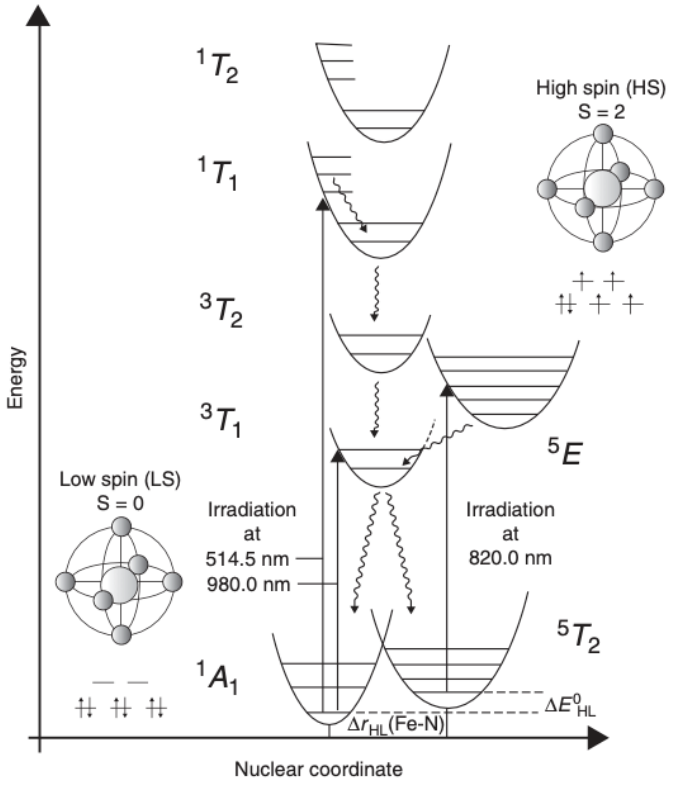

Figure 1.10 Schematic illustration of electronic configuration on Iron (II) spin-crossover complexes. The mechanism or transition pathway of LIESST and reverse-LIESST is demonstrated by direction of arrows under selective irradiation. [Adapted from Ref. 61]

induces a spin-allowed transition from the ground state $^1A_1$ to an excited singlet state ^1T_n . This excited state is unstable and typically decays quickly back to the ground state $^1A_1$. However, an alternative pathway involves decay to an intermediate $^2T_5$ state. Due to spin-orbit coupling, there is an intersystem crossing step (with ΔS = 1), leading to the formation of triplet states $^3T_1$ or $^3T_2$. At sufficiently low temperatures, the high spin state can be trapped for extended periods, as the energy barrier between the *hs* and *ls* potential surfaces is significant. This barrier is primarily due to the large difference in metal–ligand bond lengths, preventing thermal relaxation back to the *ls* state. For the reverse LIESST, Scheme 1 demonstrates the potential to revert the system to its low spin state by selectively irradiating the high spin ligand-field band in the near-infrared region. This

capability is confirmed by the absorption spectrum of $[Fe(ptz)_6](BF_4)_2$ at 10 K after irradiation at 830 nm, targeting the peak of the $^5T_2 \rightarrow {}^5E$ transition in the high-spin compound. However, the process of light-induced reversion to the *ls* state (reverse-LIESST) is not completely efficient. Despite extended irradiation, the low-spin fraction achieves only approximately 85%. This partial conversion is attributed to the spectral overlap between the $^5T_2 \rightarrow {}^5E$ band of the high-spin species and the spin-forbidden $^1A_1 \rightarrow {}^3T_1$ and $^1A_1 \rightarrow {}^3T_2$ bands of the low-spin species, leading to a steady-state condition. Varying the excitation wavelength within this overlap region results in different steady state *hs* fractions. For irradiation outside the $^5T_2 \rightarrow {}^5E$ band, especially when irradiating exclusively into the $^1A_1 \rightarrow {}^3T_1$ band at 980 nm, LIESST achieves full conversion.

In 2019, the Harding group reported a spin crossover complex $[Fe(naphBzen)_2]I$ (naphEen = 1-([2-(ethylamino)ethylimino]-methyl-2-naphthol)).[62] This complex featured two distinct *hs* FeIII centers within an asymmetric unit cell. At low temperatures, one Fe^{III} center transitioned to a *ls* state while the other remained in the high-spin state, resulting in a 50% temperature-dependent spin transition conversion. Interestingly, upon irradiation with 830 or 980 nm light, the complex exhibited reverse-LIESST effect, achieving a complete spin crossover with a 30 K hysteresis that

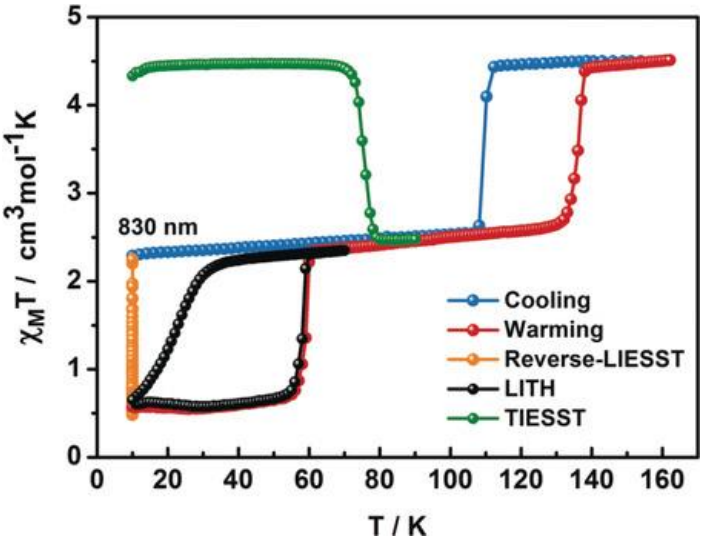

Figure 1.11 Magnetization of Fe^{III} complex. The green line is Temperature induced high spin state trapping; orange line is reverse LIESST; black line is hidden hysteresis induced by temperature. [Adapted from Ref. 62]

could not be accessed by temperature changes alone (Figure 1.11). Additionally, the complex could be quenched to a fully high-spin state by rapid cooling to 100 K, maintaining this state without decaying back until reaching 75 K. The sensitivity of the Fe^{III} complex to both temperature and light is intriguing. Although the authors did not provide a detailed explanation, it is likely related to the specific ligand used and the molecular packing within the crystal. During the spin transition, the complex undergoes significant structural transformations, where the cooperativity of C-H···I and C-H···π interaction is essential in influencing molecular property.

At the same time, the Bao group reported an unusual Fe^{II} complex that exhibits both LIESST and reverse-LIESST effects.[63] Under normal temperature variation, the complex appears to remain in the *hs* state without any noticeable magnetic transition. However, the true ground state, which is the *ls* state, can only be achieved through a prolonged relaxation process of approximately 5 hours at 80 K. In contrast, appropriate laser irradiation can rapidly induce the transition between the *hs*

and *ls* states, demonstrating the complex's advantage of fast photoswitching compared to thermal stimuli (Figure 1.12a). To understand the mechanism behind the slow thermal dynamics and the LIESST effect, the time evolution of χT was measured, revealing an activation energy as high as 580 K (Figure 1.12b-c). The study suggests that the dense molecular packing, which creates steric hindrance, and the weak ligand field around Fe^{II} significantly hinder the molecule from overcoming the energy barrier through thermal means. Conversely, light can more easily excite the molecule to surpass this barrier.

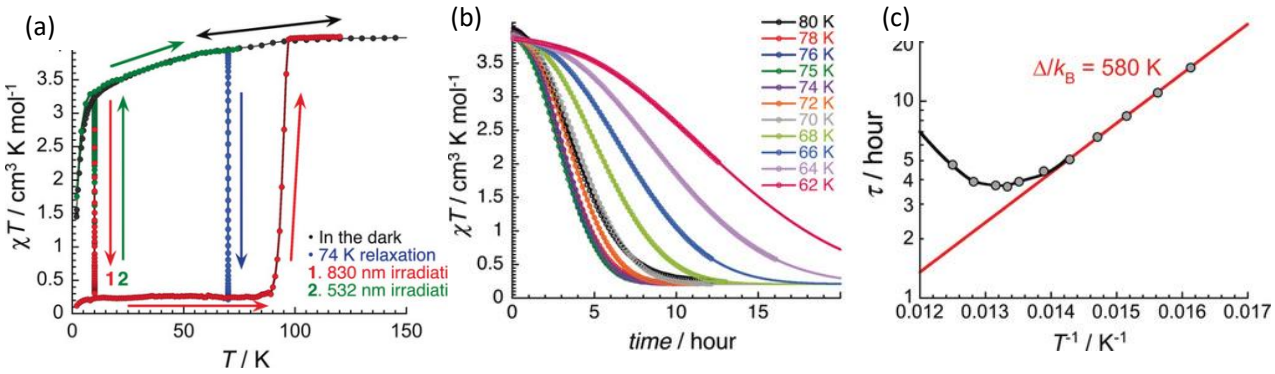

Figure 1.12 (a) The magnetization of Fe^{II} complex under thermal and light stimuli. (b) The plot of χT against time at various temperature (below 100 K) with a sweeping rate 5 K min^{-1} under darkness. (c) The plot of τ against 1/T marked in red line indicating Arrhenius behavior. [Adapted from Ref. 63]

Valence tautomeric complexes exhibit phototunable metastability, notably observed in Co complexes. A prime example is the mononuclear Co complex [Co(3,5-dbcat)(3,5-dbsq)(tmeda)] (where 3,5-dbcat is 3,5-di-tert-butyl-1,2-catecholate, 3,5-dbsq is 3,5-di-tert-butyl-1,2-semiquinonate, and tmeda is N,N,N′ ,N′ -tetramethylethylenediamine). This complex demonstrates thermal and light-induced valence tautomerism, represented by the equilibrium [*ls*-Co^{III}(3,5-dbcat)(3,5-dbsq)(tmeda)] ↔ [*hs*-Co^{II}(3,5-dbsq)$_2$(tmeda)].[64] The phototunable behavior is directly confirmed through photomagnetization using a SQUID magnetometer. At 5 K, when the

ground powder sample, covered with transparent tape, is irradiated with 532 nm visible light via optical fiber, a significant increase in magnetic moment is observed. Upon warming to 60 K, the magnetization reverts to its original value (Figure 1.13). And this operation could be repeated for many time, demonstrating the reproducibility of the light-induced effect. This photoresponse is further corroborated by spectral data. Post-illumination, the UV-vis absorption band around 800 nm, attributed to the *hs*-Co^{II} to 3,5-dbsq transition, intensifies while the ligand-ligand charge transfer band diminishes. Additionally, IR spectroscopy indicates a decrease in the C-O stretch vibration from 3,5-dbcat, suggesting electron transfer from the ligand to the Co center. All this evidence confirms the feasibility of light induced valence tautomerism.

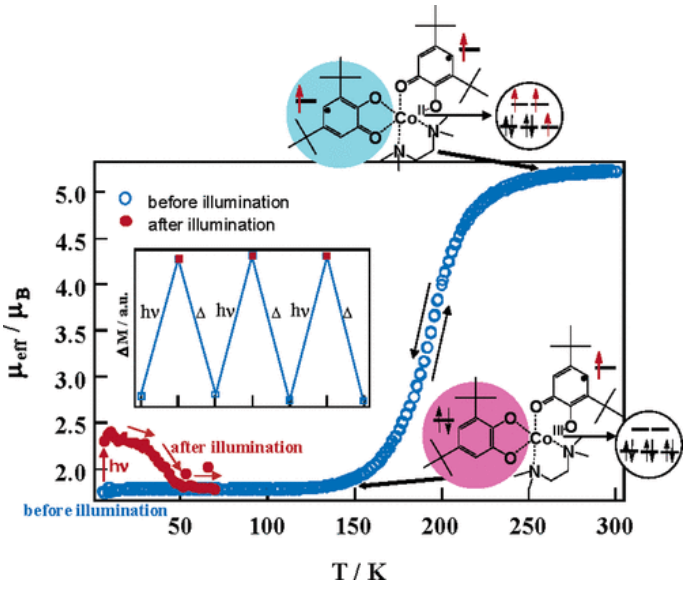

Figure 1.13 The photomagnetization of mononuclear Co complex with valence tautomerism. [Adapted from Ref. 64]

Recent advancements in dinuclear complexes exhibiting valence tautomerism have garnered attention. Notably, the Dei group successfully synthesized a typical dinuclear Co compound,

[(Co(cth))(μ-dhbq)(Co(cth))]$(PF_6)_3$, where mononuclear Co units are bridged by a dhbq ligand in a 2:1 ratio and undergo one-electron oxidation by AgPF6, resulting in *hs*-Co^{II}-$dhbq^{2-}$-*ls*-Co^{III}.[65] This compound displays a significant change in magnetization, from 0.45 to 2.53, indicating a spin transition at 175 K (Figure 1.14a). However, magnetization alone is insufficient to conclusively demonstrate valence tautomerism or spin corssover. At low temperatures, the spin state of the dinuclear Co complex can be single, whether through electron transfer (*ls*-Co^{III}-$dhbq^{3-}$-*ls*-Co^{III}) or spin crossover (*ls*-Co^{II}-$dhbq^{2-}$-*ls*-Co^{III}).

The definitive evidence for valence tautomerism was provided by Electron Paramagnetic Resonance (EPR) spectroscopy, which revealed a strong signal at g = 2 at 4 K. As the temperature increased, the intensity of the EPR signal at g = 2 gradually decreased from 100 K and disappeared by 250 K (Figure 1.14b). This temperature-dependent behavior aligns with the magnetic transition, supporting the occurrence of valence tautomerism. Additionally, photo-induced valence tautomerism was confirmed through diffuse absorption spectra analysis. Reflectivity measurements of a characteristic band around 617 nm, plotted against temperature before and after illumination at 647.1 nm, exhibited variations consistent with changes in magnetic susceptibility, further corroborating the light-induced valence tautomerism behavior. It is observed that the photoconversion efficiency, as determined by spectral analysis, is nearly complete (Figure 1.14c). This discrepancy may be attributed to the differences in sample thickness between the magnetic

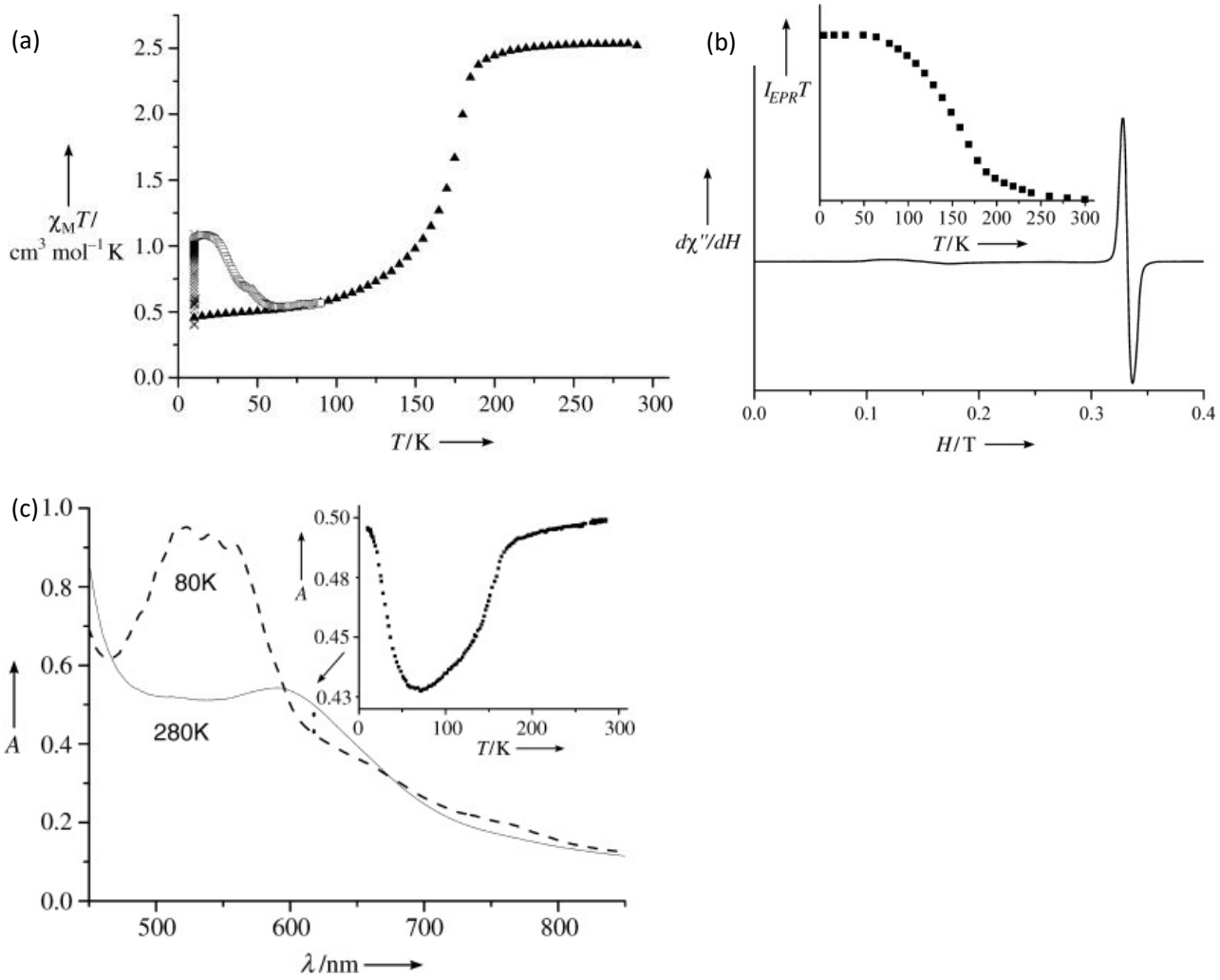

Figure 1.14 (a) Graph showing the $\chi_m T$ product versus temperature (T) for dinuclear Co complex, recorded both before (▲) and after (□) exposure to 647 nm irradiation. (b) The EPR spectrum (9.24 GHz) of dinuclear Co was measured at 4 K. The inset displays a graph showing the radical signal intensity at varying temperature. (c) Diffuse absorption spectra of dinuclear Co were measured at both room temperature and 80 K. The inset displays the reflectivity at 617 ± 5 nm plotted against temperature. [Adapted from Ref. 65]

and spectral measurements. The bulk sample hinders laser penetration, thereby reducing the detected magnetic moment.

As more valence tautomeric complexes with photomagnetization are investigated, a concern has emerged regarding the relatively small conversion fraction of the metastable state induced by light stimuli, which contrasts with the nearly complete photoconversion observed in Fe complexes. One plausible explanation is that the valence tautomeric transition in Co complexes involves two steps: *hs*-Co^{II} → *ls*-Co^{II} → *ls*-Co^{III}. Consequently, the light-induced metastable state could be an intermediate state distinct from the thermally induced *hs* state. However, Roux *et al*. conducted an investigation using X-ray absorption near-edge structure (XANES) spectroscopy to study the Co center states stimulated by temperature and light.[66] Their results showed that the Co K-edge spectra under irradiation at 11 K differed from those measured at 300 K and 11 K in isolation (Figure 1.15).[67] By simulating a spectrum composed of 300 K and 11 K data at a ratio of 0.65:0.35, they found that the simulated result closely matched the experimental spectra under irradiation. This finding indicates that the light-induced metastable state is identical to the thermally induced one.

Despite this, it is anticipated that a completely distinct metastable state can be trapped due to the excitation energy from optical sources far exceeding that of thermal energy, warranting further exploration of light-induced valence tautomeric (LIVT) complexes. Additionally, other areas of interest include improving the lifetime and relaxation temperature of the LIVT effect (upon to date,

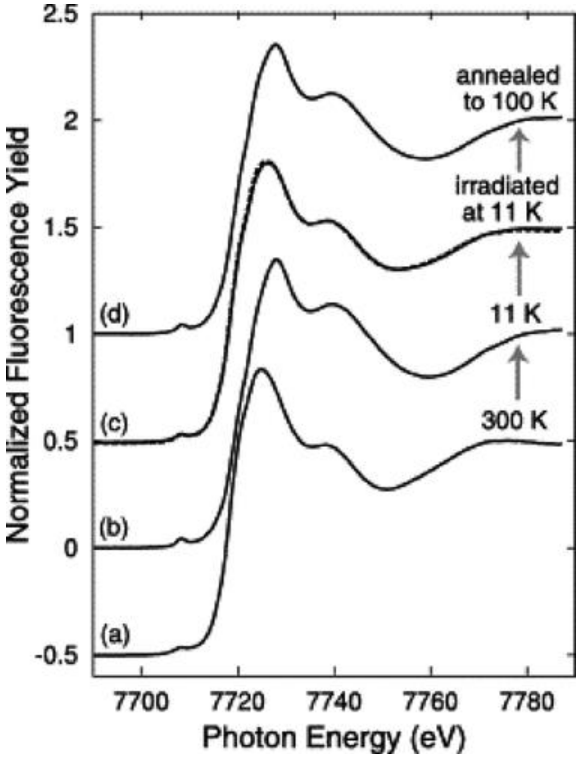

Figure 1.15 The Co K-edge XANES spectra were recorded in fluorescence-yield mode under various conditions: (a) at 300 K, (b) at 11 K, (c) during visible-light irradiation at 11 K, and (d) after annealing the irradiated sample to 100 K. A simulated spectrum, shown as a dashed line, represents the superposition of the 300 K and 11 K spectra with a ratio of 0.65:0.35. [Adapted from Ref. 67]

there is only one case of cobalt complex showing high efficiency of photoconversion and long lifetime of metastable state induced by light reported by Shultz group),[68] investigating the phenomenon in other metal centers, and exploring novel properties related to photo effects, all of which are attractive and deserving of further investigation.

1.1.3 Double Exchange

Based on the degree of interaction between the two metal centers and ligands, known as the Robin-Day classification, this process can be categorized into three groups (Figure 1.16). In Class I, no

or dull interaction occurs between the two metal centers, allowing for clear differentiation of their valency, which impedes easy interconversion. Class II involves a moderate activation energy for interconversion, enabling electron transfer from one site to another via a bridging ligand. Additionally, this class may exhibit intervalence charge transfer (IVCT) bands observable in the infrared or visible spectrum. In Class III, the mixed valence of metal centers cannot be distinguished spectroscopically, indicating electron delocalization across both sites.[69]

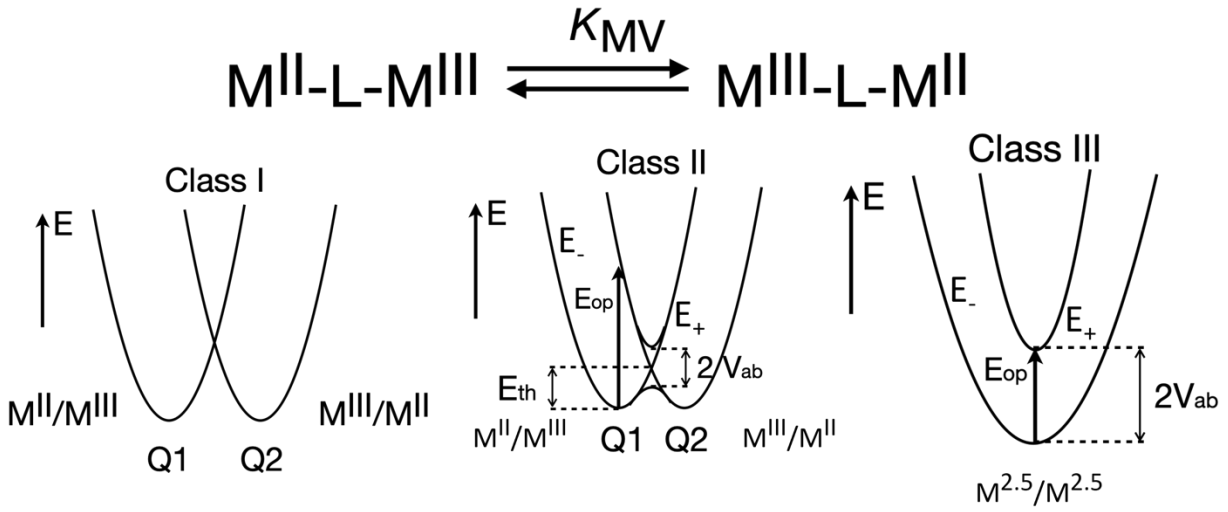

Figure 1.16 schematic illustration of potential energy curves for three distinct types of mixed-valence complexes.

Theoretical explanation:

Assuming no orbitals exist between M^{II}/M^{III} (denoted as A) and M^{III}/M^{II} (denoted as B), two equations could be obtained: $\langle\Psi_A|H|\Psi_A\rangle = \langle\Psi_B|H|\Psi_B\rangle = E^0$ (Equation 1) Ψ_A/Ψ_B: the wavefunction of Ψ_A/Ψ_B represents the state where the electron is localized on metal center A and B, respectively. H: H is the Hamiltonian, representing the total energy operator of the system (including both kinetic and potential energies). E^0: E^0 is the energy of the system when the electron is either fully localized on A or B. In this case, the system is isoelectronic, and the Hamiltonian doesn't favor one metal center over the other, leading to symmetry in the energies.

Although the energies are equal in the localized states, what typically distinguishes the behavior of the system is the off-diagonal coupling term $<\Psi_A|H|\Psi_B>$, which represents the electronic coupling between the two states Ψ_A and Ψ_B. The off-diagonal terms are crucial because they describe the probability of electron transfer or delocalization between the two metal centers. In the absence of coupling, $\langle\Psi_A|H|\Psi_B\rangle = 0$ the electron would remain localized on either A or B.

Then, the two potential energy of two distinct electronic states as expressed:

$E_A = E^0 + lQ + kQ^2/2$, $E_B = E^0 - lQ + kQ^2/2$ (Equation 2). Where E_A/ E_B represents the energy of the system when the electron is localized on metal center A or B. l is a constant that represents the linear coupling between the electronic state and the nuclear coordinates. Q is the reaction coordinate, which describes the distortion or displacement in the system as a function of electron localization. It measures the extent of nuclear rearrangement (e.g., bond lengths, angles, and positions of ligands) as the system adjusts to accommodate the electron being on either A or B. In $E_A = E^0 + lQ$, the linear term "$+lQ$" reflects the energy increase when the system distorts to stabilize the electron on center A while in $E_B = E^0 - lQ$, the linear term "$-lQ$" reflects the energy decrease. These terms account for the fact that when an electron is transferred from one metal center to the other, the surrounding ligands and atoms (the "nuclear" part of the system) need to reorganize, which changes the potential energy. k is a constant that represents the force constant of the nuclear environment, describing how resistant the system is to distortion. Essentially, it governs how difficult or easy it is to reform the system in response to changes in the reaction coordinate Q. $kQ^2/2$: this term represents the harmonic potential energy associated with nuclear displacements. This is similar to a harmonic oscillator potential and indicates that as Q deviates from 0, the system gains vibrational energy. This term is the same for both E_A and E_B, and it represents the restoring force that drives the system back toward equilibrium (i.e., towards to Q = 0). The Equations describe how the total energy of the system changes as the system undergoes structural changes (measured by Q), with an electron localized on either metal center A or B. Q = 0 typically corresponds to the equilibrium geometry of the system when the electron is perfectly delocalized

or when the system has no distortion. As Q moves away from zero, the system is distorted, and the energy changes accordingly.

In such a situation, the required electron transfer energy is called optical energy, shown as:

$$E_{op} = E_B(Q = -l/k) - E_A(Q = l/k) = 2l^2/k \text{ (Equation 3)}$$

When a mixed-valence dinuclear system presents electronic coupling between two electronic states, it implies that there is finite coupling between the two states, meaning that the electron has a non-zero probability of transitioning between the two metal centers. It could form new molecular orbitals: A bonding state, which has lower energy due to constructive interference of the wavefunctions. An antibonding state, which has higher energy due to destructive interference. This mixing of the wavefunctions results in a splitting of the energy levels at Q = 0. Thus, $<\Psi_A|H|\Psi_B>$ = V_{ab} ($V_{ab} \neq 0$). Where V_{ab} represents the electronic coupling constant (sometimes called the hopping parameter or transfer integral), which quantifies the strength of the interaction between the two localized electronic states.

Constructing the energy matrix:

Then energy matrix of the system is introduced to describes how the total energy of the system behaves in terms of these two states, and how they interact with each other. It can be represented in matrix form using the Hamiltonian operator *H*, which contains information about the system's total energy. The Hamiltonian matrix in the Ψ_A- Ψ_B basis is a 2x2 matrix where each matrix element represents the energy associated with a particular combination of the two states Ψ_A and Ψ_B. The general form of the matrix is:

$$H = \begin{pmatrix} <\Psi A|H|\Psi A> & <\Psi A|H|\Psi B> \\ <\Psi B|H|\Psi A> & <\Psi B|H|\Psi B> \end{pmatrix} = \begin{pmatrix} E_A & V_{ab} \\ V_{ab} & E_B \end{pmatrix} \text{ (Equation 4)}$$

In the system of $V_{ab} \neq 0$, we need to diagonalized the Hamiltonian matrix. The eigenvalues will give us the energy levels of the system. The eigenvalues E_+ and E_-, which represent the energies of the delocalized bonding and antibonding states, are found by solving the secular determinant:

$$\det(H - EI) = 0$$

$$\begin{vmatrix} E_A - E & V_{ab} \\ V_{ab} & E_B - E \end{vmatrix} = 0 \text{ (Equation 5)}$$

Thus, the eigenvalues give:

$$E_{\pm/} = \frac{E_A + E_B}{2} \pm \sqrt{\left(\frac{E_A + E_B}{2}\right)^2 + (V_{ab})^2} \text{ (Equation 6)}$$

E_+ is the energy of the excited state (antibonding state), E_- is the energy of the ground state (bonding state) shown in Figure 1.16. And the energy gap between ground state and excited state could be obtained by $\triangle E = E_+ - E_- = 2V_{ab}$ (Equation 7) at Q = 0.

For $V_{ab} < l^2/k$, the maximum energy barrier of E_- appears at Q = 0 between two energy minima. A possible electron transfer between metal A and B could occur by overcoming thermal energy, shown as:

$$E_{th} = E_+(Q = 0) - E_{-,min} = \frac{l^2}{2k} + \frac{{V_{ab}}^2 k}{2l^2} - V_{ab} \text{ (Equation 8)}$$

Additionally, the optical process generates an absorption band known as the intervalence band, which is a defining feature of mixed-valence compounds. The E_{op} is proportional to ${V_{ab}}^2$.

It would be different if ${V_{ab}}^2 \geq l^2/k$, it typically means that the coupling between the two centers is strong enough to favor delocalization of electrons across the centers. This results in a stable mixed-valence state, where the oxidation states of the metal centers can be considered as being in resonance with one another. At this point, there is no longer an energy barrier, and a single minimum of E_- appears at Q = 0. The energy transition from E_- to E_+ requires at least $2V_{ab}$ (see Figure 1.16).

Harris group demonstrates how a benzoquinonoid ligand mediates double-exchange coupling in a

mixed-valence Fe dimer complex.[70] The ligand 2,5-di(2,6-dimethylanilino)-3,6-dibromo-1,4-benzoquinone coordinates with Fe(II) and a capping ligand to form a dinuclear complex. Magnetic measurements and spectroscopic techniques reveal weak ferromagnetic coupling between the Fe(II) centers through the ligand, resulting in a ground state with S = 4. Oxidation to a mixed-valence state increases ferromagnetic coupling, raising the spin to S = 9/2, driven by electron hopping via double-exchange (Figure 1.17). Near-infrared spectroscopy shows intervalence charge transfer, and Mössbauer spectroscopy reveals thermally activated electron hopping, indicating the transition from valence-trapped to detrapped states. Although evidence, particularly from Mössbauer spectroscopy, was not conclusive in confirming valence delocalization at low temperatures from today's perspective, such tactic of molecular design offers valuable insights into the modification of two distinct states in mixed-valence dinuclear complexes.

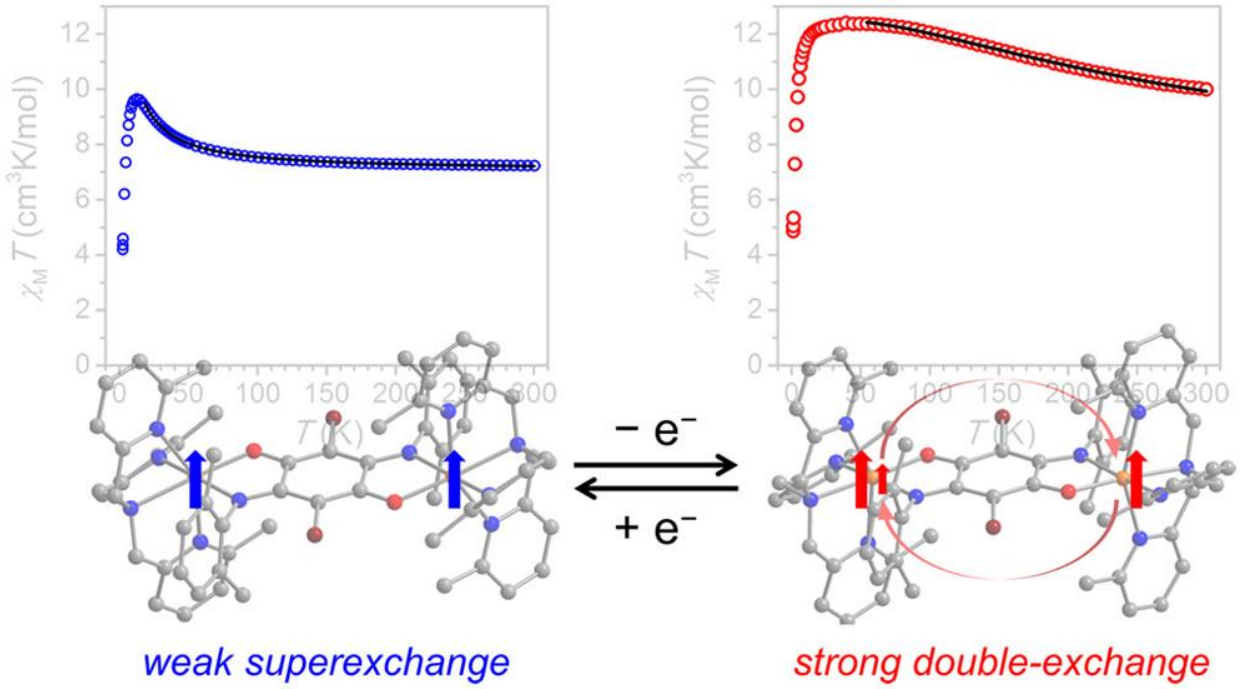

Figure 1.17 The transition from weak ferromagnetic super-exchange coupling to strong ferromagnetic exchange coupling through a redox process. [Adapted from Ref. 70]

1.2 Macroscopic Polarization Switching on Non-ferroelectrics.

Molecular polarization is a fundamental concept in chemistry that describes the distribution of electric charge within a molecule. This phenomenon arises when there is an unequal sharing of electrons between atoms in a molecule, leading to the formation of regions with partial positive and negative charges. The degree of polarization in a molecule is influenced by factors such as the electronegativity of the atoms involved, the geometry of the molecule, and the presence of an external stimuli. Switching between different polar states has garnered significant attention due to its potential applications in sensors, molecular storage, and energy conversion. Undoubtedly, the existence of ferroelectric materials has paved the way in this field, as their spontaneous polarization can be controlled and reoriented by applying an electric field (Figure 1.18 a,b).[71, 72] However, due to the collective variation of ferroelectrics within the crystal lattice, repeated switching of the polarization state can result in the degradation of their properties over time. Additionally, ferroelectric materials typically have a Curie temperature, above which they lose their ferroelectric properties and become paraelectric. This temperature sensitivity limits their use in environments where precise temperature control is challenging, as high temperatures can render them ineffective. An alternative approach has been recently proposed by the Sato group, which involves crystallizing metastable molecules, such as those exhibiting spin crossover, valence tautomerism, and delocalized mixed-valence behavior, into polar space groups.[42, 73-80] These metastable complexes are not only diverse in type but can also be switched by external perturbations, including light, magnetic fields, and temperature variations (Figure 1.18 c,d). Notably, the energy barriers between metastable states and the crystal packing arrangement can be finely tuned through rational molecular design. This innovative strategy significantly expands the scope of ferroelectric systems and opens new possibilities for the future application of non-ferroelectric materials.

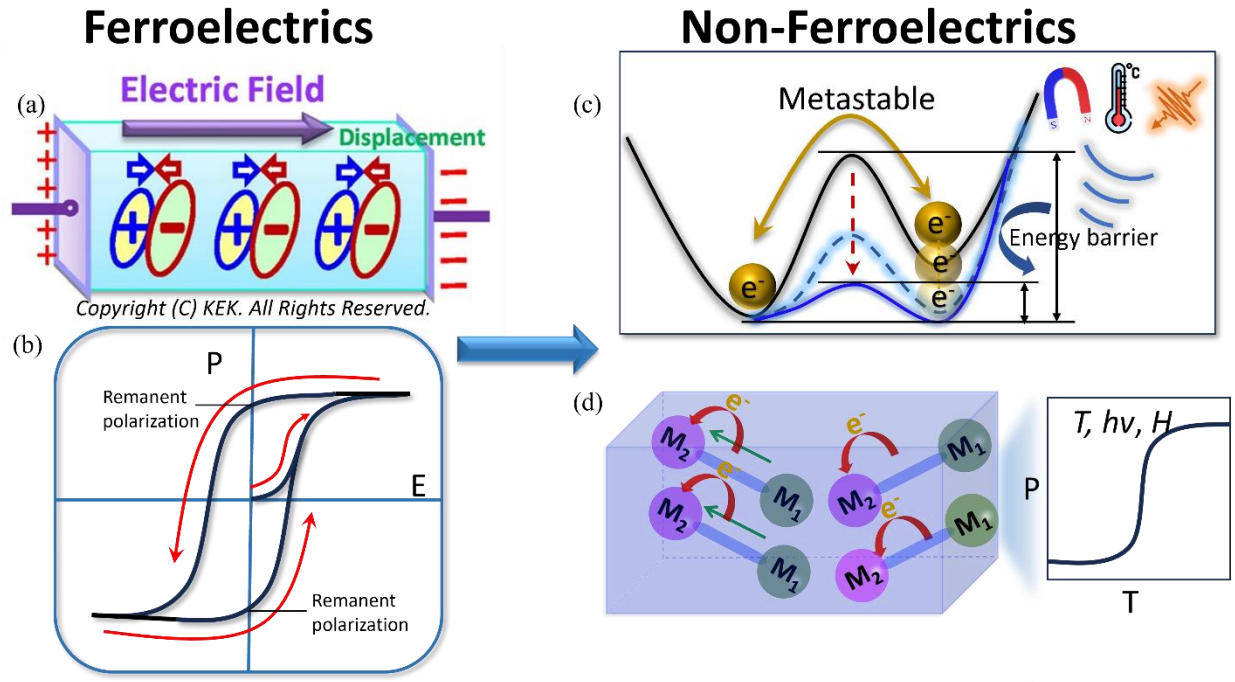

Figure 1.18 (a) Schematic illustration of ferroelectric. (b) Ferroelectric hysteresis loop. (c) Mechanism of non-ferroelectrics with metastable which could be switched by external stimuli. (d) Schematic illustration of polarization switching on non-ferroelectrics.

1.2.1 Crystal in Polar Space Group

If we analyze crystallization from the viewpoint of point group symmetry, it is known that point groups classify molecules based on their symmetry elements, such as rotation axes, mirror planes, and centers of inversion. Certain point groups are non-centrosymmetric, meaning they do not possess an inversion center, which is crucial for crystallizing in polar space groups. Examples of non-centrosymmetric point groups that can potentially lead to polar space groups include C_1, C_2, C_s, C_{2v}, and C_3. Polar space groups are a subset of non-centrosymmetric space groups where the crystal structure allows for a net dipole moment along a specific direction. Common polar space groups include $P2_1$, $P_{na}2_1$, and $R3_m$. To crystallize in a polar space group, the molecule must belong to a non-centrosymmetric point group. Molecules with inversion symmetry (e.g., C_i, D_{2h})

tend to crystallize in centrosymmetric space groups, which are not polar. For instance, a molecule in the C_2, or C_s point group could potentially crystallize in the polar space group $P2_1$. Symmetry elements such as mirror planes and centers of inversion generally cancel out dipole moments. Therefore, to favor polar crystal structures, the molecular design should minimize these elements. Molecules with only a single rotation axis (e.g., C_2) or no symmetry elements (e.g., C_1) are strong candidates for crystallizing in polar space groups. And molecules with inherent asymmetry, such as chiral molecules, are more likely to crystallize in non-centrosymmetric space groups. Chiral molecules naturally belong to point groups like C_1, C_2, and D_{2h}, which are compatible with polar space groups. Additionally, designing molecules with non-centrosymmetric functional groups or ligands can further promote crystallization in polar space groups (Figure 1.19).[43] The choice of

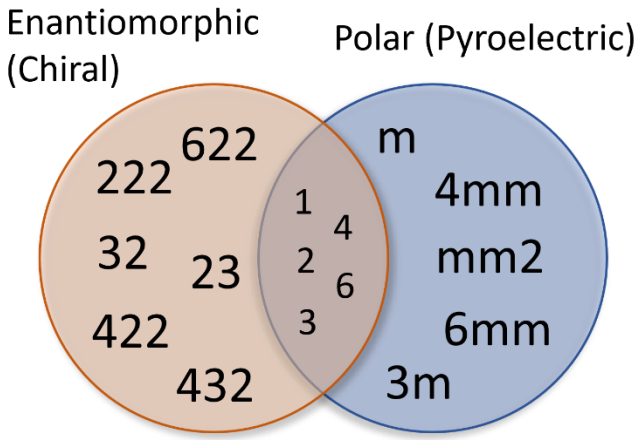

Figure 1.19 The incorporation of enantiopure ligands promotes packing in a polar space group. [Adapted from Ref. 43]

solvent can also influence the symmetry of the crystal packing. Solvents that interact with the polar regions of the molecule may stabilize a polar arrangement within the crystal. Techniques like slow evaporation, cooling crystallization, and vapor diffusion can be adjusted to favor the growth of crystals in polar space groups. In summary, crystallizing a molecule in a polar space group involves designing molecules that lack centrosymmetry, optimizing crystallization conditions to encourage non-centrosymmetric packing, and screening the resulting crystals for polar space groups. By

understanding and applying point group symmetry principles, chemists can rationally design and crystallize materials with desired polar properties for various applications.

1.2.2 Temperature Induced Polarization Switching on Co VT complexes

In 2016, the Sato group reported a dinuclear [CrCo] complex exhibiting valence tautomerism near 300 K, evidenced by magnetization and IR spectra. However, in this study, molecular design was crucial for achieving polarization switching.[78] The utilization of both redox-active and inert transition metals coordinated with enantiopure ligands (RR/SS-cth) led to the formation of two mononuclear units connected by a bridging ligand. Chirality recognition stabilized the heterometallic dinuclear complex in solution, confirmed by mass spectrometry. The molecule's pseudo-symmetric structure allowed it to pack in a polar space group, aligning electron transfer with the polar axis that is distinct from the non-polar space group in dinuclear Co complexes (Figure 1.20). Even though polarization switching, initially predicted theoretically, was experimentally confirmed through pyroelectric measurements, suggesting the potential for further exploration of heterometallic dinuclear complexes with dynamic processes.

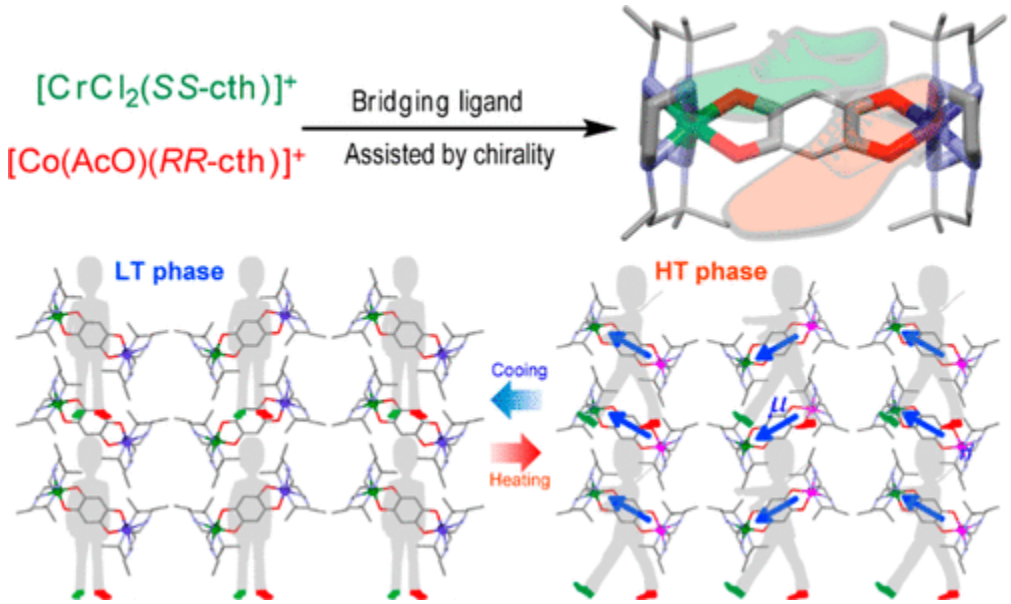

Figure 1.20 Synthetic strategy of [CrCo] dinuclear complex assisted by chiral ligand (upper).

Directional electron transfer to achieve polarization switching (lower). [Adapted from Ref. 78]

Another successful case of achieving macroscopic polarization switching through molecular design was reported in 2020 by Wu and coauthors with the complex [Co(phendiox)(Rac-cth)]·0.5 EtOH.[74] The substitution of ClO_4^- influenced the molecular arrangement and valence tautomerism (VT) transition. The formation of an asymmetric unit was driven by hydrogen bonding between oxygen from ClO_4^- and nitrogen from the cth ligand, promoting polar space group packing compared to the inversion-symmetric PF_6^- complex (Figure 1.21a). Moreover, given by this circumstance, the molecule with stronger hydrogen bond exhibited steric hindrance that result in the two-step VT transition. This unique process was also confirmed by pyroelectric measurement showing two distinct peaks (Figure 1.21 b,c). Although light-induced polarization switching was not detected due to low photoconversion efficiency, the results suggest the potential for polarization switching via multiple stimuli.

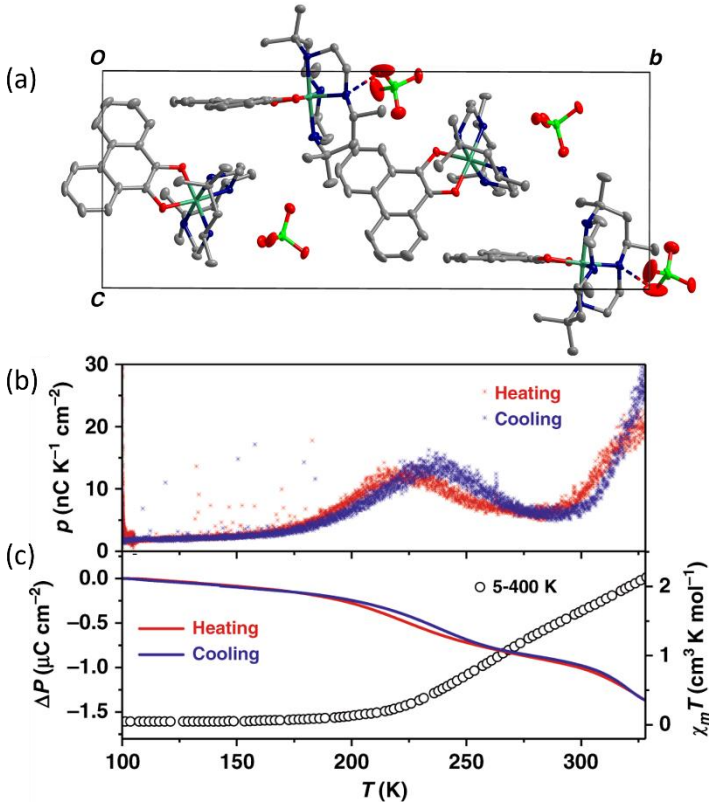

Figure 1.21 (a) Molecular packing of [Co(phendiox)(Rac-cth)]·0.5 EtOH, showing two asymmetric units due to weak hydrogen bonding interactions. (b) Pyroelectric coefficient measurement on a single crystal from 100 to 330 K with a sweep rate of 5 K/min. (d) Comparison of polarization changes (indicated by red and blue lines) with magnetization (represented by open circles). [Adapted from Ref. 74]

1.2.3 Light Induced Polarization Switching

Opto-electric materials, which convert the inexhaustible resource of light into electric power, are critically important in addressing energy crises. Polar crystals inherently exhibit pyroelectric and piezoelectric properties. When a light beam locally heats a polar crystal, it generates a transient current due to the rapid temperature changes. However, this current is too small for practical sensor applications and cannot be promptly stored as energy harvesting. Enhancing performance remains a challenge. Su et al. integrated a spin crossover Fe complex with light-induced excited spin state trapping (LIESST) into a polar crystal to achieve significant light-induced macroscopic polarization switching ca. 0.45 μC cm^{-2} (Figure 1.22 a,b).[79] Below 10 K, the low spin Fe(II) can be excited into a high spin state by a 532 nm laser and stably remianed. Above 30 K, the high spin state decays back to the lower energy ground state releasing pyroelectric current via relaxation. Interestingly, the mechanism behind light-induced polarization switching seems to primarily stem from ion displacement observed during thermally induced spin crossover, rather than electron redistribution at the metal center (Figure 1.22 c,d). This is because the light-induced excited spin state is typically considered the same phase as that induced thermally. Additionally, the significant expansion or contraction of the crystal lattice during the spin crossover provides potential space for ion displacement, contributing to the switching behavior.

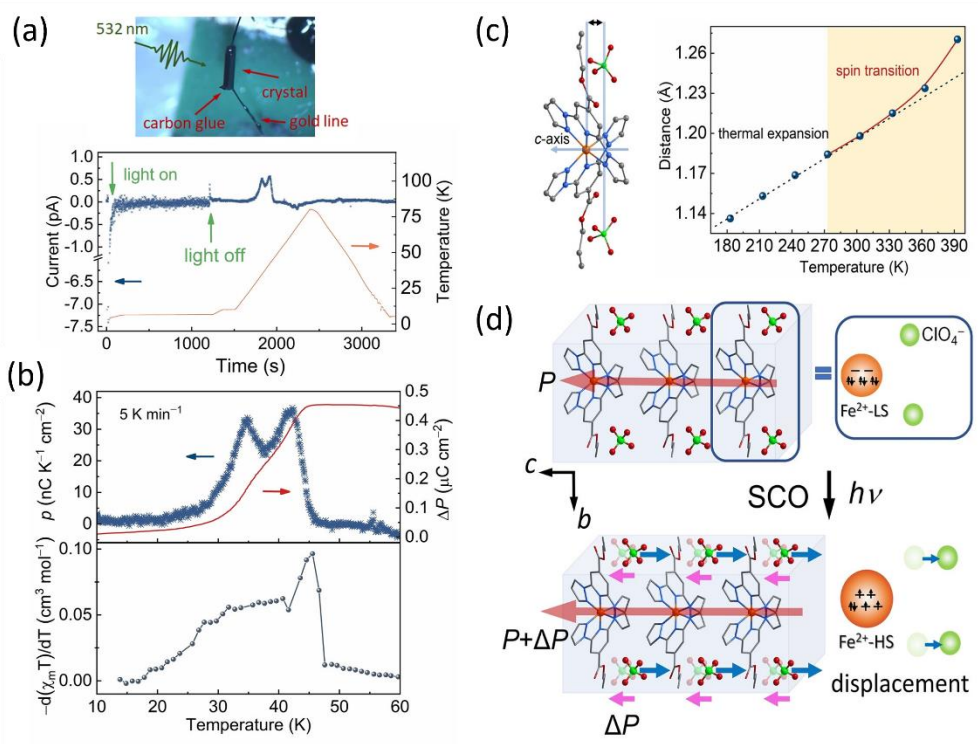

Figure 1.22 (a) Light induced pyroelectric current was measured on single crystal of Fe compelx with 5 K min^{-1}. (b) Pyroelectric coefficient and polarization change of Fe complex after light irradiation. (c) Distance curve of ion displacement of counter anion to metal center during thermal process. (d) Schematic illustration of light induced ion displacement during spin crossover. [Adapted from Ref. 79]

Similar to spin crossover, valence tautomeric complexes also exhibit the LIESST effect, with long-range electron redistribution between the metal and bridging ligand, making them promising candidates for achieving giant light-induced polarization switching. In 2023, the Sato group reported the first case of photoinduced polarization change in a [CoGa] complex.[76] They used an in-situ replacement method to substitute Cr with Ga, which shares a similar packing mode in a polar space group. This compound showed a large thermally induced polarization change of approximately 2.9 μC cm^{-2}, comparable to ferroelectrics. Simultaneously, the VT transition temperature was reduced to 200 K, significantly extending the lifetime of the photoinduced excited

phase with an 18% photoconversion rate (Figure 1.23a). Light-induced pyroelectric current was successfully detected in this crystal (Figure 1.23b). However, several intriguing questions remain, such as why substituting the inert site from Ga to Cr causes such a significant difference in VT transition temperature and integral polarization change. A deeper understanding of the electronic configuration and metal-metal interactions is likely needed to resolve these discrepancies.

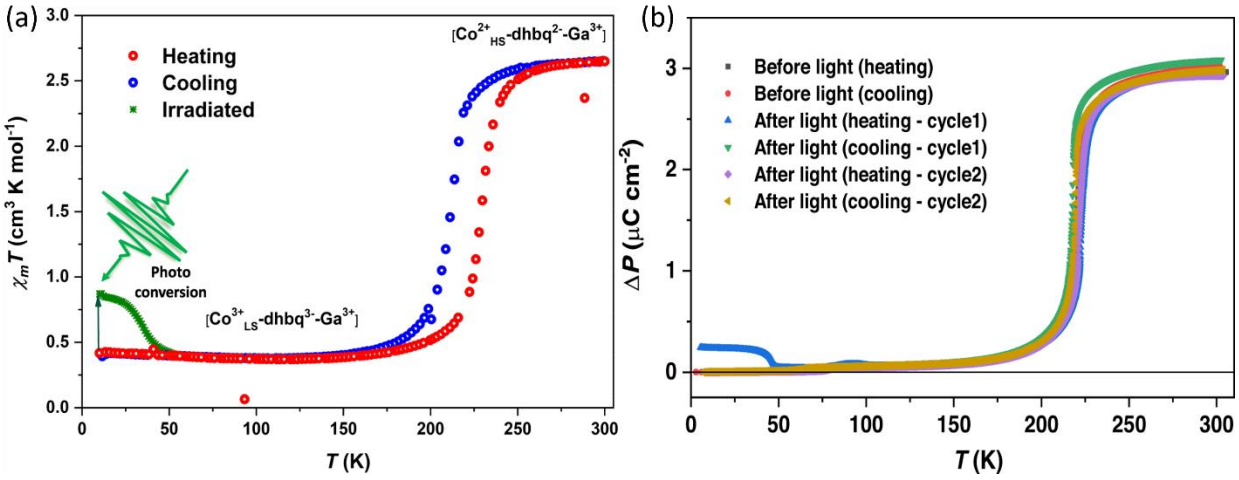

Figure 1.23 (a) Magnetic susceptibility of [CoGa] before and after light (532 nm) irradiation with sweeping rate of 5 K min^{-1}. (b) Polarization change of single crystal [CoGa] induced by light and thermal. [Adapted from Ref. 76]

Both examples offer valuable insights for developing optoelectronic molecular materials in non-ferroelectric systems. However, there remains a significant gap in improving the efficiency of photoconversion and achieving long-lived light-induced excited states through rational molecular design. With further advancements, these materials have the potential to be applied practically in molecular devices.

1.3 Overview and Scope of this thesis

Undoubtedly, exploring dynamic molecules with metastable states presents valuable opportunities for interdisciplinary research in magnetism and electronics. The incorporation of chemical

principles allows for fine-tuning electronic configurations through chemical modifications and crystal engineering, influencing intra- and intermolecular interactions. Our group has contributed to the development of dynamic polar crystals, achieving polarization switching in non-ferroelectrics through stimuli such as temperature, light, and magnetic fields. However, further stimuli like electric fields and pressure hold promise for future applications.

In this thesis, I will extend current research on polar crystals using enantiopure ligands, aiming to establish a more generalizable strategy through novel synthetic routes. The inherent asymmetry of enantiopure ligands enables even homometallic dinuclear complexes to pack in polar space groups, allowing for the exploration of mixed-valence systems for macroscopic polarization switching. Moreover, this asymmetry influences molecular structure and packing, offering new methods for polarization switching. Through careful crystal growth design, it is possible to obtain unique polar crystals with hidden multi-polarization states. These results mark an innovative breakthrough in dynamic polar molecule research, and the following chapters will delve into these findings in detail.

In **Chapter 1**, the development of molecular magnetism and dynamic molecules, including those with metastable states such as spin crossover, valence tautomerism, and mixed-valence systems, is briefly summarized. The background on the mechanism of these dynamic molecules and polarization switching based on them are reviewed. Additionally, the scope of my research, focusing on exploring these systems further, is introduced.

In **Chapter 2**, A dinuclear [CrCo]PF_6 complex with enantiopure ligands, [Cr(SS-cth)(μ-dhbq)Co(SS-cth)]$(PF_6)_3 \cdot 2.5H_2O \cdot 0.5MeOH$, was synthesized using a stepwise method that exploits the inert nature of Cr to occupy one site of the bridging ligand, forming a bonded precursor, followed by coordination with a mononuclear Co unit. This process, confirmed by mass spectrometry, prevents random occupation and solvent contamination. Magnetization and UV-vis-

IR studies revealed solvent-dependent valence tautomerism. In the pristine form, 24% valence tautomerism with a transition temperature around 170 K was observed, while the desolvated form showed nearly complete valence tautomerism with a transition temperature of 215 K. This behavior was fully reversible, as the original properties could be restored through solvent reabsorption. Both forms, before and after desolvation, crystallized in the $P2_1$ polar space group with the polar axis along the b-axis, and polarization switching was investigated in single crystals. In the pristine state, a polarization change of 0.27 μC cm^{-2} was achieved between 75 K and 230 K. Interestingly, the desolvated compound exhibited similar polarization changes as the pristine form according to theoretical calculations, attributed to a balance between more pronounced electron transfer and less favorable alignment with the polar axis. A comprehensive analysis was conducted, covering UV-vis, IR, and X-ray diffraction before and after desolvation, along with magnetization and pyroelectric measurements. Each of these techniques provided critical insights into the changes in the molecular structure and properties throughout the desolvation process. This finding demonstrates that the mode of working temperature for polarization switching in this crystal can be manipulated chemically by altering solvent content (Scheme 1.1).

Scheme 1.1 Polarization switching by chemical manipulation on [CrCo]PF6 obtained by stepwise synthetic route.

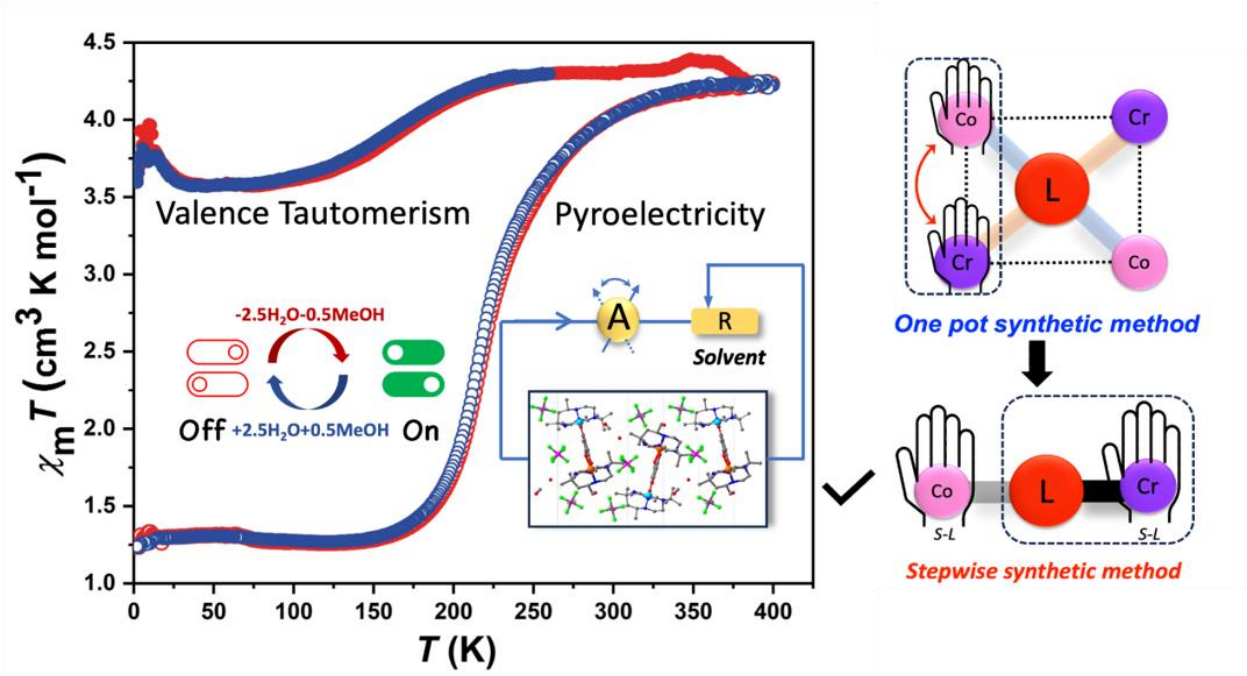

In **Chapter 3**, efforts to enhance light-induced energy harvesting in non-ferroelectrics are discussed. Achieving significant light-driven polarization change requires better alignment of electron transfer with the polar axis and higher photomagnetization efficiency. Stabilizing the high-spin state of Co at lower VT transition temperatures helps maintain the excited state after irradiation, while distorted octahedral configurations reduce decay back to the ground state by limiting lattice vibrations. Through precise molecular design and crystal growth, a novel complex, $[Cr(SS\text{-}cth)(\mu\text{-}dhbq)Co(SS\text{-}cth)](AsF_6)_3$, was developed. This complex showed significant photomagnetization, with a relaxation temperature raised to approximately 80 K and excitation induced by lasers of 532 nm, 785 nm, and 1340 nm wavelengths. Moreover, the alignment between the CrCo vector and the polar axis, similar to the previously reported $[CrCo]PF_6$ complex, ensured optimal performance without solvent. Pyroelectric measurements confirmed a remarkable polarization change under 1340 nm irradiation, reaching 2.25 μC cm^{-2} which is in contrast to thermally induced polarization change of *ca*. 1.6 μC cm^{-2}. Additionally, a hidden phase, silent in photomagnetization, was detected above 15 K (Scheme 1.2). Comprehensive analyses including

ultralow temperature single crystal X-ray diffraction before and after light irradiation, IR, UV-vis, photomagnetization, and mass spectrometry were thoroughly discussed.

Scheme 1.2 Photomagnetization (left) and polarization change (right) of crystal $[CrCo](AsF_6)_3$ after light irradiation with different wavelength.

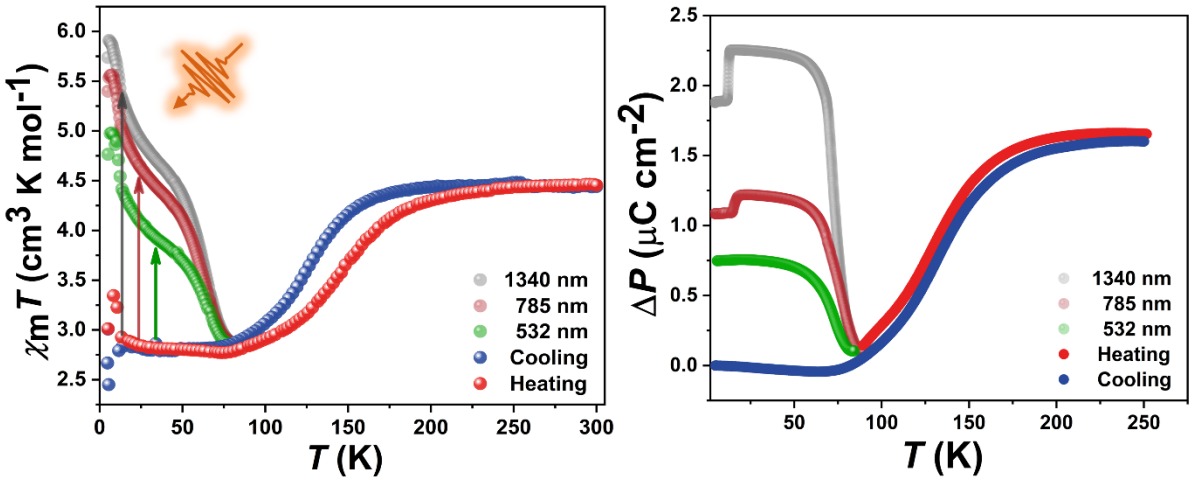

In **Chapter 4**, the theoretical assumption that mixed-valence compounds at the boundary of Robin-Day types II and III can exhibit reversible molecular dipole moments under light is explored in this study. Unlike traditional ferroelectric materials, this polarization change is transient, with the potential for sub-nanosecond responses. We investigated a polar $[Fe(RR\text{-}cth)(\mu\text{-}dhbq)Fe(RR\text{-}cth)](PF_6)_3$ dimer crystal, which packs in the $P2_1$ space group and shows electron delocalization. The faint $dhbq^{2-}/dhsq^{3-}$ IR absorption bands suggest electron hopping across the molecule different from the directional electron transfer as reported cases, while UV-vis spectroscopy revealed unique absorption bands in the near-IR range, corresponding to interconfigurational charge transfer. Interestingly, DFT calculations indicate that the polarization direction varies with different spin density distributions at distinct wavelengths, suggesting the possibility of transient polarization inversion through wavelength-specific laser irradiation (Scheme 1.3). This finding is supported by comprehensive analyses, including single-crystal X-ray diffraction, Mössbauer spectroscopy, UV-

vis, IR, and magnetization studies, all discussed in detail.

Scheme 1.3 Transient polarization inversion on delocalized mixed-valence dinuclear Fe complex with different wavelength laser.

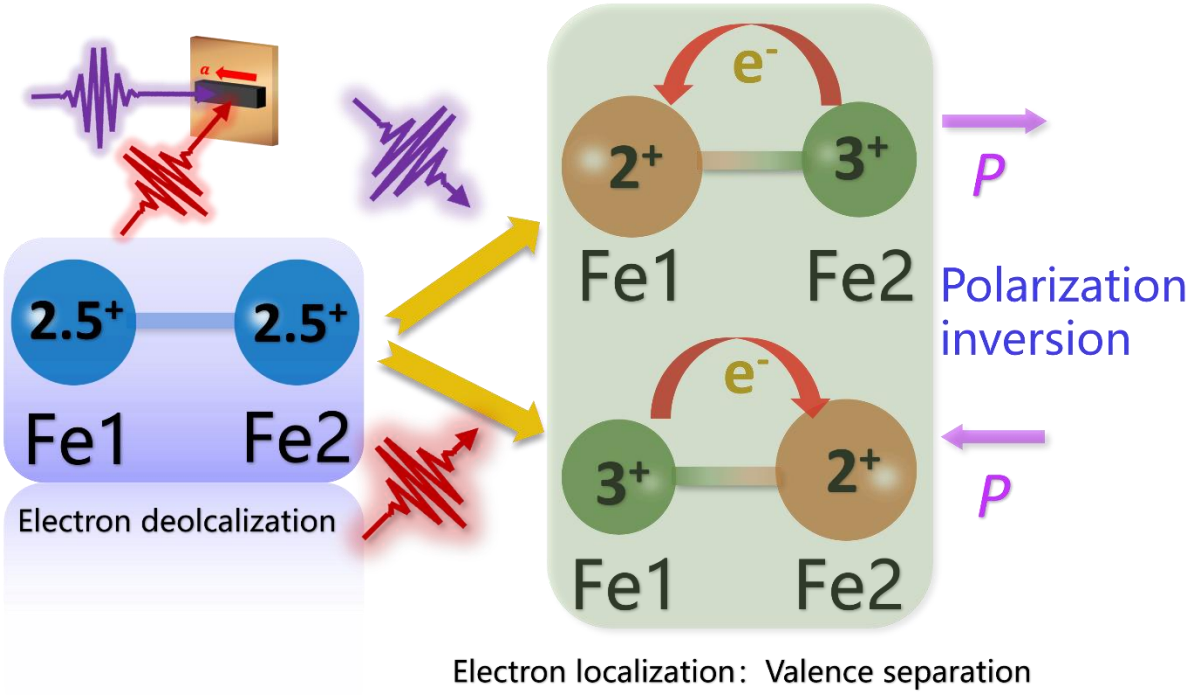

References

1. M. Brand, N. Sharon, S. Emily and https://web.archive.org/web/20090501063207/http://www.magnet.fsu.edu/education/tutorials/museum/lodestone.html.*Journal*, 1995.
2. Museum of Electricity and Magnetism, Mag Lab U. US, National High Magnetic Field Laboratory and https://nationalmaglab.org/magnet-academy/history-of-electricity-magnetism/museum/lodestone-600-bc/.*Journal*, 2009-05-01
3. T. E. o. E. m. c. E. B. Britannica, 23 Aug. 2024,

https://www.britannica.com/technology/magnetic-compass. Accessed 1 October 2024.*Journal*.

4. James Hardy, "Who Invented the Compass? A Brief History of the Compass and Its Evolution" and N. History Cooperative, 2023, https://historycooperative.org/who-invented-the-compass/. Accessed October 1, 2024.
5. W. Poole, "Introduction", W. e. in Poole, The Man in the Moone, Broadview, pp. 13–62 and I. 978-1-55111-896-3.
6. Burke, James (1978) Connections (British documentary) and episode 2.
7. Journal of the History of Ideas , Jan., 1941, Vol. 2, No. 1 (Jan., pp. 1-32 and Published by: University of Pennsylvania Press.
8. É. du Trémolet de Lacheisserie, D. Gignoux and M. Schlenker, in *Magnetism*, eds. É. du Trémolet de Lacheisserie, D. Gignoux and M. Schlenker, Springer New York, New York, NY, 2002, DOI: 10.1007/978-0-387-23062-7_1, pp. 3-18.
9. H. M. McConnell, Ferromagnetism in Solid Free Radicals, *The Journal of Chemical Physics*, 1963, **39**, 1910-1910.
10. H. H. Wickman, A. M. Trozzolo, H. J. Williams, G. W. Hull and F. R. Merritt, Spin-3/2 Iron Ferromagnet: Its M\"ossbauer and Magnetic Properties, *Physical Review*, 1967, **155**, 563-566.
11. R. Sessoli, D. Gatteschi, A. Caneschi and M. A. Novak, Magnetic bistability in a metal-ion cluster, *Nature*, 1993, **365**, 141-143.
12. T. Blachowicz and A. Ehrmann, New Materials and Effects in Molecular Nanomagnets, *Applied Sciences*, 2021, **11**, 7510.
13. J. I. Norambuena Leiva, E. A. Cortés Estay, E. Suarez Morell and J. M. Florez, On the Magnetization and Entanglement Plateaus in One-Dimensional Confined Molecular Magnets, *Magnetochemistry*, 2024, **10**, 10.
14. J. M. Frost, K. L. M. Harriman and M. Murugesu, The rise of 3-d single-ion magnets in

molecular magnetism: towards materials from molecules?, *Chemical Science*, 2016, **7**, 2470-2491.

15. D. N. Woodruff, R. E. P. Winpenny and R. A. Layfield, Lanthanide Single-Molecule Magnets, *Chemical Reviews*, 2013, **113**, 5110-5148.
16. S.-D. Jiang, B.-W. Wang, H.-L. Sun, Z.-M. Wang and S. Gao, An Organometallic Single-Ion Magnet, *Journal of the American Chemical Society*, 2011, **133**, 4730-4733.
17. A. Bousseksou, G. Molnár, L. Salmon and W. Nicolazzi, Molecular spin crossover phenomenon: recent achievements and prospects, *Chemical Society Reviews*, 2011, **40**, 3313-3335.
18. H.-J. Himmel, Valence tautomerism in copper coordination chemistry, *Inorganica Chimica Acta*, 2018, **481**, 56-68.
19. K. D. Demadis, C. M. Hartshorn and T. J. Meyer, The Localized-to-Delocalized Transition in Mixed-Valence Chemistry, *Chemical Reviews*, 2001, **101**, 2655-2686.
20. A. N. Bogdanov, A. V. Zhuravlev and U. K. Rößler, Spin-flop transition in uniaxial antiferromagnets: Magnetic phases, reorientation effects, and multidomain states, *Physical Review B*, 2007, **75**, 094425.
21. J.-F. Létard, P. Guionneau and L. Goux-Capes, in *Spin Crossover in Transition Metal Compounds III*, 2004.
22. P. Gütlich, Spin crossover–quo vadis?, *European Journal of Inorganic Chemistry*, 2013, **2013**, 581-591.
23. M. A. Halcrow, *Spin-crossover materials: properties and applications*, John Wiley & Sons, 2013.
24. P. Gütlich and A. Dei, Valence tautomeric interconversion in transition metal 1, 2-benzoquinone complexes, *Angewandte Chemie International Edition in English*, 1997, **36**, 2734-2736.
25. E. Evangelio and D. Ruiz-Molina, Valence tautomerism: New challenges for electroactive

ligands, *European journal of inorganic chemistry*, 2005, **2005**, 2957-2971.

26. U. Fuerholz, H. B. Buergi, F. E. Wagner, A. Stebler, J. H. Ammeter, E. Krausz, R. J. Clark, M. J. Stead and A. Ludi, The Creutz-Taube complex revisited, *Journal of the American Chemical Society*, 1984, **106**, 121-123.
27. R. P. Houser, V. G. Young and W. B. Tolman, A Thiolate-Bridged, Fully Delocalized Mixed-Valence Dicopper(I,II) Complex That Models the CuA Biological Electron-Transfer Site, *Journal of the American Chemical Society*, 1996, **118**, 2101-2102.
28. R. M. Buchanan and C. G. Pierpont, Tautomeric catecholate-semiquinone interconversion via metal-ligand electron transfer. Structural, spectral, and magnetic properties of (3, 5-di-tert-butylcatecholato)(3, 5-di-tert-butylsemiquinone)(bipyridyl) cobalt (III), a complex containing mixed-valence organic ligands, *Journal of the American Chemical Society*, 1980, **102**, 4951-4957.
29. D. Ruiz-Molina, K. Wurst, D. N. Hendrickson, C. Rovira and J. Veciana, A Thermally and Electrochemically Switchable Molecular Array Based on a Manganese Schiff Base Complex, *Advanced Functional Materials*, 2002, **12**, 347-351.
30. J. Chen, Y. Sekine, Y. Komatsumaru, S. Hayami and H. Miyasaka, Thermally Induced Valence Tautomeric Transition in a Two-Dimensional Fe-Tetraoxolene Honeycomb Network, *Angewandte Chemie International Edition*, 2018, **57**, 12043-12047.
31. Y. Shimazaki, F. Tani, K. Fukui, Y. Naruta and O. Yamauchi, One-Electron Oxidized Nickel(II)−(Disalicylidene)diamine Complex: Temperature-Dependent Tautomerism between Ni(III)−Phenolate and Ni(II)−Phenoxyl Radical States, *Journal of the American Chemical Society*, 2003, **125**, 10512-10513.
32. J. S. Thompson and J. C. Calabrese, Synthesis, spectroscopy, and structures of copper(II)-3,5-di-tert-butyl-o-semiquinone complexes, *Inorganic Chemistry*, 1985, **24**, 3167-3171.
33. M. A. Dunstan, A. S. Manvell, N. J. Yutronkie, F. Aribot, J. Bendix, A. Rogalev and K. S. Pedersen, Tunable valence tautomerism in lanthanide–organic alloys, *Nature Chemistry*,

2024, **16**, 735-740.

34. C. Roux, D. M. Adams, J. P. Itié, A. Polian, D. N. Hendrickson and M. Verdaguer, Pressure-induced valence tautomerism in cobalt o-quinone complexes: An x-ray absorption study of the low-spin [coiii (3, 5-dtbsq)(3, 5-dtbcat)(phen)] to high-spin [coii (3, 5-dtbsq) 2 (phen)] interconversion, *Inorganic Chemistry*, 1996, **35**, 2846-2852.
35. A. Caneschi, A. Dei, F. Fabrizi de Biani, P. Gütlich, V. Ksenofontov, G. Levchenko, A. Hoefer and F. Renz, Pressure- and Temperature-Induced Valence Tautomeric Interconversion in a o-Dioxolene Adduct of a Cobalt–Tetraazamacrocycle Complex, *Chemistry – A European Journal*, 2001, **7**, 3926-3930.
36. B. Li, F.-L. Yang, J. Tao, O. Sato, R.-B. Huang and L.-S. Zheng, The effects of pressure on valence tautomeric transitions of dinuclear cobalt complexes, *Chemical communications*, 2008, 6019-6021.
37. I. Markevtsev, M. Monakhov, V. Platonov, A. Mischenko, A. Zvezdin, M. Bubnov, G. Abakumov and V. Cherkasov, Field-induced spin phase transition in a Co complex, *Journal of Magnetism and Magnetic Materials*, 2006, **300**, e407-e410.
38. R. M. Buchanan, B. J. Fitzgerald and C. G. Pierpont, Semiquinone radical anion coordination to divalent cobalt and nickel. Structural features of the bis (3, 5-di-tert-butyl-1, 2-semiquinone) cobalt (II) tetramer, *Inorganic Chemistry*, 1979, **18**, 3439-3444.
39. D. M. Adams, A. Dei, A. L. Rheingold and D. N. Hendrickson, Bistability in the [CoII (semiquinonate) 2] to [CoIII (catecholate)(semiquinonate)] valence-tautomeric conversion, *Journal of the American Chemical Society*, 1993, **115**, 8221-8229.
40. O.-S. Jung and C. G. Pierpont, Bistability and low-energy electron transfer in cobalt complexes containing catecholate and semiquinone ligands, *Inorganic Chemistry*, 1994, **33**, 2227-2235.
41. C. G. Pierpont and O.-S. Jung, Thermodynamic parameters for cobalt-quinone electron transfer and spin transition steps of the CoIII (bpy)(3, 5-DBSQ)(3, 5-DBCat)/CoII (bpy)(3,

5-DBSQ) 2 valence tautomeric equilibrium, *Inorganic Chemistry*, 1995, **34**, 4281-4283.

42. W. Zheng, X. Zhang, Q. Shui, T. Fukuyama, W.-h. Xu, Y.-b. Huang, T. Ji, Z. Zhou, M. Uematsu and S.-Q. Su, Solvent-dependent valence tautomerism and polarization switching in a heterodinuclear [CrCo] complex, *Inorganic Chemistry Frontiers*, 2024.

43. F. Cheng, S. Wu, W. Zheng, S. Su, T. Nakanishi, W. Xu, P. Sadhukhan, H. Sejima, S. Ikenaga, K. Yamamoto, K. Gao, S. Kanegawa and O. Sato, Macroscopic Polarization Change of Mononuclear Valence Tautomeric Cobalt Complexes Through the Use of Enantiopure Ligand, *Chemistry – A European Journal*, **n/a**, e202202161.

44. D. Ruiz-Molina, J. Veciana, K. Wurst, D. N. Hendrickson and C. Rovira, Redox-tunable valence tautomerism in a cobalt Schiff base complex, *Inorganic Chemistry*, 2000, **39**, 617-619.

45. A. Vlček Jr, Metal and ligand oxidation states in dioxolene complexes: meaning, assignment and control, *Comments on Inorganic Chemistry*, 1994, **16**, 207-228.

46. A. Bencini, A. Caneschi, A. Dei, D. Gatteschi, C. Sangregorio, D. Shultz, L. Sorace and M. G. Vaz, Polyoxolenes may provide a tool for designing paramagnetic molecules with predetermined spin topologies, *Comptes Rendus Chimie*, 2003, **6**, 663-676.

47. O. Cador, F. Chabre, A. Dei, C. Sangregorio, J. V. Slageren and M. G. Vaz, Temperature-induced solid-state valence tautomeric interconversion in two cobalt− schiff base diquinone complexes, *Inorganic chemistry*, 2003, **42**, 6432-6440.

48. O. Rotthaus, F. Thomas, O. Jarjayes, C. Philouze, E. Saint-Aman and J. L. Pierre, Valence Tautomerism in Octahedral and Square-Planar Phenoxyl–Nickel (II) Complexes: Are Imino Nitrogen Atoms Good Friends?, *Chemistry–A European Journal*, 2006, **12**, 6953-6962.

49. B. A. Jazdzewski and W. B. Tolman, Understanding the copper–phenoxyl radical array in galactose oxidase: contributions from synthetic modeling studies, *Coordination Chemistry Reviews*, 2000, **200**, 633-685.

50. J. W. Whittaker, Free radical catalysis by galactose oxidase, *Chemical reviews*, 2003, **103**, 2347-2364.

51. P. Chaudhuri and K. Wieghardt, Phenoxyl radical complexes, *Progress in Inorganic Chemistry*, 2001, **50**, 151-216.

52. K. S. Min, T. Weyhermüller and K. Wieghardt, Coordination chemistry of 2-(8-aminoquinolino)-4, 6-di-tert-butylphenol with manganese (iv), iron (iii), and cobalt (ii/iii): N, O-coordinated o-iminobenzosemiquinonate (1−) π radical monoanions vs. o-iminophenolate (2−) dianions, *Dalton Transactions*, 2004, 178-186.

53. T. K. Paine, T. Weyhermüller, L. D. Slep, F. Neese, E. Bill, E. Bothe, K. Wieghardt and P. Chaudhuri, Nonoxovanadium (IV) and Oxovanadium (V) Complexes with Mixed O, X, O-Donor Ligands (X= S, Se, P, or PO), *Inorganic chemistry*, 2004, **43**, 7324-7338.

54. M. Ballester, Inert free radicals (IFR): a unique trivalent carbon species, *Accounts of Chemical Research*, 1985, **18**, 380-387.

55. D. Ruiz-Molina, J. Veciana, F. Palacio and C. Rovira, Drawbacks arising from the high steric congestion in the synthesis of new dendritic polyalkylaromatic polyradicals, *The Journal of Organic Chemistry*, 1997, **62**, 9009-9017.

56. C. Rovira, D. Ruiz-Molina, O. Elsner, J. Vidal-Gancedo, J. Bonvoisin, J. P. Launay and J. Veciana, Influence of Topology on the Long-Range Electron-Transfer Phenomenon, *Chemistry–A European Journal*, 2001, **7**, 240-250.

57. B. Li, J. Tao, H.-L. Sun, O. Sato, R.-B. Huang and L.-S. Zheng, Side-effect of ancillary ligand on electron transfer and photodynamics of a dinuclear valence tautomeric complex, *Chemical Communications*, 2008, DOI: 10.1039/B801171K, 2269-2271.

58. P. Dapporto, A. Dei, G. Poneti and L. Sorace, Complete direct and reverse optically induced valence tautomeric interconversion in a cobalt-dioxolene complex, *CHEMISTRY-A EUROPEAN JOURNAL*, 2008, **14**, 10915-10918.

59. I. Lawthers and J. J. McGarvey, Spin-state relaxation dynamics in iron(III) complexes:

photochemical perturbation of the 2T .dblharw. 6A spin equilibrium by pulsed-laser irradiation in the ligand-to-metal charge-transfer absorption band, *Journal of the American Chemical Society*, 1984, **106**, 4280-4282.

60. A. Hauser, Reversibility of light-induced excited spin state trapping in the Fe(ptz)6(BF4)2, and the Zn1−xFex(ptz)6(BF4)2 spin-crossover systems, *Chemical Physics Letters*, 1986, **124**, 543-548.

61. A. Hauser, Cooperative effects on the HS→LS relaxation in the [Fe(ptz)6](BF4)2 spin-crossover system, *Chemical Physics Letters*, 1992, **192**, 65-70.

62. T. Boonprab, S. J. Lee, S. G. Telfer, K. S. Murray, W. Phonsri, G. Chastanet, E. Collet, E. Trzop, G. N. L. Jameson, P. Harding and D. J. Harding, The First Observation of Hidden Hysteresis in an Iron(III) Spin-Crossover Complex, *Angewandte Chemie International Edition*, 2019, **58**, 11811-11815.

63. Y. S. Ye, X. Q. Chen, Y. De Cai, B. Fei, P. Dechambenoit, M. Rouzières, C. Mathonière, R. Clérac and X. Bao, Slow Dynamics of the Spin-Crossover Process in an Apparent High-Spin Mononuclear FeII Complex, *Angewandte Chemie International Edition*, 2019, **58**, 18888-18891.

64. O. Sato, S. Hayami, Z.-z. Gu, K. Takahashi, R. Nakajima, K. Seki and A. Fujishima, Photo-induced valence tautomerism in a Co compound, *Journal of Photochemistry and Photobiology A: Chemistry*, 2002, **149**, 111-114.

65. C. Carbonera, A. Dei, J.-F. Létard, C. Sangregorio and L. Sorace, Thermally and Light-Induced Valence Tautomeric Transition in a Dinuclear Cobalt–Tetraoxolene Complex, *Angewandte Chemie International Edition*, 2004, **43**, 3136-3138.

66. C. Roux, D. M. Adams, J. P. Itié, A. Polian, D. N. Hendrickson and M. Verdaguer, Pressure-Induced Valence Tautomerism in Cobalt o-Quinone Complexes: An X-ray Absorption Study of the Low-Spin [CoIII(3,5-DTBSQ)(3,5-DTBCat)(phen)] to High-Spin [CoII(3,5-DTBSQ)2(phen)] Interconversion, *Inorganic Chemistry*, 1996, **35**, 2846-2852.

67. T. Yokoyama, K. Okamoto, K. Nagai, T. Ohta, S. Hayami, Z.-Z. Gu, R. Nakajima and O. Sato, Photo-induced magnetized state of Co(DTBSQ)(DTBCat)(phen)·C6H5CH3 studied by X-ray absorption spectroscopy, *Chemical Physics Letters*, 2001, **345**, 272-276.

68. R. D. Schmidt, D. A. Shultz and J. D. Martin, Magnetic Bistability in a Cobalt Bis(dioxolene) Complex: Long-Lived Photoinduced Valence Tautomerism, *Inorganic Chemistry*, 2010, **49**, 3162-3168.

69. , Molecular Magnetism (Kahn, Olivier), *Journal of Chemical Education*, 1995, **72**, A19.

70. A. I. Gaudette, I.-R. Jeon, J. S. Anderson, F. Grandjean, G. J. Long and T. D. Harris, Electron Hopping through Double-Exchange Coupling in a Mixed-Valence Diiminobenzoquinone-Bridged Fe2 Complex, *Journal of the American Chemical Society*, 2015, **137**, 12617-12626.

71. S. Horiuchi, K. Kobayashi, R. Kumai, N. Minami, F. Kagawa and Y. Tokura, Quantum ferroelectricity in charge-transfer complex crystals, *Nature Communications*, 2015, **6**, 7469.

72. D.-W. Fu, H.-L. Cai, Y. Liu, Q. Ye, W. Zhang, Y. Zhang, X.-Y. Chen, G. Giovannetti, M. Capone, J. Li and R.-G. Xiong, Diisopropylammonium Bromide Is a High-Temperature Molecular Ferroelectric Crystal, *Science*, 2013, **339**, 425-428.

73. X. Zhang, W.-H. Xu, W. Zheng, S.-Q. Su, Y.-B. Huang, Q. Shui, T. Ji, M. Uematsu, Q. Chen, M. Tokunaga, K. Gao, A. Okazawa, S. Kanegawa, S.-Q. Wu and O. Sato, Magnetoelectricity Enhanced by Electron Redistribution in a Spin Crossover [FeCo] Complex, *Journal of the American Chemical Society*, 2023, **145**, 15647-15651.

74. S.-Q. Wu, M. Liu, K. Gao, S. Kanegawa, Y. Horie, G. Aoyama, H. Okajima, A. Sakamoto, M. L. Baker, M. S. Huzan, P. Bencok, T. Abe, Y. Shiota, K. Yoshizawa, W. Xu, H.-Z. Kou and O. Sato, Macroscopic Polarization Change via Electron Transfer in a Valence Tautomeric Cobalt Complex, *Nature Communications*, 2020, **11**, 1992.

75. P. Sadhukhan, S.-Q. Wu, J. I. Long, T. Nakanishi, S. Kanegawa, K. Gao, K. Yamamoto, H. Okajima, A. Sakamoto, M. L. Baker, T. Kroll, D. Sokaras, A. Okazawa, N. Kojima, Y.

Shiota, K. Yoshizawa and O. Sato, Manipulating electron redistribution to achieve electronic pyroelectricity in molecular [FeCo] crystals, *Nature Communications*, 2021, **12**, 4836.

76. P. Sadhukhan, S.-Q. Wu, S. Kanegawa, S.-Q. Su, X. Zhang, T. Nakanishi, J. I. Long, K. Gao, R. Shimada, H. Okajima, A. Sakamoto, J. G. Chiappella, M. S. Huzan, T. Kroll, D. Sokaras, M. L. Baker and O. Sato, Energy conversion and storage via photoinduced polarization change in non-ferroelectric molecular [CoGa] crystals, *Nature Communications*, 2023, **14**, 3394.
77. Y.-B. Huang, J.-Q. Li, W.-H. Xu, W. Zheng, X. Zhang, K.-G. Gao, T. Ji, T. Ikeda, T. Nakanishi, S. Kanegawa, S.-Q. Wu, S.-Q. Su and O. Sato, Electrically Detectable Photoinduced Polarization Switching in a Molecular Prussian Blue Analogue, *Journal of the American Chemical Society*, 2024, **146**, 201-209.
78. S. Kanegawa, Y. Shiota, S. Kang, K. Takahashi, H. Okajima, A. Sakamoto, T. Iwata, H. Kandori, K. Yoshizawa and O. Sato, Directional electron transfer in crystals of [CrCo] dinuclear complexes achieved by chirality-assisted preparative method, *Journal of the American Chemical Society*, 2016, **138**, 14170-14173.
79. S.-Q. Su, S.-Q. Wu, Y.-B. Huang, W.-H. Xu, K.-G. Gao, A. Okazawa, H. Okajima, A. Sakamoto, S. Kanegawa and O. Sato, Photoinduced Persistent Polarization Change in a Spin Transition Crystal, *Angewandte Chemie International Edition*, 2022, **61**, e202208771.
80. S. Kanegawa, S.-Q. Wu, Z. Zhou, Y. Shiota, T. Nakanishi, K. Yoshizawa and O. Sato, Polar Crystals Using Molecular Chirality: Pseudosymmetric Crystallization toward Polarization Switching Materials, *Journal of the American Chemical Society*, 2024, **146**, 11553-11561.
81. J. Tao, H. Maruyama and O. Sato, Valence Tautomeric Transitions with Thermal Hysteresis around Room Temperature and Photoinduced Effects Observed in a Cobalt−Tetraoxolene Complex, *Journal of the American Chemical Society*, 2006, **128**, 1790-1791.
82. C. Carbonera, A. Dei, J.-F. Létard, C. Sangregorio and L. Sorace, Thermally and Light-

Induced Valence Tautomeric Transition in a Dinuclear Cobalt–Tetraoxolene Complex, *Angewandte Chemie*, 2004, **116**, 3198-3200.

83. D. Kiriya, H.-C. Chang and S. Kitagawa, Molecule-Based Valence Tautomeric Bistability Synchronized with a Macroscopic Crystal-Melt Phase Transition, *Journal of the American Chemical Society*, 2008, **130**, 5515-5522.

84. K. G. Alley, G. Poneti, J. B. Aitken, R. K. Hocking, B. Moubaraki, K. S. Murray, B. F. Abrahams, H. H. Harris, L. Sorace and C. Boskovic, A Two-Step Valence Tautomeric Transition in a Dinuclear Cobalt Complex, *Inorganic Chemistry*, 2012, **51**, 3944-3946.

85. S.-Q. Su, S.-Q. Wu, S. Kanegawa, K. Yamamoto and O. Sato, Control of electronic polarization via charge ordering and electron transfer: electronic ferroelectrics and electronic pyroelectrics, *Chemical Science*, 2023, **14**, 10631-10643.

86. W.-H. Xu, Y.-B. Huang, W.-W. Zheng, S.-Q. Su, S. Kanegawa, S.-Q. Wu and O. Sato, Photo-induced valence tautomerism and polarization switching in mononuclear cobalt complexes with an enantiopure chiral ligand, *Dalton Transactions*, 2024, DOI: 10.1039/D3DT03915C.

87. A. G. Starikov, A. A. Starikova, M. G. Chegerev, S. M. Aldoshin, A. V. Metelitsa and V. I. Minkin, Spin-State-Switching Rearrangements of Bis(dioxolene)-Bridged CrCo Complexes: A DFT Study, *European Journal of Inorganic Chemistry*, 2021, **2021**, 4113-4121.

Chapter 2. Solvent-Dependent Valence Tautomerism and Polarization Switching in a Heterodinuclear [CrCo] Complex

2.1 Introduction

Polar materials, which react to external factors such as temperature, light, and electric fields, hold immense latent for advanced molecular memory devices in the future.[1-7] Among these materials, ferroelectric substances have obtained significant attention for their ability to reverse spontaneous polarization under an applied electric field, making them candidates for polarization-switching applications. However, achieving desired performance in ferroelectrics remains a significant challenge due to their inherently collective nature, posing formidable obstacles from a chemical standpoint.[8-12] To broaden the scope of polarization-switching materials, researchers have proposed a ground-up method that employs active molecules capable of switching between states with differing electric dipole moments, especially in non-ferroelectric systems seeking to achieve polarization switching. Valence tautomeric (VT) molecules represent promising structural motifs in this context, showing different electronic structure responding to external disturbances such as temperature, pressure, and fields.[13-48] Moreover, at the crystal scale exhibiting controlble macroscopic polarization, it is essential for the target molecules to crystallize in polar space groups where the dipole moment cannot be negated. However, the acquisition of such crystals remains a rare occurrence, as evidenced by the limited number of non-ferroelectric molecular crystals capable of macroscopic polarization reversal facilitated by electron transfer.. This scarcity highlights the challenges inherent in crystal engineering and underscores the reliance on fortuitous discoveries in synthesizing polar crystals with tailored molecular designs conducive to arranging molecules in polar space groups. [81-85]

Recently, our group synthesized an array of dinuclear VT complexes with heterochiral ligands in a polar space group developed through a chiral-assisted strategy. This method capitalizes on the

tendency of left-handed chiral ligands to interact with corresponding right-handed counterparts, leading to the development of a polar crystal structure. [73, 75, 76, 78] Based on this work, the introduction of enantiopure ligands was considered as a natural extension to improve the likelihood on acquisition of polar crystals. Previous studies on mononuclear cobalt complexes have highlighted the effectiveness of this approach to broaden the variety of polar crystals exhibiting VT feature.[43, 74, 86] However, applying the same crystallization approach to dinuclear systems with enantiopure ligands proved invalid due to the absence of complementary recognition of chiral ligands. Consequently, a [$Co^{II}Co^{III}$] complex utilizing enantiopure *SS*-cth ligand (cth = (7S, 14S)-5,5,7,12,12,14-hexamethyl-1,4,8,11-tetraazacyclotetradecane) was synthesized as a tentative screening. Despite existing in a high-spin (HS) state within a temperature range of 2 to 400 K, the complex crystallized in the polar $P2_1$ space group, featuring a well-defined molecular arrangement where Co^{II} and Co^{III} sites were clearly distinguished. This distinction is critical for realizing directional electron transfer, which plays a significant role in achieving polarization switching behavior. Considering the beneficial influence of chromium-dhbq facilitating the stabilization of a low-spin trivalent cobalt state, which in turn enhances the VT transition temperature in the associated racemic system, it is plausible that site-selective substitution with Cr^{III} ions for the Co^{III} sites could induce the desired VT behavior. [87] To explore this possibility, a [CrCo] complex incorporating the enantiopure *SS*-cth ligand was prepared. Employing a carefully designed synthetic approach that prioritized the incorporation of more inert Cr^{3+} sites, we successfully synthesized and purified the heterometallic dinuclear [CrCo] complex.. This complex, denoted as compound **1·sol**, comprised [Cr(*SS*-cth)(μ-dhbq)Co(*SS*-cth)]$(PF_6)_3$·2.5H_2O·0.5MeOH, where H_2dhbq represents 2,5-dihydroxy-1,4-benzoquinone. Analysis of the structure showed that **1·sol** shares structural similarities with the aforementioned [$Co^{II}Co^{III}$] complex. Magnetometry and spectroscopic studies demonstrated a partial VT transition between the Co metal center and $dhbq^{2-}$ bridging ligand in **1·sol**, allowing for direct probing of polarization switching through pyroelectric measurements. Notably, heating preserved the integrity of the crystals without altering the space

group. Notably, further structural characterization and magnetic measurements demonstrated that the desolvated complex denoted as **1**, exhibited a more thorough VT behavior. Upon exposure to mixture vapor of water/methanol, complex 1 can reabsorb solvent molecules, returning to its solvated form, **1**·sol, accompanying with partial VT transition. This solvent-driven alteration in physical behavior was consistently detected, highlighting the dynamic nature of the complex.

2.2 Experimental Section

2.2.1. Starting material and synthesis

All reagents were commercially purchased by Tokyo Chemical Industry Co., Ltd., FUJIFILM Wako, Pure Chemical Corporation, and Sigma-Aldrich Company, and directly used without further purification.

Synthesis of Racemic cth. The synthesis of racemic-cth ligand (5,5,7,12,12,14-hexamethyl-1,4,8,11-tetraazacyclotetradecane) followed established procedures from the reference article (Scheme 2.1).[54] Initially, a solution of 55.7 g of 60% perchloric acid (0.33 mol) stored in the separatory funnel was dropwise added to a 500 mL acetone solution of 1,2-diaminoethane (20 g, 0.33 mol), the mixture was put in the ice bath to avoid overheat and stirred overnight. The resulting white solid, identified as 5,7,7,12,14,14-hexamethyl-1,4,8,11-tetraazacyclotetradeca-4,11-diene diperchlorate, was collected by filtration and washed with acetone without further purification (yield: 36 g, 45%). Repeat the last step until you obtain enough precursor. Subsequently, the crude product (100 g, 0.21 mol) was dissolved in 500 mL of methanol treated by an ice bath. A mixture of $NaBH_4$ (19 g, 0.63 mol) and NaOH (16.5 g, 0.42 mol) was added gradually, followed by the addition of an aqueous solution of NaOH (50 g in 1 L water) once the solution reached room temperature, and stirring continued for an additional hour. The resulting white solid was isolated

Scheme 2.1 Synthetic route of tetradentate ligand Rac-cth

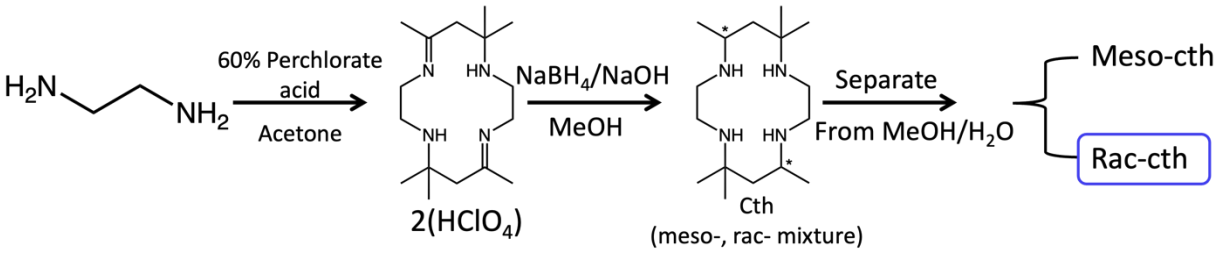

by filtration and completely air-dried. The product was then dissolved in 600 mL of methanol, and upon addition of 400 mL of water, stirring for 1 hour precipitated meso-cth, which was removed by filtration. A further 200 mL of water was added, and after stirring for an hour, the resulting precipitate was again discarded by filtration. It is noted that the amount of precipitated meso-cth should be more than half the starting material to guarantee the purity of remained racemic-cth. The solution was evaporated nearly to dryness using a rotary evaporator, and the resulting white solid product of racemic-cth monohydrate was collected by filtration and washed with a small quantity of cold water (yield: 40 g, 60%).

Synthesis of enantiopure *SS*/*RR*-cth. The enantiopure *SS*/*RR*-cth was synthesized as previously reported method (Scheme 2.2).[55] *Rac*-cth (64.0 g 0.2 mol) and nickel diacetate tetrahydrate (54.4 g, 0.24 mol) were mixed in 1.0 L methanol solution. The solution was heated up to 60℃ and stirred for half an hour. The color of solution was changed from green to blue-violet and then sodium perchlorate (48.8 g, 0.4 mol) was added. Keep stirring the solution for 30 minutes under room temperature and then put it in the ice bath for an additional 30 minutes. The blue-violet precipitate was filtered and washed with ether. The air-dried solid product (40.0 g) was dissolved in water (100.0 mL) and dropwise addition of 60% perchlorate acid (20.0 g) to afford yellow precipitate [Ni(*Rac*-cth)]$(ClO_4)_2$. The ground yellow powder (40.0 g) was gradually added to a solution of acetonitrile (1.6 L) until completely dissolved to afford a dark-purple solution. Subsequently, tetra-n-butylammonium bromide (72.0 g) was added to the solution, and a green precipitate of bromide salt [$(Ni(Br)_2$(*Rac*-cth)] was filtered and well-dried under a reduced vacuum. Similarly, the green

solid (36.0 g) was ground into tiny powder and completely dissolved in water (1.4 L) to obtain a dark yellow solution. The sodium *d*-tartrate dihydrate (4.5 g, 19.8 mmol) was dissolved with a small amount of water and poured into the dark yellow solution. After stirring for 30 minutes at room temperature, an aqueous of sodium perchlorate (5.4 g, 36.0 mmol) was added, and the color gradually changed to greenish brown. The solution was fully chilled in an ice bath overnight to afford blue-violet precipitate ($[(Ni(\textit{SS}\text{-cth}))_2(\textit{d}\text{-tart})](ClO_4)_2$) (denoted as NiSS). The precipitate was filtered and washed with cold water. The remained solution was added sodium oxalate (9.0 g) and sodium perchlorate (9.0 g). Then utilize aqueous of sodium hydroxide to basify the solution to pH∽10. The pale blue precipitate of $[\{Ni(\textit{Rac}\text{-cth})\}_2(ox)](ClO_4)_2$ was removed by filter. The pH of filtrate solution was adjusted to pH∽1 with perchlorate acid to afford blue-violet precipitate $[(Ni(\textit{RR}\text{-cth}))_2(ox)](ClO_4)_2$ (denoted as NiRR). NiSS (6.84 g) was dissolved in a mixture of ethanol (170 mL) and water (340 mL). Sodium hydroxide (6.84 g) and sodium cyanide (13.9 g) were sequentially added to the suspension. The solution was stirred and refluxed for 2 hours until the color changed from purple to light yellow. The volume of the solution was condensed by rotary evaporation to remove ethanol, resulting in the precipitate of white solids including *SS*-cth and a small amount of $Ni(CN)_6$. The white solids were then extracted in a separatory funnel using a mixture of ether and water. *SS*-cth dissolved in ether, located in the upper layer, while any remaining $Ni(CN)_6$ was absorbed by water in the lower layer. This extraction process was repeated three times, and the ether solution was subsequently evaporated to yield *SS*-cth. A similar synthetic route was employed to obtain *RR*-cth on NiRR.

Scheme 2.2 Optical resolution of *SS*/*RR*-cth

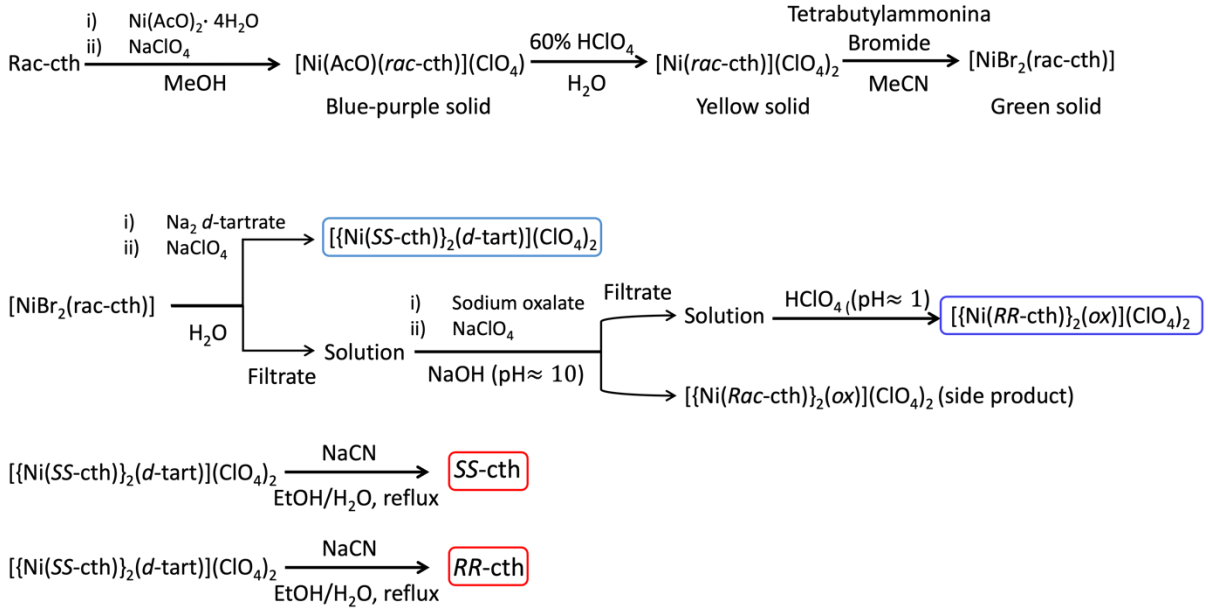

Synthesis of [Co(AcO)(*SS*-cth)]PF_6. 750 mg (3.0 mmol) of $Co(AcO)_2{\cdot}4H_2O$ and 850 mg (3.0 mmol) of *SS*-cth were introduced into a 10 mL ethanol solution. This mixture underwent stirring and heating until reaching a temperature of 60℃. Subsequently, NH_4PF_6 (540 mg, 3.3 mmol) was introduced into the solution, leading to the gradual precipitate of pink solid [Co(AcO)(*SS*-cth)]PF_6. After cooling the solution in an ice bath, the product was isolated via filtration and washed successively with cold ethanol and ether. The final yield of [Co(AcO)(*SS*-cth)]PF_6 obtained was approximately 0.96 g, yield of 76.1%.

Synthesis of [$CrCl_2$(*SS*-cth)]Cl. The synthesis of [$CrCl_2$(SS-cth)]Cl followed a procedure similar to that described in the literature for [$CrCl_2$(*Rac*-cth)]Cl, employing enantiopure *SS*-cth as the initial substance. This process yielded a greenish-blue solid product with a yield of 68.0%.[3]

Synthesis of [Zn(Aco)(*SS*-cth)]PF_6. The synthesis of [Zn(AcO)(*SS*-cth)]PF_6 followed a procedure analogous to that employed for [Co(Ac)(*SS*-cth)]PF_6, utilizing $Zn(AcO)_2$ (550 mg, 3.0 mmol) as the initial reagent. This process resulted in the precipitate of a white solid product with

a yield of 70.0%.

Synthesis of [Ni(Aco)(*SS*-cth)]PF_6. The synthesis of [Ni(AcO)(*SS*-cth)]PF_6 followed a procedure analogous to that employed for [Co(Ac)(*SS*-cth)]PF_6, utilizing $Ni(AcO)_2 \cdot 4H_2O$ (746 mg, 3.0 mmol) as the initial reagent. This process resulted in the precipitate of a white solid product with a yield of 72.0%.

Synthesis of [Cr(*SS*-cth)(μ-dhbq)]PF_6. Under an inert atmosphere, a mixture of 2,5-dihydroxy-1,4-benzoquinone (H_2dhbq; 140 mg, 1 mmol) and triethylamine (202 mg, 2.0 mmol) in methanol (50 mL) was stirred. Subsequently, solid [$CrCl_2$(*SS*-cth)]Cl (443 mg, 1 mmol) was introduced into the solution, and the temperature was raised to 60°C for one hour. Following this, an aqueous solution of $LiPF_6$ (300 mg, 2 mmol) was added to the dark-red solution. Slow evaporation of the solution resulted in the formation of a dark red precipitate, [Cr(*SS*-cth)(μ-dhbq)]PF_6. The precipitate was filtered, yielding 80% after washing with water.

Synthesis of [Co(*SS*-cth)(μ-dhbq)Cr(*SS*-cth)]$(PF_6)_3$.

A **one-pot synthetic approach** was employed to synthesize the [CrCo] complex with enantiopure ligands, following a previously reported method.[3] In this method, mononuclear [Co(AcO)(*SS*-cth)]PF_6 (547.5 mg, 1 mmol) and [$CrCl_2$(*SS*-cth)]Cl (443 mg, 1 mmol) were directly mixed in the dhbq solution to yield the crude product of [Co*(SS*-cth)(μ-dhbq)Cr(*SS*-cth)]$(PF_6)_3$ (Figure 2.1).

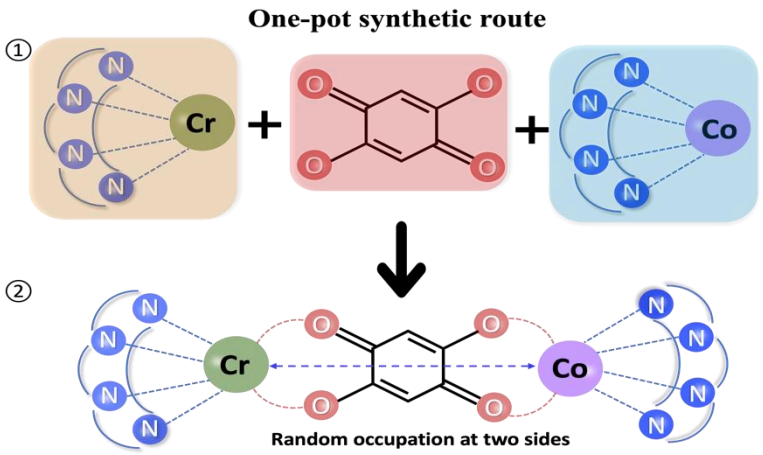

Figure 2.1. Schematic illustration for the one-pot synthetic strategy.

In the **stepwise synthetic method**, a mixture of [Co(AcO)(*SS*-cth)]PF_6 (547.5 mg, 1 mmol) and [Cr(*SS*-cth)(μ-dhbq)]PF_6 (619.5 mg, 1 mmol) was combined with methanol (50 mL) under N_2 gas. The reaction solution was stirred at room temperature for 1 hour before the addition of an aqueous solution of KPF_6 (227 mg, 1.5 mmol) to the methanol solution. The mixture was continuously stirred overnight to precipitate purple-red [Co(*SS*-cth)(μ-dhbq)Cr(*SS*-cth)]$(PF_6)_3$. The resulting precipitate was filtered, washed with water, and then dried completely under reduced pressure. The crude product underwent crystallization in a mixed solution of methanol and water with drops of acetonitrile, resulting in the formation of red stick-shaped crystals (yield = 239 mg, 83%) (Figure 2.2). Note: the schematic illustration for one-pot and stepwise synthetic route exemplified by [CrCo] to eliminate redundant information.

Synthesis of [Ni(*SS*-cth)(μ-dhbq)Cr(*SS*-cth)]$(PF_6)_3$.

In the **one-pot synthetic approach**, the [CrNi] complex with enantiopure ligands was synthesized following a previously reported method. This involved directly mixing mononuclear [Ni(AcO)(*SS*-cth)]PF_6 (546.5 mg, 1 mmol) and [$CrCl_2$(*SS*-cth)]Cl (443 mg, 1 mmol) in the dhbq solution to

produce the crude product of [Ni(*SS*-cth)(*μ*-dhbq)Cr(*SS*-cth)](PF$_6$)$_3$.

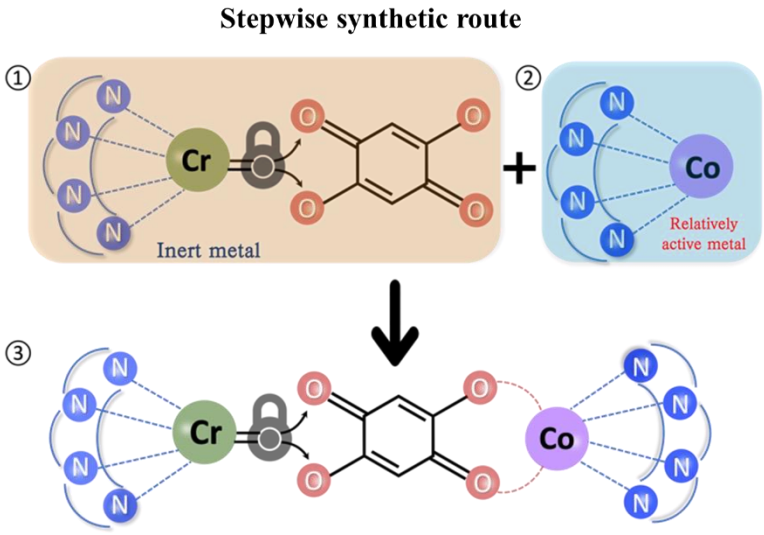

Figure 2.2. Schematic illustration for the stepwise synthetic strategy.

In the **stepwise synthetic approach**, the procedure of [Ni(*SS*-cth)(*μ*-dhbq)Cr(*SS*-cth)](PF$_6$)$_3$ is similar to that of [Co(*SS*-cth)(*μ*-dhbq)Cr(*SS*-cth)](PF$_6$)$_3$ using a mixture comprising [Ni(AcO)(*SS*-cth)]PF$_6$ (546.5 mg, 1 mmol) and [Cr(*SS*-cth)(μ-dhbq)]PF$_6$ (619.5 mg, 1 mmol) to afford the precipitation of the brown product.

Synthesis of [Zn(*SS*-cth)(*μ*-dhbq)Cr(*SS*-cth)](PF$_6$)$_3$.

Using a **one-pot synthetic approach**, the [CrNi] complex with enantiopure ligands was synthesized following a previously reported method. The procedure involved directly combining mononuclear [Zn(AcO)(*SS*-cth)]PF$_6$ (553.5 mg, 1 mmol) with [CrCl$_2$(*SS*-cth)]Cl (443 mg, 1 mmol) in the dhbq solution, resulting in the formation of the crude product [Zn(*SS*-cth)(*μ*-dhbq)Cr(*SS*-cth)](PF$_6$)$_3$.

In the **stepwise synthetic approach**, the procedure of [Zn(*SS*-cth)(*μ*-dhbq)Cr(*SS*-cth)](PF$_6$)$_3$ is similar to that of [Co(*SS*-cth)(*μ*-dhbq)Cr(*SS*-cth)](PF$_6$)$_3$ using a mixture comprising [Zn(AcO)(*SS*-

cth)]PF_6 (553.5 mg, 1 mmol) and [Cr(*SS*-cth)(μ-dhbq)]PF_6 (619.5 mg, 1 mmol) to afford the precipitation of the red product.

2.2.2. Physical measurements

Electrospray Ionization Mass Spectrometry (ESI-MS). Complexes were dissolved in methanol to prepare samples in solution. Data collection was conducted using a JMS-T100CS (JEOL) spectrometer in ESI+ mode at ambient temperature.

IR spectroscopy. Temperature-dependent IR spectra were collected employing an FT/IR spectrophotometer (*Jasco* 600Plus) equipped with a closed-cycle helium refrigerator cryostat (Rockgate Corporation) in the range of 4000 - 400 cm^{-1}. The ground-powder samples were sandwiched between grained and flat CaF_2 plates. The desolvated sample was obtained by heating up to 400 K for 30 minutes to remove the solvents and subsequently transferred to the cryostat system with reduced pressure.

UV-vis spectroscopy. Temperature-dependent UV-vis were recorded employing a SHIMADZU MPC-3100 equipped with a closed-cycle helium refrigerator cryostat (Rockgate Corporation) in the range of 300 - 800 nm. The ground-powder samples were uniformly attached to the tapes and then held between flat CaF_2 plates. The treatment of removing solvent is similar to that of IR measurement.

X-ray diffraction measurement and crystal structural determinations. Diffraction data were acquired for **1·sol** at temperatures of 100 K and 200 K under a nitrogen gas stream. Subsequently, compound **1** was obtained *in situ* by heating the crystal at 375 K for 30 minutes to remove the solvents. The diffraction data for compound **1** were collected at temperatures of 100 K, 150 K, and

375 K (Table 1). These measurements were conducted using a Rigaku XtaLab Synergy-R/DW diffractometer equipped with a HyPix-6000 area detector and multi-layer mirror monochromated Mo-Kα radiation with a wavelength (λ) of 0.71073 Å. Structural determination was achieved through direct methods and refinement via full-matrix least-squares on $\boldsymbol{F}^2$ using the SHELX program[56] implemented in the OLEX2 program[57], with anisotropic thermal parameters assigned to all non-hydrogen atoms. Hydrogen atoms were geometrically placed and refined using the riding model.

Table 1 Crystallographic Data Collection and Structural Refinement Information for 1·sol and 1.

	1·sol		**1**		
Empirical formula	$C_{38.5}H_{81}CoCrF_{18}N_8O_7P_3$		$C_{38}H_{74}CoCrF_{18}N_8O_4P_3$		
Formula weight	1313.97		1252.89		
Temperature(K)	100	200	100	150	375
Crystal system	*monoclinic*	*monoclinic*	*monoclinic*	*monoclinic*	*monoclinic*
Lattice Type	Primitive	Primitive	Primitive	Primitive	Primitive
Space group	$P2_1$(#4)	$P2_1$(#4)	$P2_1$(#4)	$P2_1$(#4)	$P2_1$(#4)
a(Å)	9.3263(2)	9.3993(2)	9.2692(2)	9.3298(2)	9.5220(5)
b(Å)	18.9286(6)	18.9744(4)	17.3930(4)	17.4539(5)	17.7433(12)
c(Å)	15.9910(4)	16.0926(3)	16.2840(4)	16.2978(4)	16.6216(9)
α(deg.)	90	90	90	90	90
β(deg.)	89.843(3)	90.051(2)	95.892(2)	95.894(3)	95.488(5)
γ(deg.)	90	90	90	90	90
V(Å^3)	2822.93(14)	2870.(05)(10)	2611.43(11)	2639.93(12)	2795.4(3)
Z value	2	2	2	2	2
D_{calc}(g/cm^3)	1.545	1.516	1.593	1.576	1.489
Light source	MoKα (λ = 0.71073 Å)				
R_1(I>2.00s(I)	0.0560	0.0480	0.048	0.0524	0.0928
wR_2(*all*)	0.1453	0.1280	0.1118	0.1252	0.2137
GOF	1.063	1.004	1.042	1.037	0.991
Flack parameter	0.01(2)	0.038(10)	0.033(12)	0.036(14)	0.02(2)
CCDC	2320504	2320506	2320375	2320376	2320374

[a]$R_1 = \Sigma||F_o| - |F_c||/\Sigma|F_o|$. [b]$wR_2 = [\Sigma\{w(F_o^2 - F_c^2)^2/\Sigma\{w(F_o^2)\}^2]^{1/2}$

Table 2 Selective bond lengths for 1·sol and 1.

	1·sol		**1**		
	100 K	**200 K**	**100 K**	**150 K**	**375 K**
Co-O1 (Å)	**2.057**	**2.067**	**1.902**	**1.911**	**2.053**
Co-O2 (Å)	**2.081**	**2.074**	**1.917**	**1.917**	**2.064**
Co-N1 (Å)	**2.201**	**2.198**	**2.068**	**2.065**	**2.177**
Co-N2 (Å)	**2.111**	**2.112**	**2.027**	**2.028**	**2.110**
Co-N3 (Å)	**2.099**	**2.101**	**2.013**	**2.013**	**2.097**
Co-N4 (Å)	**2.184**	**2.172**	**2.054**	**2.071**	**2.158**
Cr-O1 (Å)	**1.941**	**1.973**	**1.930**	**1.934**	**2.005**
Cr-O2 (Å)	**1.938**	**1.982**	**1.915**	**1.917**	**2.023**
Cr-N1 (Å)	**2.107**	**2.126**	**2.076**	**2.091**	**2.125**
Cr-N2 (Å)	**2.077**	**2.095**	**2.071**	**2.072**	**2.076**
Cr-N3 (Å)	**2.068**	**2.088**	**2.088**	**2.079**	**2.087**
Cr-N4 (Å)	**2.093**	**2.130**	**2.070**	**2.075**	**2.140**
	1·sol		**1**		
	100 K	**200 K**	**100 K**	**150 K**	**375 K**
Co-O1 (Å)	**2.057**	**2.067**	**1.902**	**1.911**	**2.053**
Co-O2 (Å)	**2.081**	**2.074**	**1.917**	**1.917**	**2.064**
Co-N1 (Å)	**2.201**	**2.198**	**2.068**	**2.065**	**2.177**
Co-N2 (Å)	**2.111**	**2.112**	**2.027**	**2.028**	**2.110**
Co-N3 (Å)	**2.099**	**2.101**	**2.013**	**2.013**	**2.097**
Co-N4 (Å)	**2.184**	**2.172**	**2.054**	**2.071**	**2.158**
Cr-O1 (Å)	**1.941**	**1.973**	**1.930**	**1.934**	**2.005**
Cr-O2 (Å)	**1.938**	**1.982**	**1.915**	**1.917**	**2.023**

Cr-N1 (Å)	**2.107**	**2.126**	**2.076**	**2.091**	**2.125**
Cr-N2 (Å)	**2.077**	**2.095**	**2.071**	**2.072**	**2.076**
Cr-N3 (Å)	**2.068**	**2.088**	**2.088**	**2.079**	**2.087**
Cr-N4 (Å)	**2.093**	**2.130**	**2.070**	**2.075**	**2.140**

Magnetic susceptibility measurement. The magnetic measurements were conducted using a Quantum Design SQUID magnetometer (MPMS-5S). Polycrystalline samples weighing approximately 10 mg were placed inside a gelatin capsule and attached to a plastic straw, which was then fixed to a sample rod. The entire measurement process occurred under an applied magnetic field (***H***) of 2000 Oe, with a sweeping rate set at 2 k min^{-1}.

Pyroelectric measurement. Pyroelectric measurements were carried out utilizing a continuous temperature ramping technique employing a Keithley 6517B electrometer and a Quantum Design MPMS-XL chamber, providing precise temperature regulation. To ensure the accurate determination of the pyroelectric current direction, the single-crystal sample was carefully sandwiched between silver paste on its (010) and (0-10) surfaces, each having an area of 0.0598 mm^2 (Figure 2.3). The temperature range for measurements was maintained between 30 and 250 K, with helium gas flow ensuring thermal stability throughout the process. Measurements were conducted at a temperature sweep rate of 10 K min^{-1}.

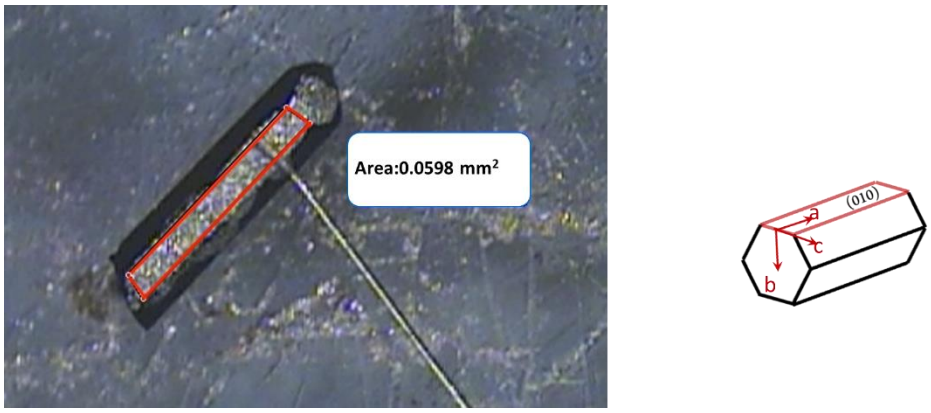

Figure 2.3. The pyroelectric measurement was carried out as a previously reported method.[2-5] The single crystal for pyroelectric measurement (Left). The index of crystal (Right). To ensure the pyroelectric current could be detected by our electrometer, the area of plane (010) should be at least 0.04 mm^2.

2.3. Results & Discussion

Synthesis pathways were employed to yield three heterometallic dinuclear complexes [MCr] (M = Co, Zn, Ni), each coordinating with enantiopure ligands *SS*-cth or *RR*-cth. Thorough characterization via mass spectra confirmed the effectiveness of obtaining pure heterometallic complexes using the stepwise method. Upon dissolvation of crude samples from both methods in methanol, mass spectrometry analyses were performed. In the one-pot synthetic approach, the spectrum revealed three distinct molecular peaks corresponding to [**1**$(PF_6)_2$]+ (m/z = 1107.9) using previously reported techniques, specifically [(CrCr)$(PF_6)_2$]+, [(CrCo)$(PF_6)_2$]+, and [(CoCo)$(PF_6)_2$]+. Interestingly, in addition to the dominant [CrCo] peaks, the [CoCo] peaks exhibited notably high intensity, suggesting a significant random distribution of metal ions across the two coordination sites during synthesis. (Figure 2.4a). On the other hand, the spectrum of [1$(PF_6)_2$]+ adopting the stepwise method was consistent with the calculated results (Figure 2.4b-

c). Here, a molecular peak of $[1(PF_6)_2]+$ (m/z = 1107.3) indicated

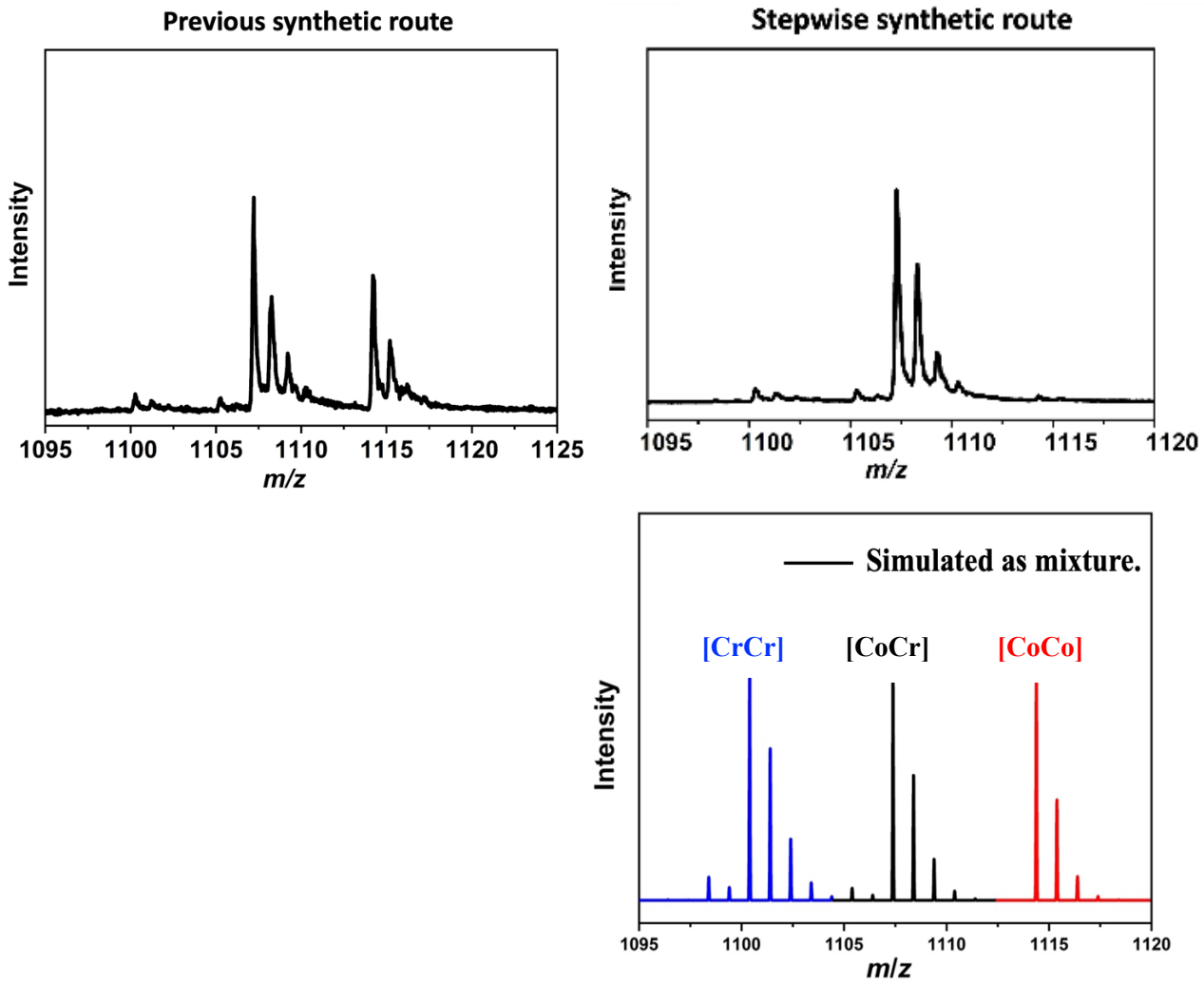

Figure 2.4 (a) Mass spectra of complex **1** synthesized by one-pot and (b) stepwise route. (c) Simulation of an equimolar mixture for $[(CoCo)(PF_6)_2]+/[(CoCr)(PF_6)_2]+/[(CrCr)(PF_6)_2]+$ provides complementary insights.

the presence of the desired complex. While minor peaks from $[(CoCo)(PF_6)_2]+$ were observed, suggesting potential partial dissociation of mononuclear Co oxidized by dissolved oxygen in methanol to form dinuclear Co complexes, the predominance of $[1(PF_6)_2]+$ underscored the stability and purity of the target complex under solution conditions. Additionally, confirmation of

1·sol purity was further supported by PXRD, elemental analysis, and crystal structure. Furthermore, mass spectra related to reference complexes, [NiCr] and [ZnCr], further validated the general applicability of the sequential synthetic approach. It's noted that the ESI-MS of $[(ZnCr)(PF_6)_2]^+$ obtained by one-pot method revealed the peaks from $[(ZnZn)(PF_6)]^+$ (m/z = 981.4) instead of $[(ZnCr)(PF_6)_2]^+$. This discrepancy is probably owing to the faster reaction rate of mononuclear Zn compared with inert Cr. On the other hand, employing a stepwise synthetic route resulted in a set of the peaks originated from $[(ZnCr)(PF_6)_2]^+$ (m/z = 1112.2) (Figure 2.5). This finding confirms the stability of complex in the solution without signs of decomposition. Besides, the observed results align with the simulated one.

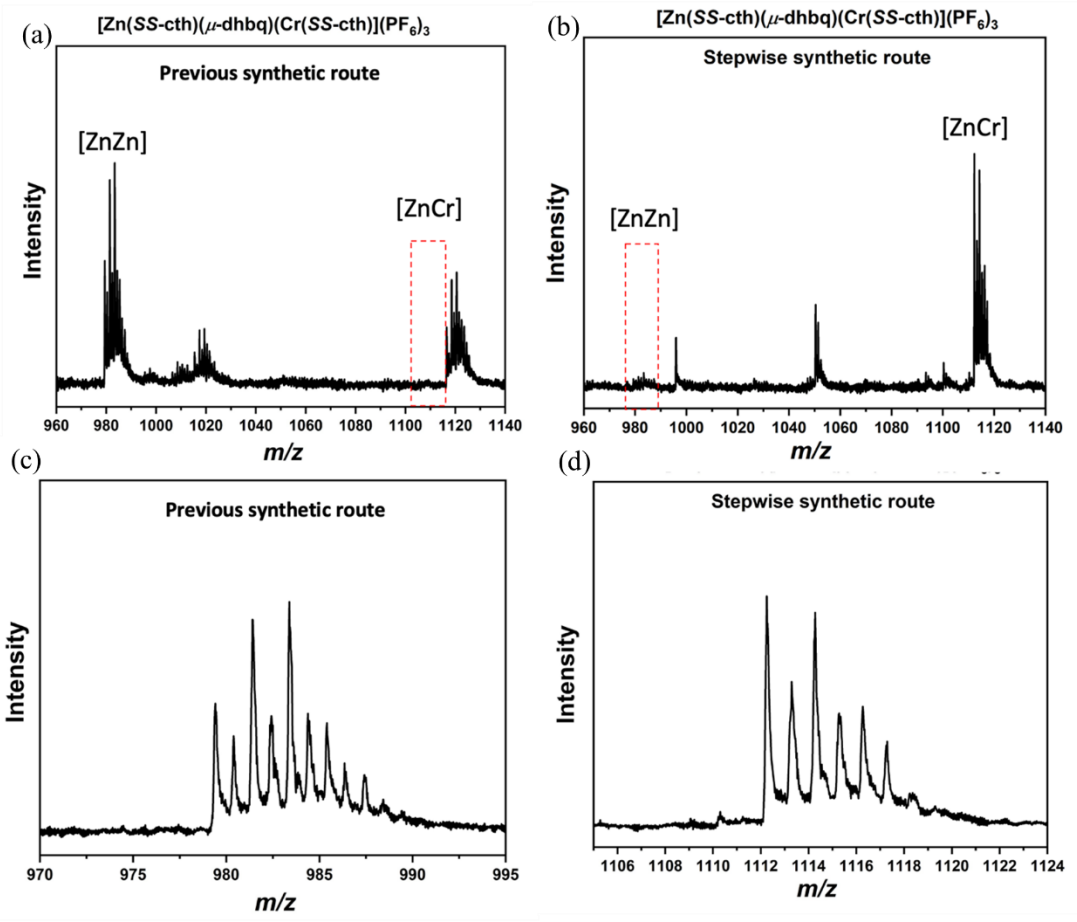

Figure 2.5 (a) The ESI-MS of $[(ZnCr)(PF_6)_2]^+$ obtained by one-pot synthetic route. (b) The mass spectrum of $[(ZnCr)(PF_6)_2]^+$ obtained by stepwise synthetic route. (c) The mass spectrum of

$[(ZnZn)(PF_6)]^+$ (m/z = 981.4). (d) The mass spectrum of $[(ZnCr)(PF_6)_2]^+$ (m/z = 1112.2).

Similarly, in the case of [NiCr], The ESI-MS of $[(NiCr)(PF_6)_2]^+$ obtained by one-pot synthetic route revealed that the predominant peak was contamination of $[(NiNi)(PF_6)]^+$ (m/z = 967.4). The desired complex of $[(NiCr)(PF_6)_2]^+$ (m/z = 1106.4) was found to occupy a minor proportion within the solution. This significant impurity poses a serious obstacle to subsequent purification processes. In contrast, the step-wise synthetic route exhibited a mass spectrum characterized by unambiguous peaks from $[(NiCr)(PF_6)_2]^+$ (m/z = 1106.3) with the absence of $[(NiNi)(PF_6)]^+$ (m/z = 967.4) (Figure 2.6). Collectively, the analysis of these complexes, including reference and [CrCo] evident that utilizing the inert Cr to coordinate with one side of dhbq is reasonable and favorable to reduce

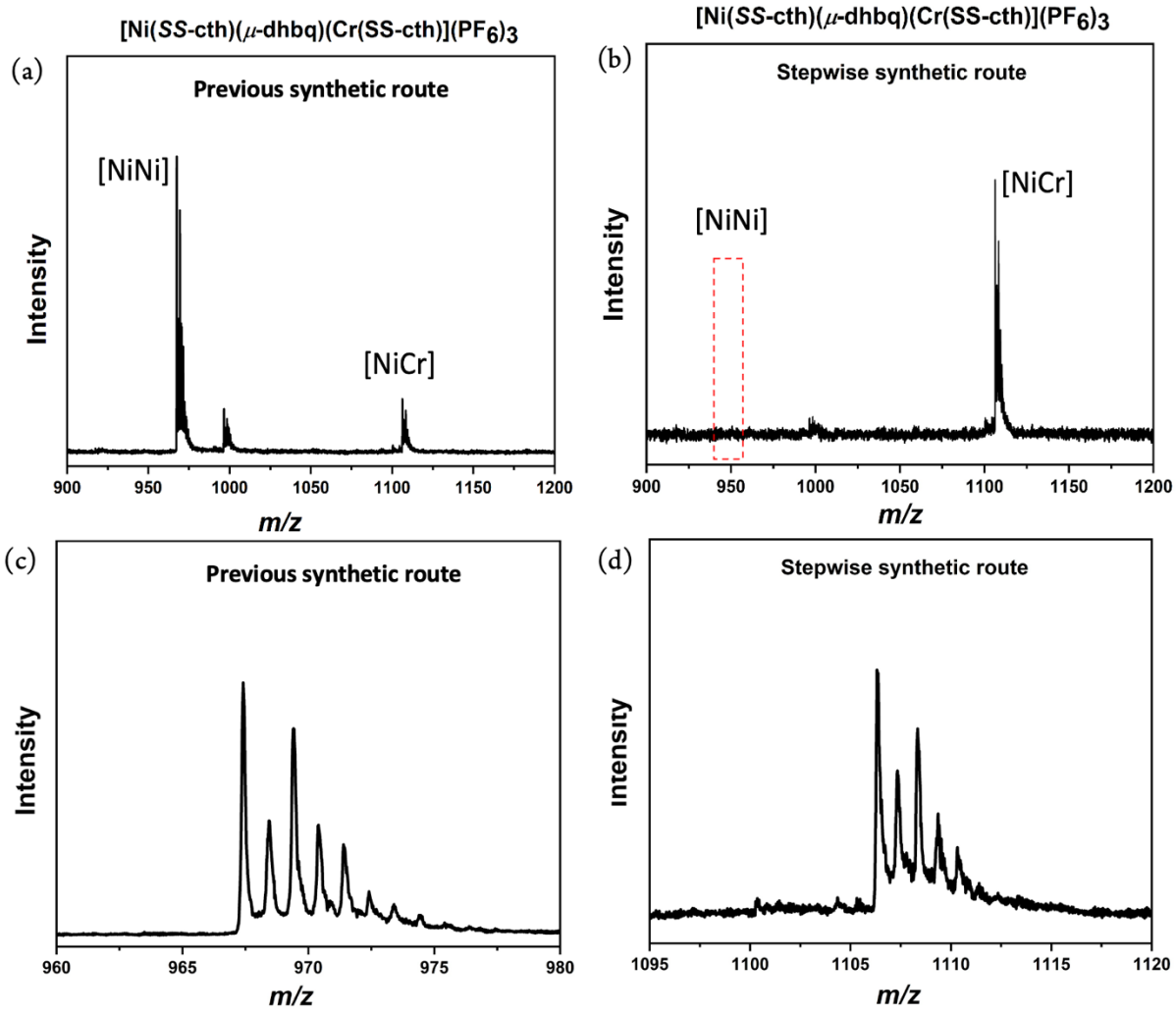

Figure 2.6 (a) The ESI-MS of $[(NiCr)(PF_6)_2]^+$ obtained by one-pot synthetic route. (b) The mass spectrum of $[(NiCr)(PF_6)_2]^+$ obtained by stepwise synthetic route. (c) The mass spectrum of $[(NiNi)(PF_6)]^+$ (m/z = 967.4). (d) The mass spectrum of $[(NiCr)(PF_6)_2]^+$ (m/z = 1106.3).

the mixtures in heteronuclear complexes. The observations provide strong support for the practicality of the novel approach for synthesizing pure heterometallic complexes using an enantiopure ligand.

Single-crystal X-ray diffraction studies conducted at varying temperatures were conducted for both **1·sol** and **1** at 100, 150, 200, and 375 K. The results indicated consistent crystallization in the polar $P2_1$ space group across the entire temperature scale. In the asymmetric unit of 1·sol, a heterodinuclear molecular ion was observed, consisting of [Co(*SS*-cth)] and [Cr(*SS*-cth)] motifs connected via a dhbq ligand, along with three PF6− anions, two and a half water molecules, and a partially occupied methanol molecule. The co-crystallized solvent composition was confirmed through thermogravimetric analysis (TGA) and elemental analysis (Figure 2.7). Notably, unlike the eclipsed conformation observed in previous reports of heterochiral [CrCo] complexes, the two *SS*-

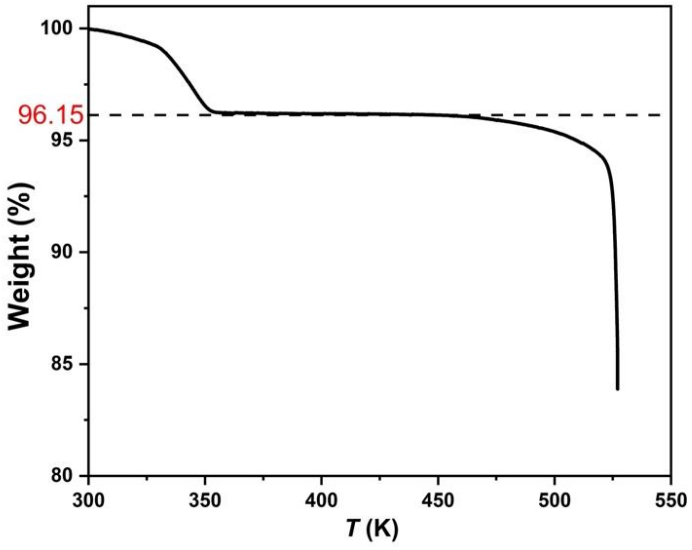

Figure 2.7. Thermal gravimetric analysis (TGA) was performed on compound **1·sol**. The results revealed that complex **1·sol** underwent desolvation with a weight loss of approximately 3.85% at a certain temperature. This almost corresponds to the loss of two lattice water molecules and half a methanol molecule. Upon further heating, the desolvated compound remained stable until approximately 460 K. The TGA results also suggested the solvents in the crystal lattice can be easily removed above 350 K.

cth ligands in the **1·sol** complex motif exhibited a slightly staggered conformation, potentially leading to variations in VT transition feature. At 100 K, **1·sol** demonstrated average Co-O and Co-N bond lengths of 2.069 and 2.149 Å, respectively, indicative of dominant Co^{2+} HS ions, while average Cr-O and Cr-N bond lengths of 1.940 and 2.086 Å, respectively, characterized Cr^{3+} ions (Table 2). Distinct metal-ligand bond lengths emphasized the clearly defined Co and Cr sites instead of random occupancy. The [CrCo] molecular motif exhibited regular packing facilitated by a 2_1-screw rotation, preserving a consistent projection angle of 70.31(7)° along the crystallographic polar *b*-axis., crucial for polarization switching manifestation. Upon heating above room temperature, poor diffraction was observed until 375 K, coinciding with solvent molecule removal according to TGA results. Desolvation was confirmed by crystal structural analysis, with subsequent diffraction data corresponding to its desolvated form, **1**. The bond lengths surrounding Co ions were consistent with those typically observed for Co^{2+} ions. However, upon cooling back to 100 K, significant volume contraction by 184 $Å^3$ was observed, accompanied by a contraction in average bond lengths around Co ions, indicative of Co^{3+}LS ions. Moreover, specific C-C bond lengths contracted while C-O bond lengths elongated, confirming the occurrence of $dbsq^{3-}$ (Figure

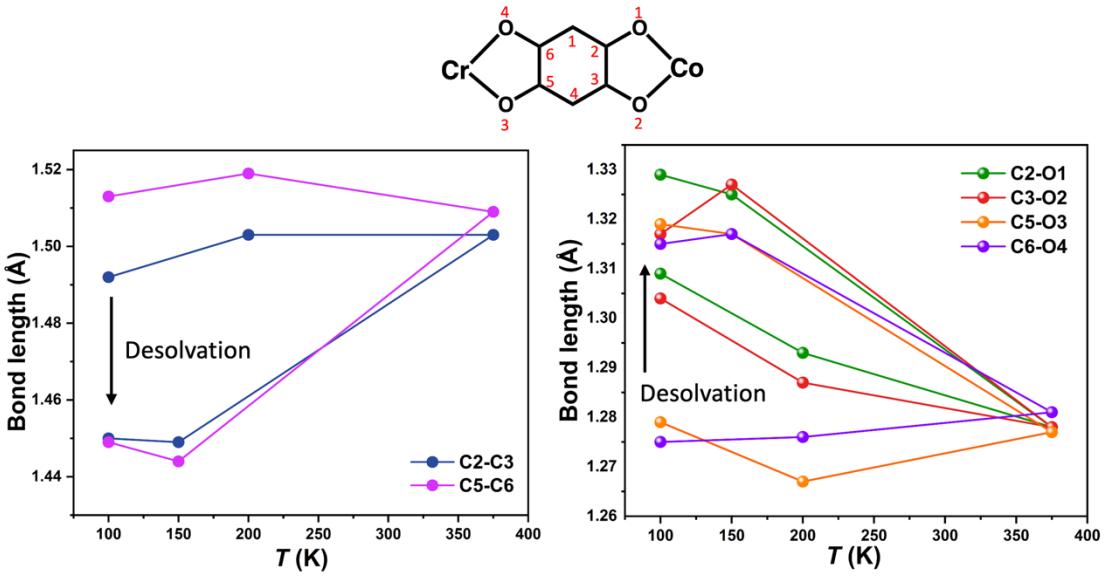

Figure S6. (a) Schematic illustration of specific carbon and oxygen from bridging ligand. (b) Temperature-dependent bond length of specific carbon-carbon before and after desolvation. (c) Temperature-dependent bond length of specific carbon-oxygen before and after desolvation.

2.8). These notable alterations in bond distances at the Co site suggest that complex **1** exhibits a more distinct VT behavior, transitioning to [Cr^{3+}-$dhsq^{3-}$-Co^{3+}(LS)] upon cooling. Furthermore, the projection angle between the [CrCo] vector and the polar *b*-axis shifted to 85.66(1)° at 375 K and 85.35(8)° at 100 K following desolvation (Figure 2.9a-c).

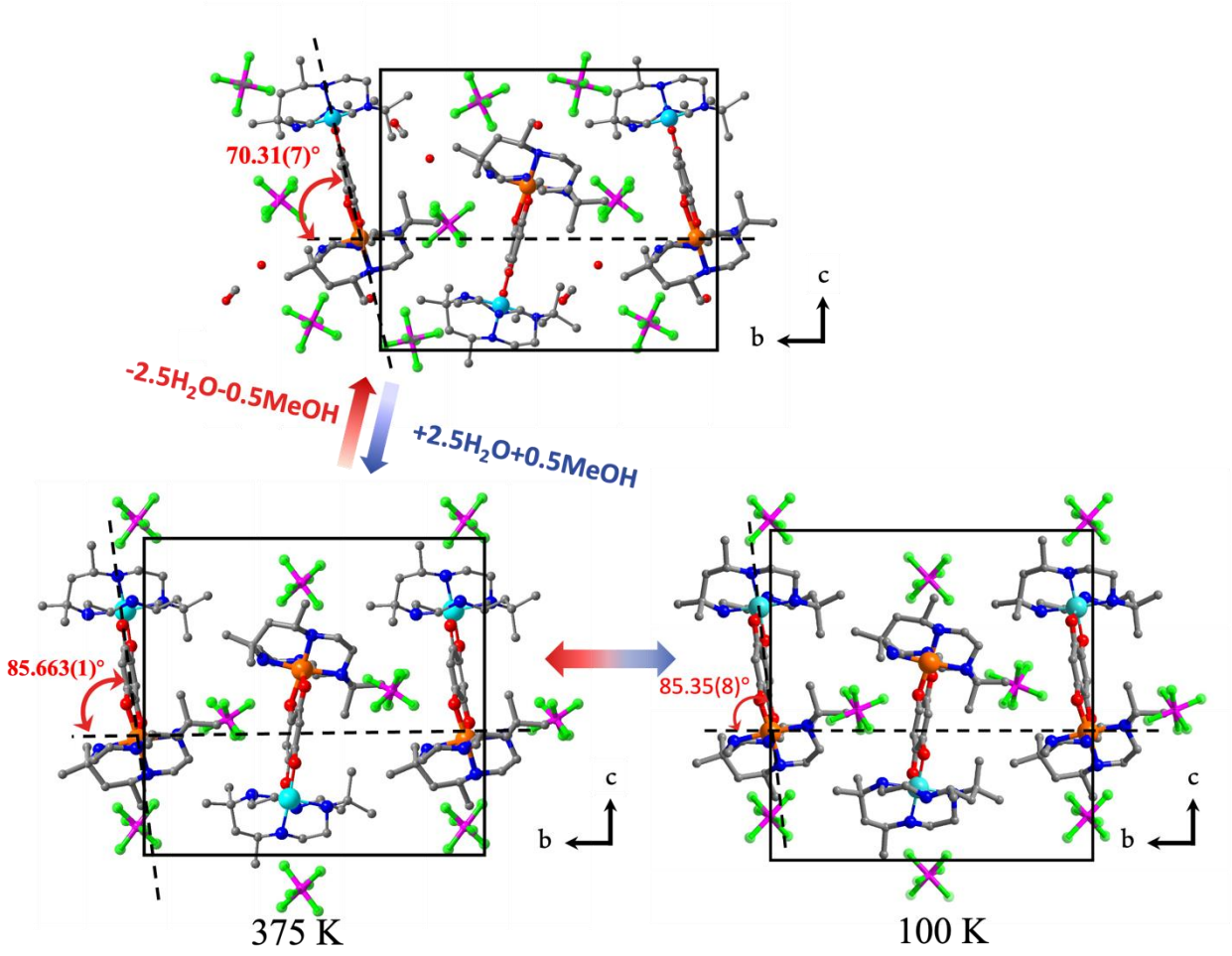

Figure 2.9 (a) Crystal structure of **1·sol** at 100 K viewed along *a*-axis. (b) and (c) crystal structure of desolvated form, **1** viewed along *a*-axis at 375 K and 100 K, respectively. Cr(pale blue), Co(orange), C(dark gray), O(red), P(deep pink), F(green); H atoms are omitted for clarity.

By investigating the VT transition magnitude and alterations in molecular packing pre- and post-desolvation, a solvent-induced polarization change at the scale of individual crystals were expected.

The Powder X-ray diffraction (PXRD) performed at varying temperatures served to validate the ability of the crystal structure to undergo reversible changes during the in situ desolvation-reabsorption process (Figure 2.10a). In order to prevent the evaporation of the extracted solvent

molecules, the powdered sample of **1·sol** underwent careful sealing with aluminum foil, followed by measurements conducted at temperatures of 230 K, 400 K, and then 230 K again. At 230 K, the PXRD patterns of **1·sol** aligned closely with the simulated ones derived from single-crystal data, with no discernible changes detected until the temperature rose to 326 K. Upon further heating to 376 K, notable and comprehensive variation in reflections occurred at 2θ = 10.0°, 11.4°, 12.3°, and 20.5°, in agreement with the calculated results for the desolvated complex **1** at 375 K, indicating the *in situ* formation of compound **1**. The powder patterns remained stable until 400 K, after which, upon cooling, the diffraction pattern recovered to that of the original compound, **1·sol**, rather than matching the simulated outcome for compound **1** at low temperatures. These results unequivocally confirm the ability of the crystal losing solvents to recapture the retained solvent. under ambient conditions, reverting to the solvated compound, **1·sol**. PXRD measurements were also conducted on compound **1** after thermal treatment, which, following exposure to MeOH and H_2O, exhibited a diffraction pattern consistent with that of **1·sol** (Figure 2.10b-c), further supporting the ability of single-crystal-to-single-crystal transformation (SCSCT) to occur reversibly.[58]

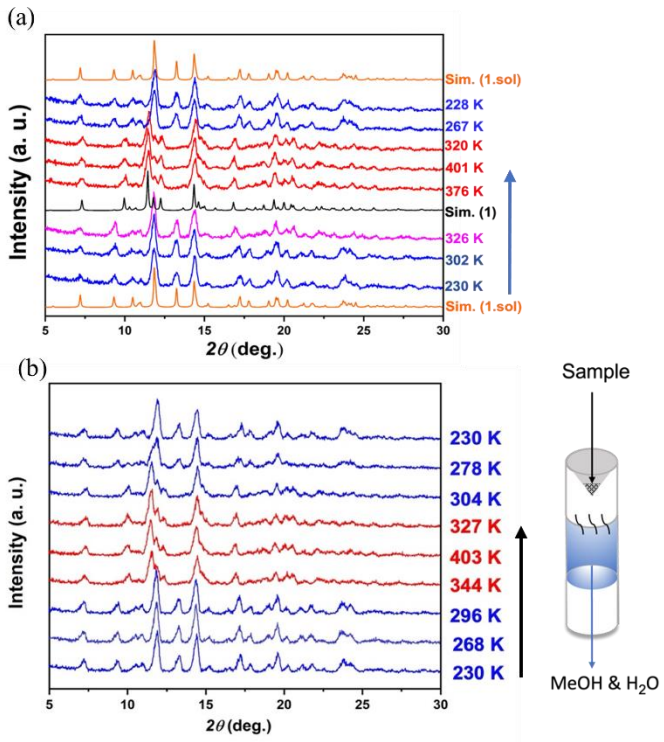

Figure 2.10 (a) Thermal cycling from 230 to 400 to 230 K was employed to generate variable-temperature powder XRD patterns. The simulation spectra, derived from single-crystal XRD data obtained at 200 K for **1·sol** and 375 K for **1**, are depicted as orange and black lines, respectively. (b) Thermally treated compound **1** was exposed to Methanol/H_2O and subsequently was performed on the PXRD with cycle of 230-400-230 K.

Magnetic susceptibility measurements of the polycrystalline sample of **1·sol** was performed across varying temperatures. To preserve the stability of solvents co-crystallized in molecules, the measurements commenced at 260 K with a cooling rate of 2 K min^{-1} under a magnetic field of 2000 Oe (see Figure 2.11). Across the temperature range from 260 to 220 K, the $\chi_m T$ value of compound **1·sol** remains nearly constant at 4.3 cm^3 K cm^{-1}, consistent with the anticipated value for independent metal centers on Cr^{3+} (S = 3/2) and high-spin Co^{2+} (S = 3/2) with unquenched orbital magnetic moment.

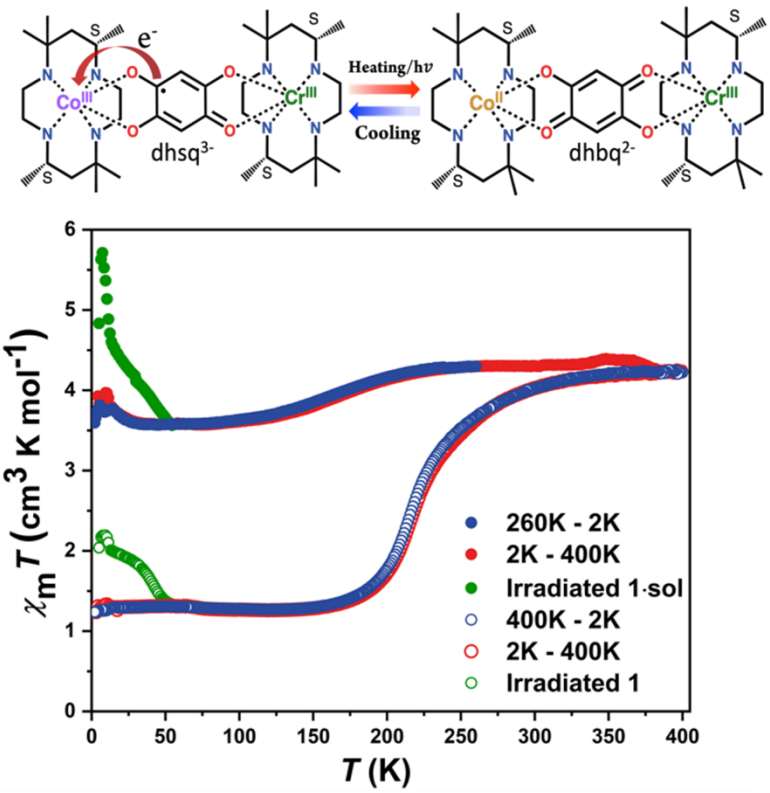

Figure 2.11 A schematic representation of valence tautomerism in **1·sol** is shown (top). The variable-temperature magnetic susceptibility data for compound **1·sol**, before and after desolvation, were collected using ground crystals with a temperature sweep rate of 2 K min^{-1} (bottom).

As the temperature continues to decrease, the $\chi_m T$ value gradually declines and stabilizes at a plateau of 3.7 cm^3 K cm^{-1} between 75 and 30 K. The VT transition temperature, determined by the peak in the temperature derivative of the $\chi_m T$ plot, is approximately 170 K. As the sample was reheated to 260 K, the $\chi_m T$ value exhibits a reversible change without notable hysteresis. To investigate the mechanism responsible for this behavior, variable-temperature spectroscopic analyses were performed in heating mode over this temperature range. The vibrational band of $dhsq^{3-}$ at 1470 cm^{-1} also shows a pronounced decrease within the same temperature range (see Figure 2.12a). Correspondingly, a gradual reduction in the intensity of

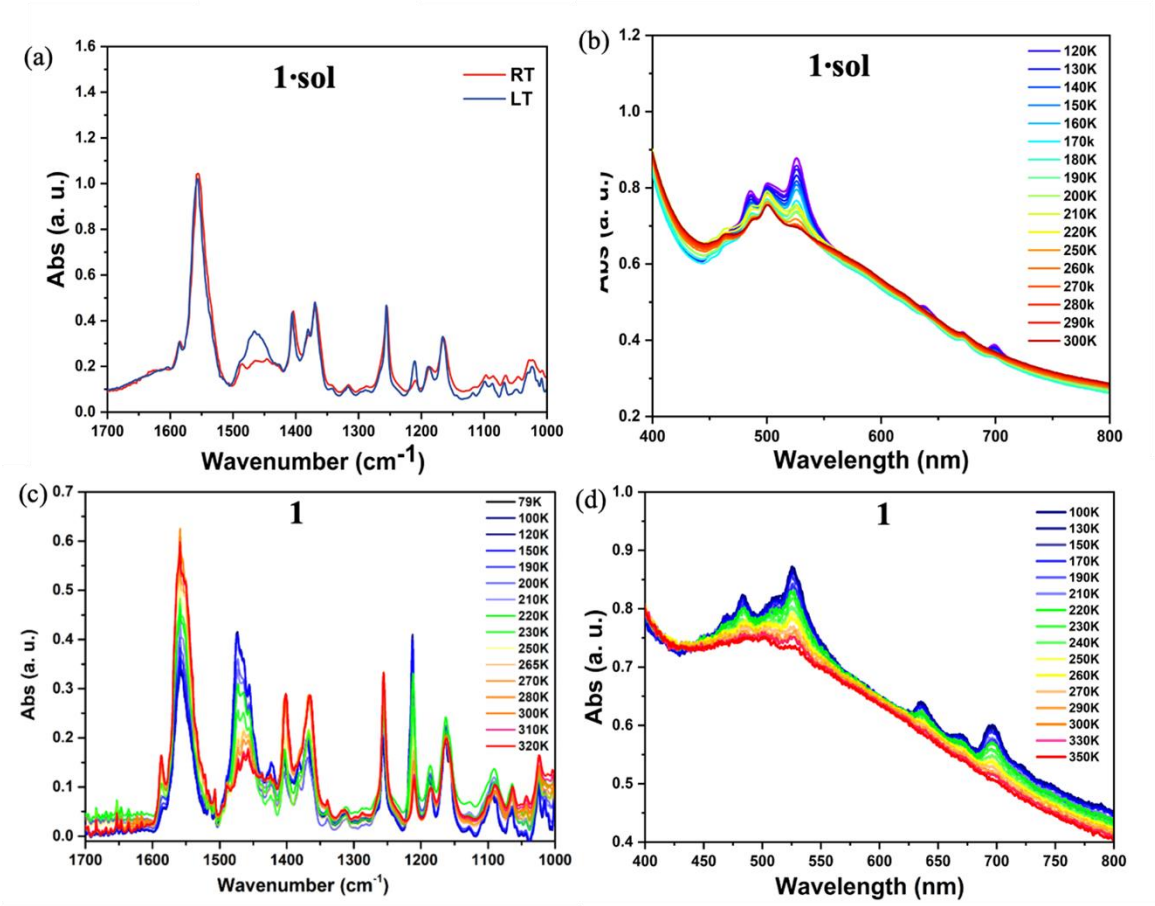

Figure 2.12 (a) The KBr pellet containing compound **1·sol** underwent measurements at both room temperature and low temperature (achieved by direct immersion in liquid nitrogen). The band around 1520 cm^{-1}, attributed to $dhbq^{2-}$, displayed decreased intensity under these conditions. (b) The temperature-dependent UV-vis spectroscopy with tape sample of **1·sol**. (c) Temperature-dependent IR spectroscopy of compound **1** was conducted from 79 K to 320 K after removing solvent on CaF_2 sample. (d) Temperature-dependent UV-vis spectroscopy of compound **1** was performed from 100 K to 350 K, following the same sample treatment as the IR measurement.

the absorption band centered at 500 nm is ascribed to ligand-to-metal charge transfer from $dhsq^{3-}$ to Co^{3+} ions, was observed (refer to Figure 2.12b). These observations indicate that the variation in $\chi_m T$ values within this temperature range can be attributed to partial electron transfer from the [Cr^{3+}-$dhsq^{3-}$-Co^{3+}LS] to [Cr^{3+}-$dhbq^{2-}$-Co^{2+}HS] state. As the temperature rises to 400 K, the $\chi_m T$

value increases to approximately 4.2 cm^3 K cm^{-1}, coinciding with desolvation. The desolvated sample, **1**, displays more significant changes. Below 340 K, the $\chi_m T$ value sharply decreases, reaching a minimum of 1.26 cm^3 K cm^{-1}, indicating an almost complete transition to the [Cr^{3+}-$dhsq^{3-}$-Co^{3+}LS] state (expected $\chi_m T$ value: 1.0 cm^3 K cm^{-1}). That is caused by strong antiferromagnetism between Cr^{3+} and $dhsq^{3-}$.[59] The transition temperature is calculated to be 215 K without evident hysteretic behavior. Similar transformations are also confirmed in the UV-vis and IR absorption spectra. The sample was ground to powder, attached to a CaF_2 plate (for IR) and transparent tape (for UV-vis), was heated to 400 K. After removing solvents co-crystallized in molecule, the samples were promptly encased in a vacuum tube to eliminate the risk of water molecules being reabsorbed from the surrounding air. Spectra of **1** were recorded from 79 to 300 K. At lower temperatures, strong absorption peaks around 1210 and 1470 cm^{-1}, attributed to the C-O stretching vibration from $dhsq^{3-}$, were observed. With increasing temperature, gradual decay of these peaks occurred, while characteristic absorption peaks at 1560 and 1270 cm^{-1} respectively associated to $dhbq^{2-}$ became more intense (Figure 2.12c). These findings provide direct evidence for changes in the electronic structure of the bridging ligand. UV-vis spectra of desolvated sample also demonstrate similar changes to those observed in the pristine compound, **1·sol**, across varying temperature range (Figure 2.12d). To directly illustrate the distinct transition temperatures between **1·sol** and **1** through spectroscopy, we plotted the variation in the absorption intensity of characteristic bands in the IR and UV-vis spectra with temperature. Notably, the temperature-dependent IR absorption bands of compound **1** at 1470 and 1558 cm^{-1} exhibit an opposite variation tendency from around 200 K to 300 K, indicating a transition from $dhbq^{2-}$ to $dhsq^{3-}$ as the temperature increases (Figure 2.13a). Similarly, the variable-temperature UV-vis spectra of compound **1** at 525 nm show a similar variation to the IR measurement at 1473 cm^{-1} (Figure 2.13b). These findings align well with the trend of magnetization transition of compound **1**, suggesting successful solvent removal and electron transfer. Furthermore, in the case of **1·sol**, the temperature-dependent UV-vis intensity changes at 526 nm demonstrate continuous variations from 100 K to

around 250 K (Figure 2.13c). This observed variation correlates with the magnetization changes in **1·sol**, thereby further confirming that the magnetization transition originates from electron transfer between Co^{2+} and $dhbq^{2-}$.

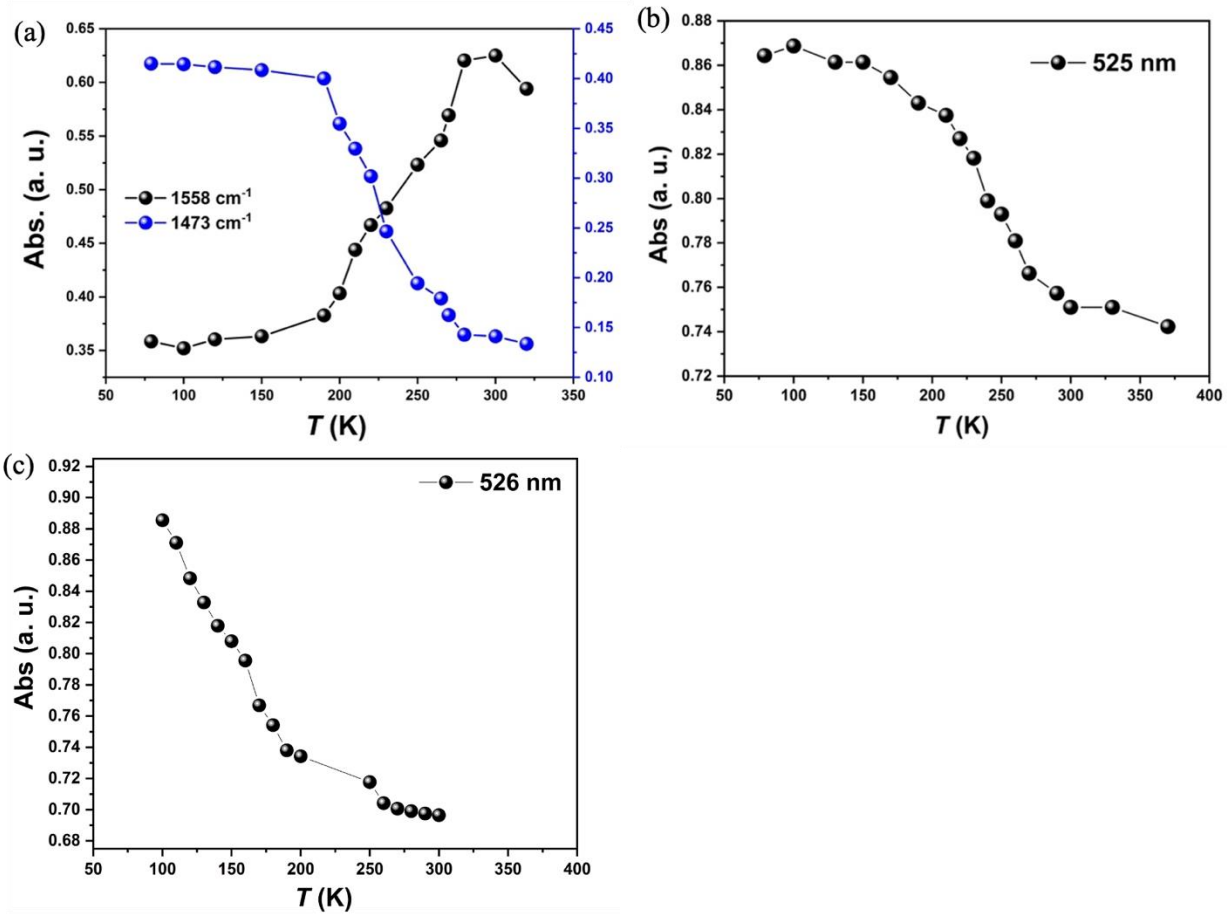

Figure 2.13 (a) The temperature-dependent IR absorption intensity of 1473 and 1558 cm^{-1} against temperature in compound **1·sol**. (b) The temperature-dependent UV-vis intensity of 525 nm against temperature in **1·sol**. (c) The variable-temperature UV-vis intensity of 526 nm against temperature in compound **1**.

Furthermore, the powder sample without solvents was positioned above a $MeOH/H_2O$ vapor overnight, avoiding any direct interaction, to facilitate solvent reabsorption. Subsequent measurements of the magnetic properties of the solvent-reabsorbed sample under identical conditions as the original sample confirmed the reversibility of magnetization. The results

demonstrated similar behavior, indicating an incomplete electron transfer transitions to a nearly complete electron transfer after the solvent is removed. (Figure 2.14). Elemental analysis provided further evidence of the transition from compound **1** to **1·sol** (Table 2), where the proportions of C, H, N match well between original and reabsorbed form. These observations suggest that solvent effect on the VT process of compound **1·sol** can be reversibly manipulated through solvent reabsorption. Moreover, both compounds **1·sol** and **1**

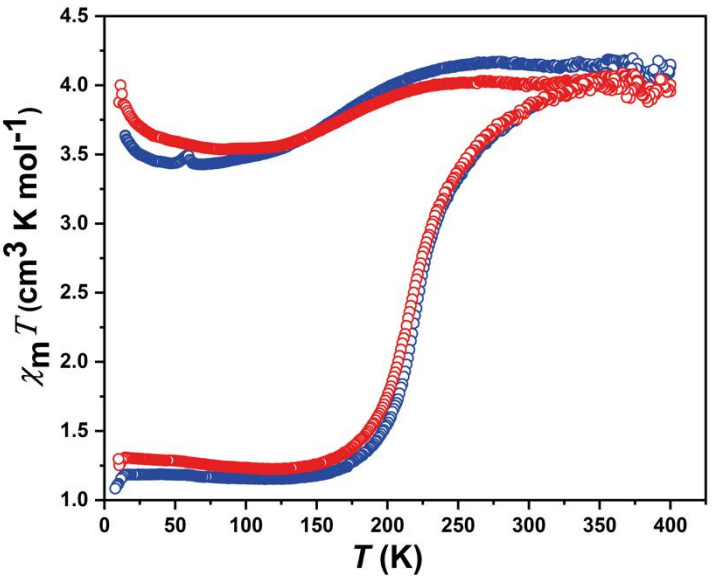

Figure 2.14 The magnetic susceptibility of the refreshed **1·sol** is depicted by the blue circle. Following a full cycle from 10 K to 400 K and back to 10 K, the sample was removed from the SQUID chamber and left above a Methanol/H_2O mixture overnight. The reabsorbed sample was then subjected to magnetization measurements again as indicated by the red circle.

Table 2. Elemental analysis

	H%	C%	N%
1·sol (orginal one)	6.25	35.49	8.75
1·sol (reabsorbed)	6.22	35.27	8.47

Calculated result of **1.sol**	6.16	35.16	8.52
NiCr (previous method, reduced pressure vacuum)	6.60	40.63	9.76
NiCr (stepwise route, reduced pressure vacuum)	6.07	36.76	8.92
Calculated result of NiCr	5.91	36.39	8.94
ZnCr(previous method, reduced pressure vaccum)	6.75	39.59	9.88
ZnCr (stepwise route, reduced pressure vacuum)	6.03	36.50	8.92
Calculated result of ZnCr	5.88	36.22	8.90

exhibited enhanced Photo-induced valence tautomerism in comparison to the earlier [CrCo] complex containing racemic ligands. Photomagnetic measurements were conducted on compounds **1·sol** and **1** with tape sample by irradiating them using 532 nm green light at 5 K. Both samples showed an evident rise in magnetization immediately after irradiation, followed by a gradual return to the ground state as the temperature increased (Figure 2.11). This feature suggests light-induced polarization switching in these complexes.

Notably, in comparison to the previously reported [CrCo] complex employing a racemic ligand, the transition temperature of complex **1** exhibits a notable decrease. To elucidate this difference, theoretical calculations using density functional theory (DFT) were conducted using the same theoretical framework. The energy discrepancy derived for the enantiopure [CrCo] complex (0.46 kcal/mol) is notably lower than that of the heterochiral counterpart (3.92 kcal/mol) in a vacuum state. Further examination revealed that this change primarily stems from the substantial stabilization (3.59 kcal/mol) of the high-spin (HS) state in the enantiopure complex, possibly attributed to a more distorted coordination geometry in this scenario. Noteworthy is the relative enhancement of stabilization observed for the electron-transferred high spin state in the enantiopure complex, which also accounts for the enhanced trapping effect observed in the measurements of photomagnetization.[60]

Compound **1·sol**, exhibiting VT behavior within the $P2_1$ polar space group, holds promise for realizing polarization switching on a macroscopic scale. To investigate the electric current associated with dipole moment variations during the VT transition, Pyroelectric measurements were performed on a single-crystal sample of compound **1·sol**. The crystal was precisely oriented and prepared, with silver paste applied to the (010) and (0−10) surfaces, which are perpendicular to the polar *b* axis. (Figure 2.3). The pyroelectric current was measured using a Keithley 6517B electrometer without application of any external electric field, while temperature control was maintained using the Quantum Design magnetic property measurement system over a range of 30–250 K, under a ramping rate of 5 K min^{-1}. Following a 30-minute short-circuiting period until the background current dropped below 0.02 pA, the pyroelectric nature of the current signal was confirmed, exhibiting opposite signs during heating and cooling runs. The variable temperature pyroelectric coefficient of compound **1·sol** exhibited a solitary wide peak, reaching maximal values of approximately 2.9 nC cm-2 K^{-1} during the cooling and heating processes at 162 K and 174 K, respectively. Integration of the pyroelectric current allowed estimation of the polarization change

as 0.27 μC cm^{-2}, with its temperature dependence aligning closely with the results of magnetic measurements on thermally induced polarization.

Electric measurements were conducted on **1.sol** while exposed to light irradiation at 5 K. A distinct instantaneous current, aligning with the direction observed during the heating process, was clearly discernible. This observation suggests electron transfer from the bridging ligand to the Co site, consistent with expectations from photomagnetic measurements. Upon switching off the light, the molecules in their metastable state gradually reverted to the ground state as the temperature increased, resulting in a release of current in the opposite direction. This experimental evidence confirms that the polarization change in **1.sol** can also be induced by light irradiation, as depicted in Figure 2.15.

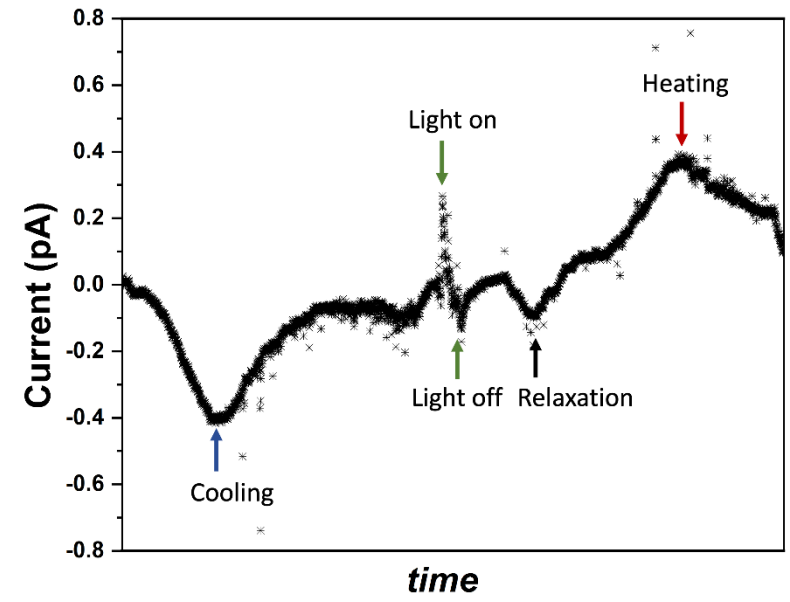

Figure 2.15 Light-induced pyroelectric current of compound **1·sol** before and after 532 nm light irradiation.

To theoretically estimate the polarization change associated to **1·sol**, we utilized the volume average of the molecular dipole moments along the *b*-axis obtained from DFT calculations, which

were 0.03 D for the triplet state and 9.16 D for the septet state. This approach allowed us to estimate the electron-transfer contribution is estimated to be 0.17 μC cm^{-2}, based on the assumption that 20% of the molecules, as inferred from magnetic data, are involved in the VT process. Additionally, considering the structural transition, we tentatively accounted for the relative displacement between cations and anions, modeled as point charges, leads to an extra polarization change of 0.02 μC cm^{-2}. The net change in polarization was calculated to be 0.19 μC cm^{-2}, which is in reasonable agreement with the experimental value of 0.27 μC cm^{-2} (Figure 2.16). Discrepancies may arise from the complete neglect of effects of solvent orientation and secondary pyroelectric phenomena, or from insufficient consideration of displacement contributions due to the oversimplified point charge model. Nevertheless, it is reasonable to conclude that the observed polarization change is primarily attributable to electron transfer.

As **1·sol** exhibits SCSCT, as confirmed by single-crystal or powder XRD, further investigation into solvent-induced polarization switching behavior remains intriguing. Theoretical estimations suggest that the contributions to polarization change from electron transfer and ion displacement could be approximately 0.17 and 0.00 μC cm^{-2}, respectively. Surprisingly, the calculated value of electron transfer-induced polarization change is similar to that of the solvated form, owing to opposite changes caused by different degrees of VT transition and changes in projection angle.

Preliminary pyroelectric measurements were conducted on the in-situ desolvated sample at 310 K, revealing a clear shift in transition temperature towards higher temperatures, in agreement with outcomes from magnetization (Figure 2.17). Nevertheless, the large crystal pieces required for pyroelectric measurements are more fragile than those used for single-crystal XRD, and the samples consistently experience partial cracking during desolvation treatment, which poses challenges obtaining accurate pyroelectric current data with an acceptable signal-to-noise ratio. Consequently, while the polarization change in the desolvated form remains unclear, the impact of

the solvent on polarization switching behavior is evident from the observed temperature shift.

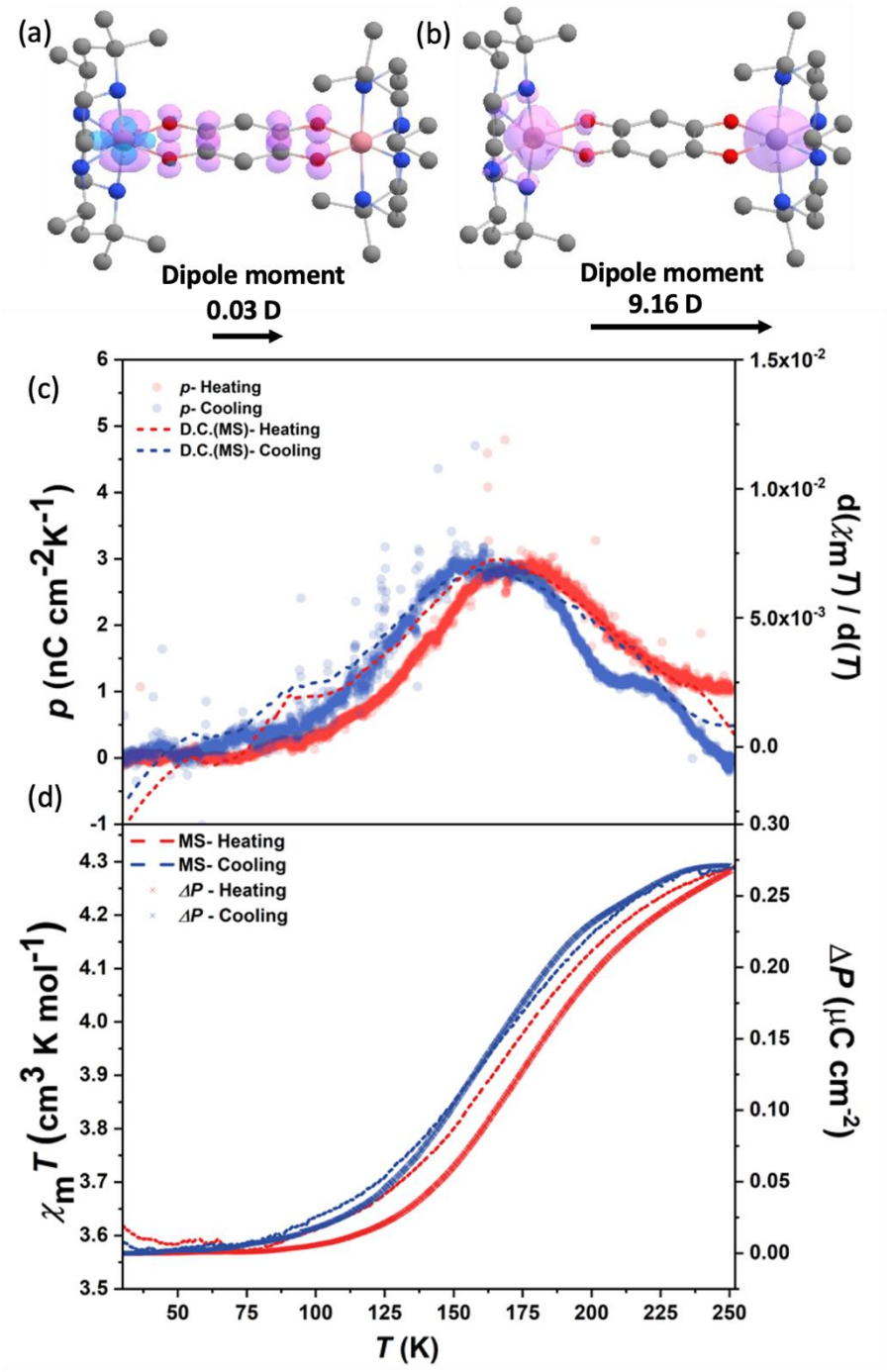

Figure 2.17 The contour value of 0.01 (spin Å^{-3}) illustrates the distribution of spin density. Structural optimization was conducted using the X-ray diffraction data of **1** at two temperatures: (a) 100 K and (b) 375 K. Additionally, (c) the temperature-dependent pyroelectric coefficient of

compound **1·sol** was measured across the range of 30 to 250 K at a sweep rate of 5 K min^{-1}. Finally, (d) the polarization change was compared to the magnetization of compound **1·sol**.

2.4 Conclusion

In summary, We have successfully developed a heterometallic dinuclear complex featuring an enantiopure ligand, exhibiting orderly molecular arrangements within a polar $P2_1$ space group. The sequential synthetic method presented in this study enhances the purity of the desired crystals, offering potential applicability to the synthesis of various heterometallic dinuclear complexes, including those lacking chirality. Notably, among the complexes prepared using this approach, the less densely packed crystal structure of the [CrCo] complexes with enantiopure ligands provides additional space for accommodating solvent molecules in comparison to Earlier reported [CrCo] complexes featuring ligands with mixed chirality. Consequently, the new [CrCo] complex exhibits a solvent-dependent Valence tautomeric transition behavior, as evidenced by structural, magnetometric, and spectroscopic analyses. Additionally, Pyroelectric measurements conclusively demonstrate the polarization change feature in the original sample. The ability for polarization switching controlled by multiple stimuli presents promising prospects for potential applications in versatile molecular systems. Our findings underscore the significance of guest molecules including solvents and counter anion, *etc* in molecular materials with polarization change, thus paving the way for advancements in molecular sensors through detailed polarization analysis..

References

1. O. Sato, Dynamic molecular crystals with switchable physical properties, *Nature Chemistry*, 2016, **8**, 644-656.

2. S.-Q. Wu, M. Liu, K. Gao, S. Kanegawa, Y. Horie, G. Aoyama, H. Okajima, A. Sakamoto, M. L. Baker, M. S. Huzan, P. Bencok, T. Abe, Y. Shiota, K. Yoshizawa, W. Xu, H.-Z. Kou and O. Sato, Macroscopic Polarization Change via Electron Transfer in a Valence Tautomeric Cobalt Complex, *Nature Communications*, 2020, **11**, 1992.

3. S. Kanegawa, Y. Shiota, S. Kang, K. Takahashi, H. Okajima, A. Sakamoto, T. Iwata, H. Kandori, K. Yoshizawa and O. Sato, Directional electron transfer in crystals of [CrCo] dinuclear complexes achieved by chirality-assisted preparative method, *Journal of the American Chemical Society*, 2016, **138**, 14170-14173.

4. S.-Q. Su, S.-Q. Wu, Y.-B. Huang, W.-H. Xu, K.-G. Gao, A. Okazawa, H. Okajima, A. Sakamoto, S. Kanegawa and O. Sato, Photoinduced Persistent Polarization Change in a Spin Transition Crystal, *Angewandte Chemie International Edition*, 2022, **61**, e202208771.

5. P. Sadhukhan, S.-Q. Wu, J. I. Long, T. Nakanishi, S. Kanegawa, K. Gao, K. Yamamoto, H. Okajima, A. Sakamoto, M. L. Baker, T. Kroll, D. Sokaras, A. Okazawa, N. Kojima, Y. Shiota, K. Yoshizawa and O. Sato, Manipulating electron redistribution to achieve electronic pyroelectricity in molecular [FeCo] crystals, *Nature Communications*, 2021, **12**, 4836.

6. C. R. Bowen, J. Taylor, E. LeBoulbar, D. Zabek, A. Chauhan and R. Vaish, Pyroelectric materials and devices for energy harvesting applications, *Energy & Environmental Science*, 2014, **7**, 3836-3856.

7. J. F. Scott, Applications of Modern Ferroelectrics, *Science*, 2007, **315**, 954-959.

8. K. Kobayashi, S. Horiuchi, R. Kumai, F. Kagawa, Y. Murakami and Y. Tokura, Electronic Ferroelectricity in a Molecular Crystal with Large Polarization Directing Antiparallel to Ionic Displacement, *Physical Review Letters*, 2012, **108**, 237601.

9. S. Horiuchi, K. Kobayashi, R. Kumai, N. Minami, F. Kagawa and Y. Tokura, Quantum ferroelectricity in charge-transfer complex crystals, *Nature Communications*, 2015, **6**, 7469.

10. A. S. Tayi, A. K. Shveyd, A. C. H. Sue, J. M. Szarko, B. S. Rolczynski, D. Cao, T. J. Kennedy, A. A. Sarjeant, C. L. Stern, W. F. Paxton, W. Wu, S. K. Dey, A. C. Fahrenbach, J. R. Guest, H. Mohseni, L. X. Chen, K. L. Wang, J. F. Stoddart and S. I. Stupp, Room-temperature ferroelectricity in supramolecular networks of charge-transfer complexes, *Nature*, 2012, **488**, 485-489.

11. N. Castagnetti, M. Masino, C. Rizzoli, A. Girlando and C. Rovira, Mixed stack charge transfer crystals: Crossing the neutral-ionic borderline by chemical substitution, *Physical Review Materials*, 2018, **2**, 024602.

12. S. Tomić and M. Dressel, Ferroelectricity in molecular solids: a review of electrodynamic properties, *Reports on Progress in Physics*, 2015, **78**, 096501.

13. A. Caneschi and A. Dei, Valence Tautomerism in a o-Benzoquinone Adduct of a Tetraazamacrocycle Complex of Manganese, *Angewandte Chemie International Edition*, 1998, **37**, 3005-3007.

14. C. Carbonera, A. Dei, J.-F. Létard, C. Sangregorio and L. Sorace, Thermally and Light-Induced Valence Tautomeric Transition in a Dinuclear Cobalt–Tetraoxolene Complex, *Angewandte Chemie*, 2004, **116**, 3198-3200.

15. J. Chen, Y. Sekine, Y. Komatsumaru, S. Hayami and H. Miyasaka, Thermally Induced Valence Tautomeric Transition in a Two-Dimensional Fe-Tetraoxolene Honeycomb Network, *Angewandte Chemie International Edition*, 2018, **57**, 12043-12047.

16. M. G. Cowan, J. Olguín, S. Narayanaswamy, J. L. Tallon and S. Brooker, Reversible Switching of a Cobalt Complex by Thermal, Pressure, and Electrochemical Stimuli: Abrupt, Complete, Hysteretic Spin Crossover, *Journal of the American Chemical Society*, 2012, **134**, 2892-2894.

17. Y. Gong, W.-K. Han, H.-S. Lu, Q.-T. Hu, H. Tu, P.-N. Li, X. Yan and Z.-G. Gu, Single

crystal to single crystal transformation of spin-crossover coordination polymers from 3D frameworks to 2D layers, *Journal of Materials Chemistry C*, 2021, **9**, 5082-5087.

18. J. Tao, H. Maruyama and O. Sato, Valence Tautomeric Transitions with Thermal Hysteresis around Room Temperature and Photoinduced Effects Observed in a Cobalt−Tetraoxolene Complex, *Journal of the American Chemical Society*, 2006, **128**, 1790-1791.

19. T. Tezgerevska, K. G. Alley and C. Boskovic, Valence tautomerism in metal complexes: Stimulated and reversible intramolecular electron transfer between metal centers and organic ligands, *Coordination Chemistry Reviews*, 2014, **268**, 23-40.

20. D.-Q. Wu, D. Shao, X.-Q. Wei, F.-X. Shen, L. Shi, D. Kempe, Y.-Z. Zhang, K. R. Dunbar and X.-Y. Wang, Reversible On–Off Switching of a Single-Molecule Magnet via a Crystal-to-Crystal Chemical Transformation, *Journal of the American Chemical Society*, 2017, **139**, 11714-11717.

21. A. Moledo Vicente Guedes, L. Sodré de Abreu, I. A. V. Maldonado, W. S. Fernandes, T. M. Cardozo, R. A. Allão Cassaro, M. Scarpellini and G. Poneti, Valence tautomerism in a cobalt–dioxolene complex containing an imidazolic ancillary ligand, *RSC Advances*, 2023, **13**, 20050-20057.

22. C. Boskovic, in *Spin‐Crossover Materials*, 2013, DOI: https://doi.org/10.1002/9781118519301.ch7, pp. 203-224.

23. D. N. Hendrickson and C. G. Pierpont, in *Spin Crossover in Transition Metal Compounds II*, eds. P. Gütlich and H. A. Goodwin, Springer Berlin Heidelberg, Berlin, Heidelberg, 2004, DOI: 10.1007/b95413, pp. 63-95.

24. O. Sato, J. Tao and Y.-Z. Zhang, Control of Magnetic Properties through External Stimuli, *Angewandte Chemie International Edition*, 2007, **46**, 2152-2187.

25. O. Sato, A. Cui, R. Matsuda, J. Tao and S. Hayami, Photo-induced Valence Tautomerism in Co Complexes, *Accounts of Chemical Research*, 2007, **40**, 361-369.

26. K. KC, T. Woods and L. Olshansky, Ligand Modifications Produce Two-Step Magnetic

Switching in a Cobalt(dioxolene) Complex, *Angewandte Chemie International Edition*, 2023, **62**, e202311790.

27. M. A. Hay, J. T. Janetzki, V. J. Kumar, R. W. Gable, R. Clérac, A. A. Starikova, P. J. Low and C. Boskovic, Modulation of Charge Distribution in Cobalt-α-Diimine Complexes toward Valence Tautomerism, *Inorganic Chemistry*, 2022, **61**, 17609-17622.

28. G. K. Gransbury, B. N. Livesay, J. T. Janetzki, M. A. Hay, R. W. Gable, M. P. Shores, A. Starikova and C. Boskovic, Understanding the Origin of One- or Two-Step Valence Tautomeric Transitions in Bis(dioxolene)-Bridged Dinuclear Cobalt Complexes, *Journal of the American Chemical Society*, 2020, **142**, 10692-10704.

29. G. K. Gransbury and C. Boskovic, in *Encyclopedia of Inorganic and Bioinorganic Chemistry*, DOI: https://doi.org/10.1002/9781119951438.eibc2785, pp. 1-24.

30. A. Droghetti and S. Sanvito, Electric Field Control of Valence Tautomeric Interconversion in Cobalt Dioxolene, *Physical Review Letters*, 2011, **107**, 047201.

31. T. T. Patricia, M. V. Sandra, L. Manuela, L. Andrea, F. Paolo, D. Andrea and R. Roberto, Transient infrared spectroscopy: a new approach to investigate valence tautomerism, *Physical Chemistry Chemical Physics*, 2012, **14**, 1038-1047.

32. F. V. R. Neuwahl, R. Righini and A. Dei, Femtosecond spectroscopic characterisation of the two-step valence tautomeric interconversion occurring in a cobalt–dioxolene complex, *Chemical Physics Letters*, 2002, **352**, 408-414.

33. D. M. Adams, B. Li, J. D. Simon and D. N. Hendrickson, Photoinduced Valence Tautomerism in Cobalt Complexes Containing Semiquinone Anion as Ligand: Dynamics of the High-Spin [CoII(3,5-dtbsq)2] to Low-Spin [CoIII(3,5-dtbsq)(3,5-dtbcat)] Interconversion, *Angewandte Chemie International Edition in English*, 1995, **34**, 1481-1483.

34. M. Wang, Z.-Y. Li, R. Ishikawa and M. Yamashita, Spin crossover and valence tautomerism conductors, *Coordination Chemistry Reviews*, 2021, **435**, 213819.

35. C. Fleming, D. Chung, S. Ponce, D. J. R. Brook, J. DaRos, R. Das, A. Ozarowski and S. A.

Stoian, Valence tautomerism in a cobalt-verdazyl coordination compound, *Chemical Communications*, 2020, **56**, 4400-4403.

36. J.-W. Dai, Y.-Q. Li, Z.-Y. Li, H.-T. Zhang, C. Herrmann, S. Kumagai, M. Damjanović, M. Enders, H. Nojiri, M. Morimoto, N. Hoshino, T. Akutagawa and M. Yamashita, Dual-radical-based molecular anisotropy and synergy effect of semi-conductivity and valence tautomerization in a photoswitchable coordination polymer, *National Science Review*, 2023, **10**.

37. A. Paul and S. Konar, Electronic pyroelectricity: the interplay of valence tautomerism and spin transition, *Journal of Materials Chemistry C*, 2022, **10**, 4980-4984.

38. G. K. Gransbury, M.-E. Boulon, S. Petrie, R. W. Gable, R. J. Mulder, L. Sorace, R. Stranger and C. Boskovic, DFT Prediction and Experimental Investigation of Valence Tautomerism in Cobalt-Dioxolene Complexes, *Inorganic Chemistry*, 2019, **58**, 4230-4243.

39. A. Singh, S. Panda, S. Dey and G. K. Lahiri, Metal-to-Ligand Charge Transfer Induced Valence Tautomeric Forms of Non-Innocent 2,2′ -Azobis(benzothiazole) in Ruthenium Frameworks, *Angewandte Chemie*, 2021, **133**, 11306-11310.

40. F. Cheng, S. Wu, W. Zheng, S. Su, T. Nakanishi, W. Xu, P. Sadhukhan, H. Sejima, S. Ikenaga, K. Yamamoto, K. Gao, S. Kanegawa and O. Sato, Macroscopic Polarization Change of Mononuclear Valence Tautomeric Cobalt Complexes Through the Use of Enantiopure Ligand, *Chemistry – A European Journal*, **n/a**, e202202161.

41. C. Metzger, R. Dolai, S. Reh, H. Kelm, M. Schmitz, B. Oelkers, M. Sawall, K. Neymeyr and H.-J. Krüger, A New Type of Valence Tautomerism in Cobalt Dioxolene Complexes – Temperature-Induced Transition from a Cobalt(III) Catecholate to a Low-Spin Cobalt(II) Semiquinonate State, *Chemistry – A European Journal*, 2023, **29**, e202300091.

42. K. S. Kumar and M. Ruben, Sublimable Spin-Crossover Complexes: From Spin-State Switching to Molecular Devices, *Angewandte Chemie International Edition*, 2021, **60**, 7502-7521.

43. K. Senthil Kumar and M. Ruben, Emerging trends in spin crossover (SCO) based functional materials and devices, *Coordination Chemistry Reviews*, 2017, **346**, 176-205.

44. B. Li, Y.-M. Zhao, A. Kirchon, J.-D. Pang, X.-Y. Yang, G.-L. Zhuang and H.-C. Zhou, Unconventional Method for Fabricating Valence Tautomeric Materials: Integrating Redox Center within a Metal–Organic Framework, *Journal of the American Chemical Society*, 2019, **141**, 6822-6826.

45. N. A. Vázquez-Mera, C. Roscini, J. Hernando and D. Ruiz-Molina, Liquid-Filled Valence Tautomeric Microcapsules: A Solid Material with Solution-Like Behavior, *Advanced Functional Materials*, 2015, **25**, 4129-4134.

46. P. Sadhukhan, S.-Q. Wu, S. Kanegawa, S.-Q. Su, X. Zhang, T. Nakanishi, J. I. Long, K. Gao, R. Shimada, H. Okajima, A. Sakamoto, J. G. Chiappella, M. S. Huzan, T. Kroll, D. Sokaras, M. L. Baker and O. Sato, Energy conversion and storage via photoinduced polarization change in non-ferroelectric molecular [CoGa] crystals, *Nature Communications*, 2023, **14**, 3394.

47. X. Zhang, W.-H. Xu, W. Zheng, S.-Q. Su, Y.-B. Huang, Q. Shui, T. Ji, M. Uematsu, Q. Chen, M. Tokunaga, K. Gao, A. Okazawa, S. Kanegawa, S.-Q. Wu and O. Sato, Magnetoelectricity Enhanced by Electron Redistribution in a Spin Crossover [FeCo] Complex, *Journal of the American Chemical Society*, 2023, **145**, 15647-15651.

48. H. Kuramochi, G. Aoyama, H. Okajima, A. Sakamoto, S. Kanegawa, O. Sato, S. Takeuchi and T. Tahara, Femtosecond Polarization Switching in the Crystal of a [CrCo] Dinuclear Complex, *Angewandte Chemie*, 2020, **132**, 15999-16003.

49. D. Kiriya, H.-C. Chang and S. Kitagawa, Molecule-Based Valence Tautomeric Bistability Synchronized with a Macroscopic Crystal-Melt Phase Transition, *Journal of the American Chemical Society*, 2008, **130**, 5515-5522.

50. K. G. Alley, G. Poneti, J. B. Aitken, R. K. Hocking, B. Moubaraki, K. S. Murray, B. F. Abrahams, H. H. Harris, L. Sorace and C. Boskovic, A Two-Step Valence Tautomeric Transition in a Dinuclear Cobalt Complex, *Inorganic Chemistry*, 2012, **51**, 3944-3946.

51. S.-Q. Su, S.-Q. Wu, S. Kanegawa, K. Yamamoto and O. Sato, Control of electronic polarization via charge ordering and electron transfer: electronic ferroelectrics and electronic

pyroelectrics, *Chemical Science*, 2023, **14**, 10631-10643.

52. W.-H. Xu, Y.-B. Huang, W.-W. Zheng, S.-Q. Su, S. Kanegawa, S.-Q. Wu and O. Sato, Photo-induced valence tautomerism and polarization switching in mononuclear cobalt complexes with an enantiopure chiral ligand, *Dalton Transactions*, 2024, DOI: 10.1039/D3DT03915C.

53. A. G. Starikov, A. A. Starikova, M. G. Chegerev, S. M. Aldoshin, A. V. Metelitsa and V. I. Minkin, Spin-State-Switching Rearrangements of Bis(dioxolene)-Bridged CrCo Complexes: A DFT Study, *European Journal of Inorganic Chemistry*, 2021, **2021**, 4113-4121.

54. Tait, A. M.; Busch, D. H.; Curtis, N. F., 5,5,7,12,12,14−Hexamethyl−1,4,8,11−Tetraazacyclo−Tetradecane (5,5,7,12,12,14−Me6 [14] Ane−1,4,8,11−N4) Complexes. In *Inorganic Syntheses*, 1978, pp 10−17.

55. House, D. A.; Hay, R. W.; Akbar Ali, M. *Inorganica Chimica Acta* **1983**, *72*, 239–245.

56. Sheldrick, G., Crystal structure refinement with SHELXL. *Acta Crystallogr. C Struct. Chem*. **71**, 3 (2015).

57. Dolomanov, O. V.; Bourhis, L. J.; Gildea, R. J.; Howard, J. A. K.; Puschmann, H., OLEX2: a complete structure solution, refinement and analysis program. *J. Appl. Crystallogr*. **42**, 339 (2009).

58. S. Xue, Y. Guo and Y. Garcia, Spin crossover crystalline materials engineered via single-crystal-to-single-crystal transformations, *CrystEngComm*, 2021, **23**, 7899-7915.

59. A. J. Schuman, A. Raghavan, S. D. Banziger, Y. Song, Z.-B. Hu, B. L. Mash, A. L. Williams and T. Ren, Macrocyclic Chromium(III) Catecholate Complexes, *Inorganic Chemistry*, 2021, **60**, 4447-4455.

60. J.-F. Létard, P. Guionneau, O. Nguyen, J. S. Costa, S. Marcén, G. Chastanet, M. Marchivie and L. Goux-Capes, A Guideline to the Design of Molecular-Based Materials with Long-Lived Photomagnetic Lifetimes, *Chemistry – A European Journal*, 2005, **11**, 4582-4589.

Chapter 3. Near Infrared Light-induced Hidden Phase Transition and Ion Displacive Polarization Change on Heterodinuclear [CrCo] Complex with Enantiopure Ligand

3.1 Introduction

Energy conversion has garnered unprecedented attention, especially in the context of the ongoing energy crisis. Among the various energy sources, light stands out as one of the most promising due to its natural, environmentally friendly, and inexhaustible characteristics. However, the efficient conversion of light into electric power remains a formidable challenge. Current research on photovoltaic materials has focused primarily on ferroelectric materials because of their high spontaneous polarization, which enables the generation of a built-in electric field. This field facilitates the separation of photogenerated charge carriers, driving them in opposite directions and thus generating a photocurrent.[1-11] As a result, the search for improved ferroelectric materials with smaller band gaps, which could enhance photoelectric energy conversion efficiency, has become a crucial objective.

On the other hand, an alternative route to achieving light-induced polarization is being actively explored in non-ferroelectric materials. These systems are based on dynamic molecules, such as those exhibiting valence tautomerism, spin crossover, and mixed-valence complexes. Unlike traditional single-species ferroelectrics, non-ferroelectrics offer greater flexibility and diversity in molecular design, allowing for more extensive tuning of their properties.[12-23] The underlying mechanism relies on the fact that the energy levels of metastable states in these molecules are relatively similar and can be easily switched by external stimuli, including temperature, magnetic fields, and light. Crucially, the energy barriers between these states can be chemically modified, opening new avenues for enhancing their functionality.

Among these dynamic molecules, valence tautomeric complexes are particularly promising for achieving significant molecular polarization through long-range electron redistribution between metal centers and ligands. This redistribution leads to substantial variations in dipole moment. When these molecules are organized in polar space groups, with proper alignment of electron transfer along the polar axis, a macroscopic polarization change can be realized. Our research aims to design and engineer polar crystals that exhibit highly efficient light-induced valence tautomerism (LIVT), ultimately enabling macroscopic, light-induced giant polarization changes.

To this end, we are exploring several strategies to improve the efficiency of LIVT. One approach involves lowering the transition temperature of valence tautomerism by stabilizing the high-spin state, thereby extending the lifetime of the light-induced excited state. Additionally, introducing a distorted and rigid octahedral molecular configuration has proven effective in maintaining the excited state for longer durations, which prevents rapid decay back to the ground state.[24]

In line with this strategy, we have synthesized a novel complex, [Cr(SS-cth)(μ-dhbq)Co(SS-cth)]$(AsF_6)_3$, utilizing the enantiopure ligand SS-cth. By replacing the large counter anion, we preserved the distorted molecular configuration observed in related [CrCo]$(PF_6)_3$ complexes, while successfully lowering the transition temperature by approximately 40 K.[21] Unlike previously reported Co valence tautomeric (VT) complexes, this complex exhibits remarkable light-induced valence tautomerism with an extended lifetime in the metastable state, achieved through careful molecular design. The molecules are packed in the $P2_1$ polar space group with an optimized arrangement, significantly reducing the projection angle along the polar axis. This results in a substantial light-induced polarization change of 2.25 μC cm^{-2}, which is currently the largest reported value for light-induced polarization change in non-ferroelectric systems. Importantly, the observed giant polarization change is not solely due to electron transfer. X-ray diffraction analysis of the crystal structure after light irradiation directly revealed ion displacement, further

contributing to the overall polarization shift. Additionally, pyroelectric measurements uncovered a hidden, light-induced metastable state, distinct from the thermally induced one. A comprehensive set of analyses, including single-crystal X-ray diffraction, magnetization studies, pyroelectric measurements, and UV-Vis-IR spectroscopy, was performed on this complex, providing a detailed understanding of its behavior under light irradiation.

3.2 Experimental section

3.2.1 Starting materials and synthesis

All reagents were commercially purchased by Tokyo Chemical Industry Co., Ltd., FUJIFILM Wako, Pure Chemical Corporation, and Sigma-Aldrich Company, and directly used without further purification. 5,5,7,12,12,14-hexamethyl-1,4,8,11-tetraazacyclotetradecane (*Rac*-cth) and its enantiopure chiral ligand (*SS*-cth) were synthesized as shown in detail in *Chapter 2* under *2.2.1*. All reactions were conducted under N_2 gas.

[Co(AcO)(SS-cth)]AsF_6. $Co(AcO)_2 \cdot 4H_2O$ (750 mg, 3.0 mmol) and SS-cth (850 mg, 3.0 mmol) were added into ethanol (10 ml). The solution was stirred and heated to 60 °C. After that, $LiAsF_6$ (650 mg, 3.3 mmol) was added to this solution and pink solid of [Co(AcO)(SS-cth)]AsF_6 was gradually precipitated. The solution was cooled down by ice-bath, then the participation was filtered and washed with cold ethanol followed by Et_2O. [Co(AcO)(SS-cth)]AsF_6 was obtained of about 1.03 g, yield: 58%.

[$CrCl_2$(SS-cth)]Cl. [$CrCl_2$(SS-cth)]Cl was synthesized in the same method as reported literature for [CrCl2(Rac-cth)]Cl using optically pure SS-cth as a starting material to afford a greenish-blue solid product (yield = 68.0%).

[Cr(SS-cth)(dhbq)]AsF_6. A mixture of 2,5-dihydroxy-1,4- benzoquinone (H_2dhbq;140 mg, 1 mmol) and triethylamine (202 mg, 2.0 mmol) in methanol (50 ml) was stirred under an inert atmosphere. Then, solid [$CrCl_2$(*SS*-cth)]Cl (443 mg, 1 mmol) was added to the solution, and heated up to 60 ℃ for one hour. An aqueous of $LiAsF_6$ (391 mg, 2 mmol) was added into the dark-red solution. Slow evaporation led to the dark red participate [Cr(*SS*-cth)(μ-dhbq)]AsF_6. The precipitation was filtered and washed by H_2O (yield = 60%).

Synthesis of [Co(*SS*-cth)(μ-dhbq)Cr(*SS*-cth)]$(AsF_6)_3$

Stepwise synthetic method: The mixture of [Co(AcO)(*SS*-cth)]AsF_6 (591.5 mg, 1 mmol) and [Cr(*SS*-cth)(μ-dhbq)]AsF_6 (663.5 mg, 1 mmol) was added to Methanol (50 ml) under N_2 gas. The reaction solution was stirred at room temperature for 1 hour and then an aqueous of $LiAsF_6$ (292 mg, 1.5 mmol) was added to the methanol solution. Keep stirring the mixture overnight to precipitate purple-red [Co(*SS*-cth)(μ-dhbq)Cr(*SS*-cth)]$(AsF_6)_3$. The precipitation was filtered and washed with water, and then completely dry under reduced pressure. The crude product was firstly crystallized in the mixed solution of Methanol/H_2O and then recrystallized with mixed solution of Ethanol/H_2O for several times to afford dark red block crystal (yield = 50 mg, 30%).

Scheme 3.1 Stepwise synthesis of [CrCo]$(AsF_6)_3$

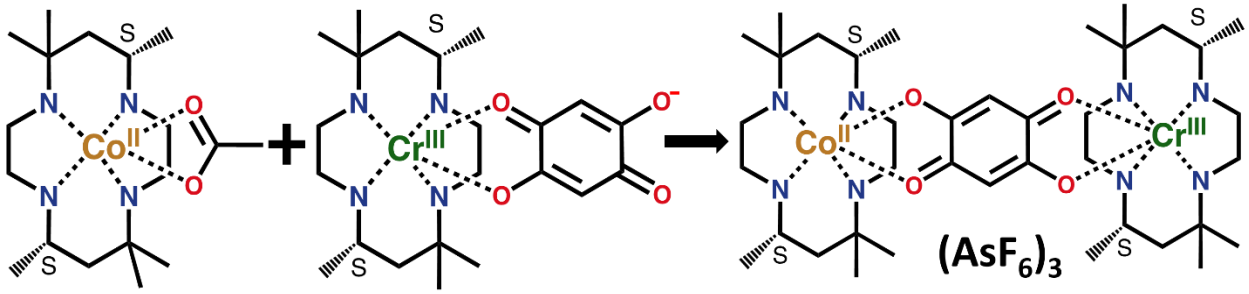

3.2.2 Physical measurement

X-ray diffraction measurement and crystal structural determinations. Diffraction data were

collected between 85 and 200 K for $1(AsF_6)_3$ under a nitrogen gas stream. The measurement was performed on a Rigaku XtaLab Synergy-R/DW diffractometer equipped with a HyPix-6000 area detector and multi-layer mirror monochromated Mo-Kα radiation of λ= 0.71073 Å. The structures were solved by a direct method and refined via full-matrix least-squares on F^2 using the SHELX program[4] implemented in the OLEX2 program[5] with anisotropic thermal parameters for all non-hydrogen atoms. The hydrogen atoms were geometrically added and refined by the riding model. The ultralow temperature data before and after 1340 nm irradiation were collected with helium gas stream at Institute for Molecular Science with Rigaku Hypix-AFCdiffractometer equipped with a Hypix-6000 area detector and multi-layer mirror monochromated Mo-Kα radiation of λ= 0.71073 Å.

IR spectroscopy. Temperature-dependent IR spectra were collected employing an FT/IR spectrophotometer (*Jasco* 600Plus) equipped with a closed-cycle helium refrigerator cryostat (Rockgate Corporation) in the range of 4000 - 400 cm^{-1}. The ground-powder samples were sandwiched between grained and flat CaF_2 plates.

UV-vis spectroscopy. Temperature-dependent UV-vis were recorded employing a SHIMADZU MPC-3100 equipped with a closed-cycle helium refrigerator cryostat (Rockgate Corporation) in the range of 3000 - 300 nm. The ground-powder samples were uniformly attached to the tapes and then held between flat CaF_2 plates.

Table 1 Crystallographic Data Collection and Structural Refinement Information for $1(AsF_6)_3$

	$1(AsF_6)_3$
Empirical formula	C38H74CoCrF18N8O4As3

Formula weight	1310.15						
Temperature(K)	85	95	120	150	200	250	300
Crystal system	*monoclinic*	*monoclinic*	*monoclinic*	*monoclinic*	*monoclinic*	*monoclinic*	*monoclinic*
Lattice Tape	Primitive	Primitive	Primitive	Primitive	Primitive	Primitive	Primitive
Space group	$P2_1$(#4)	$P2_1$(#4)	$P2_1$(#4)	$P2_1$(#4)	$P2_1$(#4)	$P2_1$(#4)	$P2_1$(#4)
a (Å)	8.9675(3)	8.9755(4)	8.9867(5)	9.0010(3)	9.0180(4)	9.0271(3)	9.0517(3)
b (Å)	30.8014(9)	30.8652(9)	30.9320(11)	31.0337(7)	31.1028(11)	31.1244(8)	31.1826(9)
c (Å)	10.4144(4)	10.4352(5)	10.4649(5)	10.4836(4)	10.5395(5)	10.5984(8)	10.6530(5)
α (deg.)	90	90	90	90	90	90	90
β (deg.)	112.812(4)	112.840(5)	112.792(6)	112.810(5)	112.689(6)	112.790(5)	112.760(5)
γ (deg.)	90	90	90	90	90	90	90
V (Å^3)	2651.58	2664.2(2)	2681.8(3)	2699	2727.4(2)	2745.29	2772.7(2)
Z value	2	2	2	2	2	2	2
D_{calc}(g/cm^3)	1.641	1.633	1.622	1.612	1.595	1.562	1.569
Light source	MoKα (λ = 0.71073 Å)						
$R_1(I>2.00s(I)$	0.0534	0.0532	0.0569	0.0628	0.0662	0.0680	0.0641
$wR_2(all)$	0.1469	0.1472	0.1641	0.1876	0.1892	0.1765	0.1677
GOF	1.025	1.033	1.052	1.037	1.026	1.165	1.102
Flack parameter	0.007(7)	0.003(5)	0.011(4)	0.009(6)	0.001(6)	0.004(6)	0.008(5)
CCDC							

[a] $R_1 = \Sigma||F_o| - |F_c||/\Sigma|F_o|$. [b] $wR_2 = [\Sigma\{w(F_o^2 - F_c^2)^2/\Sigma\{w(F_o^2)\}^2]^{1/2}$

Table 2 Selective bond lengths for $1(AsF_6)_3$ from 85 to 300 K.

	$1(AsF_6)_3$						
	85 K	95 K	120 K	150 K	200 K	250 K	300 K
Co-O1 (Å)	1.991	2.005	2.041	2.070	2.096	2.093	2.106
Co-O2 (Å)	1.988	1.990	2.015	2.088	2.119	2.126	2.137
Co-N1 (Å)	2.083	2.082	2.114	2.135	2.155	2.163	2.168
Co-N2 (Å)	2.044	2.055	2.065	2.129	2.134	2.139	2.146
Co-N3 (Å)	2.062	2.066	2.082	2.083	2.094	2.107	2.116
Co-N4 (Å)	2.070	2.085	2.107	2.147	2.164	2.147	2.139
Cr-O1 (Å)	1.934	1.942	1.945	1.955	1.958	1.958	1.953
Cr-O2 (Å)	1.942	1.946	1.953	1.949	1.950	1.947	1.961
Cr-N1 (Å)	2.103	2.099	2.105	2.113	2.119	2.117	2.130
Cr-N2 (Å)	2.088	2.080	2.093	2.083	2.076	2.062	2.067
Cr-N3 (Å)	2.074	2.093	2.079	2.089	2.076	2.077	2.074
Cr-N4 (Å)	2.116	2.111	2.118	2.090	2.088	2.083	2.093

Table 3 Ultralow Temperature Crystallographic Data Collection and Structural Refinement Information for $1(AsF_6)_3$ (LIESST and TIESST effect)

	$1(AsF_6)_3$			
Empirical formula	C38H74CoCrF18N8O4As3			
Formula weight	1384.74			
Temperature(K)	30(before light)	30(after 1340 nm)	80(after 1340 nm)	30(Quench)
Crystal system	*monoclinic*	*monoclinic*	*monoclinic*	*monoclinic*
Lattice Tape	Primitive	Primitive	Primitive	Primitive
Space group	$P2_1$(#4)	$P2_1$(#4)	$P2_1$(#4)	$P2_1$(#4)
a(Å)	8.9383(3)	10.8660(3)	8.9510(4)	10.8604(4)
b(Å)	30.9665(8)	31.2553(10)	30.8309(8)	31.1734(11)

c(Å)	10.3711(4)	15.9677(5)	10.4084(4)	15.9583(4)
α(deg.)	90	90	90	90
β(deg.)	112.866(4)	101.012(3)	112.930(5)	100.968(3)
γ(deg.)	90	90	90	90
V(Å^3)	2645.01(17)	5323.1(3)	2645.4(2)	5304
Z value	2	4	2	4
D_{calc}(g/cm^3)	1.739	1.728	1.738	1.734
Light source	MoKα (λ = 0.71073 Å)			
$R_1(I>2.00s(I)$	0.0496	0.0819	0.0537	0.0731
$wR_2(all)$	0.1226	0.2012	0.1285	0.1681
GOF	1.023	1.035	1.008	1.022
Flack parameter	0.001(5)	0.023(8)	0.033(8)	0.020(7)
CCDC				

[a]$R_1 = \Sigma||F_o| - |F_c||/\Sigma|F_o|$. [b]$wR_2 = [\Sigma\{w(F_o^2 - F_c^2)^2/\Sigma\{w(F_o^2)\}^2]^{1/2}$

Table 4 Selective bond lengths for $1(AsF_6)_3$ at 30 K before and after 1340 nm, 80 K, and 30 K quench effect.

	$1(AsF_6)_3$					
	30 K before light	30 K after 1340 nm		80 K after 1340 nm	30 K Quench	
Co-O1 (Å)	2.071	2.086	2.102	1.998	2.074	2.083
Co-O2 (Å)	2.072	2.122	2.146	2.008	2.099	2.123
Co-N1 (Å)	2.133	2.148	2.184	2.080	2.150	2.173
Co-N2 (Å)	2.107	2.112	2.099	2.063	2.111	2.090
Co-N3 (Å)	2.083	2.120	2.136	2.057	2.113	2.126
Co-N4 (Å)	2.148	2.161	2.143	2.094	2.139	2.132
Cr-O1 (Å)	1.963	1.933	1.957	1.945	1.926	1.950

Cr-O2 (Å)	1.951	1.977	1.967	1.941	1.972	1.958
Cr-N1 (Å)	2.119	2.101	2.091	2.097	2.101	2.088
Cr-N2 (Å)	2.073	2.089	2.074	2.074	2.062	2.080
Cr-N3 (Å)	2.077	2.072	2.061	2.082	2.087	2.063
Cr-N4 (Å)	2.108	2.113	2.108	2.095	2.101	2.107

Magnetic susceptibility measurement. Magnetic measurement was performed on a quantum design SQUID magnetometer (MPMS-5S). Polycrystalline samples (*ca.* ~ 10 mg) were loaded into the gelatin capsule and held by a plastic straw, which was fixed on a sample rod. The thermal magnetization was carried out under H = 2000 Oe with a sweeping rate of 5 k min^{-1} and photomagnetization was conducted under H = 5000 Oe with a sweeping rate of 0.2 K min^{-1}.

Pyroelectric measurement. Pyroelectric measurements were conducted using a continuous temperature ramping technique with a Keithley 6517B electrometer and a Quantum Design MPMS-XL chamber for precise temperature control. The single-crystal sample was carefully sandwiched between silver paste (with an area of 0.19 mm^2) on its (010) and (0-10) surfaces to ascertain the direction of the pyroelectric current with the light source aligned to the crystal and laser source through an optical fiber. The measurement temperature range was maintained between 5 and 250 K, with a helium gas flow ensuring thermal stability. The measurements were performed at a temperature sweep rate of 10 K min^{-1} and 5 K min^{-1} (Figure 3.1).

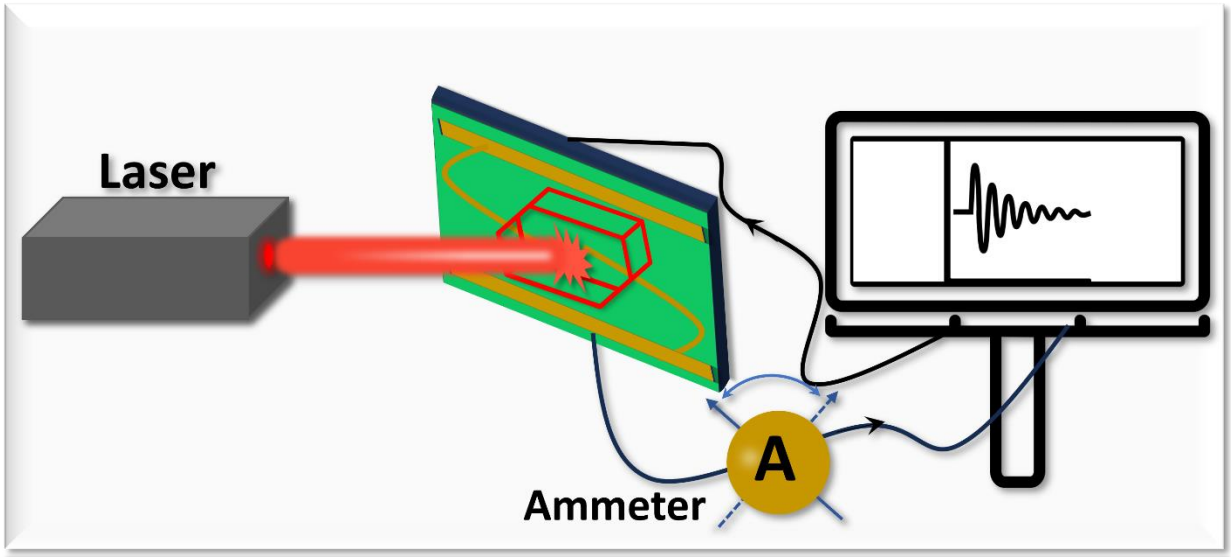

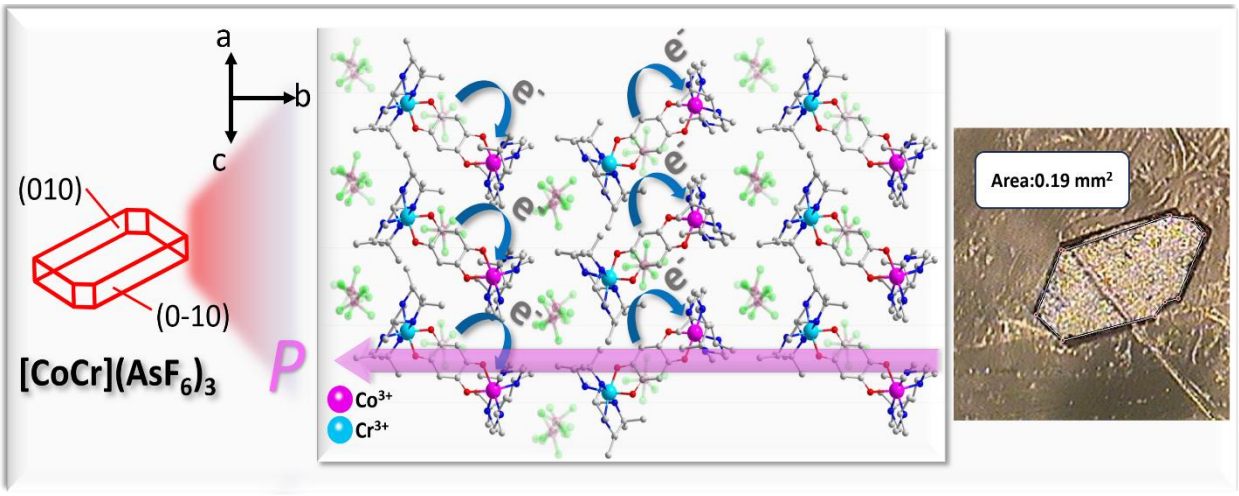

Figure 3.1 Schematic representation of the photo-electron conversion measurement system (top). The crystal's parallel polar planes (010) and (0-10), coated with silver paste, were mounted on a customized substrate connected to gold wires. An optical fiber was attached to the crystal and extended outside, aligning with the laser generator. Three different wavelength lasers 532 nm, 785 nm, and 1340 nm were used to irradiate the crystal. The rod holding the crystal was inserted into the chamber of the SQUID (Superconducting Quantum Interference Device). The temperature

variation as a function of time was recorded by the SQUID terminal. Simultaneously, the pyroelectric current, stimulated by either temperature or light, was recorded by a separate computer connected to an ammeter. A suitable red block crystal of $[CrCo](AsF_6)_3$, with an area of 0.19 mm^2, was selected for measuring the light- and thermally-induced pyroelectric current (see bottom figure). The molecular arrangement of $[CrCo](AsF_6)_3$, along with the polarization direction along the *b*-axis, is depicted in the middle of the bottom figure. Electron transfer was marked in bule arrow.

3.3 Results and Discussion

The synthesis of $[CrCo](AsF_6)_3$ was carried out via a stepwise synthetic route, as described in *Chapter* 2. The purity of the target compound was confirmed using ESI-Mass spectrometry and elemental analysis. The ESI-MS spectrum of the [CrCo] complex in methanol is shown in Figure 3.2 (upper), where the molecular ion peak appears at m/z = 1195 for $\{Cr(SS\text{-}cth)(\mu\text{-}dhbq)Co(SS\text{-}cth)_2\}^+$. This result aligns well with the calculated value (Figure 3.2, lower). Furthermore, the absence of [CrCr] or [CoCo] peaks confirms that no random occupation occurred in solution, demonstrating the stability of the $[CrCo](AsF_6)_3$ complex. Elemental analysis (Table 5), along with crystallographic data, further supports the purity of the solid sample, showing no solvent molecules trapped in the crystal lattice. A detailed discussion of the crystal structure will follow in the next section.

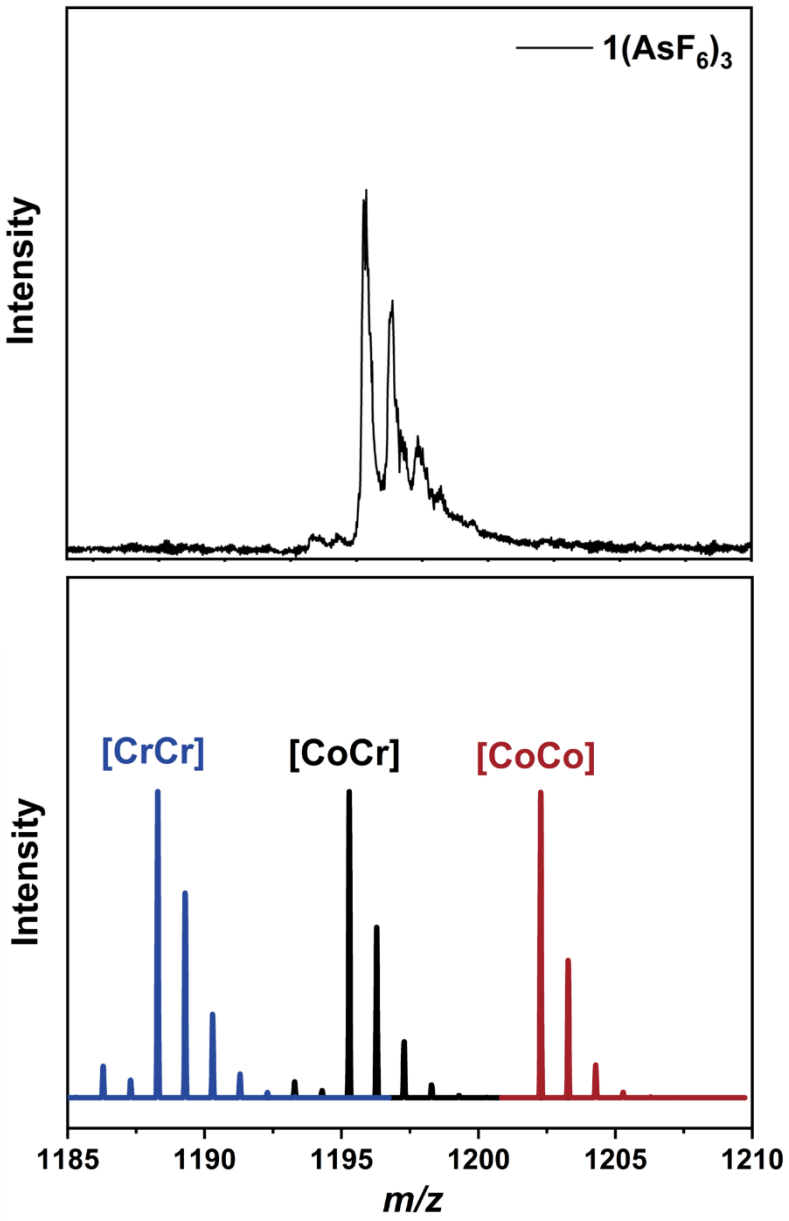

Figure 3.1 ESI-MS of $[CrCo](AsF_6)_3$ in methanol where isotope peaks corresponding to $[CrCo(AsF_6)_2]^+$ (upper). Simulation results of ESI-MS on [CrCr]/[CrCo]/[CoCo] (lower).

Table 5 Elemental analysis of **$1(AsF_6)_3$** for percentage of C,H,O.

	H%	C%	N%

1(AsF$_6$)$_3$	5.41	33.23	8.14
Calculated result of **1(AsF$_6$)$_3$**	5.39	32.96	8.09

Variable temperature magnetic susceptibility measurements were performed on a polycrystalline sample using a SQUID magnetometer under a 0.2 T field, with a sweeping rate of 5 K/min. In the high-temperature phase, the $\chi_m T$ value of **1**(AsF$_6$)$_3$ stabilized at approximately 4.45 cm^3 K mol^{-1} up to 200 K, consistent with the theoretical values for isolated high-spin Co^{2+} (S = 3/2) and Cr^{3+} (S = 3/2). As the temperature decreased, the magnetization gradually diminished, reaching 2.8 cm^3 K mol^{-1} at 60 K, indicating a transition temperature ($T_{1/2}\downarrow$) of 123 K. Below 20 K, the abrupt decrease in magnetization is attributed to zero-field splitting. Upon reheating, **1**(AsF$_6$)$_3$ displayed a similar magnetic transition, though with a slightly higher transition temperature ($T_{1/2}\uparrow$) of 145 K (Figure 3.2). This variation in magnetization at the cobalt center suggests an incomplete spin transition.

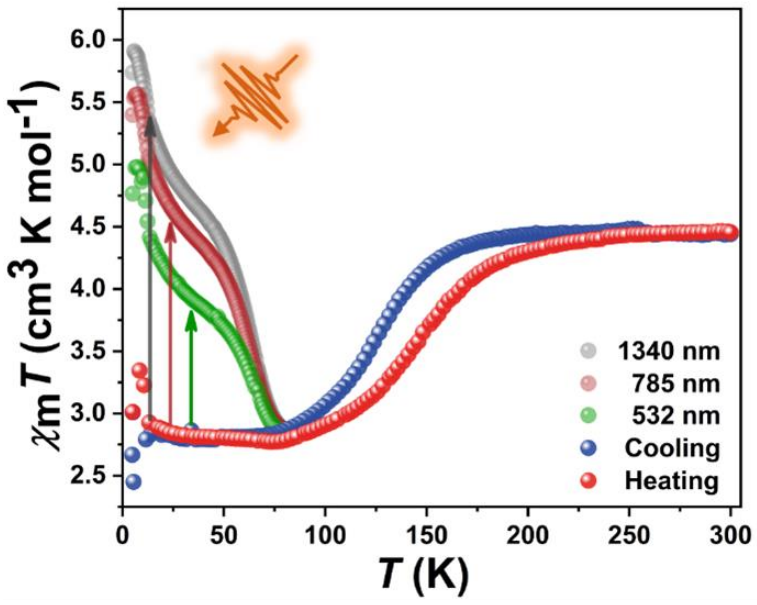

Figure 3.2 Temperature dependent magnetization of crystalline $1(AsF_6)_3$ from 5 K to 300 K under 2000 Oe with a sweeping rate of 5 K min^{-1}. Heating (red), Cooling (blue); Photomagnetization was measured with tape sample under 5000 Oe with a sweeping rate of 0.5 K min^{-1}. 532 nm (green), 785 nm (dark red), 1340 nm (grey).

To investigate this behavior further, variable-temperature spectroscopic analyses were conducted in the heating mode within this temperature range. A gradual reduction in the intensity of the absorption band centered at 523 nm was observed, attributed to ligand-to-metal charge transfer from $dhsq^{3-}$ to Co^{3+} ions (Figure 3.3a). Although several faint absorption bands were observed above 700 nm, this was further confirmed by liquid UV-Vis analysis of $1(AsF_6)_3$ and solid UV-Vis analysis of $[CrSCoR](AsF_6)_3$ with the heterochiral ligand cth. The UV-Vis spectrum of $1(AsF_6)_3$ in CH_2Cl_2 at room temperature showed a broad absorption band around 523 nm, corresponding to the electronic configuration of high-spin Co(II), and a relatively sharp peak near 1400 nm, which could also be attributed to ligand-to-metal charge transfer (LMCT) by DFT calculation (Figure 3.3b). To avoid the generation of false peaks caused by the solvent, the solvent background was also measured. By comparing the background absorption of the solvent (CH_2Cl_2), it was confirmed that the peak in the near-infrared (IR) region originates from $1(AsF_6)_3$. In the case of the magnetization of $[CrSCoR](AsF_6)_3$, it is known that valence tautomerism completes around room temperature, corresponding to the low-spin Co(III)-$dsbq^{3-}$-Cr(III) configuration (Figure 3.3c). Therefore, UV-Vis measurements of the solid sample of $[CrSCoR](AsF_6)_3$ were conducted at room temperature, revealing several clear and intense peaks in the 400–800 nm range, consistent with previous reports on $[CrSCoR](AsF_6)_3$. Additionally, a broad peak around 1400 nm was observed in the IR region, which aligns well with the peak of the liquid UV-Vis spectrum of $1(AsF_6)_3$ at the same position (Figure 3.3d). Given the similar variation in electronic configuration, it suggests that the absorption of $1(AsF_6)_3$ around 1400 nm corresponds to an LMCT band. The discrepancy in temperature-dependent UV-Vis measurements of $1(AsF_6)_3$ could be due to incomplete cooling. These results

further support the likelihood of photomagnetization in $1(AsF_6)_3$ under irradiation at 532, 785, and 1340 nm. On the other hand, the vibrational band of $dhsq^{3-}$ at 1470 cm^{-1} exhibited a significant decrease over the same temperature range (Figure 3.4). These findings strongly suggest that the variation in $\chi_m T$ values within this temperature range is associated with partial electron transfer from the $[Cr^{3+}\text{-}dhsq^{3-}\text{-}Co^{3+}LS]$ state to the $[Cr^{3+}\text{-}dhbq^{2-}\text{-}Co^{2+}HS]$ state. Calculations of magnetization estimated that approximately 48% of the valence tautomerism occurred, compared to the expected complete VT, which would correspond to a magnetization variation of 3.45 cm^3 K mol^{-1}.

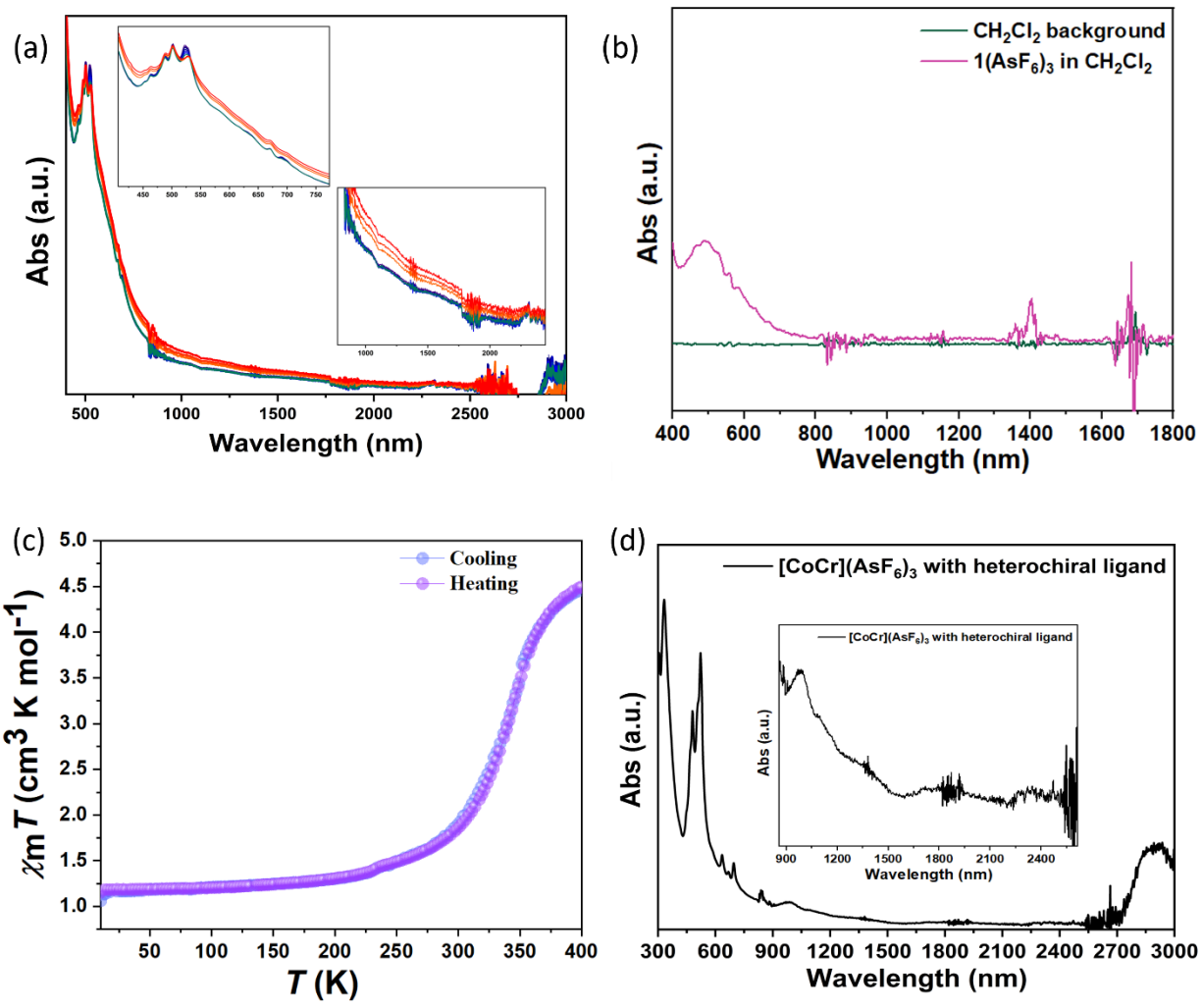

Figure 3.3 (a) Temperature-dependent UV-Vis spectrum of the solid sample $1(AsF_6)_3$ in the range

of 400 to 3000 nm. (Inset: data from 400 to 800 nm on the left; data from 900 to 2500 nm on the right). (b) Liquid UV-Vis spectrum of $1(AsF_6)_3$ in CH_2Cl_2, where the green line represents the solvent background and the pink line represents the spectrum of $1(AsF_6)_3$. (c) Magnetic susceptibility of crystalline $[CrSCoR](AsF_6)_3$ measured between 10 and 400 K, with a sweeping rate of 5 K/min. (d) UV-Vis spectrum of tape-mounted $[CrSCoR](AsF_6)_3$ at room temperature, covering the range of 300 to 3000 nm. (Inset: data from 900 to 2500 nm).

In addition, light-induced valence tautomerism in this complex was explored by measuring the magnetization of the polycrystalline sample under various light irradiations, including 532, 785, and 1340 nm, at 5 K. Initially, the sample was irradiated with a 1340 nm laser for 30 minutes until photomagnetization reached saturation. After illumination, the maximum $\chi_m T$ values peaked around 6 cm^3 K mol^{-1}, consistent with ferromagnetic coupling between high-spin Co^{2+} and Cr^{3+}. However, this ferromagnetic state was transient, with the magnetic susceptibility dropping sharply from 6 to 5.33 cm^3 K mol^{-1} at 13 K, and then gradually decreasing further until 48 K. Beyond this point, the $\chi_m T$ values rapidly decayed back to the low-temperature phase, dropping from 4.37 to 2.8 cm^3 K mol^{-1} at 80 K (Figure 3.2).

When irradiated with 532 nm and 785 nm lasers, the results showed similar trends, though with differing efficiencies of photoconversion, ranked as 1340 nm > 785 nm > 532 nm. Compared to recently reported cobalt VT complexes, compound 1 exhibits a longer relaxation lifetime after illumination and a higher relaxation temperature, evidencing a lower thermally induced VT transition temperature, which favors stabilizing the light-induced high-spin state.

Additionally, the temperature-induced excited spin state trapping (TIESST) effect was observed in this complex. The crystalline sample of $1(AsF_6)_3$ was cooled to 20 K and stabilized for several minutes before measurements. Under a magnetic field of 0.2 T with a sweeping rate of 0.5 K/min,

a relatively high $\chi_m T$ value of 3.53 cm³ K mol⁻¹ was detected at 10 K, compared to 3 cm³ K mol⁻¹ under normal conditions, indicating that a partial high-spin state of Co was quenched during rapid cooling. As the temperature increased, this value gradually decayed to the ground state at 75 K, following a similar trend to the photomagnetization (Figure 3.4). Upon further heating, the magnetization value rose, reaching the termination of electron transfer at 250 K, after which it stabilized at 4.4 cm³ K mol⁻¹ up to 300 K. During subsequent cooling and heating cycles, the compound exhibited a typical magnetic transition.

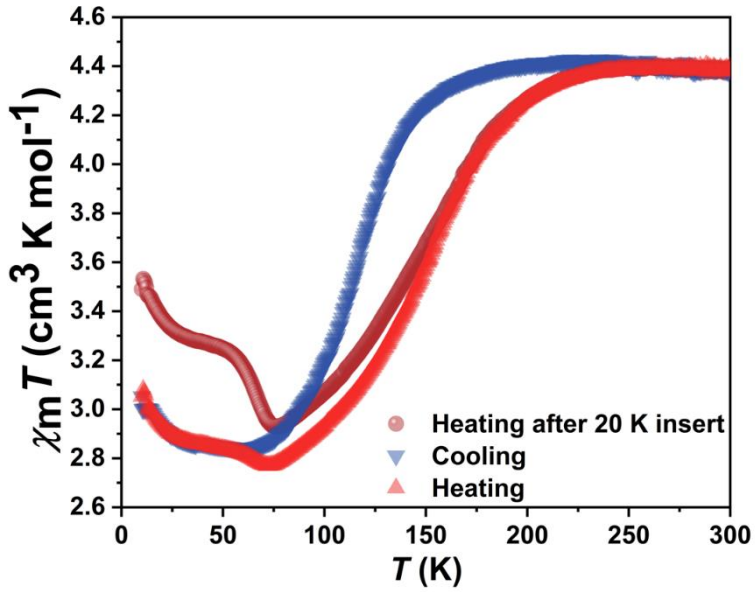

Figure 3.4 Temperature-induced excited spin state trapping (TIESST) was measured by placing a crystalline sample of $1(AsF_6)_3$ at 20 K. It took several minutes to stabilize the sample temperature, with the highest recorded temperature reaching 60 K, as indicated by the temperature detector. Magnetization measurements were then conducted at a sweeping rate of 0.5 K/min under a 2000 Oe magnetic field. The data were recorded for TIESST (red ●), cooling (blue ▽), and heating (red △).

Temperature-dependent single-crystal X-ray diffraction of $1(AsF_6)_3$ was performed to investigate

changes in the crystal structure (Table 1). The analysis revealed that cobalt (Co) and chromium (Cr) were coordinated with the enantiopure SS-cth ligand. These two mononuclear complexes were bridged by a dhbq ligand and surrounded by three AsF_6^- ions. Each unit cell contained two asymmetric units, with the molecules packed in the polar $P2_1$ space group (Figure 3.5).

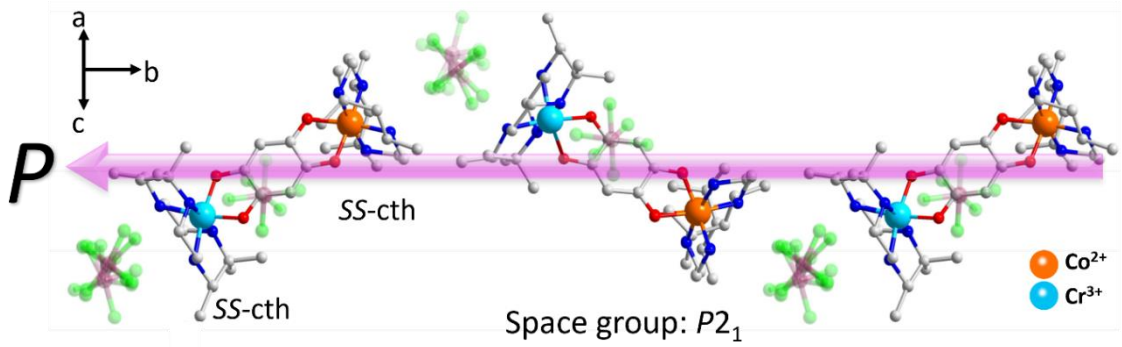

Figure 3.5 Molecular arrangement of $1(AsF_6)_3$ packed in $P2_1$ space group where the vector of CrCo is optimized to along polar *b* axis.

Notably, the new $[CrCo](AsF_6)_3$ complex combines two unique features of previously reported systems: the distorted conformation of homochiral $[CrSCoS](PF_6)_3$ complexes and the compact packing mode of heterochiral $[CrSCoR](PF_6)_3$ complexes, which lack solvent. This suggests that the electronic configuration of the new complex differs from previous examples due to variations in intra- and intermolecular interactions, leading to altered valence tautomerism behavior.

The average bond lengths of Co–O/Co–N and Cr–O/Cr–N were plotted as a function of temperature (Figure 3.6a, b). At 300 K, the average Co–O/Co–N bond lengths were 2.116 Å and 2.141 Å, indicating that the majority of the Co ions are in a high-spin Co(II) state with an octahedral coordination environment (Table 2). As the temperature decreased, the bond lengths around the Co center remained constant at 200 K and gradually decreased to 1.990 Å and 2.065 Å at 85 K. Although nearing the end of the transition, these bond lengths are still longer than those typically associated with low-spin Co(III), suggesting partial electron transfer.

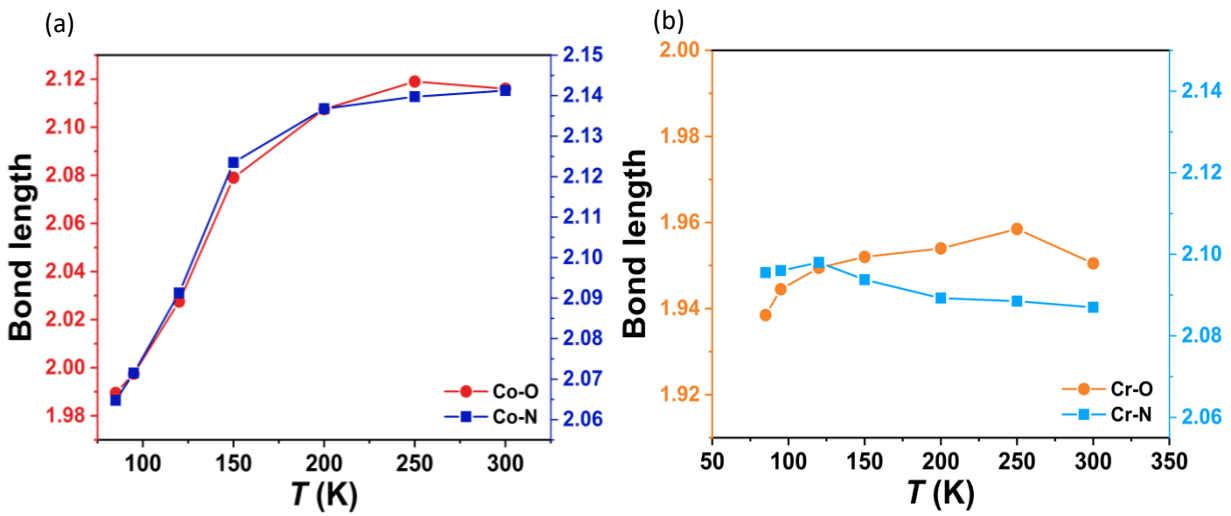

Figure 3.6 (a) The average bond lengths of Co–O and Co–N were plotted against temperature, with the Co–O bond represented by a red line and the Co–N bond by a blue line. (b) The average bond lengths of Cr–O and Cr–N were plotted against temperature, with the Cr–O bond represented by an orange line and the Cr–N bond by a pale blue line.

The deviation in average bond lengths between the high- and low-temperature phases, compared to a Co complex with complete electron transfer, indicates that the electron transfer in the new complex is approximately 50%, a result consistent with magnetization measurements.

On the other hand, the average bond lengths of Cr–O/Cr–N were 1.951 Å and 2.087 Å at 300 K, and 1.939 Å and 2.100 Å at 85 K, aligning with those typical of a trivalent Cr ion. These bond lengths remained unchanged across temperatures, supporting the idea that the Co and Cr ions, located at two distinct sites of the dhbq ligand, can be clearly distinguished due to their regular arrangement without random mixing.

Compound $1(AsF_6)_3$ crystallized in the $P2_1$ polar space group, with the polar axis aligned along the *b*-axis. Polarization changes during both thermally and light-induced valence tautomerism (VT) transitions were quantitatively determined using pyroelectric measurements. A suitably sized

single crystal was selected, and silver paste was applied to form parallel faces along the (010) and (0-10) planes. The crystal was then connected to a substrate using gold wire (Figure 3.1 bottom).

Pyroelectric measurements were conducted with a specialized setup, where a SQUID controlled the temperature and a Keithley 6517B electrometer recorded the generated current. Without applying any external field, the crystal was measured during a temperature cycle from 5 K to 250 K at a sweep rate of 5 K/min. The pyroelectric coefficient began to increase steadily from 200 K, reaching a plateau around 128 K. Below this temperature, the coefficient gradually decreased, eventually reaching zero at approximately 60 K, signaling the completion of electron transfer. As the temperature dropped further to 25 K, no significant variation was observed. Upon reheating to 250 K, the pyroelectric coefficient followed a similar trend as during the cooling process, with no detectable hysteresis (Figure 3.7a).

The total polarization change in $1(AsF_6)_3$ was calculated to be approximately 1.63 μC cm^{-2}, based on the integration of the pyroelectric current over time. This value is comparable to previously reported Co VT complexes (Figure 3.7b). To confirm that the pyroelectric current originated from electron transfer, the magnetic susceptibility of $1(AsF_6)_3$ was remeasured under the same conditions as the pyroelectric measurements, with venting enabled. The polarization change and pyroelectric coefficient were plotted alongside the magnetization and its derivative, respectively. The similar trends observed in both measurements strongly suggest that the primary contribution to the pyroelectric current was electron transfer. Additionally, the absence of hysteresis, influenced by the venting mode, suggests improved thermal conduction and accelerated thermal equilibrium during the measurement process.

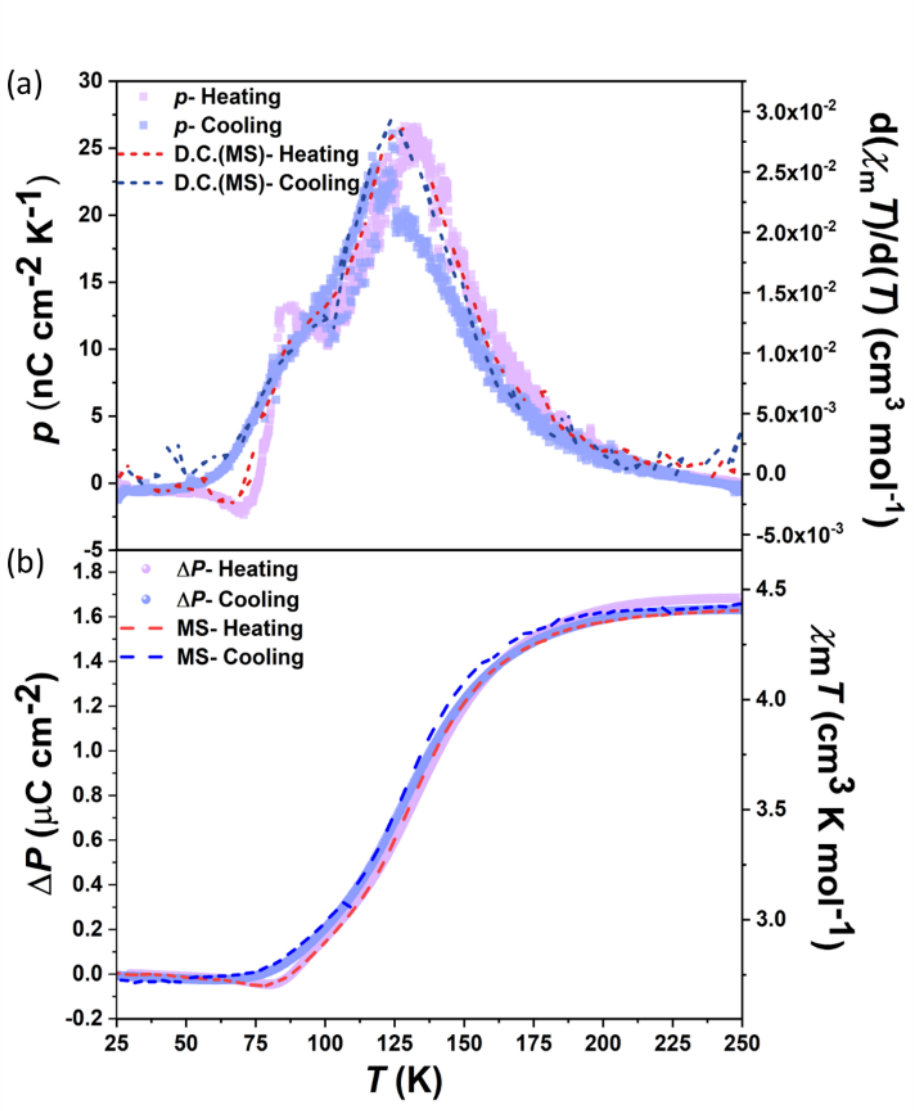

Figure 3.7 (a) Temperature-dependent pyroelectric coefficient and the derivative of magnetization for 1$(AsF_6)_3$, measured from 25 to 250 K at a rate of 5 K/min, are represented by squares and dashed lines, respectively. (b) Comparison of temperature-induced polarization change and magnetization in 1$(AsF_6)_3$.

Light-induced pyroelectric current measurements were performed using the same setup as the thermal-induced experiments, with an additional fiber aligned to the crystal as a light source. This discussion focuses on the results from 1340 nm irradiation. Initially, the crystal was cooled from 250 K to 5 K, following the same sequence as in the thermal-induced pyroelectric measurements.

A bell-shaped curve, consistent with the typical pyroelectric response, was observed. Upon activating the 1340 nm laser, a sharp and opposite pyroelectric current was generated, rapidly rising to a plateau (Figure 3.8). This current, peaking at approximately 120 pA, is about 18 times larger than the current triggered by temperature alone, indicating a transition from the Co(III)-dhsq-Cr(III) low-temperature phase to the Co(II)-dhbq-Cr(III) excited phase.

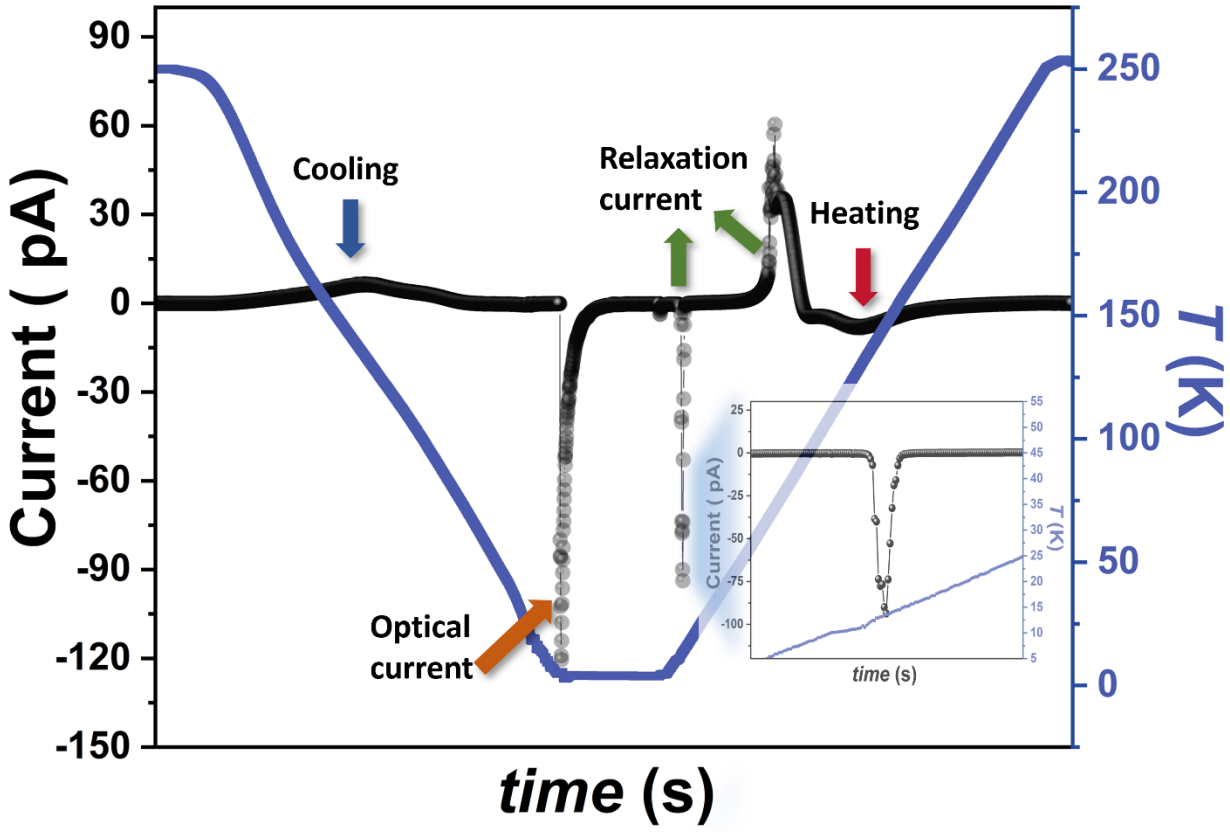

Figure 3.8 Light-induced pyroelectric current and temperature as a function of time for $1(AsF_6)_3$ (inset: data from 5 to 25 K).

To prevent significant temperature shifts caused by local heating during light irradiation, the cooling system remained active throughout the illumination process. After 5 minutes, the light-induced pyroelectric current gradually returned to baseline, suggesting that compound $1(AsF_6)_3$ had fully transitioned into and stabilized within the excited phase without reverting. When the light source was turned off, the current remained unchanged until an impulse current of about 93 pA

was detected at 12 K (Figure 3.8 insect). Upon magnifying the data around 12 K, it became evident that the variation was a continuous process, with multiple data points recorded, rather than noise or abrupt jumps. Interestingly, this current, which had the same direction as the light-induced current, was triggered by temperature. This suggests that, at ultra-low temperatures, the light-induced excited state is not fully metastable and is partially quenched. As the temperature increased, the crystal gained sufficient energy to transition into the hidden phase.

Upon further heating to 50 K, an opposite relaxation current was observed, forming two peaks at 71 K and 77 K. These peaks resulted from the counteraction between the photo-induced pyroelectric current relaxation and the thermal-induced current. Beyond 80 K, the relaxation process ended, and the system entered the thermal induction mode. Upon reaching 250 K, a symmetric current, similar to the one observed during cooling, was detected.

An analysis of the pyroelectric coefficient revealed maximum variation rates for thermal activation impulse current, light-induced relaxation time, and normal thermal pyroelectric current at 0.8, 0.14, and 0.025 nC cm^{-2} K^{-1}, respectively, indicating a significantly faster photoinduction process compared to thermal induction (Figure 3.9).

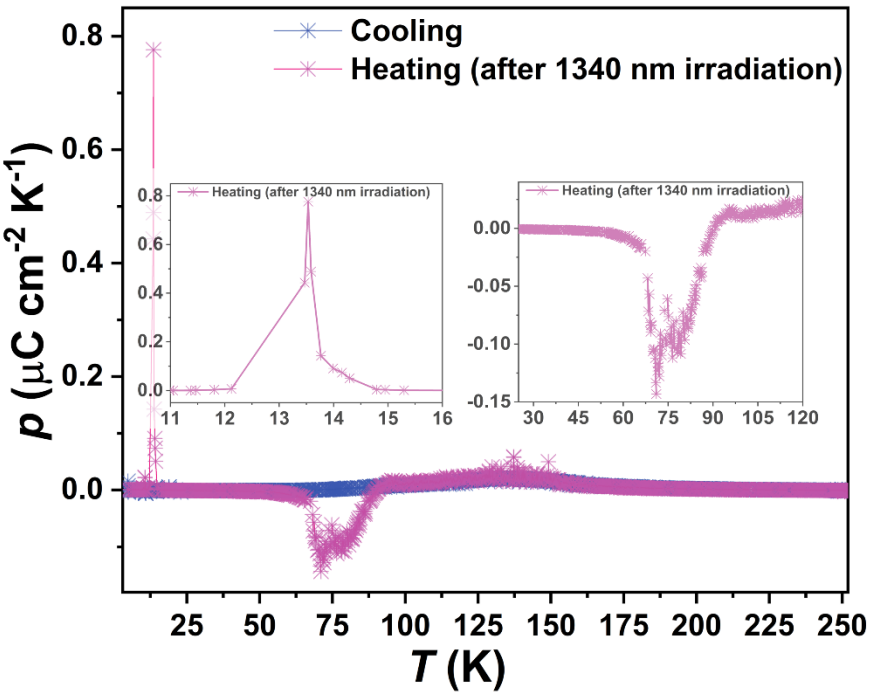

Figure 3.9 Pyroelectric coefficient of single crystal $1(AsF_6)_3$ measured between 5 K and 250 K. The purple line represents the heating process after 1340 nm irradiation, while the blue line represents the cooling process.

Additionally, the pyroelectric current and pyroelectric coefficient of the crystal $1(AsF_6)_3$ were measured at a sweep rate of 10 K/min, confirming the dependence of its pyroelectricity on the scan rate. As shown in Figure 3.10, the pyroelectric current exhibited a similar variation pattern both before and after 1340 nm irradiation. Notably, when comparing the current values at specific peaks, including the light-induced thermal relaxation at 12 K and 72 K, as well as the thermally induced pyroelectric current around 127 K, all were found to be proportional to the sweep rate. The only exception was a slight temperature shift, which is attributed to differences in thermal conduction within the single crystal. The calculated pyroelectric coefficients align well across various sweeping rates, further validating the consistency of the measurements (Figure 3.11). This evidence confirms the presence of pyroelectric current during both the heating and cooling modes and suggests that the pulse current observed at 12 K is a genuine signal resulting from the hidden

phase transition, rather than a mere anomaly or jumping point.

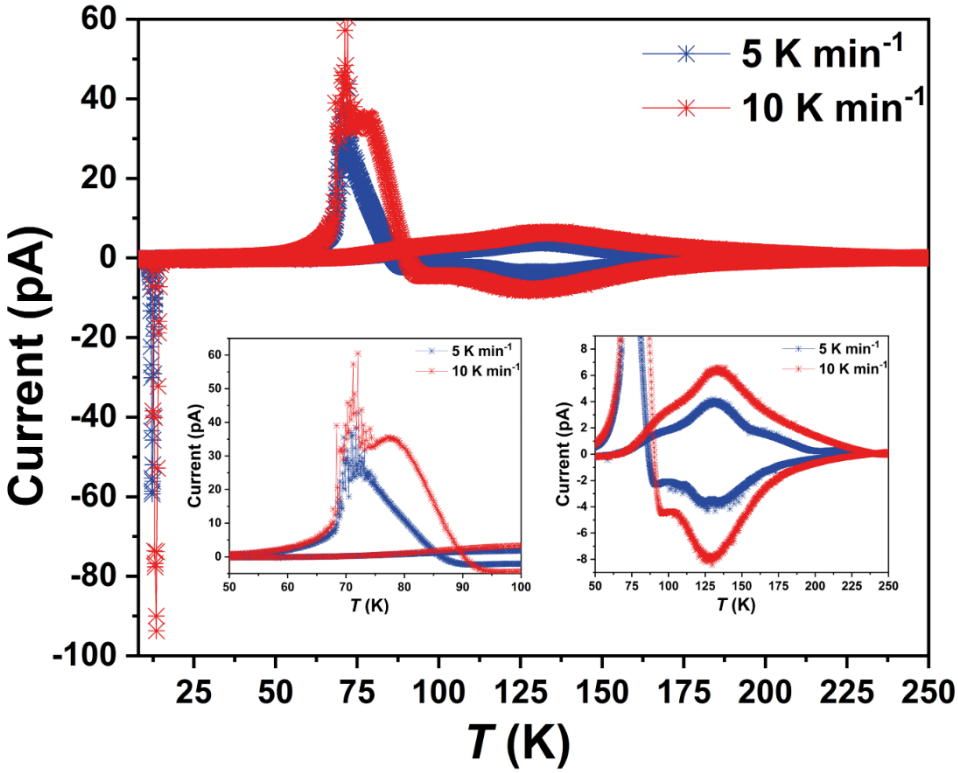

Figure 3.10 The pyroelectric current of $1(AsF_6)_3$ was measured at sweep rates of 5 K/min (blue) and 10 K/min (red), both before and after 1340 nm irradiation, over the temperature range of 5 to 250 K. The insets show the current from thermal relaxation following light irradiation (bottom left) and the thermally induced pyroelectric current (bottom right). The results demonstrate that the pyroelectric current is nearly proportional to the heating rate, further confirming the pyroelectric properties of this compound (insect: light induced relaxation from 50 to 100 K (left) and thermally induced pyroelectric current from 50 to 250 K (right)).

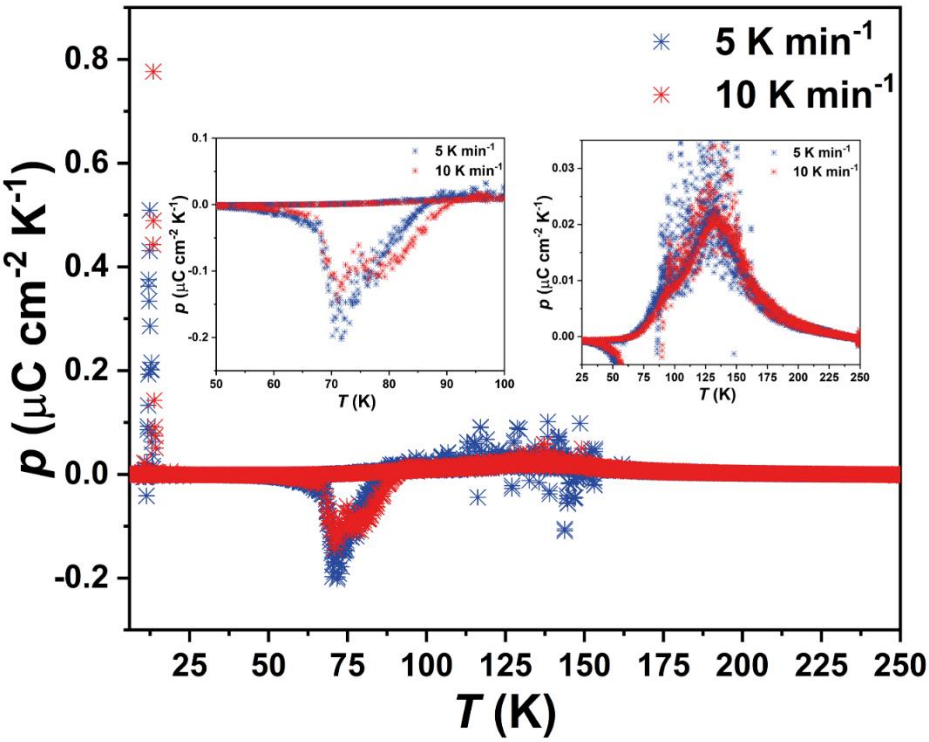

The pyroelectric coefficient of a single crystal of $1(AsF_6)_3$ was measured between 5 K and 250 K at sweep rates of 5 K/min (blue) and 10 K/min (red). The results were nearly identical across both sweep rates (insect: date from 50 to 100 K (left) and from 25 to 250 K (right)).

Integration of the pyroelectric current revealed that the light-induced polarization change at the lowest temperature reached 1.88 μC cm^{-2}, which is almost identical to the polarization change induced by temperature alone (Figure 3.12). This suggests that the excited state triggered by light closely mirrors the state induced by temperature, as confirmed by the magnetization results. Interestingly, as the sample was heated, the polarization change increased sharply to 2.25 μC cm^{-2}. The noticeable deviation of approximately 0.37 μC cm^{-2} indicates the presence of a possible hidden phase at a lower energy level, distinct from either the light-induced excited state at the lowest temperature or the high-temperature phase. This hidden phase remained stable up to 55 K, after which the light-induced polarization change dropped abruptly before increasing again due to

thermal effects from 80 K onward.

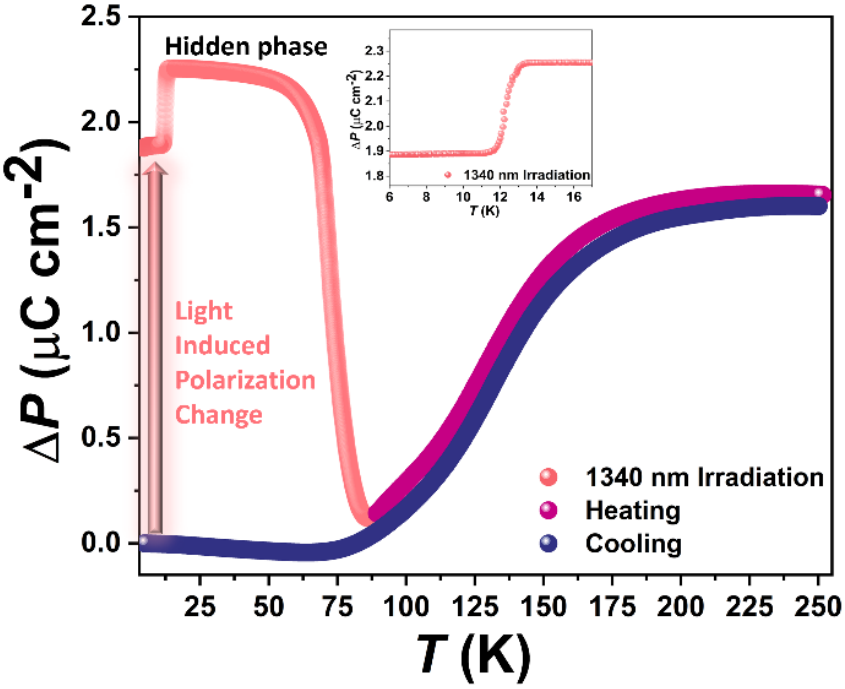

Figure 3.12 Temperature-dependent polarization change after 1340 nm laser irradiation, measured at a sweeping rate of 10 K/min (inset: polarization change between 5 and 16 K from the hidden phase).

Additionally, since this compound exhibited varying degrees of photoresponse to different laser wavelengths, the pyroelectric properties of $1(AsF_6)_3$ were further investigated using laser sources at 785 nm and 532 nm. The pyroelectric coefficients during heating and cooling showed good alignment across different laser wavelengths, indicating a consistent thermal response. However, the thermal relaxation after light irradiation showed a decreasing trend in the order of 1340 nm > 785 nm > 532 nm, with values of 0.04 μC cm^{-2} K^{-1} at 12 K and -0.05 μC cm^{-2} K^{-1} at 75 K (Figure 3.13a). Interestingly, the hidden transition observed at 12 K during thermal relaxation disappeared after 532 nm irradiation, and the thermal relaxation correspondingly decreased to -0.03 μC cm^{-2} K^{-1} (Figure 3.13 b).

By comparing the polarization changes induced by these three lasers, it becomes clear that the integral variation process after light irradiation is most pronounced under 1340 nm irradiation. This discrepancy is likely due to the different absorption levels of the crystal at each wavelength (Figure 3.13c). Notably, the polarization change induced by 1340 nm irradiation is the largest observed in non-ferroelectric systems to date.

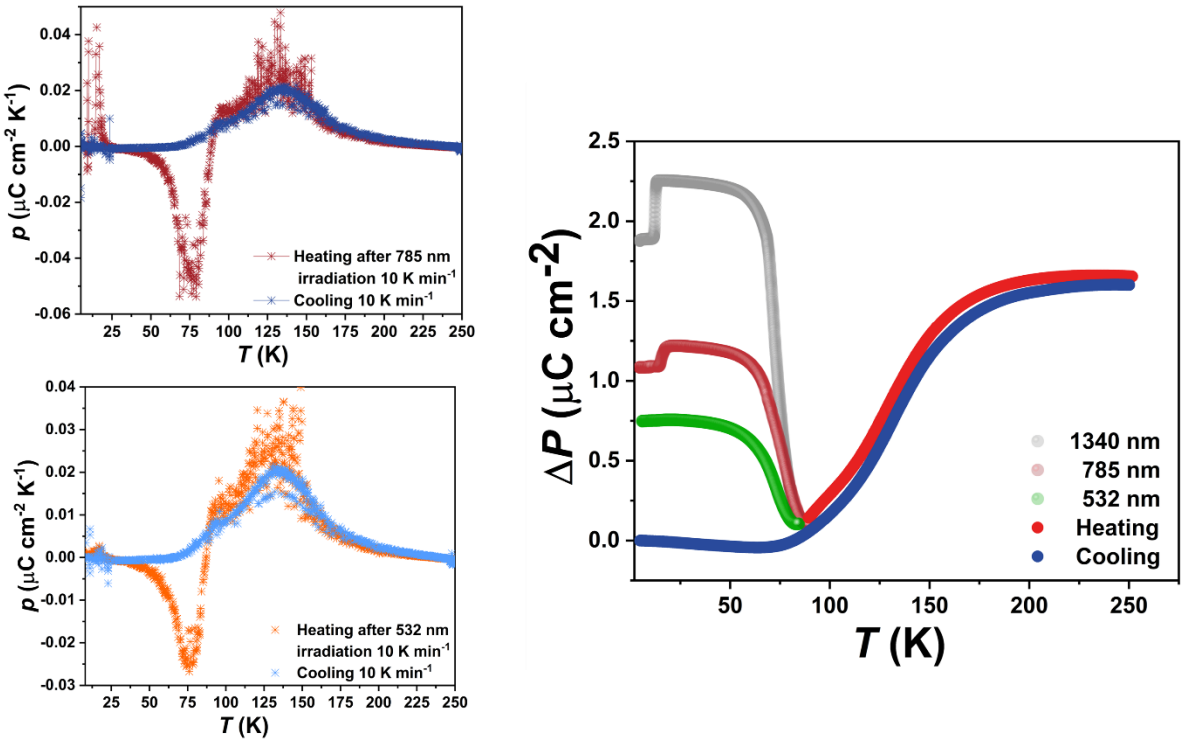

Figure 3.13 (a) The pyroelectric coefficient of $1(AsF_6)_3$ measured after irradiation at 785 nm and 5 K, during a heating and cooling cycle at 10 K/min. (b) The pyroelectric coefficient of $1(AsF_6)_3$ measured after irradiation at 532 nm and 5 K, following the same heating and cooling cycle at 10 K/min. (c) A comparison of polarization changes in $1(AsF_6)_3$ after irradiation at 1340 nm, 785 nm, and 532 nm, respectively, shows that the efficiency of polarization change induced by the lasers decreases in the order: 1340 nm > 785 nm > 532 nm. The variation in polarization change induced by different lasers is likely due to the crystal's differing levels of absorption at each wavelength.

Additionally, based on magnetization and crystal structure analysis, the nearly fully excited state

of the single crystal triggered by TIESST could be maintained up to 50 K without decaying back to the ground state. This provides an opportunity to detect the polarization change induced by the quenching effect. The pyroelectric rod-equipped crystal was directly inserted into the SQUID chamber at 20 K. After stabilizing the temperature and background current for several minutes, pyroelectric current measurements were taken during both heating and cooling cycles. As the temperature increased to 50 K, a continuous pyroelectric current, caused by the relaxation from the excited state to the ground state, was detected, peaking at around 1.5 pA at approximately 78 K (Figure 3.14a). After this point, the current gradually decreased and reversed direction beyond 90 K. From this point onward, the pyroelectric current followed the same pattern as the thermally induced pyroelectric current. In the second heating cycle, the current observed between 50 K and 90 K was absent, indicating that the sample had returned to the ground state at low temperatures. The polarization change induced by TIESST was approximately 0.15 μC cm^{-2} (Figure 3.14b). This relatively small value is likely due to incomplete cooling of the crystal below 50 K, as poor thermal exchange occurred after inserting the rod into the chamber from ambient conditions.

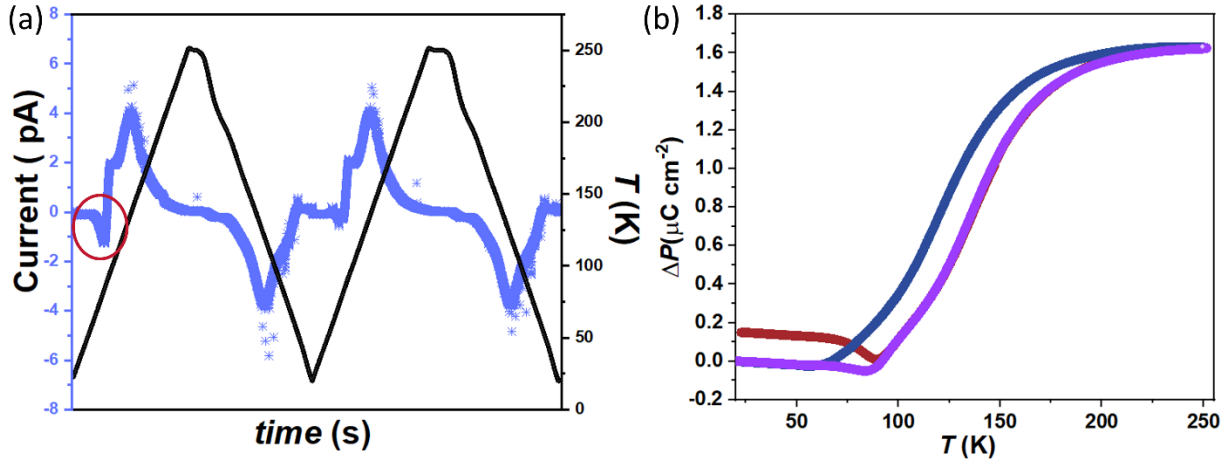

Figure 3.14 (a) Pyroelectric current of the single crystal $1(AsF_6)_3$ over two cycles induced by TIESST. (b) Polarization change of $1(AsF_6)_3$ between 20 K and 250 K, with the red line representing the TIESST-induced polarization change, the purple line representing the heating process, and the blue line marking the cooling process after TIESST.

Interestingly, during the second heating cycle, a downturn in the pyroelectric current was observed between 60 K and 80 K, followed by a positive plateau around 90 K (Figure 3.15a). This behavior suggests the emergence of a more stable thermally induced metastable state, with an additional driving force balancing the pyroelectric current. We then held the crystal of $1(AsF_6)_3$ at 76 K until the pyroelectric current returned to the baseline before continuing to heat. As the current shifted from a plateau to a sharp peak at 90 K, it indicated that the process around 70 K was effectively canceled, and the process at 90 K became dominant, significantly enhancing the positive current and increasing the polarization change (Figure 3.15b).

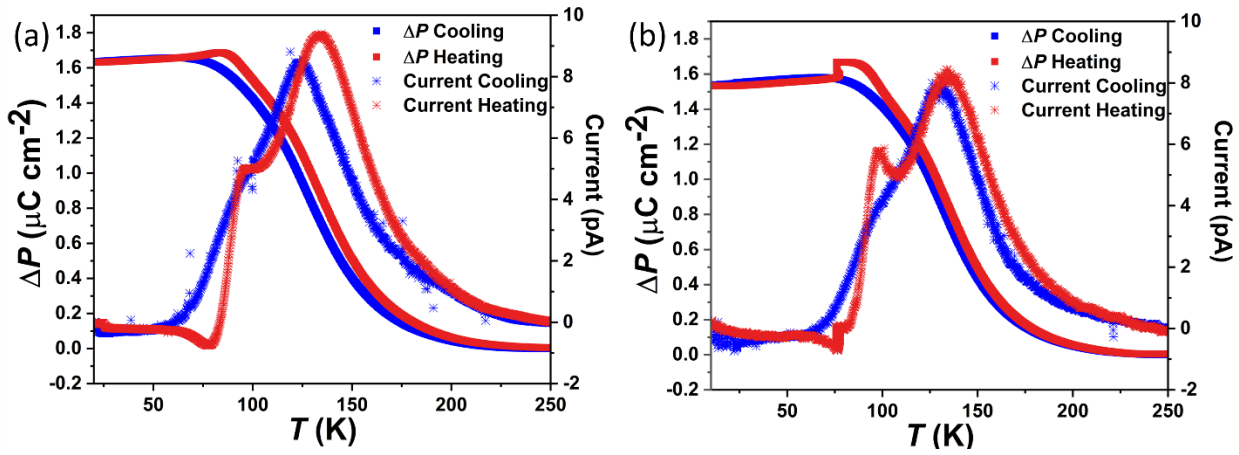

Figure 3.15 (a) Thermally induced pyroelectric current/polarization change between 10 and 250 K. (b) Cystal of $1(AsF_6)_3$ at 76 K was stabilized and pyroelectric current was measured between 10 and 250 K.

To investigate the underlying mechanism, detailed crystal structure analyses were conducted at 30 K, 70 K, 85 K, and 90K. Notably, as the temperature increased from 30 K to 70 K, the molecular arrangement along the polar *b*-axis shifted, with the angle increasing from 34.22° to 35.80°, indicating a decrease in dipole moment. However, at 85 K, while the angle between the CrCo vector and the polar axis remained unchanged, the AsF_6^- counterion became disordered. During this process, the majority contributing to polarization change shifted from molecular

rearrangement to ion displacement. As the temperature increased to 90 K, the angle returned to 34.16°, and the counterion regained its ordered structure (Figure 3.16). Therefore, the observed opposite behavior in pyroelectric current and polarization change could be attributed to the combined effects of molecular rearrangement and the variation of the counterion.

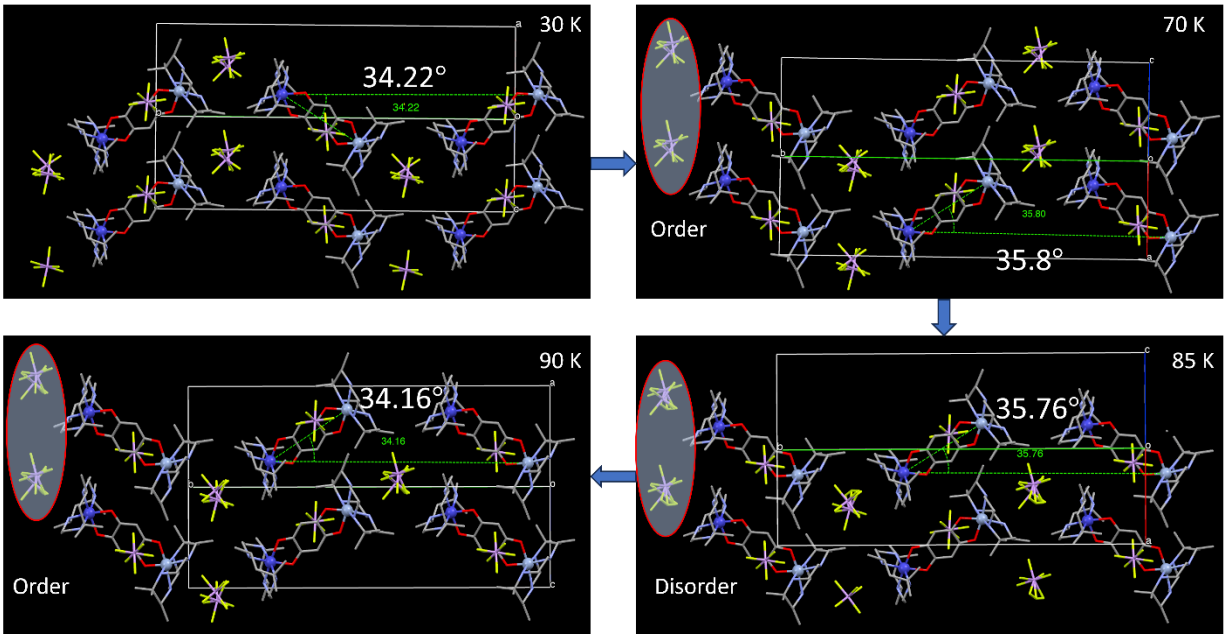

Figure 3.16 Molecular arrangement of $1(AsF_6)_3$ at 30 K, 70 K, 85 K, and 90 K where the angles between vector of CrCo and polar *b*-axis are 34.22°, 35.8°, 35.76°, and 34.16°, respectively.

In addition to this unique behavior, we are also particularly interested in investigating the origin of the discrepancies between thermal and light-induced polarization changes, especially the sudden increase in polarization around 12 K, which appears to be linked to a hidden phase that is silent in magnetization measurements. This will be explored in more detail in our ongoing study of ultralow-temperature crystal structures.

Due to the limitations of ultralow-temperature crystal structure measurements, we sought to confirm whether the hidden phase induced by 1340 nm irradiation could also be accessed at higher temperatures. To explore this, we measured the light-induced pyroelectric current of a single

crystal of $1(AsF_6)_3$ at 30 K. After stabilizing the crystal at 30 K, we irradiated it with a 1340 nm laser until it was fully excited, followed by direct heating. The light-induced polarization change at 30 K reached 2.09 μC cm^{-2}, a value close to the 2.18 μC cm^{-2} associated with the hidden phase and significantly different from the 1.80 μC cm^{-2} observed for the intermediate phase at the lowest temperature. This suggests that the light-induced excited state at 30 K is consistent with the light-induced hidden phase. To further investigate the reversibility between the hidden phase and the intermediate phase, the crystal was cooled down to 5 K after light irradiation at 30 K. However, as the temperature decreased, no significant change in polarization was observed, and no negative variation was detected. This suggests that the intermediate phase below 12 K is unstable, and the ultralow temperature prevents further transition into the hidden phase. Moreover, once the hidden phase is activated by light irradiation at higher temperatures, ion displacement does not occur upon cooling, indicating that the process from the intermediate phase at low temperatures to the hidden phase at higher temperatures is unidirectional. It also provides us opportunity to investigate the light induced hidden phase by analysis of crystal structure.

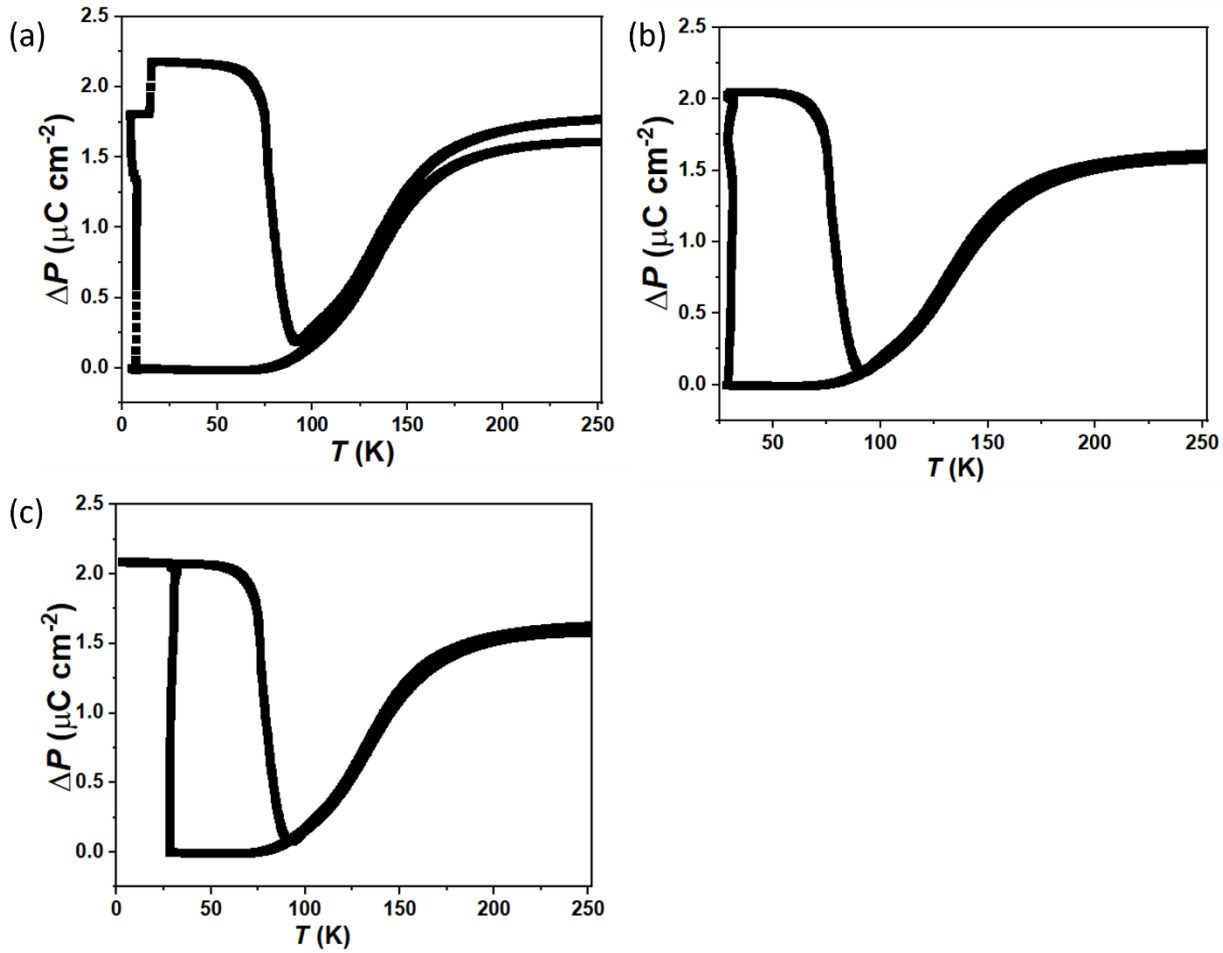

Figure 3.17 (a) Light-induced polarization change of $1(AsF_6)_3$ measured from 5 K to 250 K under normal sweeping conditions. (b) The crystal was irradiated at 30 K, followed by direct heating and cooling between 30 K and 250 K. (c) The crystal was irradiated at 30 K, then cooled to 5 K before being heated up to 250 K.

Ultralow temperature and light-induced metastable state crystal structures were investigated to identify potential hidden phases triggered by light irradiation. A single crystal was loaded at 300 K and gradually cooled to the lowest achievable temperature of approximately 30 K. Once stabilized, a 1340 nm laser source aligned with the crystal was activated (Figure 3.18), and the crystal was irradiated for 20 minutes to reach saturation. After the light source was turned off, measurements began.

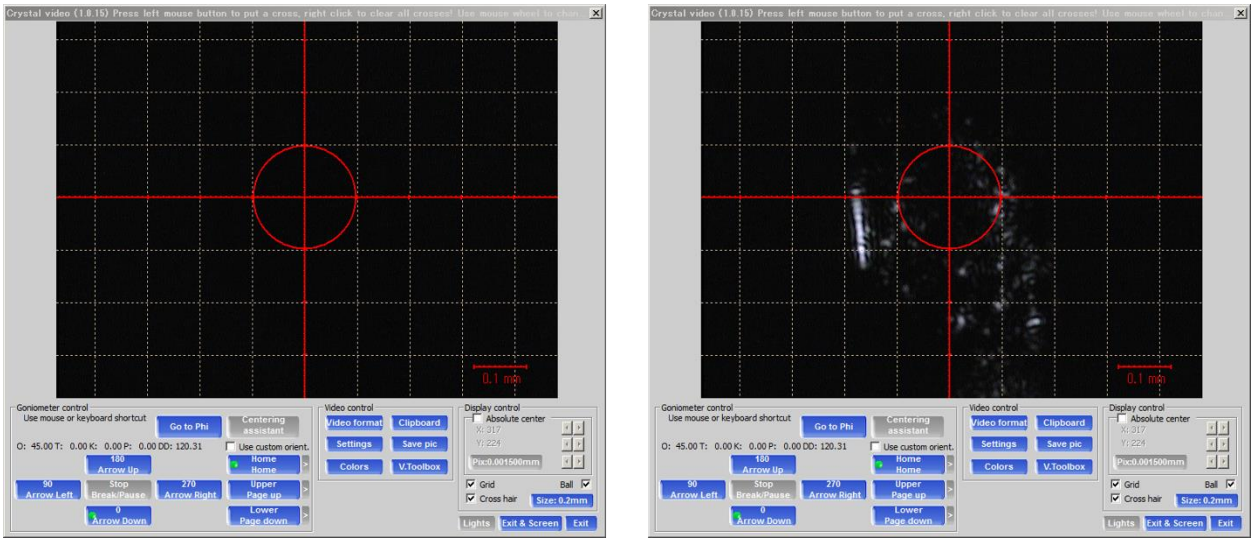

Figure 3.18 Comparison of images of the single crystal $1(AsF_6)_3$ before (left) and after (right) 1340 nm irradiation. A distinct diffraction pattern can be observed on the crystal surface, indicating that the $1(AsF_6)_3$ crystal was aligned with the laser source.

Compared to the structure before irradiation, although the space group remained unchanged, significant changes were observed in the unit cell parameters. The unit cell volume doubled, the length along the c-axis increased by 1.5 times, and the angle β decreased by approximately 10 degrees (Table 3). This resulted in the generation of two isolated molecules within the unit cell due to symmetry breaking (Figure 3.19). Crystal packing analysis revealed that the light-induced hidden phase consisted of two layers, separated by varying degrees of ion displacement of the AsF_6^- ion along the *b*- and *c*-axes. This discrepancy can be directly seen in the crystal structure after irradiation (Figure 3.20).

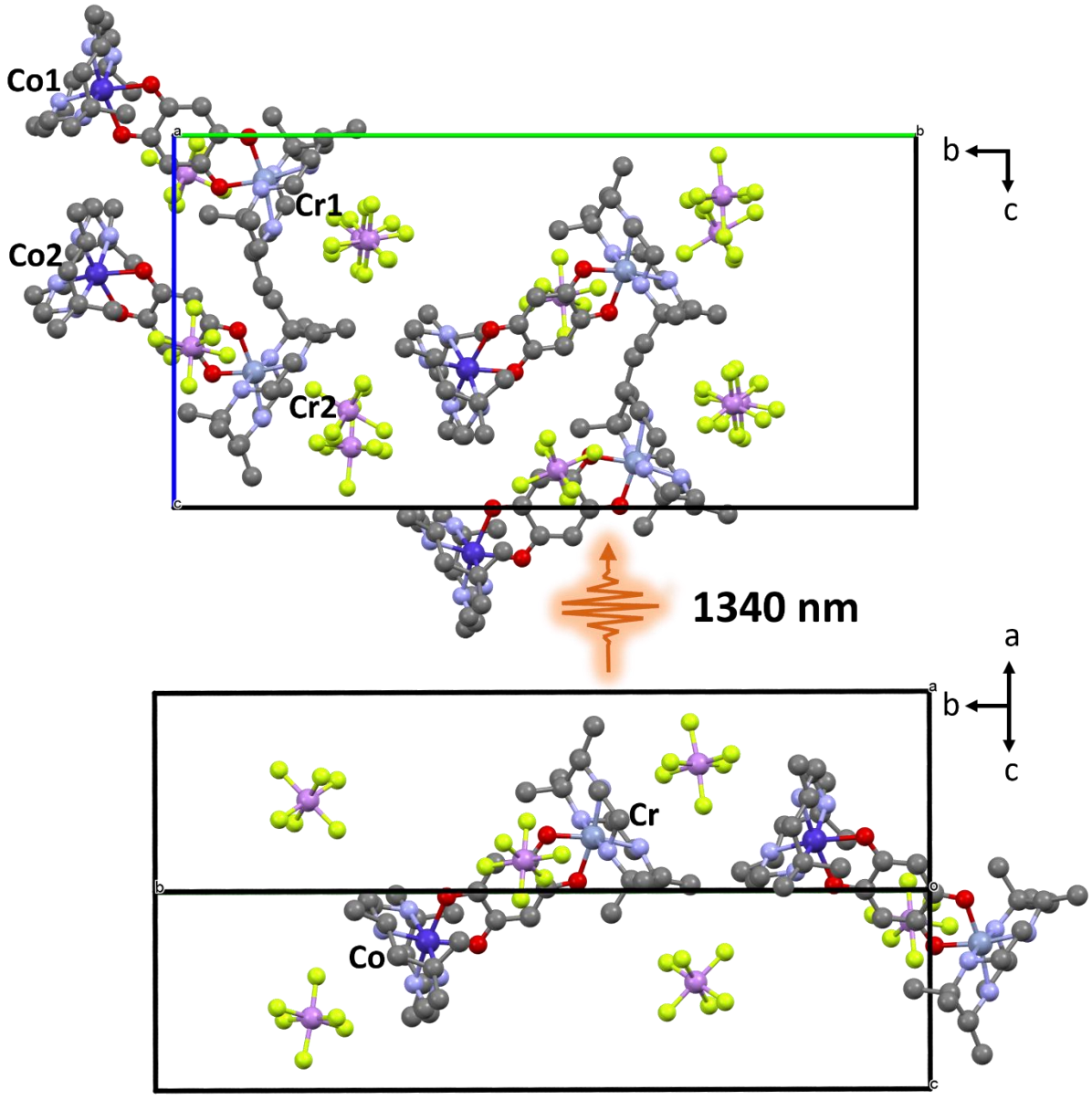

Figure 3.19 Crystal packing of $1(AsF_6)_3$ at 30 K after 1340 nm irradiation, where symmetry-breaking results in two sets of molecules, yielding four molecules per unit cell (top). Crystal packing of $1(AsF_6)_3$ at 30 K before irradiation, showing two molecules per unit cell (bottom).

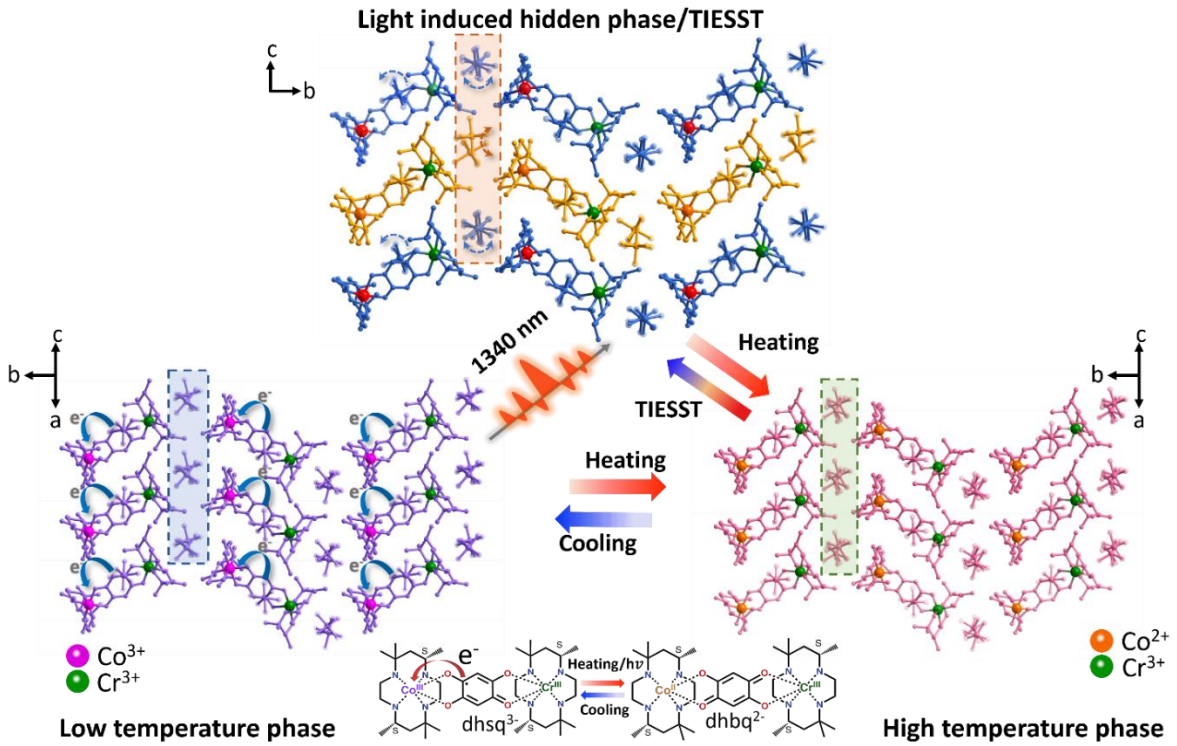

Figure 3.20 Crystal structure of $1(AsF_6)_3$ in the light-induced hidden phase or under TIESST, measured at approximately 30 K (upper). Crystal structure of $1(AsF_6)_3$ at 30 K before laser irradiation (bottom left). Crystal structure of $1(AsF_6)_3$ in the high-temperature phase (bottom right).

In comparison to the pre-irradiation packing mode, the main cation body in the hidden phase did not show significant changes. However, the AsF_6^- ion between the Co and Cr centers moved closer to cobalt along the *b*-axis, accompanied by a slight rotation in the first layer, marked in blue. The direction of the generated polarization change matched that caused by electron transfer. Additionally, two AsF_6^- ions in the intermolecular region became more overlapped due to ion displacement. In the second layer, marked in yellow, no significant changes were observed in the intramolecular AsF_6^- ions, though two other counter anions were displaced further along the *c*-axis.

The average Co/O bond lengths for the two molecules were measured at 2.125 Å and 2.107 Å,

respectively, while the Co/N bond lengths were 2.138 Å and 2.136 Å. These changes indicate that light-induced valence tautomerism occurred at the cobalt center, which is consistent with the high-spin state of cobalt observed in the high-temperature phase through magnetization studies. Therefore, the light-induced hidden phase, resulting in further enhancement of polarization change, appears to originate primarily from ion displacement. As the temperature increased to 80 K, the crystal structure reverted to an intermediate state, entering the thermally induced VT process.

Furthermore, single-crystal structure analysis under temperature-induced excited spin state trapping (TIESST) was conducted on this compound. The $1(AsF_6)_3$ complex was loaded onto the measurement platform at approximately 27 K after being quenched from ambient temperature. The quenched crystal structure exhibited a phase transition similar to the light-induced hidden phase, characterized by ion displacement. The average Co–O bond lengths for the two isolated molecules were 2.086 Å and 2.103 Å, respectively, indicating a typical high-spin state of Co(II). The difference between the partial high-spin Co(II) detected by magnetization and the full transition observed in the crystal structure can be attributed to the more thorough cooling of the single crystal compared to the bulk sample.

Although it is challenging to obtain the crystal structure at temperatures as low as 10 K after light irradiation, the excited state likely corresponds to the same state observed in the thermal process, based on the evidence from light-induced polarization change and photomagnetization. Both of these states differ from the light-induced hidden phase and the TIESST phase.

As a pyroelectric crystal sensitive to temperature variations, the crystal can generate a temporary pyroelectric current when light is switched on or off, causing a local temperature difference before thermal equilibrium is reached.[25-29] Due to the ultra-fast response of light irradiation, this behavior

holds potential for next-generation optical sensors. However, such effects are typically too small to detect because of the crystal's low pyroelectric coefficient.

For dynamic magnetic molecules with valence tautomerism, the pyroelectric coefficient becomes more sensitive and changes in response to the degree of electron transfer during the magnetic transition. By coupling these properties with a pyroelectric crystal, the light-induced pyroelectric current could be significantly enhanced.

We investigated light-induced transient pyroelectric current during the thermally induced valence tautomerism from 90 K to 200 K. The results showed a pronounced optical pyroelectric current of approximately 40 pA at 90 K when the 1340 nm laser was switched on. Once the light was switched off, thermal equilibrium was disrupted again, generating an opposite current of similar magnitude. As the proportion of electron transfer from the low-temperature (LT) phase to the high-temperature (HT) phase decreased, the light-induced pyroelectric current gradually weakened, reaching around 0.2 pA at the completion of valence tautomerism at 200 K (Figure 3.21). All these processes were reproducible over several cycles, demonstrating fast opto-electric conversion across a broad temperature range.

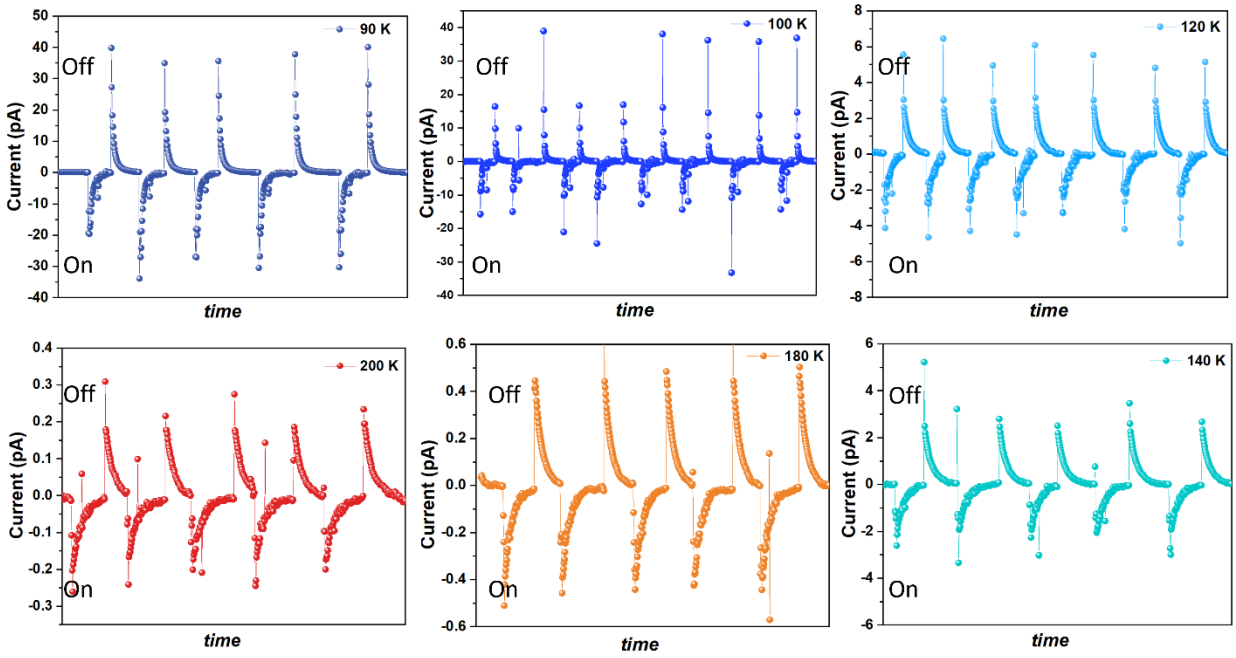

Figure 3.21 Light induced pyroelectric current of crystal $1(AsF_6)_3$ under 1340 nm laser irradiation from 90 K to 200 K where "On" represents light irradiation and "Off" represents light switch off.

3.4 Conclusion

In conclusion, we successfully synthesized a new [CrCo] dinuclear complex using an enantiopure ligand. The strategy of employing a twisted molecular structure, combined with the substitution of the counter ion with a larger one, effectively stabilized the high-spin state of the molecule and enhanced the efficiency of photomagnetization. Notably, a significant light-induced polarization change was observed, which can be attributed to the high efficiency of light-induced valence tautomerism and optimal molecular packing along the polar *b*-axis.

Interestingly, a light-induced hidden phase was detected through pyroelectric measurements and further confirmed by analyzing the crystal structure at ultralow temperatures before and after irradiation, revealing ion displacement as the key factor. This introduces a novel approach of using electric measurements to detect potential phase transitions that are not detectable through

magnetization characterization. Furthermore, this study provides an excellent example for the development of next-generation light-to-electricity harvesting materials with practical applications.

Reference

1. W.-Q. Liao, B.-B. Deng, Z.-X. Wang, T.-T. Cheng, Y.-T. Hu, S.-P. Cheng and R.-G. Xiong, Optically Induced Ferroelectric Polarization Switching in a Molecular Ferroelectric with Reversible Photoisomerization, *Advanced Science*, 2021, **8**, 2102614.
2. Y.-Y. Tang, J.-C. Liu, Y.-L. Zeng, H. Peng, X.-Q. Huang, M.-J. Yang and R.-G. Xiong, Optical Control of Polarization Switching in a Single-Component Organic Ferroelectric Crystal, *Journal of the American Chemical Society*, 2021, **143**, 13816-13823.
3. Y. Du, W.-Q. Liao, Y. Li, C.-R. Huang, T. Gan, X.-G. Chen, H.-P. Lv, X.-J. Song, R.-G. Xiong and Z.-X. Wang, A Homochiral Fulgide Organic Ferroelectric Crystal with Photoinduced Molecular Orbital Breaking, *Angewandte Chemie International Edition*, 2023, **62**, e202315189.
4. Z. Guo, K. Mao, G. Ma, G. Li, Q. Wu, J. Chen, S. S. Bao, G. Yu, S. Li, J. Zhang and X. Wu, Light-Induced Tunable Ferroelectric Polarization in Dipole-Embedded Metal–Organic Framework, *Nano Letters*, 2022, **22**, 10018-10024.
5. H. Peng, J.-C. Qi and W.-Q. Liao, Optically Controlled Polarization Switching in an Organic Ferroelectric with Light- and Temperature-Triggered Phase Transitions, *Chemistry of Materials*, 2022, **34**, 3067-3075.
6. A. Makhort, R. Gumeniuk, J.-F. Dayen, P. Dunne, U. Burkhardt, M. Viret, B. Doudin and B. Kundys, Photovoltaic-Ferroelectric Materials for the Realization of All-Optical Devices, *Advanced Optical Materials*, 2022, **10**, 2102353.
7. Y. Li, J. Fu, X. Mao, C. Chen, H. Liu, M. Gong and H. Zeng, Enhanced bulk photovoltaic effect in two-dimensional ferroelectric CuInP2S6, *Nature Communications*, 2021, **12**, 5896.
8. M. Nakamura, S. Horiuchi, F. Kagawa, N. Ogawa, T. Kurumaji, Y. Tokura and M.

Kawasaki, Shift current photovoltaic effect in a ferroelectric charge-transfer complex, *Nature Communications*, 2017, **8**, 281.

9. M. Nakamura, F. Kagawa, T. Tanigaki, H. S. Park, T. Matsuda, D. Shindo, Y. Tokura and M. Kawasaki, Spontaneous Polarization and Bulk Photovoltaic Effect Driven by Polar Discontinuity in ${\mathrm{LaFeO}}_{3}/{\mathrm{SrTiO}}_{3}$ Heterojunctions, *Physical Review Letters*, 2016, **116**, 156801.
10. M. Sotome, M. Nakamura, J. Fujioka, M. Ogino, Y. Kaneko, T. Morimoto, Y. Zhang, M. Kawasaki, N. Nagaosa, Y. Tokura and N. Ogawa, Spectral dynamics of shift current in ferroelectric semiconductor SbSI, *Proceedings of the National Academy of Sciences*, 2019, **116**, 1929-1933.
11. S.-J. Gong, F. Zheng and A. M. Rappe, Phonon Influence on Bulk Photovoltaic Effect in the Ferroelectric Semiconductor GeTe, *Physical Review Letters*, 2018, **121**, 017402.
12. O. Sato, Dynamic molecular crystals with switchable physical properties, *Nature Chemistry*, 2016, **8**, 644-656.
13. X. Zhang, W.-H. Xu, W. Zheng, S.-Q. Su, Y.-B. Huang, Q. Shui, T. Ji, M. Uematsu, Q. Chen, M. Tokunaga, K. Gao, A. Okazawa, S. Kanegawa, S.-Q. Wu and O. Sato, Magnetoelectricity Enhanced by Electron Redistribution in a Spin Crossover [FeCo] Complex, *Journal of the American Chemical Society*, 2023, **145**, 15647-15651.
14. W.-H. Xu, Y.-B. Huang, W.-W. Zheng, S.-Q. Su, S. Kanegawa, S.-Q. Wu and O. Sato, Photo-induced valence tautomerism and polarization switching in mononuclear cobalt complexes with an enantiopure chiral ligand, *Dalton Transactions*, 2024, DOI: 10.1039/D3DT03915C.
15. S.-Q. Wu, M. Liu, K. Gao, S. Kanegawa, Y. Horie, G. Aoyama, H. Okajima, A. Sakamoto, M. L. Baker, M. S. Huzan, P. Bencok, T. Abe, Y. Shiota, K. Yoshizawa, W. Xu, H.-Z. Kou and O. Sato, Macroscopic Polarization Change via Electron Transfer in a Valence Tautomeric Cobalt Complex, *Nature Communications*, 2020, **11**, 1992.

16. S.-Q. Su, S.-Q. Wu, S. Kanegawa, K. Yamamoto and O. Sato, Control of electronic polarization via charge ordering and electron transfer: electronic ferroelectrics and electronic pyroelectrics, *Chemical Science*, 2023, **14**, 10631-10643.

17. S.-Q. Su, S.-Q. Wu, Y.-B. Huang, W.-H. Xu, K.-G. Gao, A. Okazawa, H. Okajima, A. Sakamoto, S. Kanegawa and O. Sato, Photoinduced Persistent Polarization Change in a Spin Transition Crystal, *Angewandte Chemie International Edition*, 2022, **61**, e202208771.

18. P. Sadhukhan, S.-Q. Wu, J. I. Long, T. Nakanishi, S. Kanegawa, K. Gao, K. Yamamoto, H. Okajima, A. Sakamoto, M. L. Baker, T. Kroll, D. Sokaras, A. Okazawa, N. Kojima, Y. Shiota, K. Yoshizawa and O. Sato, Manipulating electron redistribution to achieve electronic pyroelectricity in molecular [FeCo] crystals, *Nature Communications*, 2021, **12**, 4836.

19. Y.-B. Huang, J.-Q. Li, W.-H. Xu, W. Zheng, X. Zhang, K.-G. Gao, T. Ji, T. Ikeda, T. Nakanishi, S. Kanegawa, S.-Q. Wu, S.-Q. Su and O. Sato, Electrically Detectable Photoinduced Polarization Switching in a Molecular Prussian Blue Analogue, *Journal of the American Chemical Society*, 2024, **146**, 201-209.

20. F. Cheng, S. Wu, W. Zheng, S. Su, T. Nakanishi, W. Xu, P. Sadhukhan, H. Sejima, S. Ikenaga, K. Yamamoto, K. Gao, S. Kanegawa and O. Sato, Macroscopic Polarization Change of Mononuclear Valence Tautomeric Cobalt Complexes Through the Use of Enantiopure Ligand, *Chemistry – A European Journal*, **n/a**, e202202161.

21. W. Zheng, X. Zhang, Q. Shui, T. Fukuyama, W.-h. Xu, Y.-b. Huang, T. Ji, Z. Zhou, M. Uematsu and S.-Q. Su, Solvent-dependent valence tautomerism and polarization switching in a heterodinuclear [CrCo] complex, *Inorganic Chemistry Frontiers*, 2024.

22. Z. Zhou, S.-Q. Wu, Q. Shui, W.-W. Zheng, A. Maeda, X. Zhang, J. Chu, S. Kanegawa, S. Su and O. Sato, A Solvent Free Neutral Cobalt Complex Exhibiting Macroscopic Polarization Switching Induced by Directional Charge Transfer, *Inorganic Chemistry Frontiers*, 2024, DOI: 10.1039/D4QI01389A.

23. P. Sadhukhan, S.-Q. Wu, S. Kanegawa, S.-Q. Su, X. Zhang, T. Nakanishi, J. I. Long, K. Gao, R. Shimada, H. Okajima, A. Sakamoto, J. G. Chiappella, M. S. Huzan, T. Kroll, D. Sokaras, M. L. Baker and O. Sato, Energy conversion and storage via photoinduced polarization change in non-ferroelectric molecular [CoGa] crystals, *Nature Communications*, 2023, **14**, 3394.

24. J.-F. Létard, P. Guionneau, O. Nguyen, J. S. Costa, S. Marcén, G. Chastanet, M. Marchivie and L. Goux-Capes, A Guideline to the Design of Molecular-Based Materials with Long-Lived Photomagnetic Lifetimes, *Chemistry – A European Journal*, 2005, **11**, 4582-4589.

25. X. Zeng, F. Li, Y. Liu, Y. Ma, Y. Chen, Y. Zhou, P. Zhu, H. Zhang, J. Luo and Z. Sun, Unprecedented Silver-Based Hybrid Pyroelectric Enabling Wide Spectral Photo-Pyroelectricity for Birefringence Photomodulation, *Angewandte Chemie*, e202411875.

26. M. Patel, H.-H. Park, P. Bhatnagar, N. Kumar, J. Lee and J. Kim, Transparent integrated pyroelectric-photovoltaic structure for photo-thermo hybrid power generation, *Nature Communications*, 2024, **15**, 3466.

27. Y. Lu, L. Liu, R. Gao, Y. Xiong, P. Sun, Z. Wu, K. Wu, T. Yu, K. Zhang, C. Zhang, T. Bourouina, X. Li and X. Liu, Ultrafast near-infrared pyroelectric detector based on inhomogeneous plasmonic metasurface, *Light: Science & Applications*, 2024, **13**, 241.

28. Y. Wang, H. Ye, P. Wang, Z. Wu, Q. Guan, C. Zhang, H. Li, S. Chen and J. Luo, Durable Photo-Pyroelectric Detection in a Diamine-Constructed Lead-Free Hybrid Perovskite Ferroelectric, *Advanced Materials*, **n/a**, 2409245.

29. Q. Guan, Z.-K. Zhu, H. Ye, C. Zhang, H. Li, C. Ji, X. Liu and J. Luo, Pyro-Phototronic Effect Induced Circularly Polarized Light Detection with a Broadband Response, *Advanced Science*, 2024, **11**, 2404403.

Chapter 4 Ultrafast Polarization Inversion Induced by Different Wavelengths on Delocalized Fe2 Complex.

4.1 Introduction

The continuous demand for faster and more energy-efficient memory and data storage technologies has driven significant research into novel materials with unique electronic, optical, and magnetic properties. Among these, light-induced polarization inversion has garnered increasing attention due to its potential for next-generation optical memory devices.[1-12] In this context, the exploration of materials capable of achieving ultrafast polarization inversion is critical for enabling rapid data storage and retrieval processes.

Mixed-valence complexes, where metal ions coexist in different oxidation states, offer a fascinating avenue of study. These complexes exhibit unusual electronic, optical, and magnetic properties due to the interplay between localized or delocalized electrons.[13-23] Electron transfer between metal ions in different oxidation states can significantly influence a material's behavior, including its response to external electric and magnetic fields. In particular, delocalized mixed-valence dinuclear complexes provide an ideal platform for investigating ultrafast polarization inversion, as their ability to facilitate charge transfer between metal centers is key to generating rapid and reversible polarization changes.

Recent studies have demonstrated that magnetoelectric (ME) coupling in mixed-valence complexes is especially intriguing due to the possibility of controlling their electronic and magnetic states via external stimuli, such as electric fields.[24-28] The intricate interactions between localized or itinerant electrons in the mixed-valence states lead to novel forms of ME coupling, distinct from those found in conventional multiferroic materials. However, thus far, light-induced polarization inversion in mixed-valence complexes remains at the level of theoretical prediction.

It has been suggested that applying light to delocalized mixed-valence systems could induce rapid polarization inversion, offering ultrafast switching speeds ideal for high-performance optical memory applications.

The challenge lies in achieving precise control over the electronic states and dynamic processes governing charge transfer and polarization changes. While metal-to-metal charge transfer at the molecular level can alter the dipole moment, it is essential to achieve a polar crystal structure to realize macroscopic polarization switching. The ultrafast response of these systems to light stimulation not only paves the way for advanced memory devices but also provides deeper insights into the fundamental mechanisms of light-matter interaction in complex materials.

In this work, we focus on a dinuclear mixed-valence complex that exists between Robin-Day Class II and III, exhibiting ultrafast polarization inversion under excitation by lasers with different wavelengths. The intrinsic asymmetry of enantiopure ligands promotes packing of the molecule into a polar space group. This molecular asymmetry, along with hydrogen bonding between solvent molecules, counterions, and the ligand, plays a crucial role in modulating the electronic configuration of the two metal centers, leading to different electron transfer processes. By combining these features—dynamic mixed-valence behavior and a polar crystal structure—we aim to achieve light-induced polarization inversion.

4.2 Experimental section

4.2.1 Starting materials and synthesis

All reagents were commercially purchased by Tokyo Chemical Industry Co., Ltd., FUJIFILM Wako, Pure Chemical Corporation, and Sigma-Aldrich Company, and directly used without further purification. 5,5,7,12,12,14-hexamethyl-1,4,8,11-tetraazacyclotetradecane (*Rac*-cth) and its

enantiopure chiral ligand (*SS*-cth) were synthesized as shown in detail in *Chapter 2* under *2.2.1*. Dinuclear [FeFe] complexes with enantiopure (*SS*-cth or *RR*-cth) and racemic ligands (*Rac*-cth) (cth = 5,5,7,12,12,14-hexamethyl-1,4,8,11-tetraazacyclotetradecane) were synthesized separately using the previously reported methods. The mononuclear precursor, $[Fe(AcO)L]PF_6$ (L = *Rac*-cth or *SS*-cth or *RR*-cth), was added into the methanol solution of dhbq (neutralized by trimethylamine) with the molar ratio of 2:1. The resulting solution was further oxidized by $AgPF_6$. It is noted that the crystallization of dinuclear [(Fe(*Rac*-cth))(μ-dhbq)(Fe(*Rac*-cth))] $(PF_6)_3$ and [(Fe(*RR*-cth))(μ-dhbq)(Fe(*RR*-cth))]$(PF_6)_3$ adopts different method. The former was prepared by dissolving it in a MeOH/H_2O mixture (1:1 ratio), adding a few drops of MeCN, and then allowing it to evaporate under nitrogen, resulting in dark-green plate crystals. In contrast, the latter was dissolved in a MeOH/H_2O mixture (2:1 ratio) and exposed to flowing nitrogen, yielding dark-green stick crystals.

[Fe(AcO)(L)]PF_6. $Fe(AcO)_2$ (521 mg, 3.3 mmol) and L (850 mg, 3.0 mmol) were added into ethanol (10 ml). The solution was then heated to 70°C and stirred until it became brown and transparent. Following this, NH_4PF_6 (3.3 mmol, 540 mg) was added, resulting in the gradual precipitation of a white solid ($[Fe(AcO)L]PF_6$). Precipitation was accelerated by cooling the solution in an ice bath for 15 minutes. The solid was then filtered, washed with cold ethanol and diethyl ether, yielding 980 mg of the product.

[(Fe(*Rac*-cth))(μ-dhbq)(Fe(*Rac*-cth))] $(PF_6)_2$. 2,5-Dihydroxy-1,4-benzoquinone (H_2dhbq, 1 mmol, 140 mg) and triethylamine (2 mmol, 280 µL) were mixed in 50 mL of methanol (MeOH) under a nitrogen (N_2) atmosphere. $[Fe(AcO)(Rac\text{-}cth)]PF_6$ (2 mmol, 1089 mg) was then added, and the mixture was stirred at 60°C for 30 minutes. Afterward, 30 mL of an aqueous KPF_6 solution (1.5 mmol, 276 mg) was added to the dark solution. The hot mixture was allowed to cool slowly

to room temperature and left overnight. The dark grey precipitate of (Fe(Rac-cth))(μ-dhbq)(Fe(Rac-cth))$_2$ was filtered and washed with water, yielding 1095 mg of product (87%).

[(Fe(*Rac*-cth))(*μ*-dhbq)(Fe(*Rac*-cth))] (PF_6)$_3$. (Fe(Rac-cth))(μ-dhbq)(Fe(Rac-cth))$_2$ (1 mmol, 1109 mg) was dissolved in 50 mL of methanol (MeOH). An aqueous solution of $AgPF_6$ (1 mmol, 252 mg) was then added to the mixture. After stirring at room temperature for 30 minutes, the solution was filtered multiple times to remove residual silver. The solvent was gradually evaporated until the crude product, (Fe(Rac-cth))(μ-dhbq)(Fe(Rac-cth))$_3$, precipitated as a dark green solid. This solid was filtered and washed with diethyl ether. For recrystallization, the crude product was dissolved in a 1:1 mixture of methanol and water, with a few drops of acetonitrile added. The solution was left to evaporate slowly under a nitrogen atmosphere over several days, resulting in the formation of dark green plate-like crystals.

[(Fe(*RR*-cth))(*μ*-dhbq)(Fe(*RR*-cth))] (PF_6)$_3$. The crude product of (Fe(RR-cth))(μ-dhbq)(Fe(RR-cth))$_3$ was synthesized using the same method as (Fe(Rac-cth))(μ-dhbq)(Fe(Rac-cth))$_3$, but with the enantiopure ligand (RR-cth). Recrystallization of the target complex was carried out in a mixed solvent of MeOH/H_2O (2:1) under a nitrogen (N_2) atmosphere, yielding dark green stick-shaped crystals.

[(Fe(*SS*-cth))(DCBQ)(Fe(*SS*-cth))](PF_6)$_3$. The crude product of (Fe(SS-cth))(DCBQ)(Fe(SS-cth))$_3$ was synthesized using the same method as (Fe(RR-cth))(μ-dhbq)(Fe(RR-cth))$_3$, with chloranilic acid as the bridging ligand and SS-cth. Recrystallization of the target complex was achieved in a mixed solvent of MeOH/H_2O (2:1) under a nitrogen atmosphere, yielding dark-green stick crystals.

4.2.2 Physical measurement

X-ray diffraction measurement and crystal structural determinations. Diffraction data were collected between 100 and 265 K for $1(AsF_6)_3$ under a nitrogen gas stream. The measurement was performed on a Rigaku XtaLab Synergy-R/DW diffractometer equipped with a HyPix-6000 area detector and multi-layer mirror monochromated Mo-Kα radiation of λ= 0.71073 Å. The structures were solved by a direct method and refined via full-matrix least-squares on F^2 using the SHELX program[4] implemented in the OLEX2 program[5] with anisotropic thermal parameters for all non-hydrogen atoms. The hydrogen atoms were geometrically added and refined by the riding model. The ultralow temperature data at 30 K were collected with helium gas stream at Institute for Molecular Science with Rigaku Hypix-AFCdiffractometer equipped with a Hypix-6000 area detector and multi-layer mirror monochromated Mo-Kα radiation of λ= 0.71073 Å.

Table 1. Crystallographic Data Collection and Structural Refinement Information for three dimer Fe.

	[(Fe(*RR*-cth))(*μ*-dhbq)(Fe(*RR*-cth))] $(PF_6)_3$			**[(Fe(*Rac*-cth))(*μ*-dhbq)(Fe(*Rac*-cth))] $(PF_6)_3$**	**[(Fe(SS-cth))(DCBQ)(Fe(SS-cth))] $(PF_6)_3$**	
Empirical formula	C39H80Fe2F18N8O4P3			C19F9FeN4O2P1.5	C40H76Cl2F18Fe2N7O7P3	
Formula weight	1299.692			589.54	1379.587	
Temperature(K)	30	100	265	100	30	100
Crystal system	*monoclinic*	*monoclinic*	*monoclinic*	*monoclinic*	*monoclinic*	*monoclinic*
Lattice Tape	Primitive	Primitive	Primitive	Primitive	Primitive	Primitive

Space group	$P2_1$(#4)	$P2_1$(#4)	$P2_1$(#4)	$P2_1$/c(#14)	$P2_1$(#4)	$P2_1$(#4)
a (Å)	9.2450(4)	9.33011(15)	9.4031(3)	8.9430(3)	9.4059(2)	9.4816(3)
b (Å)	18.7449(9)	18.8759(3)	18.8763(8)	30.8590(9)	18.6308(6)	18.7282(6)
c (Å)	16.0847(7)	16.1790(3)	16.2668(5)	10.3269(4)	16.4848(4)	16.5658(5)
α (deg.)	90	90	90	90	90	90
β (deg.)	90.441(4)	89.9946(14)	90.321(3)	110.740(4)	93.866(6)	93.989(3)
γ (deg.)	90	90	90	90	90	90
V (Å^3)	2787.3(2)	2849.36.(8)	2887.24(18)	2665.25(17)	2882.21(13)	2934.51(15)
Z value	2	2	2	4	2	2
D_{calc}(g/cm^3)	1.549	1.516	1.483	1.469	1.590	1.568
Light source	MoKα (λ = 0.71073 Å)					
R_1(I>2.00s(I)	0.049	0.0346	0.048	0.0673	0.0448	0.0367
wR_2(*all*)	0.1324	0.0958	0.1374	0.2118	0.1238	0.0969
GOF	1.027	1.029	1.019	1.044	1.024	1.036
Flack parameter	0.005(9)	0.010(3)	0.011(10)		0.003(10)	0.000(10)
CCDC						

[a]$R_1 = \Sigma||F_o| - |F_c||/\Sigma|F_o|$. [b]$wR_2 = [\Sigma\{w(F_o^2 - F_c^2)^2/\Sigma\{w(F_o^2)\}^2]^{1/2}$

Table 2 Selective bond lengths for FeRR-DHBQ-FeRR and FeRac-DHBQ-FeRac at 100 K.

[(Fe(*RR*-cth))(μ-dhbq)(Fe(*RR*-cth))] $(PF_6)_3$ 100 K			[(Fe(*Rac*-cth))(μ-dhbq)(Fe(*Rac*-cth))] $(PF_6)_3$ 100 K		
Bond length	Fe1	Fe2	Bond length	Fe1	Fe2
Fe-O (Å)	1.966	1.961	Fe-O (Å)	1.978	1.978
	1.974	1.981		1.979	1.979
Fe-N (Å)	2.198	2.215	Fe-N (Å)	2.170	2.170
	2.141	2.136		2.134	2.134
	2.143	2.122		2.147	2.147

	2.171	2.205		2.174	2.174

Table 3 Selective bond lengths for FeSS-DCBQ-FeSS at 100 K.

[(Fe(*SS*-cth))(μ-dhbq)(Fe(*SS*-cth))] $(PF_6)_3$ 100 K		
Bond length	Fe1	Fe2
Fe-O (Å)	1.963	1.987
	2.007	1.986
Fe-N (Å)	2.175	2.189
	2.137	2.122
	2.199	2.216
	2.146	2.136

Magnetization measurement. Magnetic measurements were performed using a Quantum Design SQUID magnetometer (MPMS-3). Polycrystalline samples (~15 mg) were fixed in gelatin capsules using eicosane (~5 mg) to secure them. The prepared capsules were then placed inside plastic straws and mounted onto the sample holder. Measurements for all samples were conducted in a magnetic field of 1000 Oe, with a temperature sweep rate of 2 K min^{-1}. Diamagnetic corrections were applied by calculating Pascal's constants following the methodology outlined in J. Chem. Educ. 2008, 85, 4, 532.

IR spectroscopy. Temperature-dependent IR spectra were collected employing an FT/IR spectrophotometer (*Jasco* 600Plus) equipped with a closed-cycle helium refrigerator cryostat (Rockgate Corporation) in the range of 7800 - 400 cm^{-1}. The ground-powder samples were sandwiched between grained and flat CaF_2 plates.

UV-vis spectroscopy. Temperature-dependent UV-vis were recorded employing a SHIMADZU MPC-3100 equipped with a closed-cycle helium refrigerator cryostat (Rockgate Corporation) in the range of 300 - 3000 nm. The ground-powder samples were uniformly attached to the tapes and then held between flat CaF_2 plates.

Inelastic Neutron Scattering (INS) Experiments: INS experiments were conducted at the Institut Laue-Langevin (ILL) in France, using the direct geometry time-of-flight (dg-TOF) spectrometer IN5 and the backscattering-and-time-of-flight spectrometer IN16b, and at the Spallation Neutron Source at Oak Ridge National Laboratory (ORNL) in the USA, using the dg-TOF spectrometer SEQUOIA. Approximately 1 g of polycrystalline sample, contained in annular aluminum cylinders, was used for all experiments. The relative efficiencies of the neutron detectors were normalized using a vanadium sample. Data reduction and manipulation were performed using the Mantid software suite.

For the IN5 spectra, a combination of Gaussian functions was used to model each peak, along with a polynomial background. The fitting was performed using a χ^2-method, and the excitation energies were extracted as the best-fit values of the Gaussian means. When fitting the anisotropy part of the Hamiltonian models (eq. (1)) to the extracted excitation energies, we employed Easy spin to construct the Hamiltonians and a χ^2-method to fit the parameters. The INS spectra of models that best fit the eigenvalues were simulated using mint.

At IN5, incident neutron energies (Ei) of 1.94 and 3.47 meV were used, with chopper settings that resulted in energy resolutions (FWHM) at zero energy transfer of 39 μeV and 90 μeV for Ei = 1.94 and 3.47 meV, respectively. An ILL orange cryostat cooled the sample to temperatures between 1.5 K and 50 K. Data were collected for 1 hour at Ei = 1.94 meV and for 1.5 hours at Ei = 3.47 meV, regardless of temperature. The ILL reactor operated at reduced power (27 MW), leading to

a lower neutron flux.

For the SEQUOIA experiment, Ei values of 35 and 100 meV were used, with a closed-cycle refrigerator cooling the samples to 5 K.

At IN16b, the instrument was operated in BATS mode with Si111 backscattering analyzers, corresponding to Ef = 2.08 meV, and covered a Q-range of 0.2–1.8 $Å^{-1}$. The 14° slit in the pulse chopper, spinning at 315 Hz, was used for increased flux at a relaxed resolution of 5.6 μeV. To increase the dynamic range, several acquisitions were combined, with energy transfer ranges centered at −380 μeV, −150 μeV, and +150 μeV, respectively, and a counting time of 3 hours per acquisition. During these measurements, the reactor was running at 44 MW.

High-Frequency EPR (HF EPR) Experiments: HF EPR experiments were conducted at the French Laboratory for High Magnetic Fields, Institut Néel in Grenoble, France. The samples were finely ground, pressed into pellets (to minimize torquing effects, with a thickness of approximately 3 mm), wrapped in Teflon tape, and placed in helium exchange gas inside a superconducting solenoid (T = 8–18 K, B = 0–15.8 T). Measurements were carried out using a custom-built multi-frequency spectrometer in a double-pass configuration, operating in transmission mode. Two frequency sources equipped with multipliers provided the radiation: one with a fixed frequency of 110.4 GHz and the other at 127.68 GHz, both tunable within ±10 GHz.

Unlike commercial EPR spectrometers, the custom-built setup operates without an optical cavity, resulting in uncontrolled phase changes in the microwave radiation due to the applied magnetic field, which can reverse the sign of the measured spectrum during a sweep. Additionally, it is well-known in custom EPR setups that transitions at low magnetic fields can be less intense in simulated spectra compared to experimental data. The HF EPR data were modeled using Easyspin.

X-band EPR Experiments: X-band EPR spectra were recorded using a Bruker EMX+ spectrometer at the EPSRC National Research Facility for Electron Paramagnetic Resonance Spectroscopy at the Photon Science Institute, University of Manchester, UK. Polycrystalline samples (mg scale) were ground into eicosane to immobilize them and prevent field-induced orientation effects. The spectrometer was operated with the following parameters: $\nu = 9.375$ GHz microwave radiation, 2.2 mW power, 20 dB attenuation, 0.2 mT modulation amplitude, and 100 kHz modulation frequency. A closed-cycle refrigerator cooled the samples to temperatures as low as 5 K.

Far-Infrared Magneto-Spectroscopy (FIRMS): The FIRMS experiments were conducted at the French Laboratory for High Magnetic Fields, Institute Néel in Grenoble, France. Non-polarized radiation was generated by a mercury lamp, and a Bruker Vertex 80v Fourier-transform spectrometer was used to analyze the radiation. Light-pipe optics delivered the radiation to the sample, which was placed inside a superconducting solenoid (0–16 T) immersed in liquid helium at a temperature of 4.2 K.

To ensure adequate infrared transmission through the samples, they were ground into fine powders, diluted in eicosane, and pressed into pellets. After testing several configurations, the most intense signal was achieved with a sample-to-eicosane ratio of 1:20 and pellet thickness of approximately 2 mm. The experiment was conducted in a Faraday configuration ($k \parallel B$), and a composite bolometer, positioned below the sample, detected the transmitted light. Spectra were collected in 0.25 T increments between 0 and 16 T.

Data were processed using Field-Optic. Field-dependent spectra of a pure eicosane pellet (≈0.5 mm thick) were used to account for both the eicosane contribution to the sample spectrum and the

magnetic field dependence of the bolometer's sensitivity. Field normalization was performed using the differential average option in Field-Optic, with a symmetric averaging range of ±3.75 T. To correct for a sloping baseline in the field direction of the spectrum, a linear function was fitted to the central portion of the spectrum (14–24.5 meV) and subtracted from all spectra.

4.3 Result and Discussion

Thermogravimetric analysis (TGA) of [FeRac-DHBQ-FeRac]PF_6 (denoted as 2^H) was conducted to determine the proportion of solvent molecules present. The TGA results for 2H showed no significant change in sample weight up to 550 K, indicating that no solvent was contained within the crystal lattice (Figure 4.1). Beyond this temperature, the sample began to decompose, with a sharp decrease in weight observed.

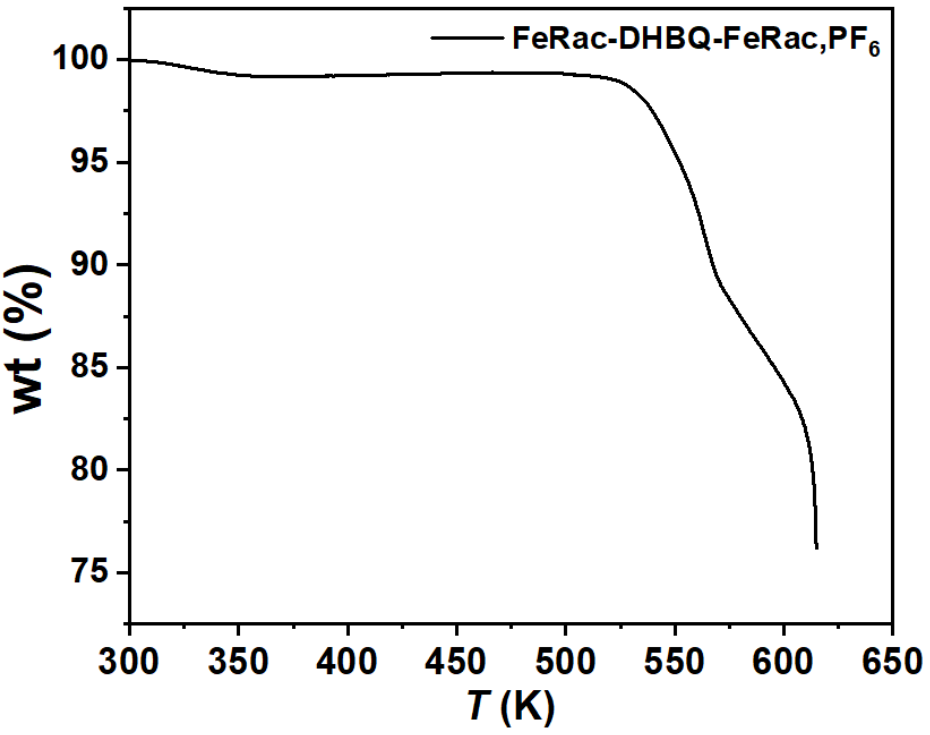

Figure 4.1 The weight loss of 2^H as a function of temperature was plotted, showing a slight decrease from 300 to 35 K, likely due to surface absorption from the ambient environment. However, the

overall weight remained above 99%, indicating that no solvent was present in the compound.

Elemental analysis of the FeRR-DHBQ-FeRR complex (denoted as 1^{H}) and the 2^{H} crystal sample was conducted to confirm their purity. The results for both samples showed good agreement between the experimental data and the simulated values, as presented in Table 2, with acceptable error margins. The analysis suggests that 1^{H} contains one H_2O molecule and MeOH, while 2^{H} contains no solvent and both showed good uniformity.

Table 4. Elemental analysis of C, H, N on 1^{H} and 2^{H}.

		H%	C%	N%
FeRR-DHBQ-FeRR,$PF_6 \cdot H_2O \cdot$MeOH	Exp.	6.2	35.6	8.56
	Sim.	6.13	35.88	8.589
FeRac-DHBQ-FeRac,$PF_6 \cdot H_2O \cdot$MeOH	Exp.	6.03	36.47	8.89
	Sim.	5.9	36.36	8.93

The purification of [FeSS-DCBQ-FeSS](PF_6) (denoted as 1^{Cl}) was confirmed by powder X-ray diffraction conducted between 5 and 30 degrees at room temperature. The overall characteristic peaks, particularly those below 20 degrees, align well with the simulated pattern at 105 K (Figure 4.2). Since this sample did not exhibit any phase transition related to temperature-dependent crystal structure, the slight intensity differences observed between 11° and 15° are likely due to thermal vibrations of the crystal lattice.

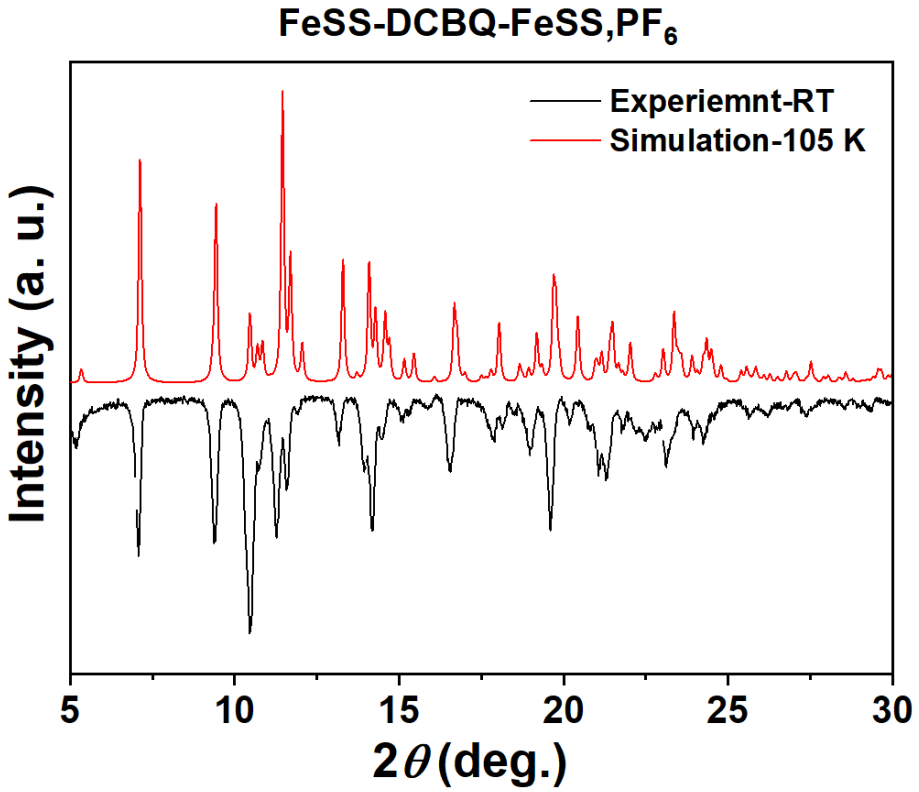

Figure 4.2 Powder X-ray diffraction patterns of 1^{Cl} between experimental result at room temperature and simulation at 105 K.

The crystal structure of 2^{H} exhibits molecular symmetry, where the entire molecule can be generated by an inversion symmetry operation along the center of the dhbq ligand. Each Fe center is coordinated with four nitrogen atoms from the cth ligand and two oxygen atoms from the dhbq ligand, forming an octahedral geometry. The molecule is packed in the nonpolar $P2_1/c$ space group, without the inclusion of solvent molecules (Figure 4.3a). The average Fe-O and Fe-N bond lengths at 100 K are 1.978 Å and 2.156 Å, respectively, indicative of intermediate high-spin Fe(II) and Fe(III) under similar coordination environments (Table 2).

In contrast, 1^{H} and 1^{Cl} share a similar structure, where two mononuclear Fe centers are bridged by DHBQ and DCBQ ligands, respectively. Interestingly, due to the use of the enantiopure cth ligand,

the dinuclear Fe complex with this ligand exhibits lower symmetry. The chiral cth ligands on either side of the bridging ligand form a distorted mirror symmetry with a 90° rotation (Figure 4.3b,c). Additionally, PF_6^- and H_2O form hydrogen bonds with the enantiopure cth ligands, which is expected to influence the electronic configuration of the two Fe centers. This symmetry breaking leads to the molecules packing in a polar $P2_1$ space group. Despite its low molecular symmetry, the average bond length of Fe-O/Fe-N on 1^H showed similar value where Fe1-O/Fe1-N is 1.97 Å and 2.163 Å while Fe2-O/Fe2-N 1.971 Å and 2.169 (Table 2). Similarly, in 1^{Cl}, the average Fe-O and Fe-N bond lengths are 1.985 Å and 2.164 Å for Fe1, and 1.986 Å and 2.166 Å for Fe2 (Table 3). Even when the crystals of 1^H and 1^{Cl} were cooled to 30 K, the average bond lengths around the two Fe centers could not clearly distinguish between the oxidation states of the Fe atoms (1^H: Fe1-O/Fe1-N: 1.970 Å, 2.163 Å; Fe2-O/Fe2-N: 1.973 Å, 2.170 Å. 1^{Cl}: Fe1-O/Fe1-N: 1.977 Å, 2.160 Å; Fe2-O/Fe2-N: 1.985 Å, 2.160 Å). These values suggest that all three compounds share a similar electronic configuration at the two Fe centers, making it difficult to precisely determine the oxidation states of Fe as either Fe^{2+} or Fe^{3+} based solely on the current crystal structure.

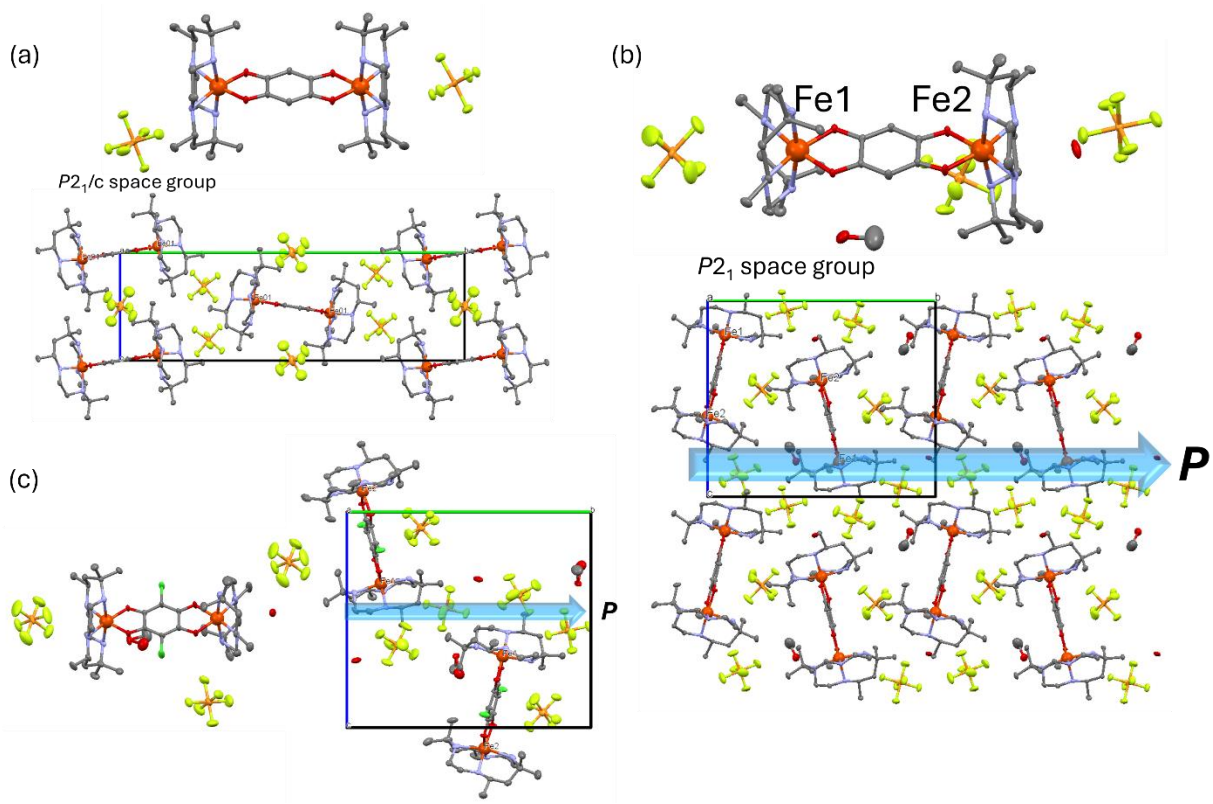

Figure 4.3 Crystal structure and packing at 100 K of 2^{H} (a), 1^{H} (b), and 1^{Cl} (c), where polarization of 1^{H} and 1^{Cl} along *b*-axis.

To further investigate the electronic configurations of the three compounds, UV-vis and IR spectra were measured using pelletized samples and CaF_2. The IR spectrum of the 1H pellet was measured at room temperature (RT). Notably, both characteristic absorption bands corresponding to $dhbq^{2-}$ at 1470 cm^{-1} and $dhbq^{3-}$ at 1540 cm^{-1} were faint compared to the low-temperature phase of CoCo (where $dhbq^{3-}$ is generated at 1470 cm^{-1} after electron transfer from Co to $dhbq^{2-}$) and the high-temperature phase of CoZn (showing a strong peak for $dhbq^{2-}$ at 1540 cm^{-1}) after normalization with PF_6^- (Figure 4.4). This suggests that the electron does not localize exclusively at either the metal center or the bridging ligand, implying that the possible combined states, such as Fe^{2+}-$dhbq^{2-}$-Fe^{3+}/Fe^{3+}-$dhbq^{3-}$-Fe^{3+}/Fe^{3+}-$dhbq^{2-}$-Fe^{2+}, cannot be distinguished on the time scale of IR measurements. Interestingly, a series of absorption bands in the near-infrared region (a very low-energy region) were observed, which can be attributed to intervalence charge transfer (IVCT) and

metal-metal charge transfer (MMCT). When the pellet sample was immersed in liquid nitrogen and thoroughly cooled, the spectrum remained unchanged for the bands associated with the bridging ligand. However, the absorption bands above 4500 cm^{-1} became sharper, and an additional weak peak appeared at 6336 cm^{-1} (Figure 4.5). It is noteworthy that the half-width of the bands observed in the NIR region is approximately 200 cm^{-1}, with a sharper cut-off towards higher energy. This behavior is markedly different from that of previously reported delocalized mixed-valence complexes. Generally, in mixed-valence dinuclear complexes, the two metal centers can be coupled electronically, leading to delocalization of the charge between the two sites. If the coupling between the metal centers is strong, the charge transfer occurs more smoothly, resulting in a sharp and well-defined absorption band. This type of intervalence charge transfer (IVCT) involves the movement of an electron between the metal centers. Strong coupling reduces fluctuations in the energy levels, leading to a narrower band because there is less variation in the energies associated with the transition. The temperature-dependent IR spectrum of 1H further supports this process, as the characteristic peaks become more intense, and an additional peak appears in the near-IR region (Figure 4.6). This distinctive behavior in the IR spectrum of 1^{H} can be attributed to its delocalized mixed-valence nature. However, the underlying mechanism causing the sharpening of the absorption bands remains unclear.

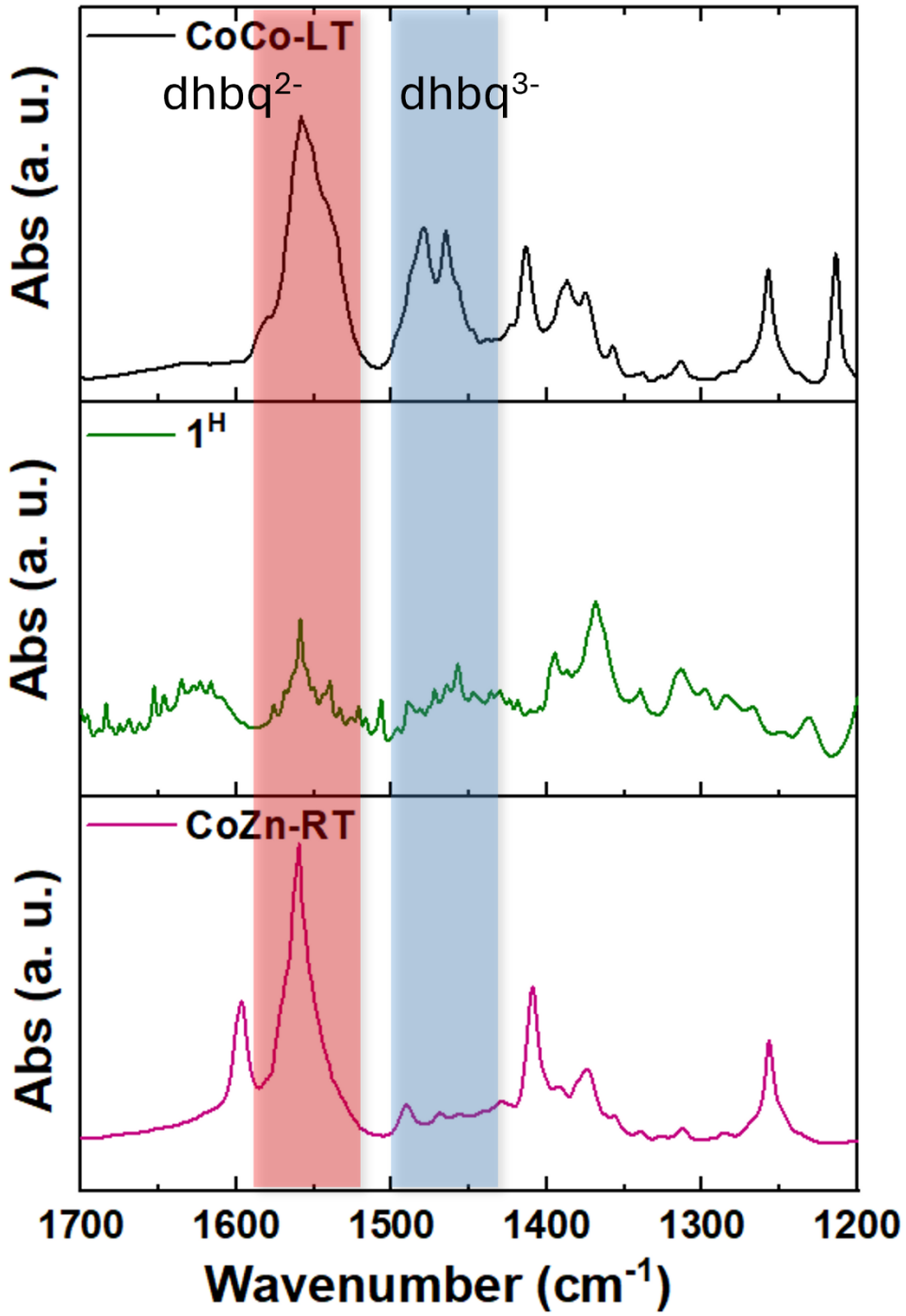

Figure 4.4 Comparison of IR spectrum for CoCo at low temperature (upper), 1^{H} at room temperature (middle), and CoZn at room temperature (bottom).

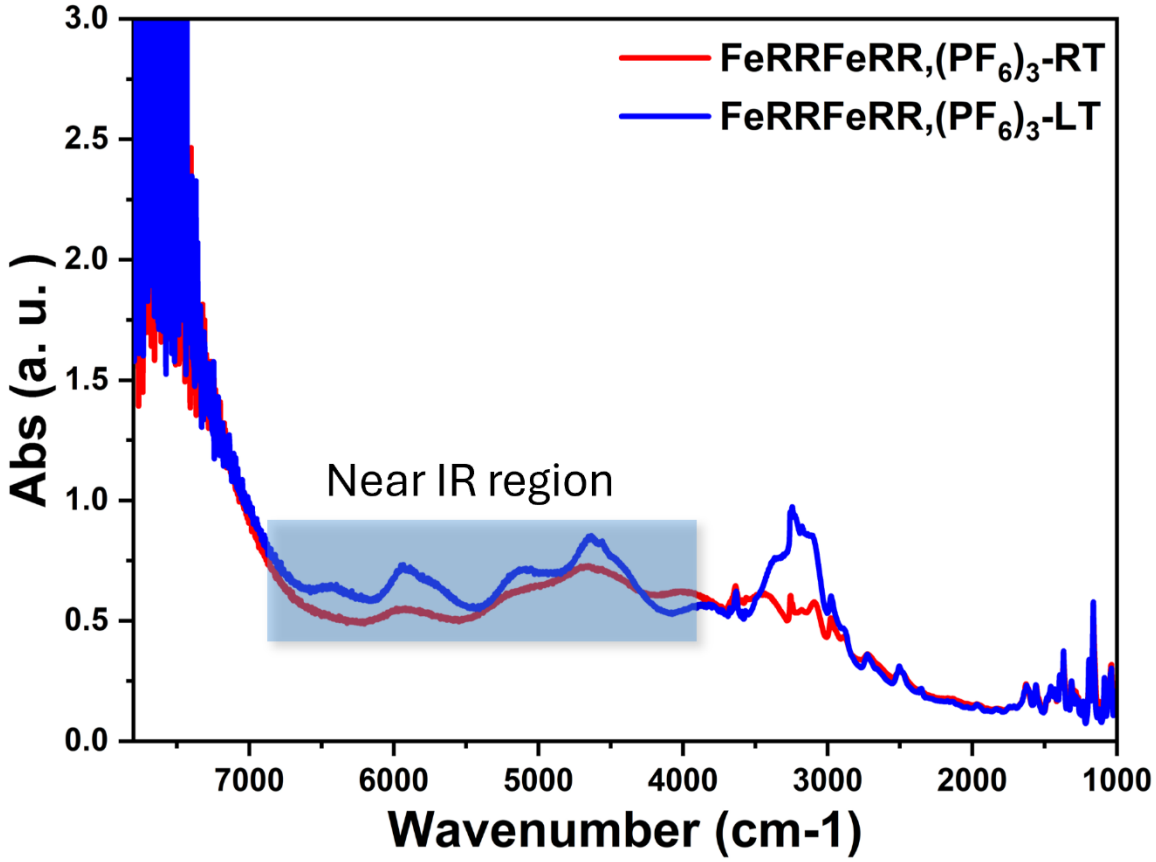

Figure 4.5 The IR spectrum of compound 1^{H} was recorded at both high temperature (room temperature) and low temperature (liquid nitrogen temperature) in the range of 1000 cm^{-1} to 7800 cm^{-1}. The characteristic absorption bands in the near-IR region are highlighted with a blue frame.

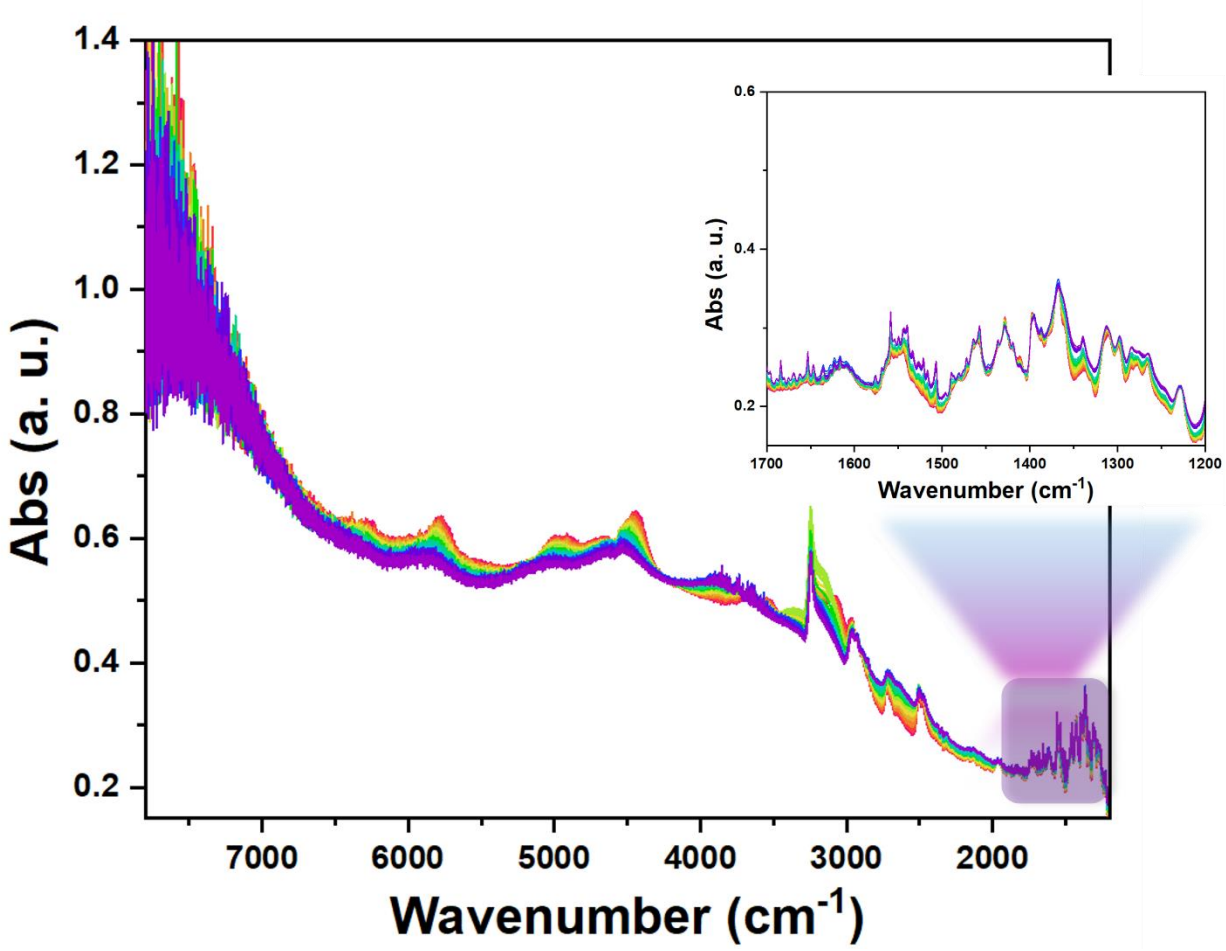

Figure 4.6 1^{H} was grounded and uniformly cover the surface of CaF_2 and Temperature-dependent IR spectrum was measured, ranging from 1000 to 7800 cm^{-1} (inset: data from 1200 to 1700 cm^{-1}).

The molecular structures of 2^{H} and 1^{Cl} differ slightly from that of 1H due to the use of heterochiral ligands and the modification of electron-withdrawing groups. These structural changes can influence the electronic configuration, thereby affecting the degree of electron delocalization. The IR spectra of 2^{H} and 1^{Cl} exhibit similar characteristic peaks to those of 1^{H}, with the exception of an intensified absorption band corresponding to the $dhbq^{2-}$ ligand (Figure 4.7a). This suggests that the Cl atom in dcbq may trap the delocalized electron between the metal centers, reducing the overall degree of delocalization.

Nevertheless, similar absorption bands in the near-IR region were observed, indicating that electron delocalization still occurs in these systems, though the complexes appear to be near the borderline between Robin-Day Class II and Class III. In the case of 2^{H}, the IR spectra between 1200 and 1700 cm^{-1} align well with those of 1^{H} (Figure 4.7b). Additionally, the absorption bands in the near-IR region retain their symmetry at both room temperature and low temperature, which could be attributed to the highly symmetric molecular configuration of 2^{H}.

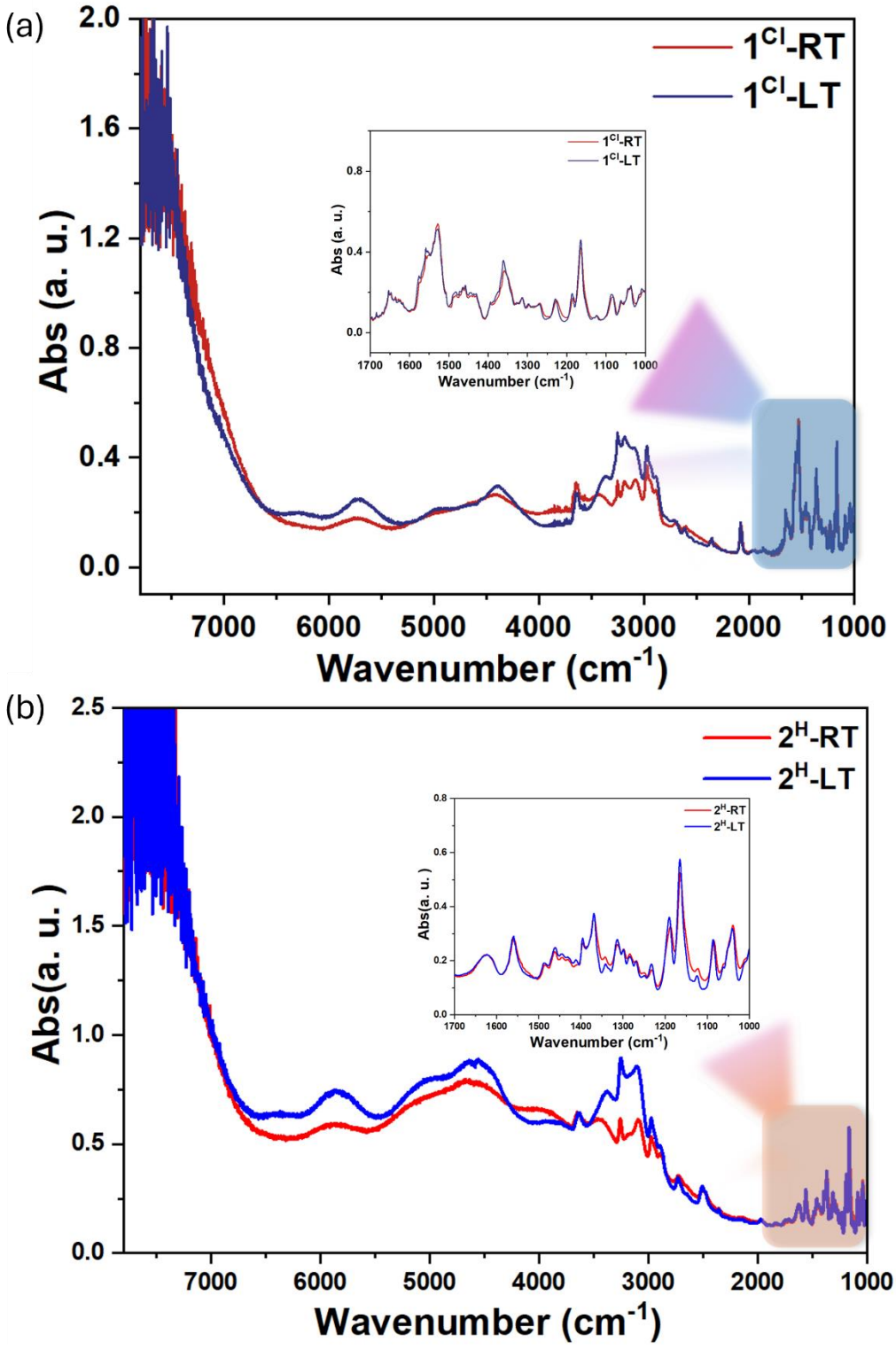

Figure 4.7 (a) The IR spectrum of pellet 1^{Cl} was measured at both room temperature (RT) and low temperature (LT) in the range of 1000 cm^{-1} to 1700 cm^{-1} (inset: data from 1000 cm^{-1} to 1700 cm^{-1}).

(b) The IR spectrum of pellet 2^H was measured at both RT and LT in the range of 1000 cm^{-1} to 1700 cm^{-1} (inset: data from 1000 cm^{-1} to 1700 cm^{-1}).

Furthermore, UV-vis measurements were performed on tape samples of 1^H and 2^H at both room temperature (RT) and low temperature (LT). Similar to the near-infrared range observed in the IR spectrum, five characteristic absorption bands were detected between 4000 cm^{-1} and 7000 cm^{-1}, showing the same variation between RT and LT (Figure 4.9,4.10). An intriguing observation was the difference in IVCT band shape between 1^H and 2^H, which generally linked to the degree of electron delocalization. For 1^H, the IVCT band at room temperature was relatively symmetric, showing a characteristic of relative electron localization. These peaks were notably narrow, averaging only around 300 cm^{-1}, aligning with the strong electronic coupling.

At low temperatures, however, an unusual phenomenon was observed in the UV-vis spectra of 1^H, where the IVCT band became even narrower and cut-off on the high-energy side, a behavior unlike typical Class III systems, which generally exhibit an asymmetric band shape with cut-off on the low energy side. This unique band shape might be explained by a transition from a delocalized ground state to a more localized excited state. In this scenario, the excitation energy at the ground state's lowest point is higher than adjacent transitions, leading to the cut-off on the high-energy side. Such a transition form from delocalization to localization could be quite rare, possibly suggesting a double-well potential in the excited state.

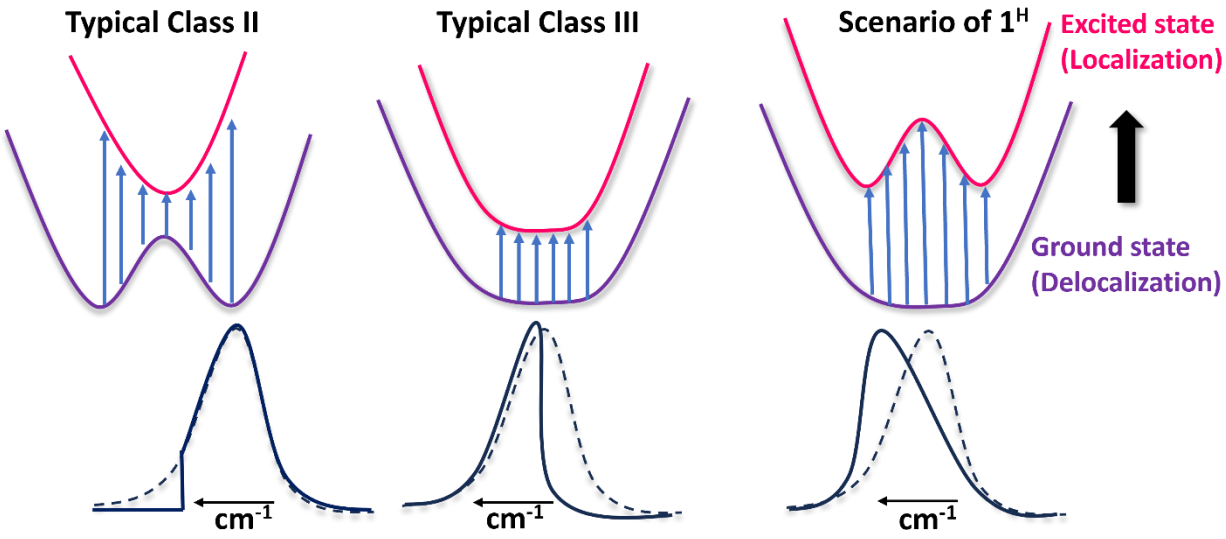

Figure 4.8 Schematic illustration of the IVCT band shapes corresponding to different types in the Robin-Day classification: Class II (left), Class III (middle), and the scenario of 1^H (right).

In contrast, the IVCT bands for 2^H remained symmetric at both room and low temperatures, consistent with a typical Class III mixed-valence complex. The likely cause of this discrepancy between 1^H and 2^H could be attributed to the distorted molecular structure and asymmetric electronic configuration in 1^H. Although both compounds exhibited the potential for delocalized electron hopping between the two Fe centers, possibly faster than the timescale of UV-vis for detecting MMCT bands, discrepancies in their electronic configurations were revealed through DFT calculations.

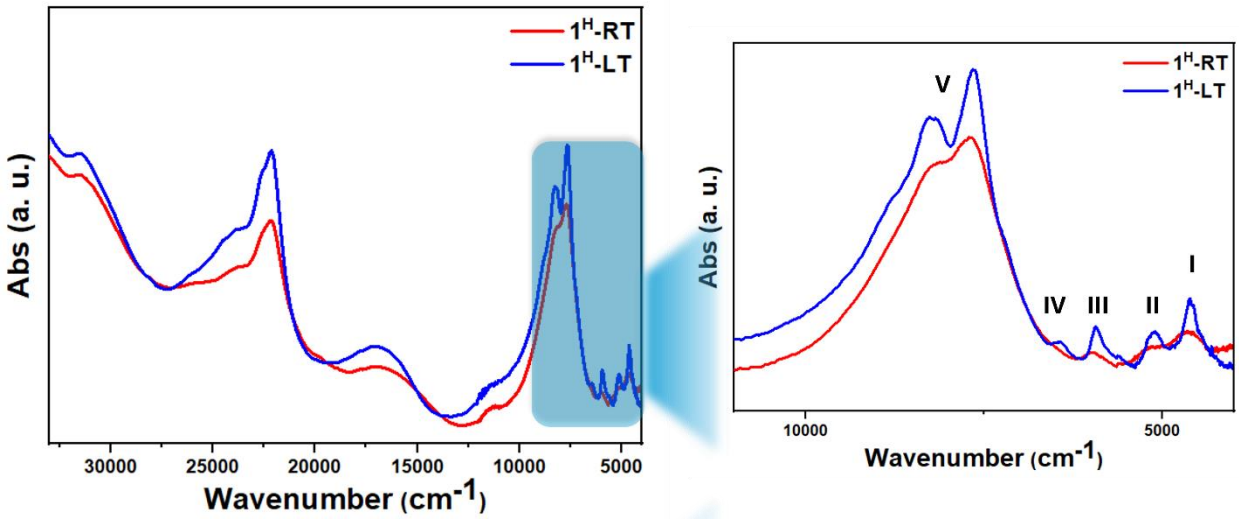

Figure 4.9 A tape sample of 1^{H} was prepared for UV-vis spectroscopy, with measurements taken between room temperature (RT) and low temperature (LT) across the range of 4000 to 33,000 cm^{-1} (left) and from 4000 to 11,000 cm^{-1} (right).

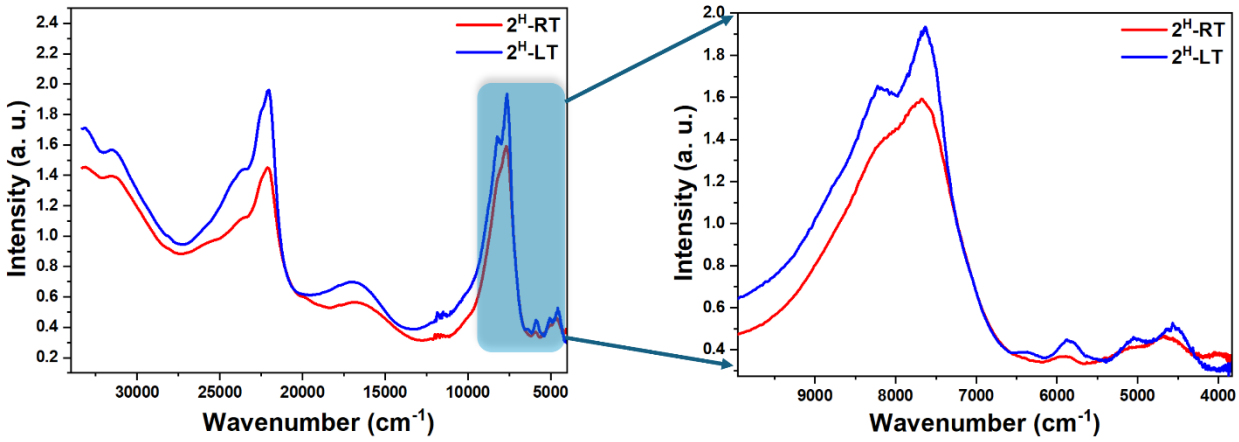

Figure 4.10 A tape sample of 2^{H} was prepared for UV-vis spectroscopy, with measurements taken between room temperature (RT) and low temperature (LT) across the range of 4000 to 33,000 cm^{-1} (left) and from 4000 to 11,000 cm^{-1} (right).

For the 1^{H} complex, molecular orbital analysis corresponding to excitations identified five absorption bands at 4990 cm^{-1}, 5690 cm^{-1}, 7479 cm^{-1}, and 10,371.8 cm^{-1}, which closely matched

the experimental results, including bands at 4617 cm^{-1}, 5118 cm^{-1}, 5943 cm^{-1}, 6443 cm^{-1}, and 7924 cm^{-1}, designated as bands I to V (Figure 4.11). In the first two absorption bands (I and II), the molecular orbitals at the left-side Fe center transition from antibonding to bonding orbitals, accompanied by a redistribution of spin. Interestingly, as the excitation progresses from bands I and II to bands III and IV, the opposite process occurs, with the spin shifting to the right-side Fe center. These two distinct excitation modes result in opposite spin transitions, ultimately leading to polarization inversion. The fifth band (V) can be attributed to a ligand-to-metal charge transfer.

In contrast, 2^{H} did not exhibit a similar spin deviation between the two metal centers, maintaining symmetric spin distribution. The difference between the two complexes can be attributed to the lower molecular symmetry and the varying degrees of hydrogen bonding on either side of the ligands in 1^{H}. Such a unique behavior of 1^{H} offers a great opportunity to investigate polarization inversion induced by various wavelength light.

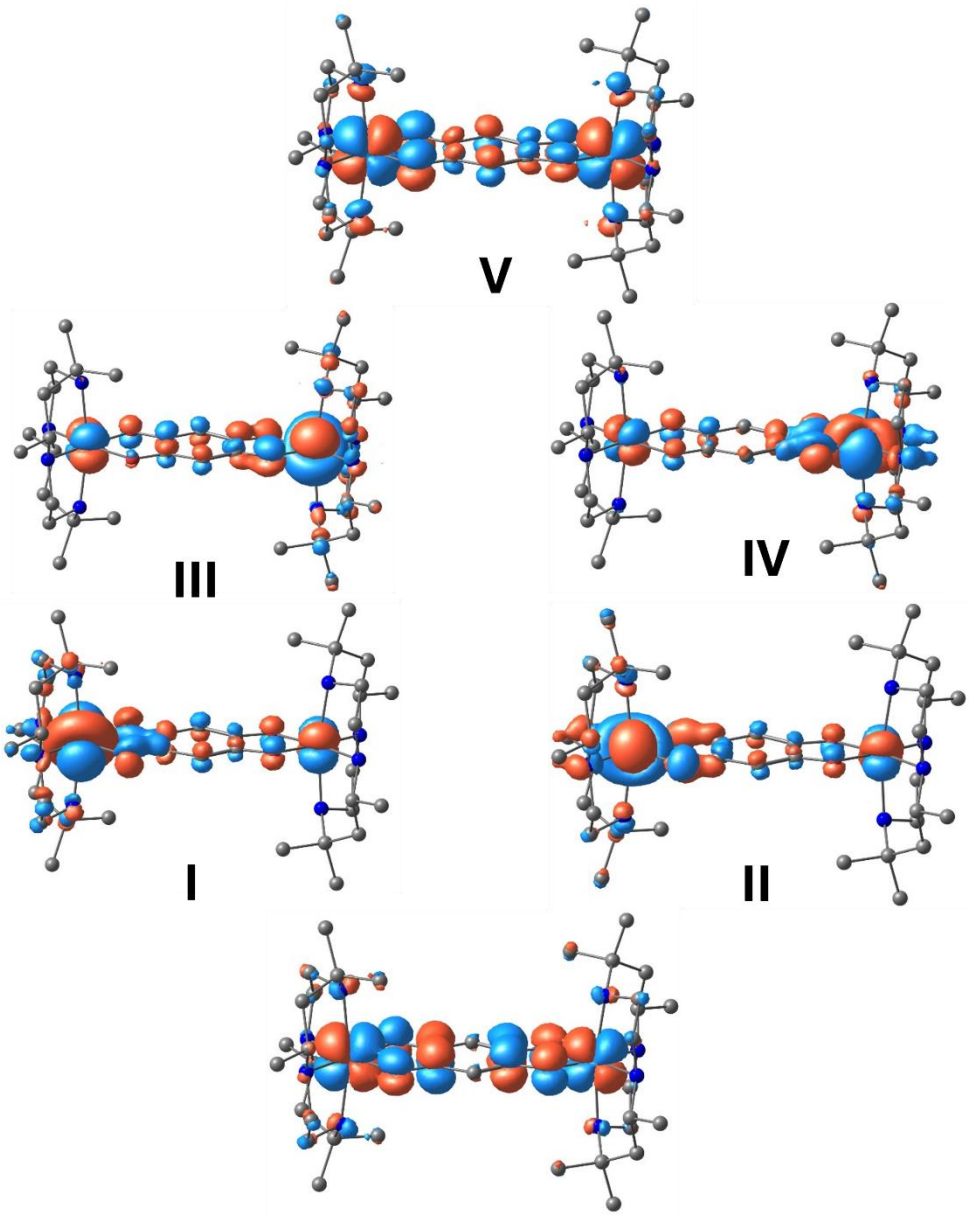

Figure 4.11 The molecular orbitals corresponding to excitations from the HOMO to LUMO in 1^{H} are associated with excitations at 4990 cm^{-1}, 5690 cm^{-1}, 7479 cm^{-1}, 7991 cm^{-1}, and 10,371 cm^{-1}, corresponding to transitions I to V.

Pump-probe spectroscopy using femtosecond laser pulses was performed on 1^{H} to investigate potential polarization switching in different electronic configurations. A suitable crystal was selected and mounted on a substrate, and lasers with energies of 0.53 eV and 0.73 eV were used to

irradiate the sample perpendicular to the a-axis (nonpolar axis), simulating the excitation of bands I and III (Figure 4.12, 4.13). Time-resolved measurements of the photoinduced reflectivity change were carried out. A significant change in reflectivity was observed immediately after excitation, with a relaxation lifetime of approximately 0.4 ps After that, the reflectivity did not return to zero directly but remained at a certain value. However, by the comparison of two excitation process the photoinduced dynamics showed little difference between the two laser wavelengths.

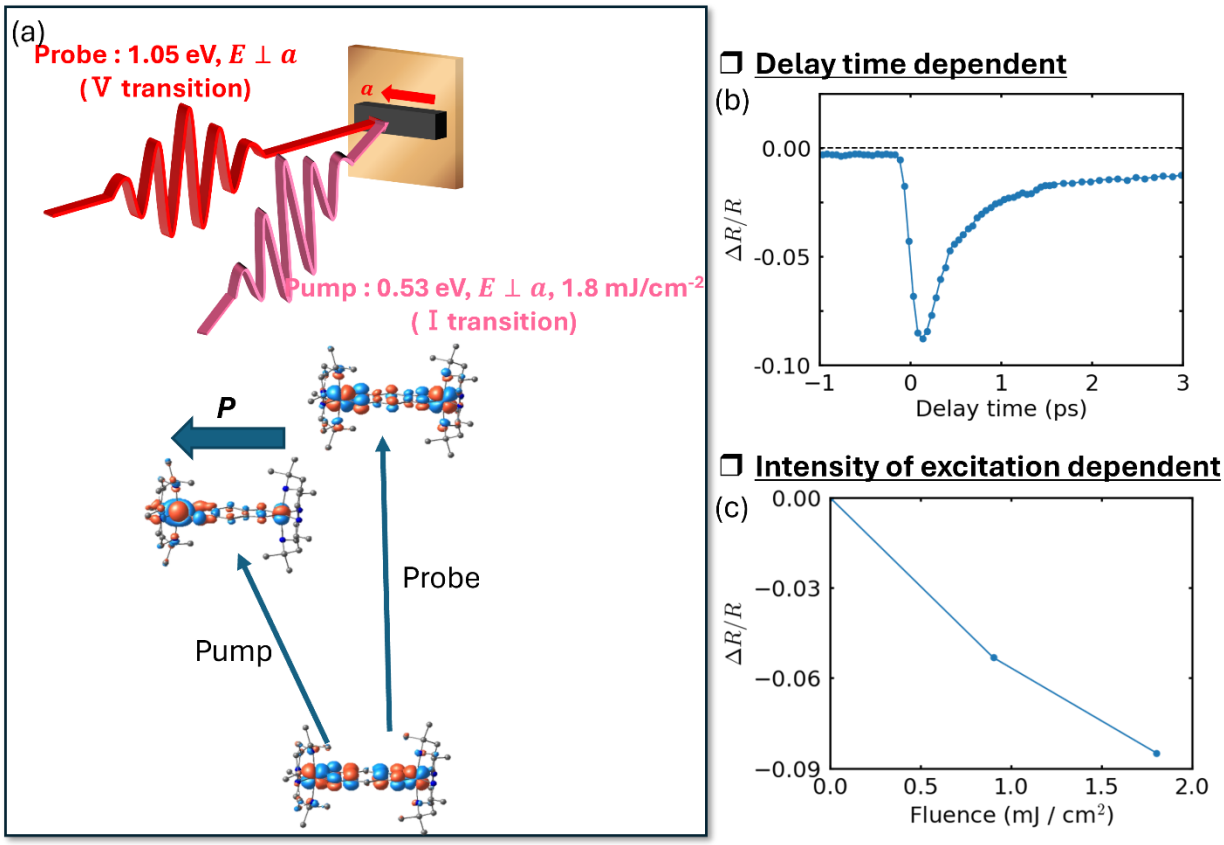

Figure 4.12 (a) Schematic representation of light-induced polarization switching in crystal 1^{H}, simulating the I process using pump-probe spectroscopy. (b) Reflectivity as a function of delay time, measured before and after excitation with 0.53 eV. (c) Reflectivity as a function of excitation intensity.

The spectral changes observed immediately after photoexcitation can be attributed to ground state bleaching (GSB). This suggests a transition from the highest occupied molecular orbital (HOMO)

to bands I or III, corresponding to different transitions from a symmetric electron configuration in the ground state to an asymmetric configuration in the excited state, as predicted by molecular orbital calculations. The residual signal after excitation originates from a probe transition from the HOMO to band V, associated with a ligand-to-metal charge transfer (LMCT). Despite this, we were unable to conclusively determine whether polarization inversion occurred in response to the different laser excitations, as the reflectivity changes were in the same direction for both wavelengths. Further optical measurements are currently underway to investigate its intriguing dynamic electronic configuration.

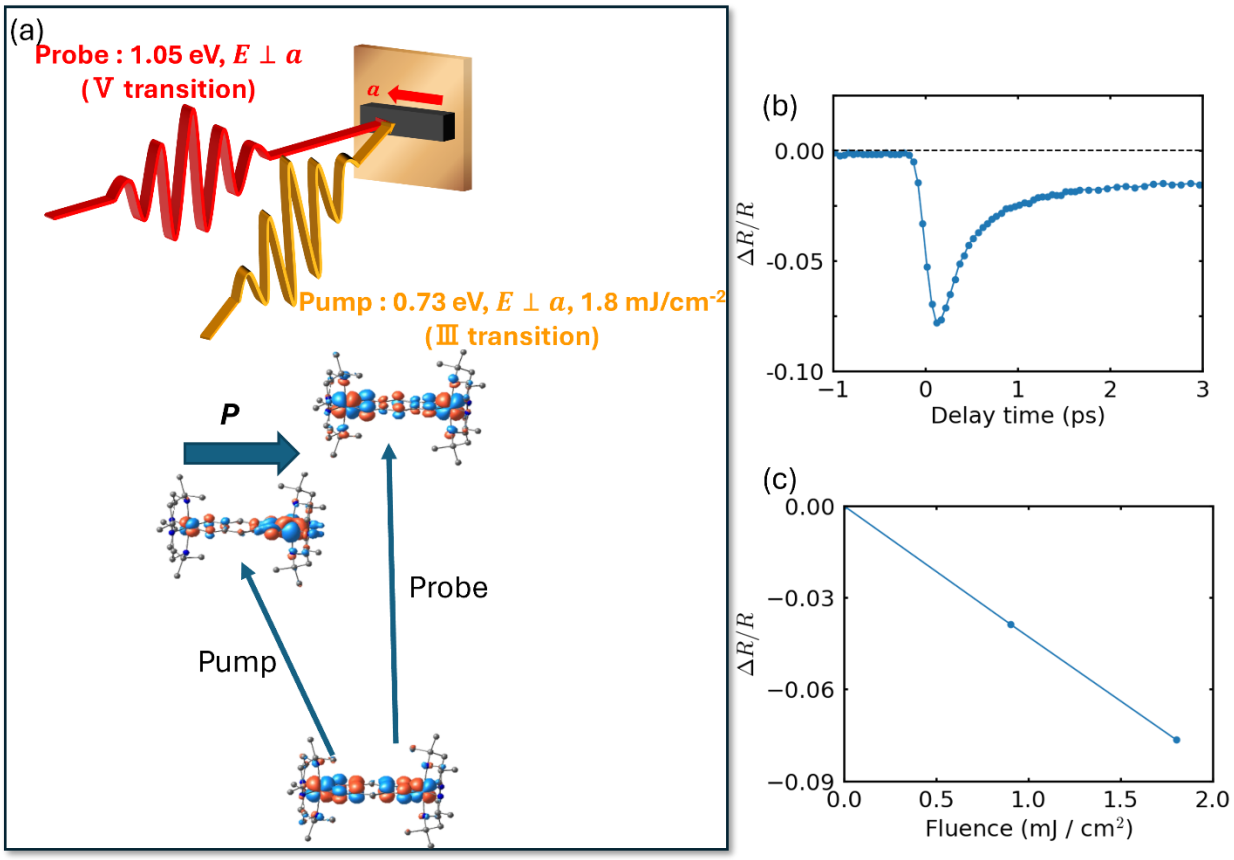

Figure 4.13 (a) Schematic representation of light-induced polarization switching in crystal 1^{H}, simulating the III process using pump-probe spectroscopy. (b) Reflectivity as a function of delay time, measured before and after excitation with 0.53 eV. (c) Reflectivity as a function of excitation intensity.

The magnetization of the three compounds was measured using crystalline samples, and the results revealed a similar variation trend in magnetic susceptibility. As the temperature decreased, $\chi_m T$ gradually increased from 10.67 to a peak of 12.2 cm^3 K mol^{-1} at around 50 K, which is close to the theoretical value of 12.375 cm^3 K mol^{-1}, corresponding to a ground state S = 9/2 with g = 2 (Figure 4.14). This suggests strong ferromagnetic coupling between high-spin Fe^{2+} and high-spin Fe^{3+}, consistent with electron delocalization observed in UV-vis and IR spectra. Additionally, it is possible that antiferromagnetic coupling occurs between the two high-spin Fe^{3+} centers and the radical in dhbq, or a combination of these two interactions could be contributing to the observed behavior.

In contrast, 1^H and 1^{Cl} showed magnetization plateaus of 11.6 cm^3 K mol^{-1} and 11 cm^3 K mol^{-1}, respectively, which significantly differ from the expected value for an isolated S = 9/2 system with g = 2. HF EPR measurements confirmed that the g-factor of all three compounds is greater than 1.99. Even when fitting with different spin states, such as S = 7/2 (7.785 cm^3 K mol^{-1}) or S = 5 (15 cm^3 K mol^{-1}), notable discrepancies remained. One possible explanation for this is the varying degrees of delocalization, which lead to different spin fluctuations.

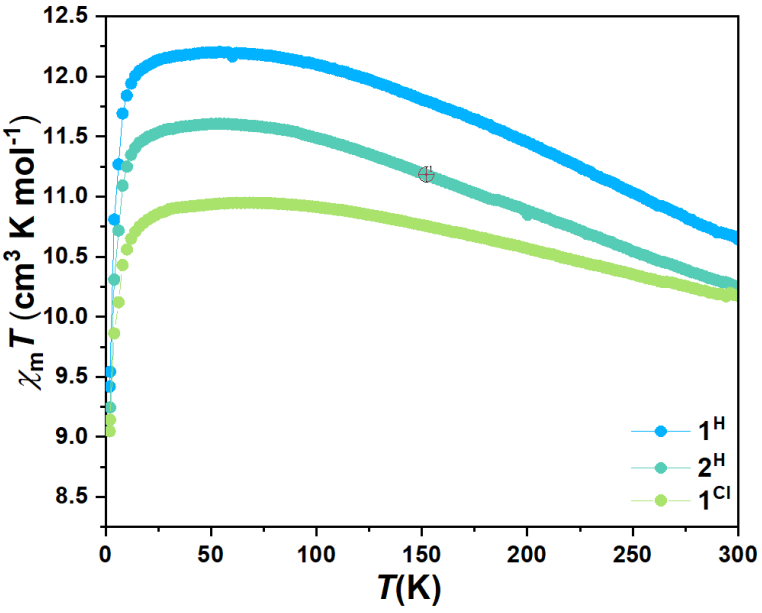

Figure 4.14 Temperature dependence of the molar magnetic susceptibility-temperature products for 1^{H} (blue circles), 2^{H} (green triangles), and 1^{Cl} (blue triangles).

The sharp decline in magnetization below 25 K for all three compounds can be attributed to zero-field splitting (ZFS), supported by inelastic neutron scattering (INS) data, which has been discussed by our collaborator (Rasmus tang Christiansen). It is worth noting that high-spin Fe^{3+} typically exhibits minimal ZFS due to its half-filled 3d subshell, leading to a spherically symmetric electron distribution, orbital angular momentum quenching, and reduced spin-orbit coupling in a highly symmetric crystal field environment. The presence of ZFS in these samples is likely caused by high-spin Fe^{2+}, further indicating the existence of mixed-valence Fe dimers. Additionally, field-dependent magnetization measurements for the three compounds were taken at 2 K, 3 K, 5 K, and 10 K, further confirming an S = 9/2 ground state (Figure 4.15). Consequently, the decrease in $\chi_m T$ above 50 K is attributed to the population of excited states with S < 9/2 at higher temperatures.

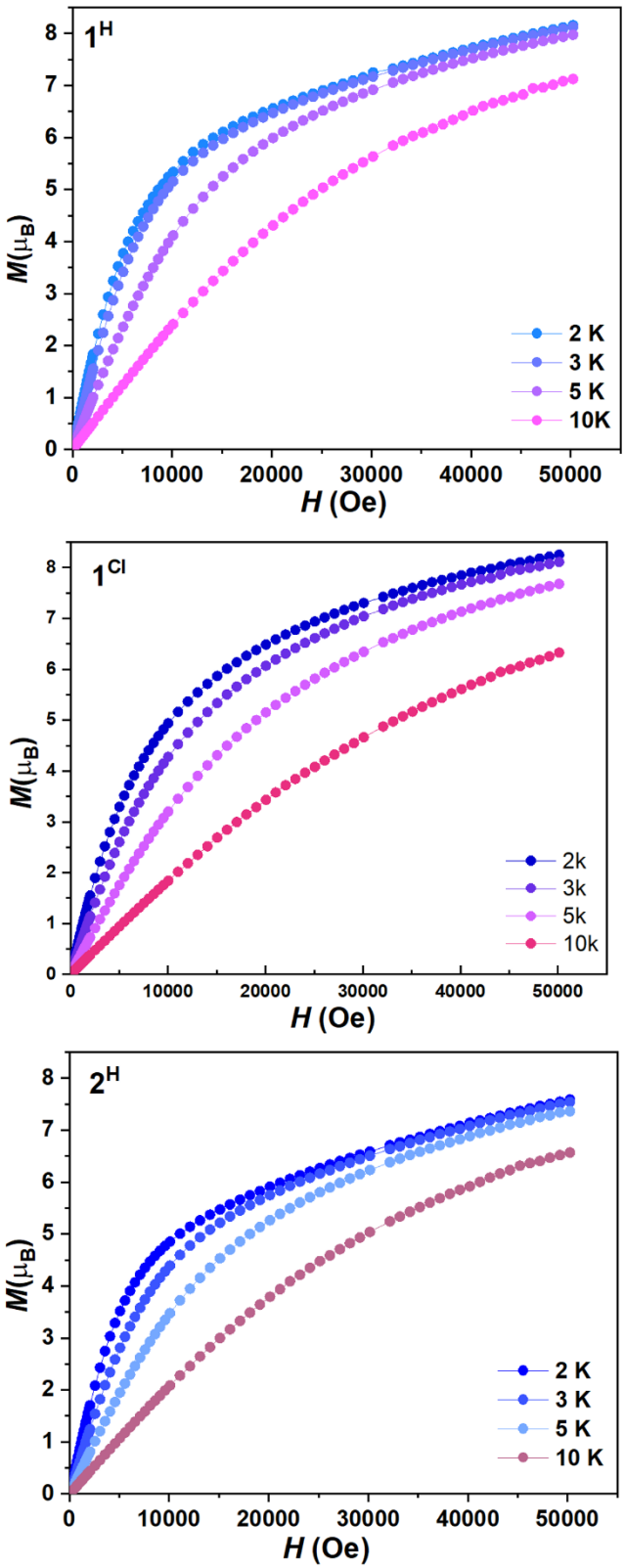

Figure 4.15 field-dependent magnetization of three compounds (1^{H}-up, 1^{Cl}-middle, and 2^{H}-down)

at 2 K, 3 K, 5 K, and 10 K.

4.4 Conclusion

We have synthesized three Fe dimers with different enantiopure ligands and bridging ligands, each exhibiting a range of intriguing properties. Basic spectroscopic analysis, including IR and UV-vis, revealed a series of absorption bands in the near-infrared region across all three compounds, which we attribute to intervalence charge transfer (IVCT) bands. Although we were unable to conclusively detect electron delocalization due to equipment limitations or sample constraints, the presence of these IVCT bands, along with faint absorption signals from $dhbq^{2-}$ or $dhbq^{3-}$ and magnetization data, suggests that these compounds are delocalized mixed-valence dinuclear Fe complexes. The degree of delocalization appears to be influenced by the molecular structure and the nature of the bridging ligand. The electronic configuration of these compounds is complex, as the mixed valence of the two Fe centers could arise not only from Fe^{2+}-$dhbq^{2-}$-Fe^{3+} or Fe^{3+}-$dhbq^{2-}$-Fe^{2+} interactions but also from Fe^{3+}-$dhbq^{3-}$-Fe^{3+}. This combination of three possible valence states adds significant complexity to understanding the true electronic configuration and dynamic mechanisms. Further investigation is essential to clarify these details. Additionally, we are interested in exploring the potential for new phases or properties by applying pressure to disrupt the mixed-valence state.

Beyond electron delocalization, the introduction of the enantiopure cth ligand in 1^H lowers the molecular symmetry, resulting in its packing in a polar $P2_1$ space group. This structural difference also contributes to distinct electronic configurations, where opposite spin distributions occur between the two Fe centers, depending on the excitation from the HOMO to LUMO orbitals. As a result, 1^H may achieve polarization inversion when irradiated by different wavelengths of laser light, a property not seen in 2^H due to its symmetric structure. Pump-probe spectroscopy using

femtosecond laser pulses provided positive evidence supporting a transition from symmetric to asymmetric spin distribution (I and III transitions), where polarization was generated based on the delay-time-dependent reflectivity. However, the specific direction of the polarization still requires further experimental confirmation.

P.s: in his doctoral thesis, our collaborator Rasmus Tang Christiansen analyzed the INS, HF EPR, X-band EPR, and FIRMS data. Here, I won't talk more about it. The study developed a model demonstrating that substituting electron-withdrawing Cl groups on the bridging ligand of 1^{H} impacts the ferromagnetic coupling between metals. The INS data indicated significant zero-field splittings (ZFS) for all three dimers, likely due to ligand-to-metal charge transfer (LMCT), as previously suggested. Interestingly, despite breaking molecular centrosymmetry with the capping ligand's chirality, the ZFS of 1^{H} remained largely unchanged compared to 2^{H}. However, the HF EPR data revealed that breaking the centrosymmetry leads to anisotropy in the g-matrix.

Reference

1. S. Pal, A. B. Swain, P. P. Biswas and P. Murugavel, Photoferroelectric phenomena in ferroelectric oxides and a Rayleigh analysis, *Physical Review Materials*, 2020, **4**, 064415.
2. J. Yang, F. Wang, J. Guo, Y. Wang, C. Jiang, S. Li, Y. Cai, X. Zhan, X. Liu, Z. Cheng, J. He and Z. Wang, Ultrasensitive Ferroelectric Semiconductor Phototransistors for Photon-Level Detection, *Advanced Functional Materials*, 2022, **32**, 2205468.
3. X. Long, H. Tan, F. Sánchez, I. Fina and J. Fontcuberta, Non-volatile optical switch of resistance in photoferroelectric tunnel junctions, *Nature Communications*, 2021, **12**, 382.
4. Z. Han, Y. Chang, B. Luo, S. Wang, W. Zhai and J. Wang, A Multistate Non-Volatile Photoelectronic Memory Device Based on Ferroelectric Tunnel Junction with Modulable

Visible Light Photoresponse, *ACS Applied Materials & Interfaces*, 2024, **16**, 19254-19260.

5. L. Tang, W. Weng, H. Chen, L. Hua, W. Guo, Y. Liu, Y. Ma, Y. Chen, J. Luo and Z. Sun, Photoexcited Ultraviolet-to-Infrared (II) Pyroelectricity in a 2D Ferroelectric Perovskite Driving Broadband Self-Powered Photoactivities, *Advanced Functional Materials*, 2023, **33**, 2214858.
6. A. He, G. Liu, H. Lu, R. Zhao, J. Gao, Q. Wu, C. Zheng, Y. Jiang and L. Li, Rewritable Optical Memory Based on Sign Switching of Magnetoresistance, *Advanced Electronic Materials*, 2020, **6**, 1900701.
7. D. Afanasiev, J. R. Hortensius, B. A. Ivanov, A. Sasani, E. Bousquet, Y. M. Blanter, R. V. Mikhaylovskiy, A. V. Kimel and A. D. Caviglia, Ultrafast control of magnetic interactions via light-driven phonons, *Nature Materials*, 2021, **20**, 607-611.
8. M. F. Sarott, M. J. Müller, J. Lehmann, B. J. Burgat, M. Fiebig and M. Trassin, Reversible Optical Control of Polarization in Epitaxial Ferroelectric Thin Films, *Advanced Materials*, 2024, **36**, 2312437.
9. J. Ordoñez-Pimentel, J. E. García, P. S. da Silva and M. Venet, Visible-Light-Control of Dielectric Permittivity in Ferroelectrics with Charged Domain Walls, *Physical Review Applied*, 2023, **19**, 034094.
10. Y. Du, W.-Q. Liao, Y. Li, C.-R. Huang, T. Gan, X.-G. Chen, H.-P. Lv, X.-J. Song, R.-G. Xiong and Z.-X. Wang, A Homochiral Fulgide Organic Ferroelectric Crystal with Photoinduced Molecular Orbital Breaking, *Angewandte Chemie International Edition*, 2023, **62**, e202315189.
11. Y. Du, W.-Q. Liao, Y. Li, C.-R. Huang, T. Gan, X.-G. Chen, H.-P. Lv, X.-J. Song, R.-G. Xiong and Z.-X. Wang, A Homochiral Fulgide Organic Ferroelectric Crystal with Photoinduced Molecular Orbital Breaking, *Angewandte Chemie*, 2023, **135**, e202315189.
12. P. Chen, C. Paillard, H. J. Zhao, J. Íñiguez and L. Bellaiche, Deterministic control of ferroelectric polarization by ultrafast laser pulses, *Nature Communications*, 2022, **13**, 2566.

13. V. C. Lau, L. A. Berben and J. R. Long, [(Cyclen)4Ru4(pz)4]9+: A Creutz−Taube Square, *Journal of the American Chemical Society*, 2002, **124**, 9042-9043.

14. S. F. Nelsen, R. F. Ismagilov, K. E. Gentile and D. R. Powell, Temperature Effects on Electron Transfer within Intervalence Bis(Hydrazine) Radical Cations, *Journal of the American Chemical Society*, 1999, **121**, 7108-7114.

15. C. A. Gould, K. R. McClain, D. Reta, J. G. C. Kragskow, D. A. Marchiori, E. Lachman, E.-S. Choi, J. G. Analytis, R. D. Britt, N. F. Chilton, B. G. Harvey and J. R. Long, Ultrahard magnetism from mixed-valence dilanthanide complexes with metal-metal bonding, *Science*, 2022, **375**, 198-202.

16. M. Parthey, J. B. G. Gluyas, M. A. Fox, P. J. Low and M. Kaupp, Mixed-Valence Ruthenium Complexes Rotating through a Conformational Robin–Day Continuum, *Chemistry – A European Journal*, 2014, **20**, 6895-6908.

17. T. J. N. Obey, M. K. Singh, A. B. Canaj, G. S. Nichol, E. K. Brechin and J. B. Love, A Delocalized Mixed-Valence Dinuclear Ytterbium Complex That Displays Intervalence Charge Transfer, *Journal of the American Chemical Society*, 2024, **146**, 28658-28662.

18. M. Makino, T. Ishizuka, S. Ohzu, J. Hua, H. Kotani and T. Kojima, Synthesis and Characterization of an Azido-Bridged Dinuclear Ruthenium(II) Polypyridylamine Complex Forming a Mixed-Valence State, *Inorganic Chemistry*, 2013, **52**, 5507-5514.

19. L. E. Darago, M. L. Aubrey, C. J. Yu, M. I. Gonzalez and J. R. Long, Electronic Conductivity, Ferrimagnetic Ordering, and Reductive Insertion Mediated by Organic Mixed-Valence in a Ferric Semiquinoid Metal–Organic Framework, *Journal of the American Chemical Society*, 2015, **137**, 15703-15711.

20. V. V. Sentyurin, O. A. Levitskiy, A. V. Bogdanov, T. S. Yankova, S. G. Dorofeev, K. A. Lyssenko, V. E. Gontcharenko and T. V. Magdesieva, Stable Spiro-Fused Diarylaminyl Radicals: A New Type of a Neutral Mixed-Valence System, *Chemistry – A European Journal*, 2023, **29**, e202301250.

21. G. E. Pieslinger, P. Alborés, L. D. Slep and L. M. Baraldo, Class III Delocalization in a Cyanide-Bridged Trimetallic Mixed-Valence Complex, *Angewandte Chemie*, 2014, **126**, 1317-1320.

22. J. M. Palasz, T. M. Porter and C. P. Kubiak, Electronic Structural Studies of the Ru3(III,II,II) Mixed-Valent State of Oxo-Centered Triruthenium Clusters, *Inorganic Chemistry*, 2020, **59**, 10532-10539.

23. D. A. Robinson, M. E. Foster, C. H. Bennett, A. Bhandarkar, E. R. Webster, A. Celebi, N. Celebi, E. J. Fuller, V. Stavila, C. D. Spataru, D. S. Ashby, M. J. Marinella, R. Krishnakumar, M. D. Allendorf and A. A. Talin, Tunable Intervalence Charge Transfer in Ruthenium Prussian Blue Analog Enables Stable and Efficient Biocompatible Artificial Synapses, *Advanced Materials*, 2023, **35**, 2207595.

24. A. Palii, S. Aldoshin and B. Tsukerblat, Mixed-valence clusters: Prospects for single-molecule magnetoelectrics, *Coordination Chemistry Reviews*, 2021, **426**, 213555.

25. C. Bosch-Serrano, J. M. Clemente-Juan, E. Coronado, A. Gaita-Ariño, A. Palii and B. Tsukerblat, Electric Field Control of the Spin State in Mixed-Valence Magnetic Molecules, *ChemPhysChem*, 2012, **13**, 2662.

26. C. Bosch-Serrano, J. M. Clemente-Juan, E. Coronado, A. Gaita-Arino, A. Palii and B. Tsukerblat, Molecular analog of multiferroics: electric and magnetic field effects in many-electron mixed-valence dimers, *Physical Review B—Condensed Matter and Materials Physics*, 2012, **86**, 024432.

27. H. Suzuki and C. Satoko, Quantitative calculation of magnetic and electric properties in a d2–d3 mixed-valence vanadium dimer complex, *Journal of Physics: Condensed Matter*, 2014, **26**, 045504.

28. A. Palii, J. M. Clemente-Juan, B. Tsukerblat and E. Coronado, Electric field control of the optical properties in magnetic mixed-valence molecules, *Chemical Science*, 2014, **5**, 3598-3602.

Chapter 5 Discussion and Conclusion

Pyroelectric materials are unique materials that generate an electric current or voltage when subjected to a change in temperature. This property arises due to the intrinsic alignment of electric dipoles within the crystal structure, which leads to a spontaneous polarization. When the temperature fluctuates, the change in polarization induces a temporary electric charge on the surface of the material, resulting in a measurable pyroelectric current. These materials have garnered significant interest due to their wide range of applications in fields like infrared (IR) sensing, thermal imaging, energy harvesting, and environmental monitoring. Pyroelectric sensors are particularly valued in infrared detectors for their ability to detect minute temperature changes, making them useful in security systems, motion detectors, and thermal cameras.

With the era of artificial intelligence advancing rapidly, data generation is experiencing an unprecedented explosion. Developing high-performance memory with greater data densities, faster operation speeds, and lower energy consumption is critical for the progression of information storage technologies. Among these advancements, the emergence of optical non-volatile memory represents a significant breakthrough, offering rapid response times, exceptional durability, and precise control. To further enhance the performance of pyroelectric materials capable of being triggered by light stimuli for practical applications, we incorporate bistable molecules, such as those exhibiting valence tautomerism and mixed valence, into a polar space group. By leveraging the substantial variation in dipole moment associated with long-range electron transfer, our goal is to achieve macroscopic polarization switching. However, recent results from our laboratory indicate significant challenges in practical applications due to low light-induced polarization switching. Addressing these challenges requires rational molecular design, optimized synthetic methods, and precise crystal growth techniques to enhance photomagnetization conversion and realize light-induced giant polarization changes.

Preliminary screening experiments and detailed theoretical calculations suggest that enantiopure ligands are promising candidates. Their intrinsic asymmetry and distorted coordination modes help maintain polar molecular packing and stabilize the high-spin (HS) state of valence tautomeric complexes. Following this approach, several complexes exhibiting valence tautomerism were successfully synthesized and characterized, including Cr(SS-cth)(μ-dhbq)Co(SS-cth)$_3$·2.5H_2O·0.5MeOH, Cr(SS-cth)(μ-dhbq)Co(SS-cth)$_3$, and two Fe dimers.

In **Chapter 2**, We propose a broadly applicable strategy a site-selective replacement approach for synthesizing heterodinuclear complexes with enantiopure ligands. Through a stepwise synthetic route, we leverage the superior stability of the inert metal Cr to selectively occupy one site of the bridging ligand, ensuring it remains securely bound. The remaining site of the dhbq ligand would be the only viable option for accommodating another metal component. This approach significantly enhances the purity of the desired crystals, effectively minimizing contamination.

Based on this methodology, we successfully obtained a novel VT complex, (([Co(*SS*-cth)(μ-dhbq)Cr(*SS*-cth)](PF$_6$)$_3$·2H_2O·0.5MeOH (**1·sol**), which is crystallized in the polar $P2_1$ space group. Remarkably, the transformation between **1·sol** and its desolvated counterpart, **1**, can be achieved through a single-crystal-to-single-crystal transition, enabling solvent-dependent polarization switching at the single-crystal level. Moreover, the pyroelectric technique allows us to directly track the polarization changes occurring during the VT process. These results highlight the efficacy of using enantiopure ligands by stepwise synthetic method in the development of polar crystals with versatile polarization switching behavior and lay a solid fundamental for further improving light induced polarization change. Furthermore, they also emphasize the importance of guest molecules in these materials.

In **Chapter 3**, Building on the work with **1·sol** in **Chapter 2** and its comparable energy barrier between the high-spin (HS) and low-spin (LS) states under a distorted configuration, We aimed to further lower the transition temperature and enhance photomagnetization conversion by manipulating chemical pressure through the incorporation of larger counterions. Therefore, a novel polar crystal [Co(SS-cth)(dhbq)Cr(SS-cth)]$(AsF_6)_3$ (**1**$(AsF_6)_3$) was successfully synthesized. This complex was obtained by recrystallization in ethanol, resulting in a solvent-free crystal lattice and a precise alignment of the Cr–Co vector along the polar *b*-axis, significantly enhancing the dipole moment loss. Its electronic configuration is relatively simple and stable without solvent, in contrast to the complex discussed in **Chapter 2**. The inclusion of the large AsF_6^- counterion effectively lowers the transition temperature and stabilizes the high-temperature phase following light irradiation.

This complex exhibit pronounced light-induced valence tautomerism, responding to 532 nm light and achieving complete photoconversion under 1340 nm irradiation that is a rare phenomenon to our knowledge. Notably, light-induced pyroelectric measurements revealed an unprecedented polarization change of 2.25 μC cm^{-2}) under 1340 nm irradiation, which is significantly higher than other non-ferroelectric materials with the LIESST effect (previous highest value: 0.45 μC cm^{-2})). This value surpasses the threshold for practical optical memory applications, typically around 1 μC cm^{-2}).

Interestingly, the light-induced excited state also differs from the thermally triggered state, as confirmed by ultralow-temperature crystal structure analysis before and after irradiation. An evident symmetry-breaking event, accompanied by counterion displacement in the crystal lattice, was observed upon light activation, not through normal temperature changes. Additionally, the rare hidden phase, characterized by its long-lived high-spin state, was accessible through thermal quenching, as demonstrated by magnetization and crystal structure analysis. It would be a new

phenomenon in realizing near IR induced considerable polarization change by hidden phase.

In **Chapter 4**, we present three mixed-valence Fe dimers, where 1^{H} and 1^{Cl} are arranged in a polar space group due to the use of enantiopure ligands, in contrast to 2^{H}, which incorporates heterochiral ligands. The reduced symmetry at both the molecular and crystal levels in 1^{H} impacts its electronic configuration. A series of unique absorption bands associated with intervalence charge transfer (IVCT) were identified in the near-IR range through UV-vis and IR spectroscopy. Notably, the high-energy cut-off of these bands suggests a distinct transition from a delocalized ground state to a relatively localized excited state. Theoretical predictions indicated a polarization reversal induced by different wavelengths, highlighting the potential for ultra-fast, light-driven polarization inversion in electron hopping complexes between metal centers crystallized in polar structures.

Throughout this thesis, we report several novel pyroelectric materials exhibiting dynamic responses. These findings strongly support the effectiveness and versatility of our strategy, utilizing rational molecular design to achieve significant polarization changes/switching triggered by multiple stimuli, especially light. This approach offers valuable insights for the development of next-generation optical memory. Additionally, these complexes' robust molecular interactions and flexible guest molecule including counter anions and solvents pathways suggest promising directions for creating pyroelectric bistable materials with valence tautomerism or delocalized mixed-valence properties, advancing the field toward functional devices.

Acknowledgement

I would like to express my heartfelt thanks to those who provided invaluable assistance to me during my doctoral course at Kyushu University.

I first express my deepest thanks to my supervisor, Professor Osamu Sato, who takes me into the palace of coordination chemistry and shows me the treasure in it. Under his guidance, I can successfully complete this thesis.

I would like to express my sincere thanks to Dr. Shu-Qi Wu and all other members of our group. I got a lot of helpful suggestions and great helps from them. Discussions with them have greatly broadened my horizons. Thanks to Institute for Molecular Science for providing paramount opportunity on ultra-low temperature single crystal X-ray diffraction measurement before and after light irradiation. Thanks to Spring-8 offered machine time to measure tiny crystal structure.

I would also like to express my deepest gratitude to my wife (Jieyu Xu) for her unconditional love and support during my study abroad. Her encouragement served as the driving force behind the continuation of my doctoral research, my affection for her knows no bounds.

My parents and brother have also bestowed upon me their encouragement and support, for which I am truly grateful for their dedication.

List of Publication

1. W. Zheng, X. Zhang, Q. Shui, T. Fukuyama, W.-h. Xu, Y.-b. Huang, T. Ji, Z. Zhou, M. Uematsu and S.-Q. Su, Solvent-dependent valence tautomerism and polarization switching in a heterodinuclear [CrCo] complex, *Inorganic Chemistry Frontiers*, 2024. 11, 3847-3854.
2. W. Zheng, S-Q. Wu, Q. Shui, S. Kanegawa, S-Q. Su, O. Sato. Giant Near Infrared Induced Polarization Change via a Hidden Phase of a Valence Tautomeric [CrCo] Dinuclear Complex. (in preparation)
3. R. T. Christiansen, W. Zheng (co-first auther), A.-L. Barra,‖ F. Le Mardel´e, M. Orlita, A. I. Kolesnikov, M. Appel, R. Cl´erac, J. Ollivier, S.-Q. Wu, O. Sato, and M. L. Baker, A strategy to quantify strong exchange coupling within molecular magnets exemplified for radical-bridged iron dimers (in preparation)